

Durham E-Theses

The Effects of Unsteady On-Road Flow Conditions on Cabin Noise

OETTLE, NICHOLAS,RICHARD

How to cite:

OETTLE, NICHOLAS,RICHARD (2013) *The Effects of Unsteady On-Road Flow Conditions on Cabin Noise*, Durham theses, Durham University. Available at Durham E-Theses Online:
<http://etheses.dur.ac.uk/7731/>

Use policy

The full-text may be used and/or reproduced, and given to third parties in any format or medium, without prior permission or charge, for personal research or study, educational, or not-for-profit purposes provided that:

- a full bibliographic reference is made to the original source
- a [link](#) is made to the metadata record in Durham E-Theses
- the full-text is not changed in any way

The full-text must not be sold in any format or medium without the formal permission of the copyright holders.

Please consult the [full Durham E-Theses policy](#) for further details.

The Effects of Unsteady On-Road Flow Conditions on Cabin Noise

NICHOLAS OETTLE

School of Engineering and Computing Sciences

Durham University



A thesis submitted for the degree of

DOCTOR OF PHILOSOPHY

2013

For Heather

Abstract

On-road, a vehicle experiences unsteady flow conditions due to turbulence in the natural wind, moving through the unsteady wakes of other road vehicles and traveling through the stationary wakes generated by roadside obstacles. There is increasing concern about potential differences between steady flow conditions that are typically used for development and the transient conditions that occur on-road.

This work considers whether steady techniques are able to predict the unsteady results measured on-road, the impact of this unsteadiness on the noise perceived in the cabin and whether minor changes made to the geometry of the vehicle could affect this. Both external aerodynamic and acoustic measurements were taken using a full-size vehicle combined with measurements of the noise inside the cabin. Data collection took place on-road under a range of wind conditions to accurately measure the response of the vehicle to oncoming flow unsteadiness, with steady-state measurements taking place in full-scale aeroacoustic wind tunnels.

Overall it was demonstrated that, using a variety of temporal and spectral approaches, steady techniques were able to predict unsteady on-road results well enough to assess cabin noise by correctly taking into account the varying on-road flow conditions. Aerodynamic admittance values remained less than unity in the sideglass region of the vehicle, with the exception of the the region nearest the A-pillar. The reducing unsteady energy at frequencies greater than 10 Hz, combined with the corresponding roll-off in admittance, implies that unsteady frequencies below 10 Hz affect the vehicle most, where the response remains quasi-steady.

Quasi-steady cabin noise simulations allowed a subjective assessment of the predicted unsteady cabin noise, where the impact of cabin noise modulations were quantified and found to be important to perception. Minor geometry changes affected the sensitivity of cabin noise to changes in yaw angle, altering modulation and therefore having an important impact on the unsteady wind noise perceived on-road.

Declaration

The work in this thesis is based on research carried out at the School of Engineering and Computing Sciences, Durham University, UK. No part of this thesis has been submitted elsewhere for any other degree or qualification and it all my own work unless referenced to the contrary in the text.

Copyright © 2013 by Nicholas Richard Oettle.

The copyright of this thesis rests with the author. No quotations from it should be published without the author's prior written consent and information derived from it should be acknowledged.

Acknowledgements

It is my pleasure to thank my supervisors, Dr Robert Dominy and Dr David Sims-Williams for their tireless enthusiasm, guidance and dedication to this work. They have provided me with countless opportunities during this time and I could not have asked for better academic role models.

I would also like to acknowledge other members of staff at the School of Engineering and Computing Sciences who have supported this work in innumerable ways. In particular, I would like to thank Mr Colin Wintrip, Mr Ian Hutchinson and Mr Gary Parker who provided me with technical assistance throughout the course of the project. Thanks should also go to postgraduate students from the department, including Michael Wilson, Fred Hamlin and Mark Rosamond who in particular gave their valuable time, assisting greatly in the manufacture of the pressure measurement probes. I am also grateful to those who I was fortunate enough to share office space with and those willing volunteers who participated in the jury testing investigation.

This project would also not have been possible without the support of Jaguar Land Rover in providing apparatus and wind tunnel testing time. In particular I would like to thank: Jon Darlington, who provided initial stimulus for the project in addition to generously providing test vehicles; Claire Freeman, for arranging the subjective listening study and who has been a continual source of support; and all those who at some point

assisted with the project, from its inception to completion, including all those that took part in the listening study. Thanks should also go to the staff at the wind tunnels of Ford of Europe, Merkenich and of Pininfarina, Turin.

I would also like to thank all those who made me feel so welcome during my months at IVK/FKFS, Stuttgart. Particular thanks goes to Dr Martin Helfer and Professor Jochen Wiedemann for making such a visit possible.

I am grateful to the Engineering and Physical Sciences Research Council for funding this project. The Royal Academy of Engineering should also be acknowledged for the allocation of travel funds to support the time spent in Stuttgart.

Finally, I would like to thank my parents and sister who have provided me with the foundations and support allowing me to get to where I am today, and to Heather, for her tireless patience, her unending encouragement and for making this journey all the more enjoyable.

Contents

List of Figures	xvii
List of Tables	xxvii
Nomenclature	xxix
1 Introduction and Aims	1
1.1 Motivation	1
1.2 Vehicle Aerodynamics	3
1.2.1 Time-Averaged Flow Field Around a Typical Vehicle	3
1.2.2 Unsteady Flow Structures Around a Vehicle	7
1.2.3 Wind Tunnel Testing	9
1.2.3.1 Flow Conditons	9
1.2.3.2 Wind Tunnel Configurations	10
1.2.3.3 Coordinate System	13
1.2.3.4 Capturing the Time-Averaged Environment	15
1.2.4 Key Remarks on Vehicle Aerodynamics	19
1.3 Aeroacoustics	20
1.3.1 Background	20
1.3.2 Acoustic Measurement	21
1.3.2.1 Sound Pressure and Sound Pressure Level	21

CONTENTS

1.3.2.2	Spectral Content of Sounds	22
1.3.3	Aeroacoustic Mechanisms	25
1.3.4	Typical Vehicle Wind Noise Sources	28
1.3.4.1	General Observations	28
1.3.4.2	A-Pillar	30
1.3.4.3	Door Mirrors	32
1.3.4.4	Windscreen Wipers	34
1.3.4.5	Cavity Noise	35
1.3.4.6	Other Noise Sources	36
1.3.5	Wind Noise Measurement	38
1.3.5.1	Aeroacoustic Wind Tunnels	38
1.3.5.2	In-Cabin Noise	40
1.3.5.3	External Noise	42
1.3.6	Computational Aeroacoustics	48
1.3.7	Psychoacoustics	51
1.3.7.1	Loudness	51
1.3.7.2	A-Weighting	53
1.3.7.3	Articulation Index	54
1.3.7.4	Other Metrics and Jury Testing	56
1.3.8	Key Remarks on Aeroacoustics	62
1.4	The Unsteady Environment	62
1.4.1	Contributing Factors	62
1.4.2	Characterisation of the Unsteady Environment	65
1.4.2.1	Probability Density Functions	65
1.4.2.2	Spectral Methods	66
1.4.2.3	Turbulence Intensity	67

1.4.2.4	Turbulence Length Scale	68
1.4.3	The Unsteady Environment as Experienced by a Vehicle	71
1.4.4	Characterisation of the Vehicle's Response To Unsteadiness	76
1.4.4.1	Quasi-steady Limits	77
1.4.5	Quantifying the Response	80
1.4.5.1	Techniques Assuming Quasi-Steady Behaviour	81
1.4.6	Assessing Vehicle Response Directly	84
1.4.7	Assessing Vehicle Response Indirectly through Simulation	93
1.4.7.1	Simulation of Wind Vector Relative to Vehicle	93
1.4.7.2	Simulation of Vehicle Movement Relative to Wind	103
1.4.8	Key Remarks on the Unsteady Environment	108
1.5	Summary and Objectives	109
1.5.1	Summary	109
1.5.2	Related Literature	111
1.5.3	Objectives	111
1.5.4	Thesis Outline	112
2	Experimental Techniques	115
2.1	Introduction	115
2.2	Instrumentation	115
2.2.1	Flow Measurements	115
2.2.1.1	Choice of Probe Type and Location	115
2.2.1.2	Five-Hole Probes	121
2.2.1.3	Sideglass Pressures	130
2.2.1.4	Pressure Transducers	132
2.2.1.5	Transducer and Probe Transfer Function Correction	133
2.2.2	Data Logging	135

CONTENTS

2.2.2.1	Filtering	137
2.2.2.2	Specific On-Road Instrumentation	138
2.2.3	Acoustic Measurements	139
2.2.3.1	Synchronisation	139
2.2.3.2	Cabin Noise	140
2.2.3.3	Surface Noise	142
2.2.4	Software Integration	143
2.2.5	Schematic of Overall Logging System	145
2.2.6	Terminology	146
2.3	Apparatus	147
2.3.1	Vehicles	147
2.3.1.1	Specification	147
2.3.1.2	Geometry Modifications	148
2.3.2	On-Road Testing	152
2.3.3	Wind Tunnel Testing	154
2.3.3.1	Ford Wind Tunnel	155
2.3.3.2	Pininfarina Wind Tunnel	156
2.3.3.3	Tunnel Comparison	158
2.4	Data Handling	165
2.4.1	Five-Hole Probe Data	166
2.4.2	Sideglass Pressure Data	166
2.4.3	Acoustic Data	167
2.4.4	Subjective Testing	167
2.4.4.1	Paired Comparison	168
2.4.4.2	Ranking	173

3 The Time-Averaged Vehicle Response	175
3.1 Introduction	175
3.2 Data Averaging	176
3.3 Flow Conditions	179
3.3.1 On-Road	179
3.3.2 Pininfarina Turbulence Generation System	184
3.4 Cabin Noise	189
3.4.1 Subjective Cabin Noise Assessment	189
3.4.2 Steady Wind Tunnel	193
3.4.2.1 Relationship Between Cabin Noise and Flow Speed	193
3.4.2.2 Relationship Between Cabin Noise and Vehicle Geometry	196
3.4.2.3 Relationship Between Cabin Noise and Yaw Angle	198
3.4.3 On-Road	209
3.4.3.1 Relationship Between Cabin Noise and Flow Speed	209
3.4.3.2 Relationship Between Cabin Noise and Yaw Angle	217
3.4.4 Unsteady Wind Tunnel	221
3.5 Surface Pressures	223
3.5.1 Relationship with Flow Speed	224
3.5.2 Steady Wind Tunnel	226
3.5.3 On-Road	229
3.5.4 Unsteady Wind Tunnel	233
3.6 Surface Noise	236
3.6.1 Steady Wind Tunnel	237
3.6.2 On-Road	238
3.6.3 Unsteady Wind Tunnel	243
3.7 Summary	245

CONTENTS

3.7.1	Cabin Noise	245
3.7.2	Sideglass Surface Pressures	246
4	The Time-Resolved Vehicle Response	247
4.1	Introduction	247
4.2	Assessment of the Transient Response	248
4.2.1	Typical Admittance and Transfer Function Approaches	248
4.2.2	An Alternative Linearised Transfer Function Approach	251
4.3	Surface Pressures	252
4.3.1	Determination of the Quasi-Steady Response	253
4.3.1.1	Simulation Technique	253
4.3.1.2	Temporal Comparison of On-Road and Simulated Data	254
4.3.2	Assessment of the Frequency Response	257
4.3.2.1	Linearised Transfer Functions	257
4.3.2.2	Self-Excited Effects	267
4.3.2.3	Separation of External and Self-Excited Unsteadiness	269
4.4	Cabin Noise	275
4.4.1	Steady State Cabin Noise Characteristics	275
4.4.2	Assessment of the Frequency Response	279
4.4.2.1	Linearised Transfer Functions	279
4.4.2.2	Broadband Modulation Approach	283
4.4.2.3	Third-Octave Modulation Approach	293
4.5	A Subjective Assessment of Simulated Cabin Noise	301
4.5.1	Generation of Cabin Noise Simulations	302
4.5.1.1	Effect of Yaw Sensitivity	303
4.5.1.2	Effect of an Increase in Level	304
4.5.1.3	Effect of Modulation Frequency	305

4.5.1.4	Control Characteristics	307
4.5.2	Responses	310
4.5.3	Analysis	311
4.5.3.1	The Impact of Level and Yaw Sensitivity on Perceived Cabin Noise	311
4.5.3.2	The Impact of Modulation on Perceived Cabin Noise . . .	315
4.6	Summary	318
4.6.1	Surface Pressures	318
4.6.2	Cabin Noise	319
4.6.3	Subjective Response to Cabin Noise Modulations	320
5	Conclusions and Further Work	323
5.1	Conclusions	323
5.2	Suggestions for Further Work	327
	References	329

List of Figures

1.1	Focus of this research	2
1.2	A and C-pillar vortices, modified from Hucho (1998)	3
1.3	Simplified flow around the windscreen, modified from Hucho (1998)	4
1.4	The main flow separations around the three types of car back, modified from Hucho (1998)	5
1.5	Examples of tunnel configurations	11
1.6	Wind and resultant flow vectors relative to absolute and vehicle reference frames	14
1.7	Components of the resultant flow vector relative to vehicle reference frame	14
1.8	The possible flow regimes for a given flow speed and yaw	16
1.9	The range of vehicle and wind speeds simulated by a wind tunnel test at 130 km h ⁻¹ at various yaw angles	17
1.10	The range of vehicle and wind speeds captured by an example wind tunnel testing strategy	18
1.11	Comparison of overall level, third-octave and narrowband spectra	24
1.12	Aeroacoustic noise sources	26
1.13	Sound sources in the sideglass region, modified from Blumrich (2006)	29
1.14	Typical vortex structure around A-pillar, from Howell et al. (2006)	30

LIST OF FIGURES

1.15 Examples of bumps and grooves on production vehicle mirrors, from Helfer (2005)	33
1.16 Cabin measurement using binaural acoustic heads	41
1.17 Acoustic mirror as used in an aeroacoustic wind tunnel, from Helfer (2005)	43
1.18 Aeroacoustic sound intensity probe, from Helfer (2000b)	45
1.19 Examples of microphone arrays used in beamforming	47
1.20 Equal loudness contours according to ISO226:2003	52
1.21 Frequency response of the A-weighted filter	54
1.22 Articulation Index calculation graphs	55
1.23 Sharpness weighting function, $g(z)$, defined by Fastl and Zwicker (2007)	58
1.24 Just-noticeable modulation degree, from Terhardt (1998)	59
1.25 Example power spectra with equivalent turbulence intensities and von Kármán length scales, from Wordley (2009)	70
1.26 Mast-mounted probe, from Watkins (1990)	72
1.27 Front-mounted probe rake, from Wordley (2009)	74
1.28 Turbulence conditions in different on-road environments, modified from Wordley (2009)	75
1.29 On-road cross-flow spectra, from Wordley (2009)	76
1.30 Expected bounds for vehicle quasi-steady response	78
1.31 Wind, vehicle and resultant flow vectors relative to the vehicle	83
1.32 Side door pressure tappings, from Gilhome and Saunders (2002)	85
1.33 Probe mounted ahead of windscreen, from Mayer et al. (2007)	86
1.34 Yaw moment admittance, modified from Mayer et al. (2007)	87
1.35 Roof-mounted probe, from Watkins et al. (2001)	88
1.36 Front-mounted probe, from Lindener et al. (2007)	89

1.37 Wind noise prediction of 4 kHz octave band, modified from Lindener et al. (2007)	90
1.38 Cabin noise modulation and oncoming flow turbulence, from Lindener et al. (2007)	91
1.39 Example of an anemometer used in coastdown testing, from Walter et al. (2001)	92
1.40 Wind tunnel turbulence targets, from Wordley (2009)	94
1.41 Examples of passive grids, from Watkins (1990)	95
1.42 Examples of passive methods used to generate a range of scales	96
1.43 Examples of the use of vehicles to generate turbulence	96
1.44 The Turbulence Generation System of the Pininfarina wind tunnel	98
1.45 Examples of lift-based active turbulence generation systems	99
1.46 Active aerofoil gust generator, from Schröck et al. (2009a)	100
1.47 Modifications made to an SAE reference body, from Schröck et al. (2011)	101
1.48 Aerodynamic admittance functions, modified from Schröck et al. (2011)	102
1.49 Oscillating models	105
1.50 Crosswind generator, from Sedarous et al. (2007)	107
2.1 Probe mounting options	117
2.2 Probe mount	121
2.3 Typical five-hole probe head with numbering convention	122
2.4 Five-hole probes used during experimentation	123
2.5 Calibration surfaces for Probe 5H50012	126
2.6 Calibration surfaces for Probe 5H50015	127
2.7 Effect of vehicle on probe flow measurement on-road	129
2.8 Location of pressure tappings on vehicle sideglass	131
2.9 Diagram of transducer and probe transfer function correction apparatus	134

LIST OF FIGURES

2.10 Transfer function of probe and tubing system (central hole)	136
2.11 Transfer function of sideglass pressure tapping and tubing system	136
2.12 Acoustic head installed in front passenger seat	141
2.13 Location of surface microphones on vehicle sideglass	142
2.14 Images of surface microphone attachment to sideglass	143
2.15 Schematic of LogVoltsGPS	144
2.16 Example of data output from LogVoltsGPS	144
2.17 Schematic of overall logging system	145
2.18 Acoustic head channel names and positions	146
2.19 Vehicle at yaw with positions of external instrumentation	147
2.20 Jaguar XF © Jaguar Land Rover	148
2.21 Comparison of Geometry 1 and 2 door mirrors	150
2.22 Vehicle geometries used for cabin noise measurements	151
2.23 Vehicle geometries used for sideglass measurements	151
2.24 Images of bonnet kicker and attachment to existing bonnet	152
2.25 Typical on-road conditions	153
2.26 Testing locations for Geometry 1 and 2 vehicles (Map data © OpenStreetMap contributors, CC BY-SA)	154
2.27 Testing locations for Geometry 2 and 3 vehicles (perspex sideglass) (Map data © OpenStreetMap contributors, CC BY-SA)	155
2.28 Ford of Europe Wind Tunnel	156
2.29 Pininfarina Wind Tunnel	157
2.30 Images of the mirror configurations as tested at the Pininfarina AWT . .	158
2.31 TGS as used during testing	158
2.32 Ford AWT: Error of roof-mounted probe measurements (Geometry 1) . .	160
2.33 Pininfarina AWT: Error of roof-mounted probe measurements	162

2.34 Comparison of third-octave tunnel spectra	164
2.35 Alternative offset method in dividing the sound file	169
2.36 Relative lengths of sound samples within a comparative pair	170
3.1 Bin-averaging process	177
3.2 Sets of bins used to average the on-road data	179
3.3 Distribution of on-road data between each of the bins	180
3.4 Probability distributions of on-road flow conditions	181
3.5 Probability distributions for individual vehicle geometries	183
3.6 Turbulence conditions measured on-road	184
3.7 On-road flow turbulence conditions reported by each vehicle geometry .	185
3.8 Relationship between yaw and turbulence intensity	186
3.9 Probability distributions of yaw generated by the Pininfarina TGS	187
3.10 Turbulence conditions as generated by the Pininfarina TGS	188
3.11 Generation of subjective index to cabin noise annoyance	190
3.12 Assessment of subjective index against psychoacoustic metrics	192
3.13 Steady AWT cabin noise at various wind tunnel speeds (Geometry 1) . .	194
3.14 Nature of noise sources in AWT (Geometry 1)	196
3.15 Steady AWT (Pininfarina) variation of cabin noise at $\psi = 0^\circ$ between Geometry 1 and 2	197
3.16 Steady AWT (Pininfarina) variation of third-octave cabin noise at $\psi = 0^\circ$ between Geometry 1 and 2	199
3.17 Steady AWT (Pininfarina) variation of overall SPL at yaw	200
3.18 Steady AWT (Pininfarina) variation of LHLE cabin noise spectra at yaw (Geometry 1)	202
3.19 Steady AWT (Pininfarina) variation of RHRE cabin noise spectra at yaw (Geometry 1)	203

LIST OF FIGURES

3.20 Steady AWT (Pininfarina) variation of LHLE cabin noise spectra at yaw (Geometry 2)	204
3.21 Steady AWT (Pininfarina) variation of RHRE cabin noise spectra at yaw (Geometry 2)	205
3.22 Steady AWT (Pininfarina) variation of LHLE cabin noise spectra at yaw between Geometry 1 and 2	207
3.23 Steady AWT (Pininfarina) variation of RHRE cabin noise spectra at yaw between Geometry 1 and 2	208
3.24 On-road and AWT overall SPL at various flow speeds (Geometry 1) . . .	210
3.25 Calculated on-road sound source contributions (Geometry 1)	213
3.26 Calculated third-octave on-road sound source contributions (Geometry 1)	214
3.27 Calculated R^2 of third-octave on-road sound source contributions (Ge- ometry 1)	215
3.28 Flow speed when third-octave wind noise dominates other sound source contributions (Geometry 1)	216
3.29 On-road variation of overall SPL with yaw, compared with equivalent AWT data	218
3.30 On-road variation of overall and 800 Hz third-octave band SPL with yaw	219
3.31 On-road variation of 2, 4 and 8 kHz third-octave bands with yaw	220
3.32 AWT (Pininfarina) variation of 2, 4 and 8 kHz third-octave bands with yaw	221
3.33 Variation in cabin noise between vehicle geometries at various TGS modes	222
3.34 Variation in 4 kHz cabin noise between vehicle geometries at various TGS modes	223
3.35 On-road sideglass pressure characteristics (Geometry 2)	225
3.36 Steady AWT sideglass pressure characteristics (Geometry 1 SG)	227

3.37 Steady AWT sideglass pressure characteristics (Geometry 2 SG)	228
3.38 On-road sideglass pressure characteristics (Geometry 2 SG)	230
3.39 On-road sideglass pressure characteristics (Geometry 3 SG)	232
3.40 TGS sideglass pressure characteristics (Geometry 1 SG)	234
3.41 TGS sideglass pressure characteristics (Geometry 2 SG)	235
3.42 AWT (Pininfarina) sideglass surface noise characteristics	237
3.43 On-road sideglass surface noise characteristics	239
3.44 On-road surface pressure characteristics at equivalent surface microphone positions (Geometry 2 SG)	242
3.45 On-road sideglass surface noise characteristics	243
4.1 Method to determine the transient response of a vehicle via admittance .	249
4.2 Method to determine the transient response of a vehicle via an alterna- tive linearised approach	251
4.3 Determination of the simulated quasi-steady predicted surface pressure response	254
4.4 Comparison of the simulated quasi-steady predicted surface pressure response with that measured on-road	255
4.5 Vehicle Geometry 2 (perspex sideglass): Mirror region	256
4.6 Vehicle Geometry 2 (perspex sideglass): Vortex region	258
4.7 Vehicle Geometry 2 (perspex sideglass): Reattachment region	259
4.8 Determination of the constituent spectra for the overall surface pressure transfer function	260
4.9 Vehicle Geometry 2 (perspex sideglass): Mirror region	261
4.10 Vehicle Geometry 2 (perspex sideglass): Vortex region	262
4.11 Vehicle Geometry 2 (perspex sideglass): Reattachment region	263
4.12 On-road to AWT sideglass pressure transfer functions (Geometry 2 SG) .	265

LIST OF FIGURES

4.13 Fluctuation of c_p measured on-road against AWT quasi-steady prediction at low and high frequencies (Tapping 8, Geometry 2 SG)	268
4.14 Fluctuation of c_p measured on-road against AWT quasi-steady prediction at narrower frequency range (Tapping 8, Geometry 2 SG)	269
4.15 Contributions of external and self-excited unsteadiness to overall side-glass pressure transfer functions (Mirror wake region, Geometry 2 SG) .	271
4.16 Contributions of external and self-excited unsteadiness to overall side-glass pressure transfer functions (A-pillar vortex region, Geometry 2 SG)	272
4.17 Contributions of external and self-excited unsteadiness to overall side-glass pressure transfer functions (Vortex reattachment region, Geometry 2 SG)	273
4.18 Vehicle Geometry 1 AWT cabin noise third-octave characteristics	277
4.19 Vehicle Geometry 1 AWT cabin noise characteristic	278
4.20 Temporal comparison between cabin noise measured on-road and quasi-steady predicted from steady wind tunnel (4000 Hz, Geometry 1)	280
4.21 Transfer functions between quasi-steady predicted and on-road measured cabin noise, based on steady AWT characteristics (Geometry 1) . .	281
4.22 Cabin noise simulation using time-averaged characteristic alone	283
4.23 Cabin noise simulation through modulation of the time-variant cabin noise	284
4.24 Temporal comparison of broadband simulated and measured cabin noise (Geometry 1)	285
4.25 Comparison between third-octave and overall SPL under changes to resultant flow speed in AWT (Geometry 1)	288
4.26 Comparison between third-octave and overall SPL under changes to yaw angle in AWT (Geometry 1)	289

4.27 Transfer functions between quasi-steady predicted and on-road measured cabin noise, using broadband modulation simulation technique (Geometry 1)	291
4.28 Cabin noise simulation through third-octave modulation of the time-variant cabin noise	295
4.29 Temporal comparison of third-octave simulated and measured cabin noise (Geometry 1)	296
4.30 Transfer functions between quasi-steady predicted and on-road measured cabin noise, using third-octave modulation simulation technique (Geometry 1)	297
4.31 Standard deviation of quasi-steady predicted and on-road measured cabin noise fluctuations, using third-octave modulation simulation technique (Geometry 1)	299
4.32 Yaw time history 20090619bHist3,8-16s used in subjective assessment .	302
4.33 YawSens0 characteristic and simulated time history	303
4.34 YawSens1 characteristic and simulated time history	304
4.35 YawSens0Plus characteristic and simulated time history	305
4.36 YawSens1Plus characteristic and simulated time history	306
4.37 YawSens0Stretched yaw angle and simulated time history	307
4.38 YawSens0Compressed yaw angle and simulated time history	308
4.39 AWT characteristic and simulated time history	308
4.40 AWTave characteristic and simulated time history	309
4.41 AWTMax characteristic and simulated time history	310
4.42 Subjective response data of cabin noise simulations	311
4.43 Effect of yaw sensitivity	312
4.44 Effect of an increase in level	313

LIST OF FIGURES

4.45 Effect of an increase in SPL	314
4.46 Effect of modulation	316
4.47 Comparative effect of overall SPL and SPL fluctuation of selected sound samples	317

List of Tables

2.1 Probe specifications 124

2.2 Acoustic head channel names 146

2.3 Summary of all vehicle geometries used 148

2.4 Summary of vehicle geometries tested on-road 153

2.5 Summary of vehicle geometries tested in the Ford AWT 155

2.6 Summary of vehicle geometries tested in the Pininfarina AWT 157

2.7 Specifications of wind tunnels 159

2.8 Methods used in calculating various psychoacoustic parameters 167

2.9 Randomisation of sample pairs 171

Nomenclature

Roman Symbols

A_f	Vehicle frontal area [m ²]
AI	Articulation index [%]
$AI'(k)$	Specific articulation index [% / band]
A_N	Wind tunnel nozzle area [m ²]
a	Effective speed of sound [ms ⁻¹]
b_0, b_1	Regression constant and coefficient
$C_{xx}(t)$	Autocovariance
c_D	Drag coefficient [-]
$c_{D,WA}$	Wind-averaged drag coefficient [-]
D	Probe head diameter [mm]
d	Characteristic dimension [m]
d	Number of circular triads in a paired comparison
\hat{E}	East (unit vector) [-]
$F(t)$	Oncoming flow (general form)
f	Frequency [Hz]
f_s	Sample frequency [Hz]
f_v	Vortex shedding frequency [Hz]

NOMENCLATURE

$G_{xx}(f)$	Autospectral density
$G_{xy}(f)$	Cross-spectral density
$g(z)$	Sharpness weighting function [-]
$H(f)$	Transfer function (Frequency response function)
I	Sound intensity [W/m ²]
I	Turbulence intensity [%]
i, j, k	Unit vectors aligned with the vehicle reference frame
i, n	Generic index variables
k	Frequency band number
k	Reduced frequency [-]
L	Effective tubing length [m]
L	Sound pressure level [dB _{SPL}]
L	Turbulence length scale [m]
M	Mach number [-]
m	Degree of modulation [%]
N	Loudness [sones]
$N'(z)$	Specific loudness [sones/bark]
N	Number of sound samples used for jury testing
N_s	Number of recorded samples
\hat{N}	North (unit vector) [-]
\mathbb{N}	Set of real, positive integers
\mathcal{N}	Normal distribution
n	Number of observations
n	Sound sample number

n	Source index
P	Pressure [Pa]
$P(X)$	Probability of X
$R(t)$	Vehicle response (general form)
Re	Reynolds' number [-]
r	Subjective score [-]
\bar{r}	Averaged subjective score [-]
\hat{r}	Normalised subjective score [-]
S	Sharpness [acum]
St	Strouhal number [-]
T	Characteristic time scale [s]
T	Lighthill turbulence stress tensor
T	Total time [s]
t	Time [s]
\mathbf{u}	Flow velocity vector [ms^{-1}]
\bar{u}	Mean flow speed [ms^{-1}]
\mathcal{U}	Uniform distribution
W	AI weighting factor [-]
X	Generic random variable
X, Y	Fourier transforms of x and y
x, y	Generic variables
\bar{x}, \bar{y}	Mean values of x and y
\hat{y}	Predicted value of y
z	Critical band number [bark]

NOMENCLATURE

Subscripts

0...4	Quantities relating to the corresponding holes in a five-hole probe
Avg	Average
AWT	Relating to the aeroacoustic wind tunnel
c	Centre
d	Dipole
Dyn	Dynamic
File	Related to the sound file used for a paired comparison
M	Measured
Max	Maximum quantity
Min	Minimum quantity
Mod	Modulation
m	Monopole
Pair	Related to an individual comparison pair
QS	Quasi-steady predicted
q	Quadrupole
Ref	Reference quantity
Res	Resultant
RMS	RMS quantity
S	Simulated
Set	Related to a set of sound samples used for a paired comparison
s	Sampling
Test	Related to an entire paired comparison test
Test	Test quantity

Tot	Total
Veh	Vehicle
x, y, z	Quantities aligned with vehicle reference frame

Greek Symbols

α	Flow pitch angle [°]
β	Vehicle heading [°]
γ	Wind heading [°]
δ_{ij}	Kronecker delta
ζ	Coefficient of consistence [-]
θ	Phase angle [°]
λ	Wavelength of unsteadiness [m]
μ	Mean value
ρ	Density of air [kg/m ³]
$\rho_{xx}(t)$	Correlation function
σ	Standard deviation
τ	Time shift [s]
ϕ	Wind direction relative to vehicle [°]
ϕ	Wind tunnel blockage ratio [-]
ψ	Flow yaw angle [°]
ψ_{AWT}	AWT turntable angle [°]

Acronyms

ASD	Autospectral density
-----	----------------------

NOMENCLATURE

AWT	Aeroacoustic wind tunnel
CAA	Computational aeroacoustics
CFD	Computational fluid dynamics
CFL	Courant-Friedrichs-Lewy condition
CSD	Cross-spectral density
DNS	Direct Numerical Simulation
FFT	Fast Fourier transform
FSS	Full-scale span, the output voltage range of a pressure transducer
GPRMC	GPS recommended minimum sentence C
GPS	Global Positioning System, used to determine absolute vehicle velocity
ISA	International Standard Atmosphere, 15 °C and 101325 Pa at sea-level
LDV	Laser Doppler velocimetry
LHLE	Left head, left ear
LIDAR	Light detection and ranging
PDF	Probability density function
PIV	Particle image velocimetry
QS	Quasi-Steady
RHRE	Right head, right ear
RMS	Root-mean-square
RSO	Roadside obstacles
SG	Relating to the instrumented perspex sideglass
SPL	Sound pressure level
TF	Transfer function (frequency response function)
TGS	Turbulence generation system, as used in the Pininfarina AWT

CHAPTER 1

Introduction and Aims

1.1 Motivation

The relative contribution of the engine, powertrain, wheels and wind in producing the overall noise heard inside the passenger compartment of a car varies at different vehicle speeds. At higher speeds aerodynamic noise tends to dominate. This is especially the case in the luxury vehicle sector, where other sound sources tend to be located away from the passengers and relatively well insulated, as noted by Helfer and Busch (1992). The generation of wind noise in areas near to the vehicle occupants can lead to wind noise being a prominent source of noise. The reduction of this interior cabin noise is desirable, since a decrease in this increases both the level of passenger comfort inside the vehicle and the perception of the vehicle's quality. The importance of this is highlighted in the J. D. Power customer satisfaction rankings, where in both 2005 and 2008 wind noise was the most frequently reported customer complaint throughout the automotive industry, from Tews (2008). Wind noise can also be significant in road safety, since high levels of noise can lead to driver fatigue and a reduction in concentration.

1. INTRODUCTION AND AIMS

There are increasing amounts of research comparing aerodynamic and aeroacoustic data measured both in the wind tunnel and on-road. The motivation being that the conditions experienced in a wind tunnel have very low turbulence levels and these tend not to be experienced on the road. There is concern that data obtained in these steady flow environments do not capture the vehicle's response to unsteady fluctuations in the inherently turbulent external surroundings.

Figure 1.1 highlights the main topics relevant to this research. This includes: the fields of road vehicle aerodynamics, typically assessed in the steady environment of the wind tunnel; how the vehicle responds to unsteady conditions, both those occurring on-road and simulated; and how these conditions affect the aerodynamic noise of the vehicle and what impact this has on the vehicle occupants.

This introductory chapter focusses on these three key areas, before concluding with a summary of how the work presented in this thesis combines and expands these topics.

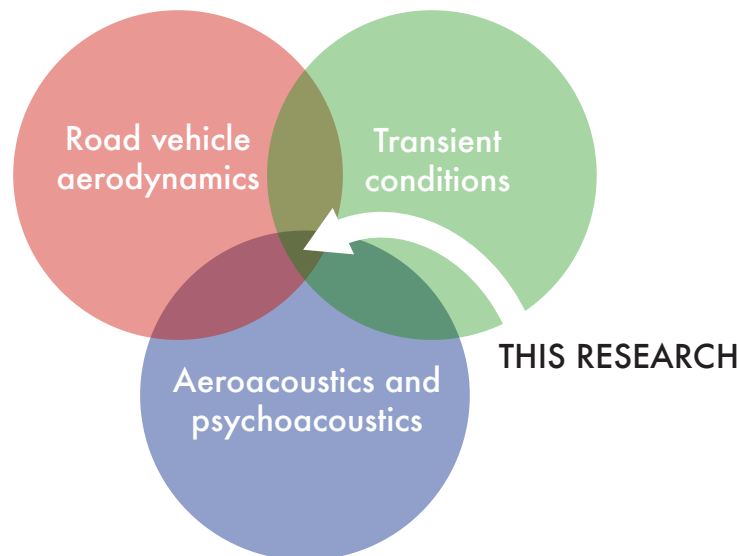


Figure 1.1: Focus of this research

1.2 Vehicle Aerodynamics

1.2.1 Time-Averaged Flow Field Around a Typical Vehicle

The shape of a passenger car is driven primarily by a combination of styling, ergonomics and safety, with aerodynamics only part of the overall form considerations. The combination of each of these requirements results in a vehicle being a bluff body rather than a streamlined body, with a low aspect ratio dictating that the flow structures formed around the vehicle are strongly three-dimensional. The interaction of these complex flows from different parts of the vehicle dictate that the aerodynamics of the entire vehicle must be studied, with two-dimensional approximations generally inappropriate.

The flow over the vehicle is dominated by the trailing vortex structures generated by the slanted A and C-pillars, at the front and rear of the vehicle respectively. Figure 1.2 shows these structures as formed by a generically shaped vehicle.

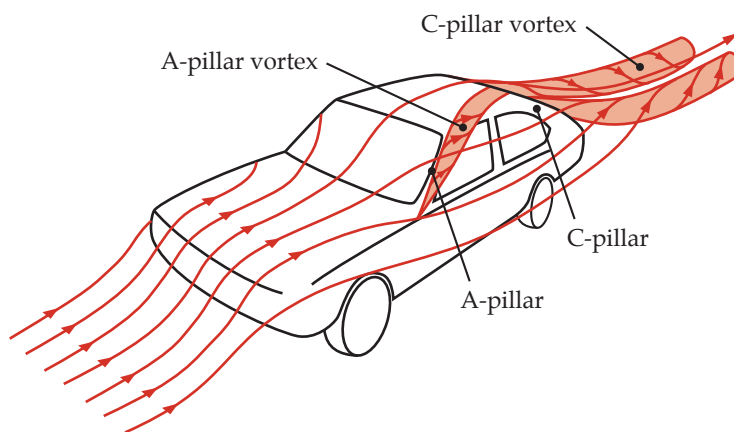


Figure 1.2: A and C-pillar vortices, modified from Hucho (1998)

These separated flow structures are prone to unsteadiness and can lead to low-frequency unsteady behaviour, affecting the response of the vehicle. This can have

1. INTRODUCTION AND AIMS

implications for vehicle handling and stability, and as is the focus of this thesis, the generation and modulation of wind noise particularly in the A-pillar region. Figure 1.3 shows a highly simplified representation of the typical flow structures around the windscreen region.

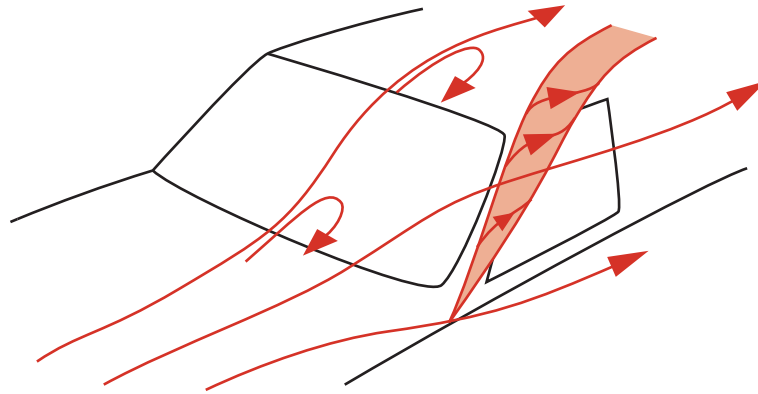


Figure 1.3: Simplified flow around the windscreen, modified from Hucho (1998)

The separated flow region at the base of the windscreen, in the area commonly known as the cowl, can impact the windscreen and lead to unsteady loading that can affect wind noise. The windscreen wipers are also in this region and fluctuations in this separation can interact with the wipers causing flutter. Depending on the cowl geometry, the wipers may be 'aerodynamically hidden,' out of the flow and enclosed within the cowl below the bonnet line or positioned above the bonnet and visible both in the literal sense and to the oncoming flow. If this is the case, flow structures generated by the wipers themselves can not only impact on the windscreen, but also interact with the A-pillar vortex and mirror wake, leading to increased fluctuations and unsteadiness. The size of the separation from the top of the windscreen is dependent on the angle of the windscreen. This in turn is driven not only by styling, but by passenger impact safety where a shallower angle is preferred, as well as aerodynamics, where a shallower angle can reduce drag and frontal lift, Hucho (1998). This region tends

to be less important from a wind noise perspective in the case of a metal roof where attenuating headlining materials can reduce the impact of such separations, but can be more significant with glass panoramic roofs and sunroofs.

The separated flow structures at the rear of the vehicle have a greater impact on drag and fuel economy, and less of an impact on wind noise than those structures at the front of a vehicle, since these are generally further away from a passenger's ear. Also as suggested by Cooper (2002), the vehicle handling can be sensitive to the flow at the rear of the vehicle. In the studies of vehicle aerodynamics, it is common to divide the various rear-end shapes of a vehicle into three categories: the square-back, the fast-back and the notch-back. These three shapes are shown in Figure 1.4 with their corresponding separated flow structures, as modified from Hucho (1998) and originally developed from work by Ahmed and Baumert (1979).

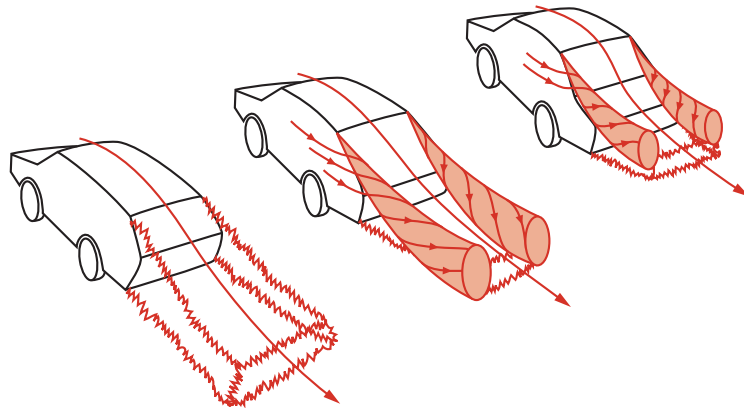


Figure 1.4: The main flow separations around the three types of car back, modified from Hucho (1998)

There are two main types of flow separation and these can be both present in the wakes behind a vehicle. The first form occurs parallel to a line of separation, with the resulting free vortices forming being generally weak and dissipating through the turbulent mixing action of the free shear layer. The nature of this separation can gen-

1. INTRODUCTION AND AIMS

erally be considered to be quasi-two dimensional. Examples of this include the cowl and roof separations as shown in Figure 1.3 and the large-scale separation that occurs at the rear of a square-back vehicle and shown on the leftmost image of Figure 1.4. The separation here forms at the rear edge of the roof and creates a recirculating wake of *dead water* behind the vehicle. The second type of separation is where the oncoming flow interacts with an angled edge and rolls up, forming a conical vortex. Such a mechanism is exploited to create lift in delta-winged aircraft. It is these separations that form the vortex structures around the A-pillars, but also from the angled C-pillars in fast-back and notch-back vehicles.

The sloping rear screen of a fast-back vehicle, as shown in the central image of Figure 1.4 leads to a very different flow structure than that of the square-back vehicle. Two large vortices form from the C-pillars, with the resulting low pressure region in the vortex cores leading to an increased drag penalty over that of the square-back, contrary to the name of the fast-back. The low pressure over the rear also leads to rear lift. At the base of the rear screen, quasi two-dimensional separation occurs, similar in nature to the separations at the top of a rear screen on a square-back. As observed by Ahmed et al. (1984), with increasing rear screen angle from the horizontal, there is an initial drag reduction as the base area of the vehicle and thus the size of the separated wake is reduced. A drag minimum is reached at a critical angle of approximately 15° . As the angle of the rear screen continues to become steeper, the strength of the trailing vortices increase and with it the negative pressure level, similar to behaviour observed of a delta wing at incidence. Beyond a critical angle of approximately 30° these vortices collapse and the behaviour reverts to that of a square back, with the quasi two-dimensional separation returning to the top of the rear screen.

The behaviour of a notchback vehicle is similar to that of the fast-back in that there are the same two observable types of flow separations, as shown in the rightmost im-

age of Figure 1.4. These flow structures are typically more complex, with increased interaction between the separated flow structures and body geometry than that of the fast-back. Owing to the different aspect ratio of the inclined rear screen, the strength of the vortices is generally weaker. Observations by Nouzawa et al. (1992) have shown that the critical angle in a notch-back vehicle is driven not by the angle of the rear screen alone, but by the angle made between the top of the rear screen and the edge of the boot. With the aim of reducing drag by achieving a 15° effective backlight angle, this has resulted in raising the height of the boot deck. This has led to the 'boxy' traditional notch-back design evolving into a design more similar to the fast-back, blurring the distinctions between the two styles.

1.2.2 Unsteady Flow Structures Around a Vehicle

Unsteadiness in a flow field can lead to noise generation, however this unsteadiness is not solely due to that encountered on-road. Self-excited unsteadiness, such as Kármán vortex shedding, is unsteadiness that is generated through flow–structure interactions and this can be important in terms of noise generation and vehicle dynamics. In some cases, such as described by Blevins (1990), the unsteadiness encountered on-road can in fact reduce the levels of self-excited unsteadiness by breaking up coherent unsteady structures. This section focusses on the larger-scale unsteady flow structures associated more with vehicle dynamics and handling, whereas unsteady structures focussed more on noise generation are discussed in Section 1.3.4.

Sims-Williams (2001); Sims-Williams et al. (2001) investigated unsteady flow structures in the wake of real and idealised hatchbacks. It was found that there were strong similarities between these geometries, indicating that smaller changes in geometry may have little effect in changing the unsteadiness present in the wakes of vehicles. The investigation was extended to incorporate CFD, from Sims-Williams and Duncan

1. INTRODUCTION AND AIMS

(2002). Further investigations presented by Sims-Williams et al. (2006) focussed on the formation regions of the trailing C-pillar vortices of a vehicle using an idealised model in a water tow-tank. In a related study, Howell and Baden Fuller (2010) investigated the relationship between lift and lateral aerodynamic characteristics and found that lower lift tended to lead to a lower yawing moment, affecting crosswind stability. The flow structures causing this were not fully investigated, but were linked to the C-pillar trailing vortices.

Another flow phenomenon that can be present at the rear of notchback vehicles is bistable asymmetric flow structures, even though the geometry of a vehicle is itself symmetric. Gaylard et al. (2007) investigated this periodic flow asymmetry and reviewed the findings of other authors, including Sims-Williams and Hetherington (2006) and whilst the complex wake structure was assessed, no explanation was determined as to why the wake structure could be strongly asymmetric. It was suggested that small perturbations were sufficient to cause degeneration of the unstable regions of the symmetric flow structure, as identified by Gilhome et al. (2001). Further evidence to suggest this is found in the work of Schröck et al. (2009b), who found that by increasing the level of turbulence in a model tunnel, the wake of an idealised body became more symmetric than under smooth flow conditions. Work by Sims-Williams et al. (2011) continued by investigating the link between notchback geometry and unsteady wake structures and determined a relationship between notch angle and rear flow structures. Unsteady CFD calculations allowed both symmetric and asymmetric structures to be resolved, with the asymmetric structures lost in steady-state calculations. Another form of bistable unsteadiness was observed by Janssen and Hucho (1975) where the rear flow structures of a vehicle flipped between those of a square-back and a fast-back within a critical backlight angle range and separation could occur at either the top or bottom of the rear windshield.

1.2.3 Wind Tunnel Testing

1.2.3.1 Flow Conditions

The study of road vehicle aerodynamics has a history beginning at the start of the twentieth century, shortly after the controlled, heavier-than-air flight pioneers had begun their investigations in earnest. However, it was not until after the Second World War that the technique of testing vehicles in the controlled environment of a wind tunnel developed. These facilities, originally designed for the aerospace industry, conditioned the flow so that turbulence levels were very low and the flow was homogenous. As new tunnels were built, these too followed the same principles of low turbulence. The recommendations by SAE J2071 (1994), that open-throat wind tunnels should have turbulence intensities no greater than 0.5%, stand as testament to this.

There are a number of reasons why low turbulence wind tunnels have continued to be used as a tool to design road vehicles that are used in higher turbulence conditions. Firstly, by having wind tunnels around the world based on similar principles, results obtained in different wind tunnels should be broadly comparable. It is much easier to have a consistency in smoothness of flow rather than drawing comparisons with the added complications of turbulence generation. However in reality, owing to the wide array of different tunnel designs and sizes, results obtained in different tunnels are not as comparable as one may assume. Secondly, and perhaps more relevantly, is that work to fully describe the turbulent conditions experienced by a vehicle on the road has only recently started to move to the fore. With the emergence of this new work tunnels have begun to start to incorporate these findings into technologies that attempt to simulate on-road unsteadiness, thus making the conditions in the wind tunnel more closely resemble those on road. This has culminated in a number of solutions to simulate this unsteadiness, which are discussed further in Section 1.4.1.

1. INTRODUCTION AND AIMS

1.2.3.2 Wind Tunnel Configurations

There are principally two wind tunnel configurations. A closed-return tunnel, also commonly known as a Prandtl or Göttingen type tunnel, named after the pioneer and location of its original development, drives the air round in a closed circuit. The open-return tunnel, also known as an Eiffel tunnel after its pioneer, who was one of Prandtl's contemporaries, takes air from the surroundings which passes through the test section before being expelled. There are advantages and disadvantages to both systems. A Göttingen tunnel's main benefit is its lower power requirements than an open-return tunnel, which brings in savings in terms of smaller fans, motors and electricity. Disadvantages include the larger costs associated with a larger facility incorporating a return leg in addition to the larger amount of space taken up by such a facility. Owing to the recirculation of the air in the tunnel, the temperature in the tunnel can rise significantly during a long testing session and this can affect clay models and also aeroacoustic measurements, for example by affecting the compliance of the door seals. Therefore, some tunnels incorporate a heat exchanger to control the tunnel conditions, for instance Walter et al. (2002). The advantages of an open-return tunnel are the converse of the closed tunnel's disadvantages. An open-return tunnel can take up less area than a close-return tunnel, and therefore can be more suited to an location where space is limited, such as Pininfarina, as noted by Hucho (1998). To maximise the space efficiency of a closed-return tunnel, BMW's current state-of-the-art facility in Munich comprises two closed-return tunnels, with a smaller tunnel configured in a vertical loop, surrounded by another closed-return tunnel in the horizontal plane, as described by Duell et al. (2010). Two examples of wind tunnel configurations are shown in Figure 1.5, with Figure 1.5(a) showing an closed-return configuration whilst Figure 1.5(b) shows an open-return configuration.

Tunnel test section configurations also come in a variety of different designs. Per-

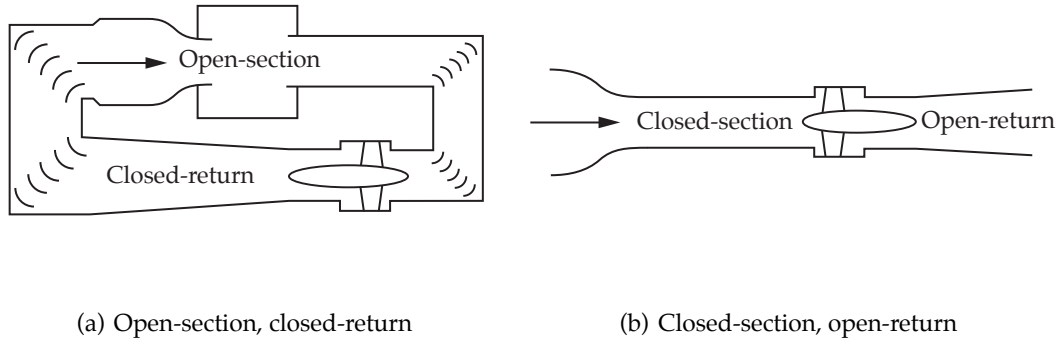


Figure 1.5: Examples of tunnel configurations

haps confusingly the two main configurations are also known as closed and open. An open-jet wind tunnel used in automotive testing is not fully open and is best described as three-quarters open, since the floor representing the road closes the lower surface of the jet. In an open test section, the vehicle under test is immersed in the flow from the wind tunnel nozzle, in that the flow is allowed to diverge around the vehicle. In reality, the streamlines diverge more than in the free air, as shown by Mercker and Wiedemann (1996), and therefore the local velocity in the vicinity of the vehicle is slower than on-road. By contrast, the presence of a vehicle in a closed test section causes the flow in the vicinity of the vehicle to speed up, owing to the reduction in flow area and the principles of continuity. This reduction in flow area is described by a blockage ratio ϕ and is the fraction of nozzle area A_N taken up by the frontal area of the vehicle A_f , such that $\phi = \frac{A_f}{A_N}$. As described by Hucho (1998), in addition to the carry-over of low turbulence tunnels from the aeronautics industry, so was the requirement for a blockage ratio of $\phi = 0.05$ in the first automotive tunnels. With frontal areas of vehicles approximately two square metres, this leads to nozzle areas of $A_N \approx 40 \text{ m}^2$. Later research showed that a larger ratio was acceptable, with $\phi = 0.10$ reasonable with suitable blockage correction, although up to $\phi \approx 0.20$ is not uncom-

1. INTRODUCTION AND AIMS

mon in smaller wind tunnels. Corrections can be made for these blockage effects, with an extensive summary of the various wind tunnel interference effects given by Wickern (2007). In addition, Gleason (2007) assessed blockage effects in closed wall wind tunnels and found that blockage ratios greater than 5% lead to distortions in flow field which are not readily corrected. Furthermore, Zimmer et al. (2001b) assessed A-pillar flow structures in a high blockage closed-jet wind tunnel and found results to be satisfactory, so long as the local velocity in the region of interest is matched to a comparative condition. However, it is likely that this may not be the case for regions further downstream which may be more affected by upstream changes. An example of an open-section wind tunnel is shown in Figure 1.5(a), with Figure 1.5(b) showing a closed-section configuration.

Open-jet wind tunnels are common for automotive testing for a number of reasons. The primary advantage of an open-jet wind tunnel is that, dependent on the arrangement of the tunnel, the static pressure in the jet should remain constant and atmospheric along its length, more accurately replicating on-road conditions. However, one of the largest drawbacks is the limited useable length, since the width of the core of the jet decreases rapidly. The jet can also exhibit some unstable modes which can lead to wind tunnel pulsations. Conversely, the closed-section wind tunnel has a much longer useable length, although suffers from pressure gradient disadvantages. A more hybrid approach is the design of a slotted-wall wind tunnel, which attempts to combine the advantages of the open and closed-jet tunnels by keeping the pressure in the test section constant whilst constraining the flow and thus increasing the length of the jet. However, an additional advantage of the open-jet tunnel is the ease of positioning of out-of-flow measurement apparatus, which can be more difficult with a slotted or closed-jet wind tunnel.

1.2.3.3 Coordinate System

The coordinate system used throughout this thesis is shown in Figures 1.7 and 1.6. As far as practicable, conventions in coordinate system definition and terminology have been followed from SAE J 1594:2010 (2010).

In this thesis, the resultant vector of the flow approaching the vehicle is defined with the symbol \mathbf{u} or sometimes for increased clarity \mathbf{u}_{Res} or $\mathbf{u}_{\text{Probe}}$. This is a vector combination of two other flow vectors: the flow velocity induced by the motion of the vehicle, defined as \mathbf{u}_{Veh} , and the wind velocity as defined with the symbol \mathbf{u}_{Wind} . The velocity \mathbf{u}_{Wind} is not solely comprised of the instantaneous prevailing wind conditions at that particular moment in time and space, but also encapsulates the instantaneous influence of other factors, such as the passage through the wakes of stationary roadside objects and the wakes of other vehicles on the road. A more complete commentary of these influences is discussed in Section 1.4.1. Figure 1.6 shows the alignment of \mathbf{u} in the absolute reference frame. This frame is aligned with North \hat{N} and East \hat{E} , which are defined via the measured instantaneous heading of the vehicle β . The alignment of the wind vector \mathbf{u}_{Wind} to this coordinate system is given by the wind heading γ . These vectors are also shown relative to the vehicle reference frame, with the direction ϕ describing the direction of the wind vector relative to the vehicle such that $\phi = 0^\circ$ is a pure head wind and $\phi = 180^\circ$ is a pure tail wind.

Figure 1.7 shows the components of the oncoming resultant flow vector \mathbf{u} relative to the vehicle reference frame. The unit vectors \mathbf{i} , \mathbf{j} and \mathbf{k} are aligned with the principle axes of the vehicle, and the corresponding quantities u_x , u_y and u_z are the components of \mathbf{u} aligned with these axes. The vehicle, and therefore the coordinate system, travels at u_{Veh} and is by definition aligned with \mathbf{i} , such that $\mathbf{u}_{\text{Veh}} \equiv -u_{\text{Veh}}\mathbf{i}$. Angles ψ and α describe yaw and pitch respectively of \mathbf{u} relative to the vehicle reference frame.

1. INTRODUCTION AND AIMS

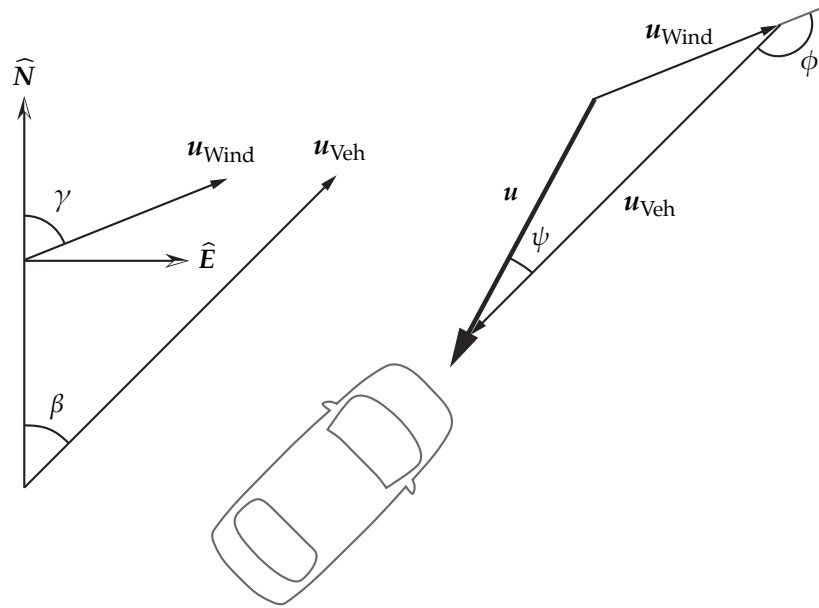


Figure 1.6: Wind and resultant flow vectors relative to absolute and vehicle reference frames

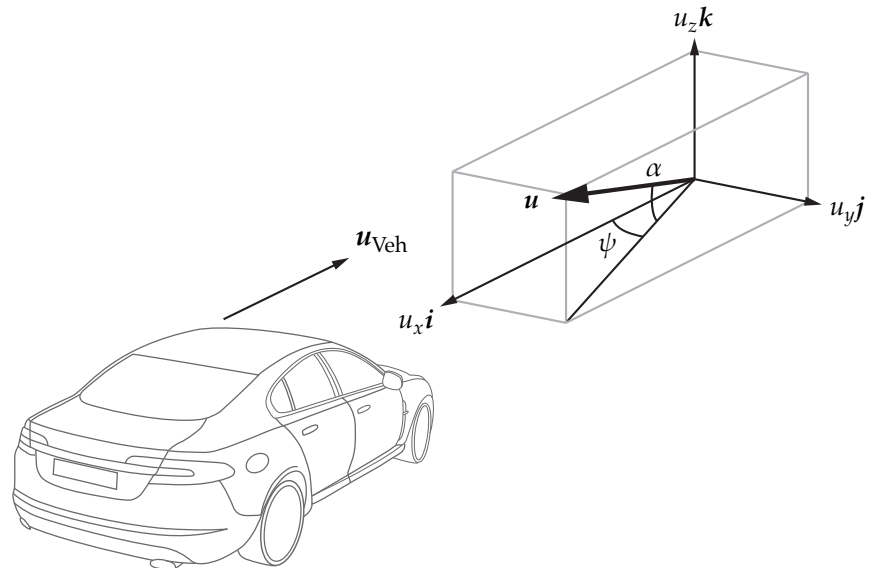


Figure 1.7: Components of the resultant flow vector relative to vehicle reference frame

1.2.3.4 Capturing the Time-Averaged Environment

The wind tunnel and on-road testing environments are different, not just from a perspective of unsteadiness, but from what can be controlled. On-road, testing tends to take place at constant vehicle velocity, since this is the most readily controlled parameter. One exception to this is coast-down testing, where the drag of a vehicle is inferred from its deceleration. Unfortunately, the resultant velocity of the onset flow cannot be held constant on-road due to the unpredictable nature of the wind environment. Conversely, in the wind tunnel, resultant velocity along with yaw angle are the two key degrees-of-freedom that are controlled during a test. These differences can have implications when comparing results from the two environments in terms of the range of wind conditions a vehicle experiences.

As stated by Cooper (1991), wind tunnel tests tend to be divided into two categories: measurements at constant test speed and variable yaw angle; and measurements made at a fixed yaw angle and variable test speed. The latter is used to examine Reynolds' number behaviour, whereas the former used to assess how a vehicle responds to various vehicle speeds and mean wind velocities (both speeds and directions). A particular mean onset flow speed and yaw angle as set in a wind tunnel can be generated by a range of different combinations of vehicle speeds and wind velocities. Figure 1.8 shows an example of the various vector combinations of these driving conditions, each resulting the same onset flow speed and yaw angle.

Figure 1.8(a) shows the reference condition, with the vehicle yawed at angle ψ as it would be in a wind tunnel, being subjected to a resultant flow speed of u (also known as u_{Res}). On-road, this condition can be created by a pure crosswind of strength u_{Wind} acting in a perpendicular direction to a vehicle travelling at speed u_{Veh} , as shown by Figure 1.8(b). This condition corresponds to the minimum wind speed required to produce a particular yaw angle onto the vehicle. The same resultant flow conditions can

1. INTRODUCTION AND AIMS

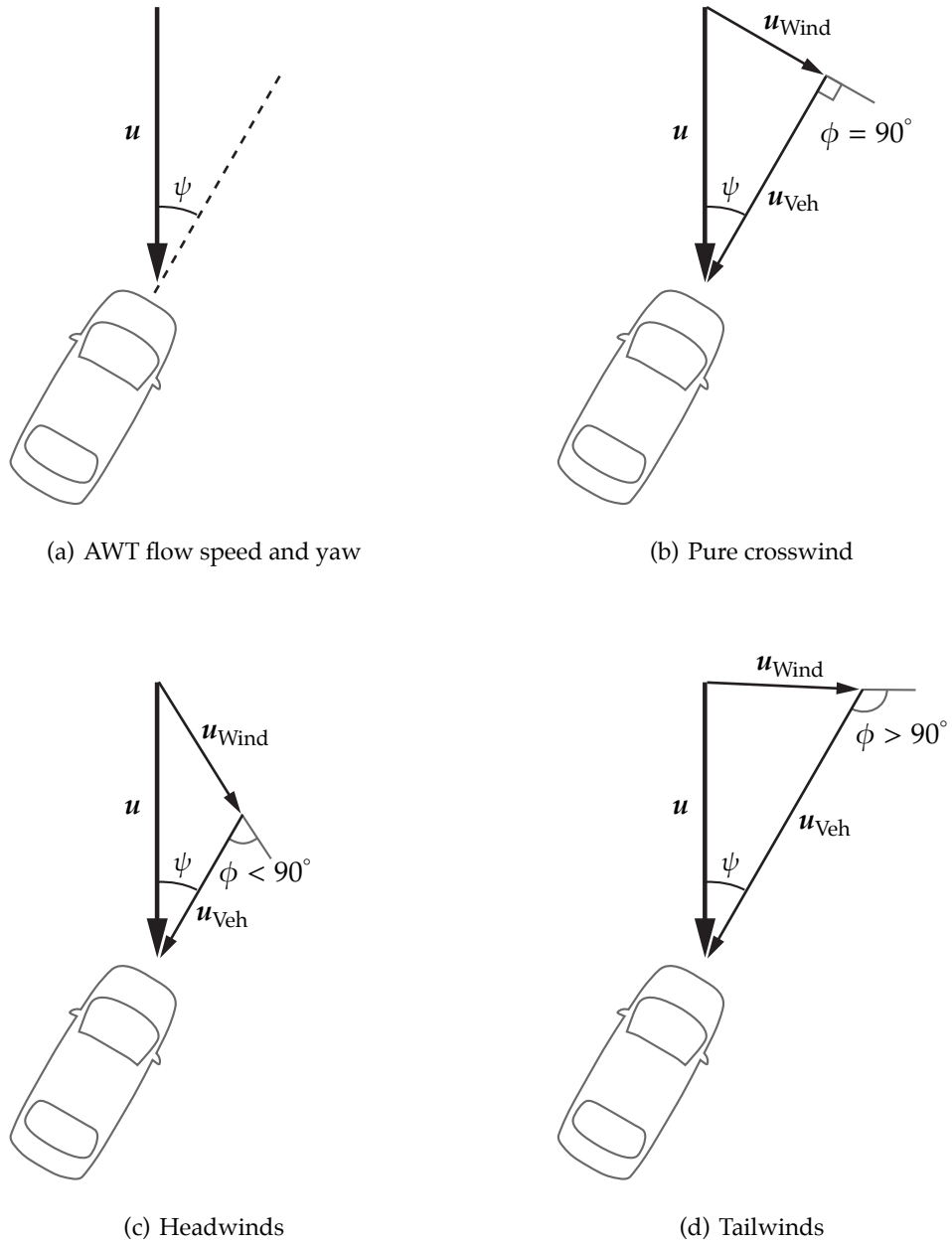


Figure 1.8: The possible flow regimes for a given flow speed and yaw

also be created with a wind acting with a component in both a headwind or tailwind direction, as shown by Figures 1.8(c) and 1.8(d) respectively. Each of these different resultant conditions is a combination of the various parameters of wind speed u_{Wind} , wind direction relative to the vehicle ϕ and vehicle speed u_{Veh} . The relationship of these parameters is given by the cosine rule, described by Equation 1.1.

$$u_{\text{Wind}}^2 = u_{\text{Res}}^2 + u_{\text{Veh}}^2 - 2u_{\text{Res}}u_{\text{Veh}} \cos \psi \quad (1.1)$$

A graphical representation of the various wind and vehicle speeds that can combine to give a particular resultant mean flow speed and yaw angle is given by Figure 1.9. This shows three specific onset flow conditions of a resultant mean flow speed of $u = 130 \text{ km h}^{-1}$ and yaw angles of $\psi = 0^\circ$, 10° and 20° , describing the range of conditions that can be simulated during a typical set of wind tunnel tests.

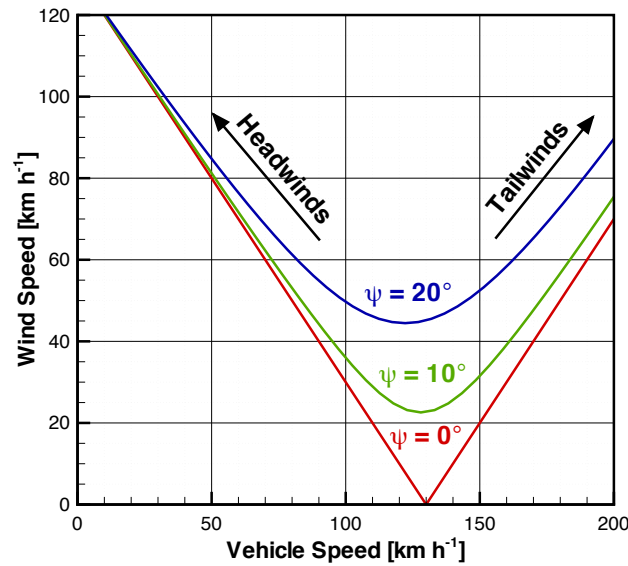


Figure 1.9: The range of vehicle and wind speeds simulated by a wind tunnel test at 130 km h^{-1} at various yaw angles

1. INTRODUCTION AND AIMS

The minima of each of the family of curves is the minimum wind speed required to create a specific yaw angle for a given vehicle velocity. For a wind tunnel test condition comprising a yaw angle of 20° and a resultant velocity of 130 km h^{-1} , the minimum wind speed to create these driving conditions is approximately 45 km h^{-1} , or a Force 6 wind. This same condition may also be generated for a wind of strength 60 km h^{-1} (a Force 8 gale) and a vehicle speed of either 80 or 160 km h^{-1} , depending on the direction of the wind.

Figure 1.10 plots similar curves for resultant flow velocities of 100, 130 and 160 km h^{-1} , each with the region between 0 – 20° yaw shaded. This shows the range of conditions possible to be simulated for a sweep of up to 20° for a given tunnel speed. Therefore, the combination of the three shaded areas highlight the total range of driving conditions that can be simulated during the course of a typical wind tunnel test campaign.

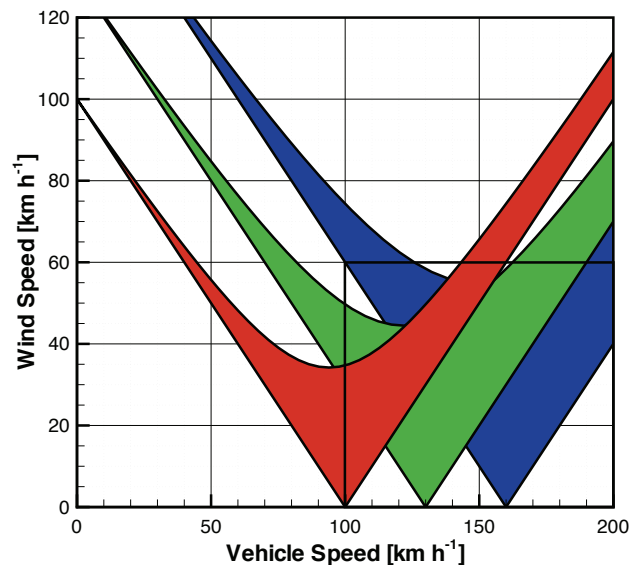


Figure 1.10: The range of vehicle and wind speeds captured by an example wind tunnel testing strategy

The lower-right quadrant of the graph has been highlighted, bounded by vehicle speeds greater than 100 km h^{-1} and wind speeds below 60 km h^{-1} . This region serves as a rudimentary and approximate region where wind noise issues would typically affect a vehicle. Wind noise starts to dominate at highway speeds which are typically above 100 km h^{-1} . A 60 km h^{-1} wind is equivalent to strong gales of Force 8. Although wind-engineering 50-year-maximum maps of wind speeds over the UK and Europe, such as those published by Miller (2003) show speeds up to 80 km h^{-1} , it can be imagined that at these speeds the driver is more concerned with the handling of the vehicle rather than aeroacoustic effects.

For this range of typical wind tunnel test conditions, coverage of this area is reasonably complete. Therefore this indicates that whilst it would be unfeasible to simulate every condition that may be experienced on road, a typical wind tunnel test campaign can adequately cover the majority of mean driving conditions most commonly experienced by a driver.

1.2.4 Key Remarks on Vehicle Aerodynamics

- Wind noise in the cabin is dominated by separated flow structures on the vehicle sideglass region, primarily due to the A-pillar vortex and wake of the door mirror.
- Low turbulence wind tunnels are a commonly used tool to assess vehicle aerodynamics and aeroacoustics. These conditions can be very different to those typically experienced on-road.
- The wind environment experienced by a vehicle travelling on-road is a result of the vector combination of the oncoming flow velocity, induced by the motion of the vehicle, and the velocity of the external wind.

1.3 Aeroacoustics

1.3.1 Background

Aeroacoustics is the study of acoustics that are generated either by the interaction of fluids with solid boundaries or through the turbulent nature of the flow itself. The study of ‘sound generated aerodynamically’ (which later become known as aeroacoustics) was pioneered by Sir James Lighthill in his first paper published in 1952. From his obituary by Pedley (2001), before Lighthill there was no real understanding of how sound was generated by jet engines, which became an increasing problem during the 1950s as jet-propelled aircraft developed rapidly.

Lighthill’s theory was relatively simple, but had extensive consequences. Suppose that the sound originates from a bounded region of disturbed air, such as the turbulent exhaust of a jet engine. If the region surrounding the source is still, then the sound will propagate according to the classical wave equation. Thus the disturbed region can be thought of as a source of the sound. This led Lighthill to rearrange the Navier-Stokes equations of fluid motion in the form of the inhomogeneous wave equation:

$$\frac{\partial^2 \rho}{\partial t^2} - a^2 \nabla^2 \rho = \frac{\partial^2 T_{ij}}{\partial x_i \partial x_j} \quad (1.2)$$

with the linear wave operator on the left-hand side and a derivative of what became known as the *Lighthill turbulence stress tensor*, T on the right, defined as:

$$T_{ij} = \rho v_i v_j + p_{ij} - a^2 \rho \delta_{ij} \quad (1.3)$$

where δ_{ij} is the *Kronecker delta*. This acoustic analogy led to the result that with only a small understanding of the nature of the turbulence, a lot could be deduced about the intensity of the radiated sound. One of the consequences of this work predicted

that for a subsonic jet engine, the sound intensity scaled with the eighth power of jet speed, identifying the importance of reducing jet speed to aero-engine designers. In the second paper of Lighthill (1954) on the subject, a more detailed analysis was given to subsonic jet turbulence, including the prediction of the frequency spectrum of the radiated sound. Lighthill's analogy is revisited in Section 1.3.6 during a discussion of computational aeroacoustics. The various mechanisms for aeroacoustic noise generation are discussed in Section 1.3.3, after the following section describing the measurement of sound.

1.3.2 Acoustic Measurement

1.3.2.1 Sound Pressure and Sound Pressure Level

Sound pressure is the local pressure deviation from the ambient pressure due to acoustic wave propagation. The SI unit of sound pressure is the pascal (Pa). Owing to the wide range of hearing sensitivity spanning a number of orders of magnitude, from approximately 2×10^{-5} Pa (threshold of hearing) to up to 2×10^2 Pa (threshold of pain), the logarithmic sound pressure level (SPL), L , is commonly used. This is expressed as a ratio of the RMS pressure P_{RMS} to the reference pressure of $P_{\text{Ref}} = 2 \times 10^{-5}$ Pa and measured in dB_{SPL} , with the definition given by:

$$L = 10 \log \left(\frac{P_{\text{RMS}}^2}{P_{\text{Ref}}^2} \right) = 20 \log \left(\frac{P_{\text{RMS}}}{P_{\text{Ref}}} \right) \quad (1.4)$$

When combining the contributions of multiple sound sources, it should be noted that since SPL is measured logarithmically, the levels of individual sources do not combine linearly. For broadband incoherent sources (such as the noise heard inside a vehicle's cabin) the sound pressures (not sound pressure levels) sum in a linear fashion. For

1. INTRODUCTION AND AIMS

tonal sounds, phase information is important since it can lead to cancellation, but for broadband noise phase information can be ignored.

By rearranging the definition of SPL for an individual sound contribution, the sound pressure as a function of sound pressure level can be determined by:

$$L_i = 10 \log \left(\frac{P_i}{P_{\text{Ref}}} \right)^2 \quad \therefore \left(\frac{P_i}{P_{\text{Ref}}} \right)^2 = 10^{\left(\frac{L_i}{10}\right)} \quad (1.5)$$

By summing all of the sound pressures of each of the contributing sound sources and substituting in the definition of SPL from Equation 1.5, the following summative rule can be shown:

$$\begin{aligned} L_{\Sigma} &= 10 \log \left(\frac{P_1^2 + P_2^2 + \dots + P_n^2}{P_{\text{Ref}}^2} \right) \\ &= 10 \log \left(10^{\left(\frac{L_1}{10}\right)} + 10^{\left(\frac{L_2}{10}\right)} + \dots + 10^{\left(\frac{L_n}{10}\right)} \right) \\ &= 10 \log \sum_{i=1}^n 10^{\left(\frac{L_i}{10}\right)} \end{aligned} \quad (1.6)$$

For instance, when combining two sound sources with sound pressure levels of 79.5 dB and 70 dB, the total SPL would be 80 dB. The addition of a further source with a sound pressure level of 70 dB would only raise the total SPL to 80.4 dB.

1.3.2.2 Spectral Content of Sounds

Characterising a particular sound by its overall sound pressure alone can hide much of the nature of the sound. The ability to look at the spectral content of a sound provides a greater insight into not only how the sound may be heard, but also some information as to the nature of the sound sources.

By taking a Fast Fourier Transform (FFT) of the sampled sound data, the spectral

content can be revealed. The resulting narrowband spectrum has a frequency resolution of:

$$\Delta f = \frac{f_s}{N_s} \quad (1.7)$$

with f_s the sampling frequency of the signal and N_s the number of samples used in the FFT window.

Whilst the narrowband spectrum provides the most detailed spectral record of a particular sound, for many applications, dividing the spectrum into a series of coarser octave bands (and fractions thereof) can often be more convenient. One octave is a doubling of frequency, for instance a frequency of 2 Hz is one octave higher than 1 Hz, with 4 Hz an octave beyond. One of the more usual methods in presenting cabin noise spectral data is through the use of third-octave bands. The centre-frequency of each of these bands increases by one-third of an octave, so that three third-octave bands span an entire octave of frequency. The centre frequency for each third-octave band k is commonly defined relative to the centre frequency of 1000 Hz as is given by:

$$f_c(k) = 2^{k/3} \cdot 1000 \text{ Hz} \quad (1.8)$$

These frequencies are rounded to the nearest preferred frequency, thus for the band where $k = 4$, the centre frequency is rounded to 250 Hz from 252 Hz.

Figure 1.11 compares the overall SPL, narrowband and third octave spectra for the same sound. To extract the third-octave spectrum from the narrowband spectrum, the spectral content falling within each third-octave frequency band is combined, using the same method as described by Equation 1.6. The same process is used when determining the overall SPL, where the overall spectral content over the entire recorded frequency range is combined. This has the implication that spectra with a coarser frequency resolution appears to have a larger SPL than data of a finer frequency reso-

1. INTRODUCTION AND AIMS

lution. Therefore care must be taken when comparing data of differing spectral resolution. An advantage of third-octave spectra is that the frequency bands are commonly defined, allowing a consistent comparison between different data without the need to specify a narrowband frequency resolution.

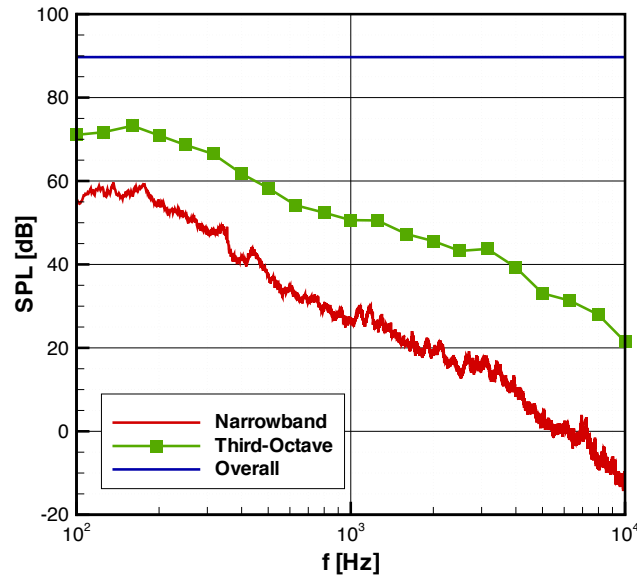


Figure 1.11: Comparison of overall level, third-octave and narrowband spectra

For tonal sounds, the narrowband spectra can be more appropriate. The relatively coarse frequency bands of a third-octave spectrum can spread the tonal ‘spikes’ present in a narrowband spectrum over the width of a third-octave band, leading to a reduction in definition of the particular frequency of the tone. In some cases, this can lead to tonal spikes becoming lost in the overall spectrum. In the case of a narrowband spectrum, these can be clearer and provide more detail as to the level and tonal frequency of these sounds.

Another advantage of a third-octave spectrum is that above 300 Hz, third-octave bands approximate *critical bands*, measured in bark. These are a psychoacoustic phenomenon (the topic of psychoacoustics is discussed further in Section 1.3.7) related to

spectral masking. Masking occurs when two sounds of a similar frequency are played simultaneously, leading to the human perception that only a single sound is present. This is thought to be due to the limitation of the cochlea in resolving the frequency of a sound. Further analysis of this phenomenon is given by Fastl and Zwicker (2007). A critical band can be thought of as the greatest extent that two frequencies can be separated before they become noticeable as two separate sounds. This provides some justification in combining the spectral content into a particular third-octave frequency band.

1.3.3 Aeroacoustic Mechanisms

There are three principle mechanisms for aeroacoustic noise generation as described by Norton (1989), Hucho (1998) and others. Each of these can be approximated by way of an idealised model. The first mechanism originates from unsteady volumetric flow, such as that emanating from a leak into the cabin of a vehicle, or from the exhaust of a piston engine. This is idealised by a monopole source, which is a fluctuating pressure source. The second mechanism arises from the interaction of unsteady pressures upon a rigid surface. Von Kármán vortex shedding is an example of this type of acoustic source, where the vortex-induced pressure fluctuations form a dipole sound source on the body surface. This can be modelled using a dipole sound source comprising two adjacent monopole sources oscillating out of phase. The final mechanism is caused by unsteady internal stresses in a fluid and is modelled by the quadrupole source, which is a combination of two dipole sources. A diagram of each of these sources is shown in Figure 1.12.

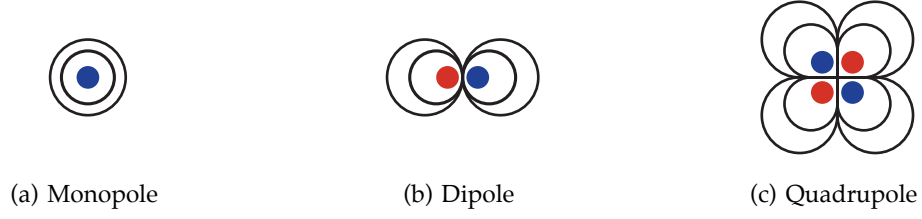


Figure 1.12: Aeroacoustic noise sources

Each of these sound sources scales differently with flow speed u and Mach number M , leading to the relationships:

$$I_m \sim \frac{\rho}{a} u^4 = \rho u^3 M \quad (1.9)$$

$$I_d \sim \frac{\rho}{a^3} u^6 = \rho u^3 M^3 \quad (1.10)$$

$$I_q \sim \frac{\rho}{a^5} u^8 = \rho u^3 M^5 \quad (1.11)$$

showing the relationship between flow speed, Mach number and sound intensity I for each source respectively, after Helfer (1998a,b). ρ represents air density and a represents the effective speed of sound.

At the relatively low speeds that a vehicle travels on road, where $M \ll 1$, the monopole sound source dominates, followed by the dipole source. Typically, quadrupole sources are neglected in the study of vehicle aeroacoustics, whereas in the absence of leak noise, dipole sources tend to dominate the overall cabin noise of a road vehicle. It is also shown that the sound intensity of such a monopole is proportional to the flow velocity raised to the fourth power, whilst the dipole sound source is proportional to the flow velocity raised to the sixth power. As the most significant aerodynamic noise mechanisms in vehicles are either monopoles or dipoles, experimental observation tends to find that the intensity of this aerodynamic noise increases with flow speed

raised to between the fourth and sixth power, as noted by Helfer (2005).

The flow speed scaling laws of various sound sources were also investigated by Wickern and Brenberger (2009b). By assessing the sensitivity of both exterior and interior noise to flow speed, a valuable insight can be gained into the physics of the sound sources. It was found that whilst the overall broadband noise of a vehicle typically scales with u^6 , in smaller details these scaling laws can vary and can combine to form a sensitivity made up of a combination of different powers. Therefore, since wind noise is particularly sensitive to wind speed, care must be taken to either keep wind speed constant during wind tunnel tests or recorded when testing on-road. This also implies that local velocity effects due to the body shape of a vehicle can also be extremely significant in the generation of aerodynamic noise.

According to George (1990), the relationship between local flow speed u , free-stream flow speed u_∞ and surface pressure coefficient c_p is:

$$\left(\frac{u}{u_\infty}\right)^6 = (1 - c_p)^3 \quad (1.12)$$

This relationship is shown with the flow speed ratio raised to the sixth power, as would be the case when relating this ratio to a change in SPL for a pure dipole source. The relationship between c_p and SPL increase then simply follows as:

$$\begin{aligned} \Delta\text{SPL} &= 10 \log \left(\frac{u}{u_\infty} \right)^6 \\ &= 10 \log (1 - c_p)^3 \end{aligned} \quad (1.13)$$

highlighting the impact of a change of local flow speed on a dipole wind noise source.

Therefore, for a position where the flow speed is increased such that $c_p = -1$, the wind noise generated in this position will tend to be 9 dB louder than that which has a

1. INTRODUCTION AND AIMS

$c_p = 0$. In the A-pillar region it is not uncommon to have $c_p = -2$, which is equivalent to an approximate 14 dB increase in SPL, from Helfer (2000a). This serves to highlight the significance of the location of external features such as door mirrors on the level of aerodynamic noise of a vehicle.

1.3.4 Typical Vehicle Wind Noise Sources

1.3.4.1 General Observations

Early work by Stapleford and Carr (1971) separated aerodynamic noise into three principle classifications: broadband wind rush noise, caused through the passage of air-flow around the vehicle; tonal noise, caused by sharp edges and gaps in the bodywork; and resonances caused through open windows and sunroofs, often called buffeting.

Other early work by Thomson (1964) noted that the aerodynamic shape of a vehicle was insignificant in the overall wind noise, whereas small air leaks in critical areas such as the A-pillar region are the principle cause of objectionable wind noise. It was also stated that wind noise could be eliminated through good sealing about the doors and windows. These conclusions certainly belong to a previous era of aeroacoustic research, although they do emphasise some important points that are still valid today. Firstly, that monopole sound sources caused through aspiration noise can dominate the overall cabin noise if door and window sealing is not optimised. Secondly, since vehicles in the 1960s spent less time cruising at modern-day highway speeds, this highlights that wind noise only tends to dominate the overall cabin noise when the vehicle is travelling sufficiently fast. Finally, owing to the years leading up to the present, manufacturers have significantly refined and reduced noise from the engine and powertrain, so that today wind noise is much more significant than in the past. This continues today, since through the increasingly widespread development of electric and hybrid technologies, for example the Chevrolet Volt, from Tortosa and Karbon

(2011), wind noise is set to become more significant still in the overall noise heard by the occupant of a vehicle cabin.

Since flow behaviour and noise generation are inextricably linked, investigations into the flow around areas of a vehicle which are relevant in the production of noise are important in this research. Stapleford and Carr (1971) and Stapleford (1972) concluded that aeroacoustic noise is highly dependent on separated flow structures, particularly those of the A-pillar vortex. Since both the shape of the body and external features affect separation, a development of this conclusion results in a direct link between vehicle shape and wind noise. The work of Ullrich (2008) and shown by Blumrich (2008) assessed the comparative influence of both the body shape and external features on the overall aerodynamic noise of a vehicle. It was found that the aerodynamic noise contribution due to the influence of the body affected frequencies generally below 500 Hz, whilst sealing and external components affected frequencies greater than 500 Hz. Figure 1.13 is adapted from Blumrich (2006), showing examples of the three different sound sources in the sideglass region of a vehicle, which is dominated by flow structures around the A-pillar and door mirrors.

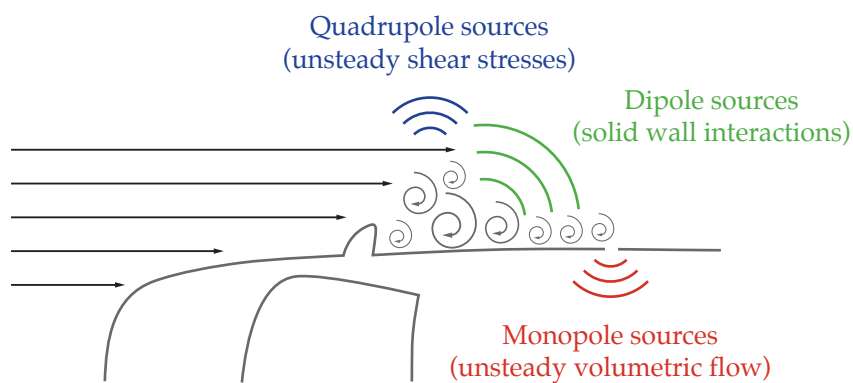


Figure 1.13: Sound sources in the sideglass region, modified from Blumrich (2006)

Helfer (1999) gives a good summary of the range of aerodynamic sound sources

1. INTRODUCTION AND AIMS

typically present on a road vehicle. In the following sections, these are discussed with examples from the investigations of other authors.

1.3.4.2 A-Pillar

One area of importance in generating wind noise is the A-pillar region, which is positioned forward of the front doors of the vehicle. This region is an area of flow separation and is near to the ears of the driver and passengers. The A-pillar vortex dominates the flow around the A-pillar and sideglass and this is shown in Figure 1.14, adapted from that of Howell et al. (2006).

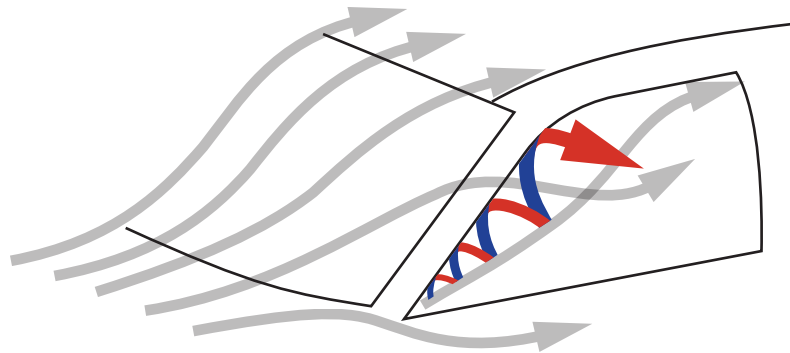


Figure 1.14: Typical vortex structure around A-pillar, from Howell et al. (2006)

The importance of this region at higher road speeds ($> 100 \text{ km h}^{-1}$) in noise generation was highlighted by George (1990). Haruna et al. (1990) looked in more detail into the sound generated by the A-pillar vortex and concluded that the separated region of the flow produced a much higher sound pressure level than the reattached flow region. A summary of work that assessed the strength of the A-pillar vortices as a vehicle was yawed was published by Watkins (1999). This stated that the vortex on the leeward side of the vehicle is larger and therefore tends to produce a greater noise.

It was also noted that of all the A-pillar studies completed at the time of writing, all had been carried out in smooth-flow wind tunnels.

Newnham et al. (2008, 2006) investigated the leading edge radius of the A-pillar under various simulated turbulence conditions and found that with a small increase in free-stream turbulence, the critical Reynolds' number for flow transition reduced whilst drag increased significantly. This investigation was extended to visualise flow using PIV and found that increased turbulence intensity alters the nature of the flow separation. Further work by Howell et al. (2009) and Baden Fuller (2009) found that oncoming unsteadiness reduced the vortex suction, but increased the RMS pressure fluctuations, although not the peak pressures. Mean pressures are related to door loads and can change the sealing properties of the door, leading to increased leak noise. Fluctuating pressures are related to dipole-sourced wind noise. Vio et al. (2003) found that, during an investigation into the behaviour of the A and C-pillars, increased turbulence reduced the size of A-pillar vortex, but increased the size of the C-pillar vortex. This corroborates the previously noted findings of Newnham et al. and the observed drag increase.

Alam et al. (1998) also investigated the flow structure around the A-pillar and found that whilst changes occurred at yaw, between 60 and 120 kph there were only slight changes in structure. Further work as described by Alam et al. (2001) involving idealised models found that changes in the A-pillar radius can significantly reduce fluctuating pressures. However these shapes were extremely rounded to the extent that they were no longer representative of typical vehicle A-pillar geometries. It was also noted that yaw can change the size of the leeward separated region by an order of magnitude, indicating that the A-pillar region tends to be dominated by separated flow structures. The work was further extended by Alam et al. (2003) to investigate the effect of rounding the A-pillar of a production vehicle and was also found to reduce pressure fluctuations.

1. INTRODUCTION AND AIMS

A number of numerical studies have been completed investigating noise generation of the A-pillar region. Gaylard (2006) investigated the solution accuracy of a Lattice Boltzmann solver. It was found that this method tended to over-predict the size of the A-pillar vortex, whilst a RANS solver tended to under-predict. The cause of over-prediction was suggested to lie in the limitation of the turbulence model. It was also found that a higher level of local resolution than previously thought was required to model this behaviour, leading to higher levels of computational expense. Li et al. (2003) assessed various methods of predicting noise from the A-pillar, finding that reducing the size of the A-pillar vortex, noise generation was reduced. Matsushima and Kohri (2005) and Li et al. (2006) also undertook studies focussing on the accuracy of numerical noise solvers, focussing on the A-pillar of both commercial and passenger vehicles respectively. Further work on a simplified body of this region was undertaken by Murad et al. (2004), assessing various RANS turbulence models and found that the $k-\omega$ turbulence model gave best correlation with available experimental data. However, it must be noted that all of these studies, whilst either modelling or simulating small-scale turbulence directly, did not consider the effect of the larger time scale transient conditions experienced on-road.

1.3.4.3 Door Mirrors

Door mirrors tend to be located in a region of high speed turbulent flow and therefore have a high potential for noise generation. The wake of the mirror is also relatively large and can impinge on the sideglass if the mirror is located nearby. The impingement can be reduced if the mirror is located a greater distance from the car body. An increase in the gap between the mirror body and door can also reduce any increase in flow speed between the mirror body and the vehicle, thus reducing noise.

Tonal mirror noise can be caused either by coherent shedding structures as a result

of the flow interacting with the external shape of the mirror, or through fluid resonance in the cavity of the mirror body. Research into the former was carried out by Lounsberry et al. (2007) to investigate the cause of tonal mirror whistle. It was found that tripping the boundary layer to turbulence reduced the whistle significantly. Bumps and grooves are occasionally placed on mirror bodies and stems, such as those shown by Blumrich (2006) and Helfer (2005), to break up coherent tonal shedding structures. Milbank (2004) conducted a thorough investigation into cavity noise, particularly focussing on door mirrors. In determining an empirical relationship to predict cavity resonance, it was observed that the natural cavity resonances of the mirror could couple with the oscillations present in a wind tunnel, from sources such as the fan and instabilities in the jet, leading to a discrepancy in mirror performance between the wind tunnel and on-road. The importance of assessing a mirror in the context of the overall vehicle flow structures was also noted, since flow structures originating from other parts of the vehicle can lead to coupling with the natural cavity resonances.

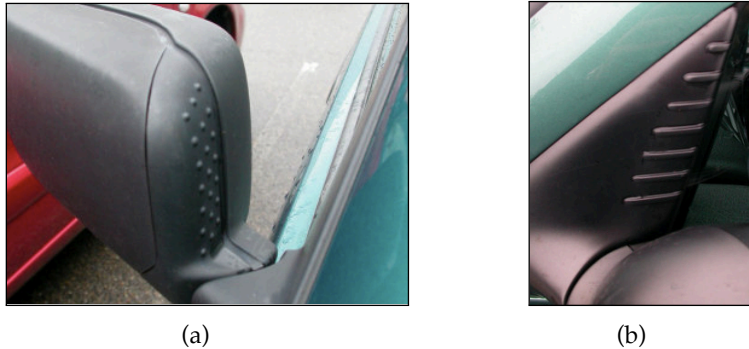


Figure 1.15: Examples of bumps and grooves on production vehicle mirrors, from Helfer (2005)

In a study by Watkins (2004) investigating the causes of mirror vibration, it was found that lower frequency vibrations were dominated by inputs from the road, rather than aerodynamic causes. Aerodynamics had greater influence in the larger leeward

1. INTRODUCTION AND AIMS

separated flow region present whilst the vehicle was at yaw. This work was continued by Alam et al. (2007) and Jaitlee et al. (2007) who found that by using a shrouding frame around the mirror glass, thus reducing the effect of the mirror wake on the glass, vibration could be reduced.

A number of authors have investigated mirror designs in isolation, or in semi-isolation where only a part of the vehicle body is used. For instance, Howell et al. (2006) used a front vehicle quarter cut from a full size aero-buck in a model tunnel. This allowed a more rapid development of mirror geometry without using a full scale tunnel. However, it was noted that it was important for the vehicle geometry to be sufficiently large so that the flow around the mirror is sufficiently representative. It should also be noted that whilst such a technique allows mirror optimisation, it does not allow the effect of mirror changes on other parts of the vehicle geometry to be captured. Another isolated mirror study carried out by Khalighi et al. (2008) and Chen et al. (2009) compared the wakes of two mirror designs, one from an SUV and another from a saloon. The wakes were investigated using surface microphones positioned on a plate downstream of the mirror. It was found that the main differences between the mirrors occurred below 1 kHz, with the more rounded SUV mirror being 10-15 dB louder than the sharper-edges saloon mirror at these frequencies.

1.3.4.4 Windscreen Wipers

Windscreen wipers are another example of how relatively small changes in geometry can have a large effect on noise generation. George (1990) noted that with the windscreen wipers of a vehicle removed, external pressure fluctuations can be reduced by up to 6 dB, whilst the removal of door mirrors can reduce these local fluctuating pressures by up to 20 dB. Whilst it is more challenging to remove the door mirrors owing to legislation, it is possible to design the vehicle so that the wipers are hidden behind

the bonnet whilst in a lowered position in an *aerodynamically hidden* configuration. A study by Zaccariotto et al. (1997) found that raising the height of the rear of the bonnet by 10 mm could reduce noise generation by approximately 5 dB.

1.3.4.5 Cavity Noise

There are two main sources of cavity noise on a vehicle: noise generated by large cavities such as an open sunroof or windows; and also cavity noise from smaller cavities such as gaps in body panels. Resonances caused by open windows and sunroofs, is also known as *booming*, *wind throb* or, more recently, *buffeting*, from An et al. (2004). There have been a great number of studies involving the sunroof in particular, especially CFD studies using an open sunroof and the effect of a deflector as a test case. The deflector acts to reduce vortex impingement on the rear of the opening of the sunroof. Blumrich (2008) amongst others also noted that a notched sunroof deflector further reduces low frequency buffeting by breaking up these coherent vortex structures, although this has high frequency implications. CFD studies include those of Ukita et al. (1997) who predicted the reduction of vorticity using a deflector; Müller and Seydell (2002) who used an early example of a Lattice-Boltzmann-based solver; An and Singh (2006, 2007), who found that through the use of either a partially closed sunroof or a dividing bar buffeting was reduced; and Crouse et al. (2009), who further assessed the use of LBM-based solvers in the simulation of Helmholtz resonator-driven conditions. Similar CFD studies have been carried out focussing on physically similar rear window buffeting, for instance another study by An et al. (2005) where buffeting reduction methods were investigated, including dividing bars and C-post venting. In an experimental investigation, Slaboch et al. (2009) compared PIV results from a real vehicle with idealised experimental models and found a good correlation, indicating that control strategies can be tested in isolation.

1. INTRODUCTION AND AIMS

In each of these studies, larger-scale transient conditions were not simulated and these conclusions may not necessarily be representative of typical on-road conditions. However an experimental rear side window buffeting study by Maffei et al. (2009) used the Pininfarina turbulence generation system to simulate transient conditions on the flow structures. PIV was used in the investigation and found that the buffeting fluctuation reduced at increased turbulence, with the flow structures becoming more complex. This again is likely to be due to break-up of the larger scale coherent structures by the oncoming flow unsteadiness.

As introduced previously, gaps in body panels are also a cause of cavity noise. One reason why body gaps are taped over during aeroacoustic wind tunnel testing is to avoid any gap noise, since body panel gap variation between vehicles can otherwise colour acoustic results. Wickern and Brenberger (2009a) investigated the mechanisms behind this gap noise. This behaviour was related to that of a Helmholtz resonator, with pressure fluctuations from the turbulent boundary layer found to be large enough to excite the fluid within the cavity leading to noise generation.

1.3.4.6 Other Noise Sources

A range of other aerodynamic noise sources are also present on a vehicle. Some sources, such as the wheel arches are particularly relevant to the external noise radiated from the vehicle, although tend to have a reduced impact on the vehicle occupants. Another source that is relatively simple to mitigate is radio aerial noise, which can be reduced by increasing the angle of the aerial, from Helfer (1999), wrapping the cylindrical profile with a helical strake, from Blevins (1990) or even removing the necessity for the device entirely.

As the noise levels of major sources are reduced, the level of the more minor noise sources become prominent. One example of this is noise transmission through the

floor of the vehicle. Components mounted under the vehicle can lead to complex flow structures, potentially exciting resonant modes of the floorpan of the vehicle. A study by Ih et al. (2005) assessed noise generation using an acoustic holography technique and found that small holes in side members could also have a significant impact on noise generation.

Roof bars are commonly known as a noise source on a vehicle, as well as creating additional levels of parasitic drag. Karbon and Dietschi (2005) investigated roof bar noise using CFD. A RANS-based CFD code was used, coupled with an acoustic analogy, which found that relative levels of noise generation were predicted with sufficient accuracy. The hoods of convertible vehicles also create levels of discomfort and noise for passengers. Relatively recent advances in transient coupled CFD–FEA codes allow these flow–structure interactions to be modelled. A study by Juvé (2009) investigated the effect of ballooning and wind noise, and found indications of strong transient effects.

Whilst not related to wind noise, tyre noise is also an additional cause of passenger discomfort from within the cabin. A numbers of studies have been undertaken to measure tyre noise by removing its contribution to the overall cabin noise, so that aerodynamic noise can be more clearly assessed. Kim et al. (2007, 1997) investigated tyre induced in-cabin noise and proposed a method to separate this noise from other sources by exciting the wheel and tyre when attached to the vehicle to determine the transfer function from wheel to cabin. Fieles-Kahl and Riegel (2010) and Riegel and Wiedemann (2008) also used a method of assessing tyre noise, again with a view to remove this contribution from overall cabin noise. An on-road trailer was used to measure tyre noise directly in the absence of other noise sources. This was used in conjunction with an acoustic transfer function measurement between the tyres and cabin, allowing the road noise contribution to the overall cabin noise to be isolated. In

1. INTRODUCTION AND AIMS

principle the method is similar to that of Mayer and Wiedemann (2003, 2007) where a trailer was used to assess rolling resistance and windage drag of a wheel to remove these factors from the overall drag of a vehicle.

1.3.5 Wind Noise Measurement

1.3.5.1 Aeroacoustic Wind Tunnels

Aeroacoustic wind tunnels differ from conventional wind tunnels in that they are optimised for acoustic measurements. Key features of aeroacoustic wind tunnels include low levels of background noise and an acoustically treated anechoic test section. Automotive aeroacoustic testing is almost always carried out at full-scale, owing to the challenges in achieving equivalence in both Reynolds' number (to capture the correct flow regime) and flow speed (to capture the correct aeroacoustic scaling).

As described in Section 1.2.3, a number of different wind tunnel configurations are used when assessing the aerodynamics of vehicles. Of these, the open-jet wind tunnel is particularly suited to aeroacoustic studies, since the walls of the plenum can be easily acoustically treated. In addition, the space outside of the jet allows a range of far-field measuring apparatus to be located, such as acoustic mirrors and microphone arrays. However, a disadvantage of an open-jet wind tunnel is that the shear layer at the edge of the fluid jet can lead to aeroacoustic noise, as well as scattering and distortion of the sound field. However these quadrupole sound sources, as previously discussed, tend not to be significant at low Mach numbers. Closed-section wind tunnels are limited in that measurements can only be taken using microphone arrays embedded flush in the test section walls. Slotted-section tunnels are also less commonly used, since the presence of the slots can lead to noise generation, although this can be avoided with careful design.

Examples of aeroacoustic wind tunnels include:

Audi, Wickern and Lindener (2000); **BMW**, von Heesen et al. (1996); **Chrysler**, Walter et al. (2003); **DNW**, Mercker and Pengel (1994); **Ford (Europe)**, Volkert and Kohl (1987); **Ford (US)**, Walter et al. (2002); **GIE S2A**, Waudby-Smith et al. (2004); **Hyundai**, Kim et al. (2001); **IVK/FKFS**, Potthof et al. (1994), Künstner et al. (1995); **Pininfarina**, Cogotti (2006)

Wall treatment is used to achieve two objectives. The first is to provide an anechoic environment within the test section, to create a close-to free-field environment by reducing the reverberation and reflection of sound waves from the noise sources of the vehicle. This is important in terms of sound source localisation. Secondly, wall treatment in the duct is used to prevent the propagation of noise from the fan into the test section. A number of different absorption methods are used for the different frequencies of noise: porous material to absorb higher frequencies; and membrane or panel absorbers, acting like tuned Helmholtz resonators, to absorb lower frequencies, from Helfer and Wiedemann (2006).

The fan and motor may be considered to be the main acoustic sources in a wind tunnel. The fan requirements for an aeroacoustic tunnel differ from those of a conventional wind tunnel in that fan efficiency is not the primary consideration. Care must be taken to minimise blade passing noise, noise emanating from the leading edges of the blades as well as general turbulence and boundary layer noise.

Low-frequency pulsations can also be an issue in an aeroacoustic wind tunnel and a range of studies have been carried out to minimise these effects. In a study by Arnette et al. (1999), it was found that whilst the underlying physics of these pulsations is not fully understood, the pulsations originate as coherent vortex structures generated at the nozzle, which then travel through the test section at a fraction of the jet speed, before impinging on the collector. These can then couple with other acoustic modes

1. INTRODUCTION AND AIMS

in either a section or all of the tunnel. There are two main methods of controlling this behaviour. Firstly, Seiferth Wings, from Seiferth (1947), which are tabs or teeth on the edges of the nozzle, can be used to break up the shear layer vortices. However, these are generally unsuitable for aeroacoustic tunnels since they can generate higher frequency noise of their own. Loudspeakers mounted adjacent to the nozzle exit have proved to be a suitable alternative active method, from von Heesen and Höpfer (2004). Passively, low-frequency buffeting can also be suppressed using a tuned Helmholtz resonator, which was demonstrated to reduce buffeting by 10 dB, from Beland (2007). The work of Beland also investigated the use of an aerofoil shaped collector to reduce the effect of vortex impingement. This also had the advantage of being able to be adjusted to improve the static pressure gradient of the wind tunnel, reducing the effect of horizontal buoyancy on drag measurements.

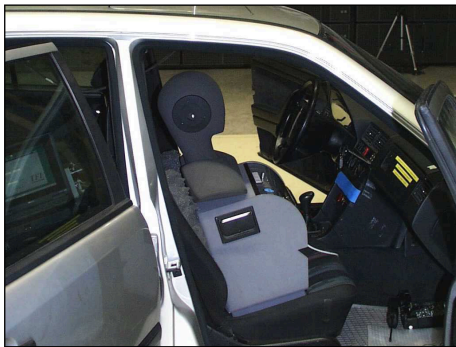
It should be noted that since sound levels are measured logarithmically, there is almost no benefit in attenuating minor components of noise without focussing on the attenuation of the major noise sources. As a rule-of-thumb, background noise levels in an aeroacoustic wind tunnel should be around 10 dB below the noise levels of interest, from Helfer and Wiedemann (2006). This follows from Section 1.3.2.1 previously, where it was shown that when combining two sound sources, the contribution of a source 10 dB lower than another to the total only adds 0.4 dB to the SPL of the greater source.

1.3.5.2 In-Cabin Noise

The most popular method for measuring in-cabin noise is through the use of a binaural acoustic head. This is a mannequin of a head and torso, with microphones positioned in the ears. The use of binaural recording systems developed from the work of Genuit (1984) at the Rheinisch-Westfälische Technische Hochschule, Aachen, Germany.

Hence this measurement apparatus is also known as an *Aachen head*. The aim of this technique is to record the in-cabin noise as would be heard by a passenger, accounting for the transfer function between sound in the free-field, to that measured by a passenger at the eardrum.

This is a common technique used routinely by manufacturers to characterise the noise inside the vehicle's cabin during development work in an aeroacoustic wind tunnel. The technique is so widespread that it is impossible to list all instances here, although examples of usage include studies by Watkins et al. (2001) and Cogotti (2004), as shown in Figure 1.16. Since this technique is not limited to use solely in the wind tunnel, a number of authors including Peric et al. (1997), Lindener et al. (2007) and Nor et al. (2008) have used an acoustic head to measure cabin noise on-road.



(a) Watkins et al. (2001)



(b) Cogotti (2004)

Figure 1.16: Cabin measurement using binaural acoustic heads

Another technique used for example by Cogotti (2006), employed a spherical array of surface microphones mounted in the centre of a vehicle to create a spatial distribution of the various acoustic sources inside the passenger compartment. This technique is fundamentally an application of beamforming, discussed in the following section. A spherical microphone array was also used by Li et al. (2006), who used a binaural head, spherical microphone array and surface microphones to assess the accuracy of numerical techniques.

1. INTRODUCTION AND AIMS

1.3.5.3 External Noise

As an alternative to measuring the noise inside the cabin, the external sound field generated by the form of the vehicle can be investigated. These methods are particularly advantageous in sound source localisation investigations, where the origin of a particular problematic form noise may be unclear. For vehicle development programmes where clay models, aerobucks or other early-stage physical test properties may be available for wind tunnel investigation, external noise measurement has the advantage over in-cabin measurement since it can be undertaken at an earlier stage in the vehicle development cycle, where only the external surface geometry of a vehicle may be defined.

Conventional microphones are generally unsuitable for aeroacoustic measurements owing to the interference of the flow on the measurement membrane, leading to pseudo-noise generation. Also, there is a risk of parasitic aeroacoustic noise from the interaction between the flow and the geometry of the microphones, preamplifiers and associated supporting structures, leading to interference with the noise measurement of interest. Therefore specialist aeroacoustic measurement devices tend to be used, after Helfer (2005).

Acoustic Mirror

Acoustic mirrors have been used for sound source localisation for a number of years, with perhaps the first use of such technology being used for enemy aircraft detection during wartime. Helfer (2009) provides a review of this history and the underlying principles of their operation. In an automotive application, an acoustic mirror consists of either a parabolic or elliptical mirror body with a microphone positioned at its focus. This is then traversed alongside a vehicle to determine the noise generated by

a particular point of vehicle geometry. Figure 1.17 shows an acoustic mirror used in an aeroacoustic wind tunnel as taken from Helfer (2005).

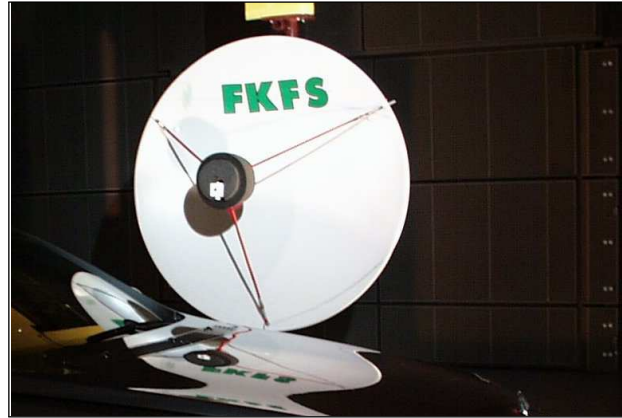


Figure 1.17: Acoustic mirror as used in an aeroacoustic wind tunnel, from Helfer (2005)

Owing to the size of such a device, their use is limited to open jet wind tunnels, where the mirror can be positioned out of the flow. Both parabolic or elliptical mirrors can be used. Parabolic mirrors are commonly used in the communications field and are more widely available, with elliptic mirrors generally having to be custom made for a particular application. Elliptic mirrors have two foci, where one focus is the point of measurement and the other the location of the microphone. Parabolic mirrors accept plane waves that are focussed at the position of the microphone, although their poorer spacial resolution can be mitigated in part by an ellipsoid-based microphone position. More recent advances in acoustic mirrors have included the use of cameras and lasers for increased positioning precision.

Advantages of using an acoustic mirror include their relatively simple operation, which can allow for identification of the main exterior sound sources of a vehicle without extensive data processing. However, owing to the speed of the traverse mechanism, a full characterisation of the external aeroacoustic sound field of a vehicle can take a considerable time.

1. INTRODUCTION AND AIMS

Intensity Probes

Acoustic intensimetry uses multiple microphones to determine the spatial distribution of noise sources. A sound intensity probe allows direct measurement of the sound intensity at a point of interest. Sound intensity is a measure of the directional sound flux at a particular point and is defined in Equation 1.14, from Helfer (2000b).

$$I = \frac{1}{T} \int_0^T p(t) \cdot a(t) \, dt \quad (1.14)$$

Therefore, to determine the sound intensity, both sound pressure and sound velocity must be determined. A common method to measure the sound velocity a , is by a two microphone technique, where two microphones are separated by a distance Δx , which also determines the frequency range of the probe. Therefore to capture a wide frequency range, a number of different microphone spacings must be used. Sound velocity can then be determined using Equation 1.15.

$$a(t) = -\frac{1}{\rho} \int \frac{p_B(t) - p_A(t)}{\Delta x} \, dt \quad (1.15)$$

The directional sensitivity of a sound intensity probe is limited in certain directions and therefore is most suited to determining the sound intensity close to the source of interest. Care must be taken in locating a probe such that it does not generate any noise of its own; Helfer (2000b) and Cogotti (1997) developed intensity probes suitable for use in an aeroacoustic wind tunnel. Both of these probes are protected from flow-excitation using a microphone wind shield. However, as found by Cogotti (1997), these are most effective when in line with the flow; this direction may not be known *a priori*.

An example of an intensity probe suited for aeroacoustic measurement as described by Helfer (2000b) is shown in Figure 1.18

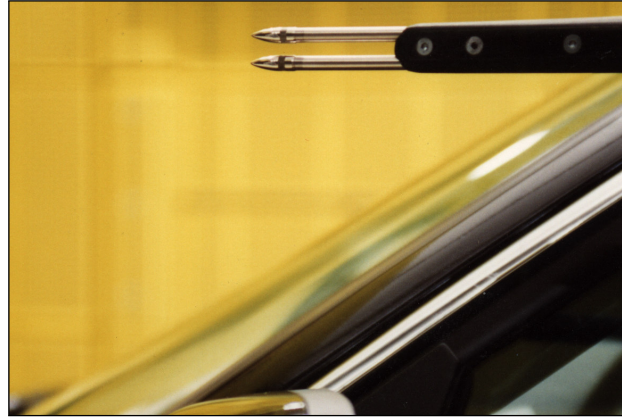


Figure 1.18: Aeroacoustic sound intensity probe, from Helfer (2000b)

As with an acoustic mirror, intensity probes only measure at a specific point in space. Therefore, to capture the characteristic sound field around a vehicle, the probe must be traversed. The use of two microphones only allows the sound intensity vector to be resolved in two-dimensions. An additional orthogonal measurement is required to resolve in three-dimensions, however since intensity measurements are best suited close to the geometry of the vehicle, this can lead to limitations in accessing certain regions of the vehicle with the probe.

Acoustic Holography

Acoustic holography is an array-based measurement technique using multiple microphones. A number of different solutions exist to process the microphone data, but are based on cross-spectra in either the frequency or wave-number domain. The underlying principle is to take the sound field measured in one plane and transform it spatially to an alternative plane, determining parameters such as sound pressure and intensity on the plane of interest. Previously, the spacing of the microphones was restricted to

1. INTRODUCTION AND AIMS

either being in an evenly spaced traversing line, or alternatively in a perpendicular grid. However, developments in signal processing have relaxed this restriction, from Deblauwe et al. (2007). Unlike other array-based measurement systems, the main advantage of acoustic holography is that there is no link between the spatial resolution of the measured sound field and the frequency. Both of these parameters are governed by the inter-microphone spacing. Examples of traversing systems installed in wind tunnels include those of Pininfarina, from Cogotti (1997), and FKFS, from Helfer (2005).

Beamforming

Like acoustic intensimetry and holography, beamforming is a technique of sound source localisation using multiple microphones. The underlying concept behind this method is using a time-difference-of-arrival method to determine the position of a sound source. The surface of the vehicle is scanned by virtually focussing the array on different measurement points. Based on the distance between the measurement point and an individual microphone, the sound wave propagation delay can be determined and the recorded signal corrected. By summing the contributions of each microphone with their respective time delays, noise sources located at that point will sum together whereas uncorrelated noise sources will destructively combine. By completing this process at various points in space, an overall profile of various sound sources can be determined. This has the advantage over a physically traversing array in that microphone measurements are taken simultaneously, thereby avoiding the need to traverse a probe, saving considerable data collection time depending on the size of the area of interest. However, these advantages are offset by larger data storage requirements and an increased time required to process the data; although these disadvantages become more insignificant with advances in computing power.

A number of beamforming solutions exist and include fixed microphone arrays such as the wall and ceiling-mounted arrays in the Pininfarina wind tunnel, and more portable arrays. These are shown in Figure 1.19.



(a) Fixed arrays, from Cogotti (2005)



(b) Portable array, from HEAD Acoustics NVH Division (2010)

Figure 1.19: Examples of microphone arrays used in beamforming

As discussed by Deblauwe et al. (2007), the spatial resolution of the measured sound field is proportional to the ratio of the array size to distance between the measurement point and the array. At a closer distance between the array and the vehicle, the spatial resolution of the sound field is improved. However, in a wind tunnel environment, this may not be practical and the array is frequently positioned out of the airflow in an open-jet wind tunnel. This increased distance to the vehicle can be counteracted through the use of a larger array, such as the two arrays in the Pininfarina wind tunnel.

Beamforming is better suited to the measurement of higher frequency content noise, with the highest measured frequency governed by the inter-microphone spacing. Holography is better for lower frequency noise, however methods have been developed to combine both techniques using a single array, from Deblauwe et al. (2007).

1. INTRODUCTION AND AIMS

Surface Microphones

Another method of directly measuring the sound field is through the use of surface microphones. These are thin devices which are fixed directly to the surface of the vehicle and record the sound source directly at that point. To gather a picture of the entire field, multiple microphones at different positions must be investigated. Surface microphones have the advantage over other external noise measurement techniques in that they can be used in the on-road environment. Surface microphones are useful in assessing localised regions of a vehicle, such as in work by Zimmer et al. (2001a), who used surface mounted microphones to assess noise generation in the A-pillar and sideglass region. Studies by Khalighi et al. (2008) and Chen et al. (2009) investigated different door mirror geometries in isolation, with surface microphones measuring the effect that these had on surface noise in the sideglass region. Recently this technique has started to become more widespread as work continues to assess the accuracy of numerical noise predications against experimental data. Studies include those of Li et al. (2003) and Lepley et al. (2010), where surface microphones were used to correlate CFD data in a study which aimed to simulate the noise transmission path from the external surfaces of the vehicle to the interior cabin noise.

1.3.6 Computational Aeroacoustics

Computational aeroacoustics (CAA) is based on CFD software, with the CFD providing information on the pressure fluctuations present on solid boundaries and in fluid wakes. These fluctuations are significant sources of sound waves and as previously discussed, surface pressure fluctuations leading to dipole sound sources tend to dominate over the quadrupole sources present in wakes.

In principle, sound sources and wave propagation can be directly calculated using CFD, from a direct numerical simulation (DNS) of all scales; both turbulent and acous-

tic. Thus the small turbulence length scales and the larger acoustic scales are solved in parallel. Since the acoustic wavelengths are larger than the turbulence scales, it is these scales and the resolved geometry that determine the required spatial resolution Δx . However, owing to the fast propagation of acoustic waves, the time step Δt has to be very small to satisfy the Courant-Friedrichs-Lewy (CFL) condition, from Courant et al. (1928).

$$\Delta t \leq \frac{\Delta x}{2a} \quad (1.16)$$

Owing to the very large demands on computing resources as a result of this criterion, currently the use of DNS to solve aeroacoustic cases is restricted to small-scale academic investigations, from Blumrich (2006). Therefore, with the exception of DNS in which both the turbulence and acoustic scales are resolved, the majority of CFD approaches rely on modelling the turbulence scales. These are combined with a method to solve the acoustic field.

One approach is to utilise hybrid methods, which separate the flow and acoustic solutions, first solving the flow field and using these terms to then solve the sound field. This allows a scale separation and consequently a reduction in computational expense. The link between the flow and sound fields is through the use of acoustic analogies, whereby the compressible forms of the Navier-Stokes equations are rearranged into a form of the classical acoustic wave equation. The earliest and perhaps most celebrated of these analogies is the previously described method of Lighthill (1952, 1954), used to calculate acoustic radiation from small regions of turbulent flow within an infinite homogenous fluid. The success of the acoustic analogy led to the work being extended by Curle (1955), Ffowcs Williams and Hawkins (1969) and Ffowcs Williams and Hall (1970) to include the effects of solid boundaries, which are especially relevant in the field of automotive aeroacoustics. More recently, Ask (2008) and Ask and David-

1. INTRODUCTION AND AIMS

son (2010) investigated Curle's equation with respect to wind rush noise. It was found that the analogy predicted the amplitude of the noise satisfactorily, although the directivity of the noise could be affected by distortions in flow field from dominant flow structures, such as A-pillar vortices. Assessments have also been made by a number of other authors, including El Hachemi et al. (2002).

With the increases in available computing power, the focus is shifting towards a more direct computational approach, where the near-field sound sources are largely resolved, whilst acoustic analogies are still employed to determine far-field sound propagation. Amongst others, both LES and LBM are widely used in such studies. An early application of this work by Duncan et al. (2002) explored LBM to separate different frequencies of fluctuations on an idealised body, through the use of spectral techniques to help identify noise-producing areas. More recent developments include coupling with structural solvers to determine the impact of door-seal shape changes on aeroacoustics, Blumrich (2009), and the structural transmission paths of external sound sources to predict cabin noise, Lepley et al. (2010).

The research presented in this thesis concerns transient aeroacoustics. This is particularly challenging from a CFD computational expense perspective, since these simulations generally combine an acoustic need for a small time-step with longer simulation times to not only simulate lower acoustic frequencies, but to capture the transient nature of the flow. Therefore transient aeroacoustic simulations are not currently widespread. This contrasts with transient force investigations, which, owing to their more moderate computational requirements are becoming more common, including those of Tsubokura et al. (2010), Gaylard et al. (2010) and Mankowski et al. (2011).

1.3.7 Psychoacoustics

Psychoacoustics is the study of sound perception, linking acoustics with both the physiological response of how the body receives a sound and the psychological response of how the received sound is then perceived by the brain.

As introduced in Section 1.3.2, there are a number of methods available to quantify the physical properties of a noise source. Psychoacoustics take this a step further, by studying the perception of this noise by a passenger. The study of psychoacoustics is an attempt at quantifying one's perception of noise and is of importance in the automotive industry.

1.3.7.1 Loudness

Loudness is a psychoacoustic parameter describing how the ear perceives the strength of a particular sound. Human hearing sensitivity varies with frequency owing to the transfer function between acoustic waves in the ear to the cochlea. This frequency-dependent sensitivity can be described through use of equal-loudness contours, which are shown by Figure 1.20. These are lines plotting a contour of equal hearing sensation in the frequency domain. Hearing sensitivity is reduced at low frequencies, whilst is at its greatest between 3 and 4 kHz owing to resonances of the auditory canal. These contours were originally defined by work undertaken by Fletcher and Munson (1933) and further revised by Robinson and Dadson (1956), forming the basis of the original ISO226:1961 (1961) standard. This standard was later revised into its current form of ISO226:2003 (2003) taking into account a larger set of respondent data, including data from a range of different countries. The contours were generated with pure tones using headphones and are therefore only valid for side presentation, which is not the typical manner in which real-world sounds are presented to a listener. However, these contours can be altered to be more applicable to a human listener through the head-related transfer function.

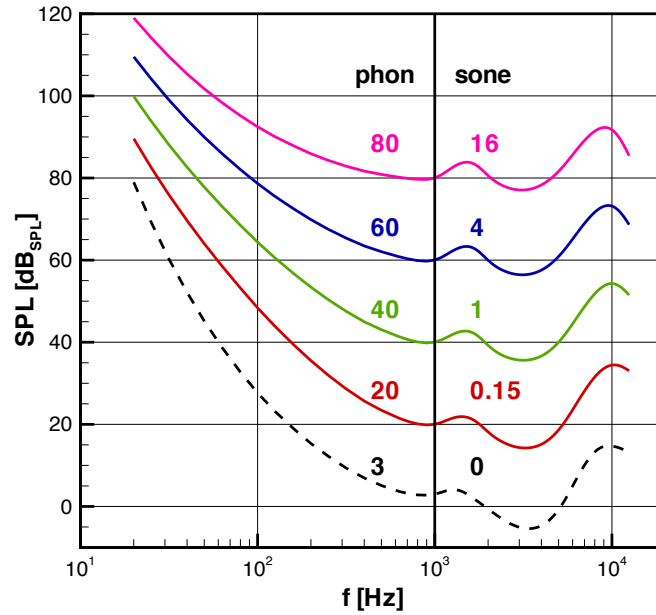


Figure 1.20: Equal loudness contours according to ISO226:2003

A number of contours are plotted, each intersecting 1 kHz at a different sound pressure level. It is this level, measured in dB_{SPL} , which acts as the reference for the *phon* scale of loudness. This scale is one of the two methods for quantifying the curves. An alternative measurement scale to characterise loudness is the *sone* scale, expressed by the unit N . This is a method to linearise the subjective perception of loudness of an acoustic signal. One sone is defined as corresponding to the equal loudness contour that intersects the frequency of 1 kHz at 40 dB_{SPL} . Sounds perceived twice as loud have a loudness of two sones. The dashed line is the contour for the average threshold of hearing, indicating that the $P_{\text{Ref}} = 2 \times 10^{-5}$ Pa reference for overall dB_{SPL} measurements is not the absolute threshold at all frequencies.

To determine the overall loudness of a particular sound, a number of methods are available. These essentially take the measured sound and combine it with the appropriate equal-loudness contour to determine an overall parameter of loudness. Of these, the *Zwicker model of loudness* is the most commonly used, based on critical bands

and incorporating the effects of masking and forms part of the ISO532:1975 (1975) standard. Interestingly the less commonly used *Stevens* method, based on octave bands, is also included in the same standard. Moore and Glasberg (1996) have since refined these loudness models and this work forms part of the standard ANSI/ASA S3.4-2005 (2005).

1.3.7.2 A-Weighting

The loudness models discussed previously aim to quantify how the level of a sound is perceived by a human. However, these methods require a number of calculation steps and can be relatively complex, particularly the method proposed by Moore and Glasberg (1996). Prior to the development of these models, a number of electronic filters were developed to approximate the equal-loudness contours of Fletcher and Munson. These electronic filters were originally designed to be incorporated into sound level meters, so as to provide an overall SPL more representative of how an average person would perceive the level of the sound. Since the profiles of the equal-loudness contours are not constant for different sound levels, a number of filters were designed.

Commonly used is the A-weighted filter, shown in Figure 1.21, which approximates the equal-loudness contour of 40 phon, or 1 sone. The data has been taken from the defining standard ANSI/ASA S1.42-2001 (2001). Owing to the limitations in the design of the electronic filter at the time of development, the resonant peaks of the equal-loudness contours are not captured. However, the main advantage of this filter was its simplicity of use, in that a sound level meter can report a weighted overall SPL, with no data processing required. This convenience led to the widespread adoption of the A-weighted sound pressure level measurement, denoted by the unit dB(A).

With the development of modern electronics, the requirements to have a relatively simple filtering circuit have diminished. However, the popularity of the measurement

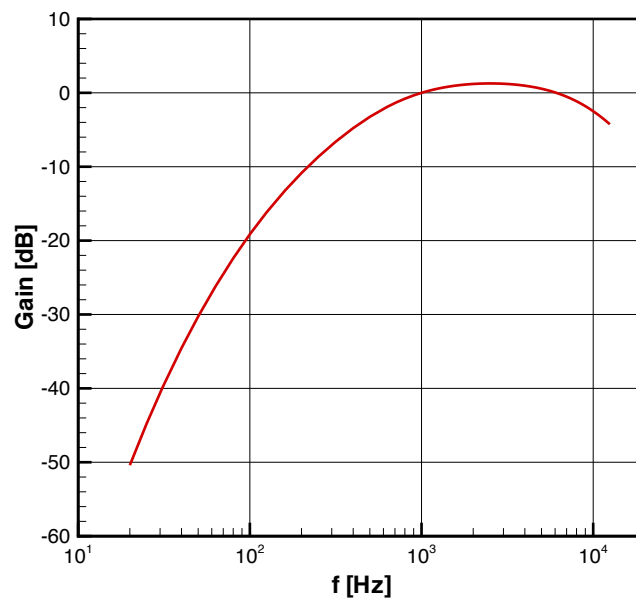


Figure 1.21: Frequency response of the A-weighted filter

has continued. It also should be noted that the A-weighting filter was designed to approximate the 1 sone equal loudness contour. The typical loudness inside a vehicle in a wind tunnel at moderate speed is an order of magnitude greater than this. Therefore the A-weighted filter tends to over-estimate the attenuation of lower frequencies. These limitations have been discussed by a number of authors, including Hellman and Zwicker (1987). However, through the use of a combination of measures, for instance comprising not only the overall A-weighted values but also the spectral content, useful information about the nature of the sound can be gained using this convenient measurement.

1.3.7.3 Articulation Index

To assess how much a particular noise affects the intelligibility of speech, the parameter of articulation index (AI) can be used. This is defined in a number of different ways, although each has the same aim in characterising a particular noise in a scale

between 0–100%, with 100% as perfect speech intelligibility and 0% where speech is completely masked by the noise.

The concept of articulation index was originally developed to characterise speech intelligibility in the field of communications by Fletcher and Steinberg (1929). Later, Kryter (1962) described procedures for computing AI, which were formalised and formed part of the ANSI/ASA S3.5-1969 standard. The procedure to calculate AI according to the standard was quite involved and this led to an alternative, simpler method being developed by Van Ligten (1982), cited by Onusic et al. (2000), oriented towards the automotive industry.

This method takes the third-octave dB(A) spectrum of a noise and compares it against a defined spectral range of typical human speech. Each third-octave band is then combined with a weighting factor, emphasising important frequencies and from this, the articulation index is generated and measured as percentage articulation. Figure 1.22(a) shows the SPL range relevant to speech quality in addition to the weighting factor that indicates that frequencies around 1–2 kHz are particularly significant.

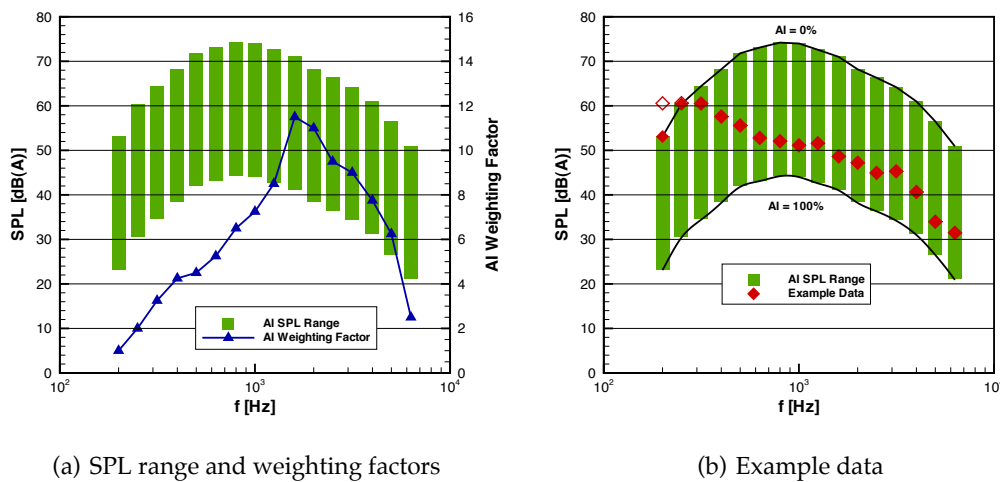


Figure 1.22: Articulation Index calculation graphs

1. INTRODUCTION AND AIMS

The method involves first calculating the A-weighted third-octave spectrum of a particular noise. For each frequency band, this SPL is compared against the AI SPL range and given a value between 0 and 1. Levels above the maximum AI level for that particular frequency band are fixed at unity, whilst levels below the minimum are fixed at zero. Frequencies between the AI SPL range are linearly scaled between these minimum and maximum values. This number is then multiplied by the weighting factor to form the frequency-specific articulation index $AI'(k)$, defined by:

$$AI'(k) = \frac{L(k) - L_{AI, \min}(k)}{30} \cdot W(k) \quad (1.17)$$

An example of this process is shown in Figure 1.22(b), where example data is plotted against the AI SPL range. The 200 Hz component of the example noise exceeds the AI range and this point is indicated by an unfilled point. This value is consequently fixed at the maximum level in the AI range and is shown by a filled point.

To form the overall AI for a particular noise, the specific AI components are summed over the third-octave bands between 200 Hz and 6.3 kHz and subtracted from unity, as shown by:

$$AI = 1 - \sum_{\text{all } k} AI'(k) \quad (1.18)$$

An articulation index close to zero implies very poor speech intelligibility and close to unity implies very good speech intelligibility. The example data shown in Figure 1.22(b) has an AI of 64.5%, exhibiting moderately good speech intelligibility.

1.3.7.4 Other Metrics and Jury Testing

A wide range of other psychoacoustic parameters are available and many are summarised by Fastl and Zwicker (2007). These include parameters to quantify the spectral content of a noise such as sharpness, and those to characterise temporal fluctua-

tions such as roughness, fluctuation strength and modulation degree. Sharpness is calculated in a similar manner to loudness, although placing more emphasis on the higher frequency content of the noise. As stated by Helfer and Busch (1992), the sharpness of the vehicle cabin noise is dominated by wind noise, since wind noise sources dominate the higher frequencies. Sharpness is not a standardised parameter and therefore a number of calculation methods exist. The method proposed by Fastl and Zwicker (2007) requires the calculation of specific loudness, which is the component of the overall loudness at each critical band. Specific loudness sums over the 24 critical bands to equal the overall loudness, according to:

$$N = \sum_{z=0}^{24} N'(z) \quad (1.19)$$

Sharpness is then calculated through the summation of the product of specific loudness and a weighting function $g(z)$, over the 24 critical bands by:

$$S = 0.11 \frac{\sum_{z=0}^{24} N'(z) \cdot g(z) \cdot z}{N} \quad (1.20)$$

It is this weighting function that emphasises the importance of the higher frequency content to sharpness, with the function presented by Figure 1.23 as a function of critical band number, z .

Above 14 bark, the weighting function begins to rise rapidly above unity, thereby increasing the importance of higher frequencies in the calculation of sharpness. In addition to the weighting function, frequency is also plotted against z allowing a conversion to be made between the critical band domain and the frequency domain. This shows that frequencies above 2 kHz play an increasing role in the sharpness level of a particular noise.

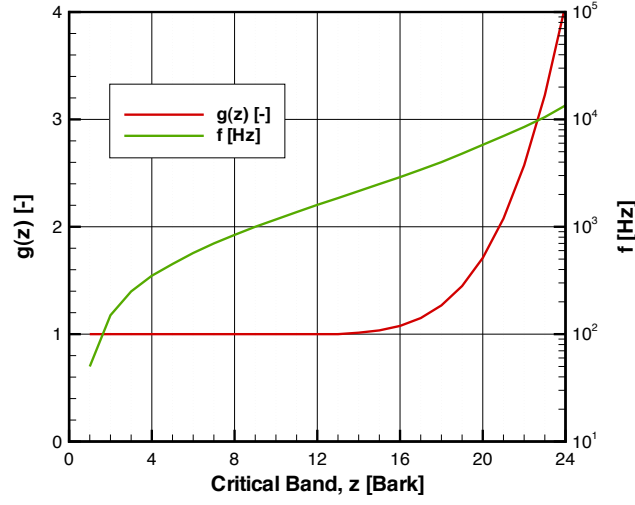


Figure 1.23: Sharpness weighting function, $g(z)$, defined by Fastl and Zwicker (2007)

Roughness and fluctuation strength are related and are associated with the temporal fluctuation of a sound signal. Fluctuations at frequencies greater than 10 Hz increase roughness, with those below increasing fluctuation strength. According to Fastl and Zwicker (2007), fluctuation strength scales with modulation frequency as follows:

$$F \sim \frac{\Delta L}{(f_{\text{Mod}}/4 \text{ Hz}) + (4 \text{ Hz}/f_{\text{Mod}})} \quad (1.21)$$

This relationship indicates the importance of the 4 Hz modulation frequency. This is also shown by Terhardt (1998) in a plot of just-noticeable changes in modulation degree at various modulation frequencies, presented by Figure 1.24. The degree of modulation, m , describes the strength of modulation and is calculated as a ratio of the fluctuating component to the constant component of the modulation signal, in the same manner as modulation depth is calculated for AM (amplitude modulated) signals. A smaller noticeable change of m indicates a greater human sensitivity toward this modulation frequency.

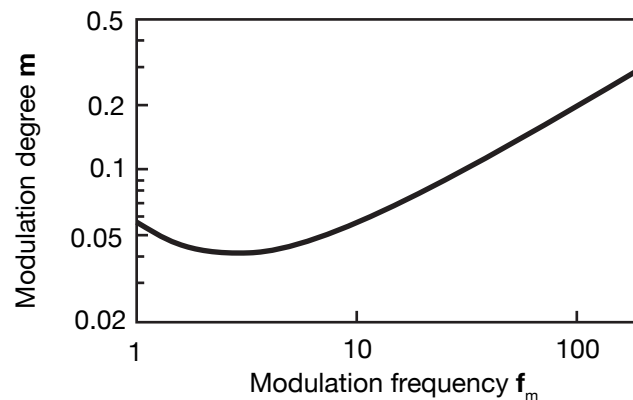


Figure 1.24: Just-noticeable modulation degree, from Terhardt (1998)

The 4 Hz sensitivity to amplitude modulations by a person is thought to be linked to the average speaking rate of four syllables per second, Fastl and Zwicker (2007). In work discussed later, in Section 1.4.6, it is known that fluctuations in the approaching flow can lead to noise modulation. Thus it follows that vehicle occupants may be particularly sensitive to fluctuations in the higher frequency component of cabin noise due to unsteadiness in the oncoming flow at around 4 Hz.

To ensure that a particular psychoacoustic parameter is appropriate to characterise a particular noise, jury testing can be used to correlate the quantitative parameter with the qualitative response of a listener. For instance, both Otto and Feng (1995) and Hoshino and Kato (2002) assessed a number of parameters to determine which best characterised the component of wind noise in the overall noise heard inside the cabin. Jury testing was used, in which listeners heard a number of sound samples and recorded a subjective opinion. This subjective data was then correlated against a number of parameters. In both instances, loudness was found to be the dominating parameter. However, the sound samples of wind noise were assessed on-road under still conditions, overlooking the effects of unsteadiness in the oncoming wind leading to sound modulation.

1. INTRODUCTION AND AIMS

In addition to assessing how well a single parameter can characterise a subjective evaluation, jury testing can be used to create a composite index, comprising a range of different parameters to capture important features of cabin noise. In this case, a number of parameters are assessed against subjective responses, which are weighted and combined to build up a composite metric. As noted by Gade (2007), many vehicle manufacturers consider the nature of these composite metrics secrets and seldom publish their findings. However, a number of researchers have completed similar studies, including work completed by Nor et al. (2008) who used combinations of a number of parameters and a weighted average method to develop an overall perception index of road vehicle cabin noise. To determine the weightings, a number of perception tests were completed by participants, where it was determined that these weightings were dependent on the type of road surface. Bergeron et al. (2010) used sensory science techniques to assess different features of vehicle cabin noise. This involved generating composite metrics to most closely relate to certain commonly used words to describe cabin noise. In particular, the 800-4000 Hz band described as *hissing* is particularly relevant to wind noise.

A number of jury testing techniques are available to obtain subjective data from listeners. One of these techniques is the paired comparison, whereby two short sound samples are presented in quick succession. The listener then selects which sample of each pair was either the more annoying, pleasant, or whichever feature of the sound the tester is assessing. From this, each sound sample can then be ranked and correlations between subjective and objective measures assessed.

An alternative method is to rank a number of sound samples. This can be either relative to one another, such that a group of samples are ordered by a listeners opinion, or alternatively arbitrary scores can be assigned, from which the samples can then be

ordered. In comparing ranking to paired comparison methods, Kendall and Babington Smith (1940) states:

Such “inconsistent” preferences can never appear in ranking, for if A is preferred to B and B to C , then A must automatically be shown as preferred to C . The use of ranking thus destroys what may be valuable information about preferences

The number of inconsistent responses can be used to assess the reliability of a respondent in assessing various sounds. Methods used to assess the number of inconsistent responses to that obtained by chance are discussed in detail by Moran (1947) and Kendall (1955).

Whilst paired comparisons are considered to be the more rigorous form of jury testing, the number of pairs that can be assessed in a given time is much less than the number used for ranking, particularly for a large number of samples. For instance, for a paired comparison where all combinations of N sound samples are compared, the total number of combinations is shown by:

$${}^N C_2 = \frac{N!}{2!(N-2)!} = \frac{1}{2}N(N-1) \quad (1.22)$$

To obtain the total number of samples to be played, the number of comparisons is multiplied by a factor of two, since a paired comparison comprises two sound samples, giving $N(N-1)$. This contrasts with ranking where the N different samples are played once, although this number may increase if opportunity is given to the listener to replay the samples. Thus a paired comparison may take up to $N-1$ times as long to complete than a ranking exercise, which can lead to impracticably long testing times, or small amounts of data being assessed. Therefore, ranking tends to be a more common jury testing technique used to subjectively assess sounds in practise.

1.3.8 Key Remarks on Aeroacoustics

- Aeroacoustics is the study of acoustics generated either by the interaction of fluids with solid boundaries or through the turbulent nature of the flow itself.
- Noise measured in the cabin of a vehicle is sensitive to both flow speed and direction, with the level of noise typically increasing in proportion to velocity raised between powers of four and six.
- Key areas of noise generation are the separated flow structures in the A-pillar region and in the wake of the door mirror.
- Aeroacoustic wind tunnels are commonly used to assess the noise generated both internally and externally on a vehicle. The majority of aeroacoustic investigation takes place using binaural acoustic heads inside of the vehicle cabin, measuring noise as would be heard by a vehicle occupant.
- Psychoacoustics is the study of sound perception linking acoustics with both the physiological response of how the body receives a sound and the psychological response of how the received sound is then perceived by the brain. A wide range of psychoacoustic parameters exist, each attempting to capture the different ways in which a person responds to sounds.

1.4 The Unsteady Environment

1.4.1 Contributing Factors

Whilst the steady-flow wind tunnel is the standard development environment for the aeroacoustic aerodynamicist, there is increasing research comparing aerodynamic and

aeroacoustic data measured in the automotive wind tunnel and on-road. The motivation being that the conditions experienced in a wind tunnel have very low turbulence levels, which tend not to be experienced on the road. There is concern that data obtained in these steady flow environments do not capture the vehicle's response to unsteady fluctuations in the inherently turbulent external surroundings. This was summarised by a review by Watkins and Cooper (2007) who concluded that there is evidence suggesting that this on-road unsteadiness can significantly affect the aerodynamics of some road vehicles.

The unsteady environment experienced by a moving vehicle is different to that observed from a single point in space, typically measured during studies of wind engineering. These fixed-location measurements only capture the conditions of a particular point in space and therefore can only hope to record a fraction of the unsteadiness experienced by a vehicle as it traverses the on-road environment. For example, a vehicle will experience fluctuations as it traverses between these different wind environments, which will not be completely captured though the simple addition of the vehicle's velocity vector onto this data. Wind engineering measurements are also recorded typically 10 m above the ground, well above the height of relevance for a car. Whilst this data can be extrapolated down to heights more applicable to road vehicles using an atmospheric boundary layer logarithmic relationship, described by Cooper and Watkins (2007) amongst others, it was noted by Lawson (1980) that care should be exercised at the extremes of the fitted range of the law. This is particularly applicable to the typical height of a car on-road.

A number of reviews have taken place of the on-road environment including those of Howell (2000), Cooper and Watkins (2007) and Sims-Williams (2011). The review of the unsteady on-road environment by Sims-Williams (2011) succinctly highlights the

1. INTRODUCTION AND AIMS

contributions of various factors to the overall unsteadiness experienced by a vehicle traversing the environment through the total differential:

$$\frac{Du}{Dt} = \frac{\partial u_{veh}}{\partial t} + \frac{\partial u_{wind}}{\partial t} + u_{veh} \frac{\partial u_{wind}}{\partial x} \quad (1.23)$$

The first term $\frac{\partial u_{veh}}{\partial t}$

This represents the fluctuations in the oncoming flow as seen by the vehicle, owing to variations in the vehicle's velocity. Typically, a vehicle travelling on-road will experience relatively slow changes in vehicle speed meaning that the contribution of this term to the overall on-road unsteadiness will be relatively small. Therefore this term can usually be ignored, particularly in the case of this work where on-road testing took place at constant vehicle speed. Conversely, this term is much more significant in the case of a racing car on a track, where acceleration and deceleration can be much more dominant, from Sims-Williams (2008).

The second term $\frac{\partial u_{wind}}{\partial t}$

This is due to the fluctuations in wind speed as measured from a single point in space. This is the the term that was classically used in early studies of the unsteady wind environment, where stationary data was taken from masts typically at 10 m in height. This data was translated to a height more applicable to a road vehicle using an imperfect assumed boundary layer model, such as that shown by Howell (2000) and Saunders and Wordley (2006). The vehicle velocity was then superposed onto this vector.

The third term $u_{veh} \frac{\partial u_{wind}}{\partial x}$

This is perhaps the most significant term and can only be measured by a vehicle traversing the on-road environment. This term takes the spatial variations in the wind veloc-

ity and converts them into the temporal variation that the vehicle experiences as unsteadiness as it travels at velocity u_{veh} . Taylor's Hypothesis, for example as described by ESDU 74030 (1976), states that environmental turbulence is essentially a series of static perturbations convected with the mean wind velocity, so that a stationary observer experiences these perturbations in time. Roadside furniture and other stationary objects, such as trees and bridges, will result in steady spatial variations. A moving vehicle that traverses through these variations will perceive them as further unsteady fluctuations, the rate of which is affected by the vehicle's speed. This cannot therefore be derived from measurements taken at a fixed location. In addition to the wakes of stationary objects, traversing through the wakes of other road vehicles will also result in unsteady fluctuations. An investigation by Howell (2011) revealed that the decay of a vehicle's wake scales with $x^{-2/3}$, indicating that on a relatively busy motorway, a large proportion of driving time can be spent in various levels of other vehicle wakes.

1.4.2 Characterisation of the Unsteady Environment

As introduced, the unsteady environment experienced by a moving vehicle is produced by combination of different factors. These generate an ensemble of gusts of a range of different sizes and fluctuation intensities. A number of approaches are commonly used to characterise this environment and are outlined in the following sections.

1.4.2.1 Probability Density Functions

A probability density function (PDF) describes the relative likelihood that a particular variable will take a given value. To represent the probability density function for a given recorded variable X , the range of observed values is first divided into a number of equally-spaced bins, with the probability recorded for the data collected in a par-

1. INTRODUCTION AND AIMS

ticular bin n . The sum of the resulting probability distribution over the entire range is equal to unity:

$$\sum_{\text{all } n} P(X = n) = 1 \quad (1.24)$$

The probability distribution provides a convenient method for presenting the average range of conditions experienced by a vehicle, with an indication of the standard deviation and mean of these conditions. This technique also allows the distribution of the environment to be made. Probability distributions have been used by a number of authors in presenting the on-road conditions experienced by a vehicle, for instance Lawson et al. (2008) in presenting the range of oncoming flow yaw angles, and Watkins and Saunders (1998) in discussing the distribution of the components of the oncoming flow vector in different terrains.

1.4.2.2 Spectral Methods

One method of characterising the unsteady environment is through the use of an *autospectral density function* (ASD), also commonly known as the power spectral density. This is a frequency-dependent function, presenting the various spectral contributions that make up the overall time record. This function is defined by:

$$G_{xx}(f) = \frac{2}{T} |X(f)|^2 \quad (1.25)$$

according to Bendat and Piersol (1993), where X is the Fourier transform of the time record of x , of overall length T . One of the properties of the ASD is that the result of integrating over the entire frequency range is equal to the variance of the measured variable, as shown by:

$$\int_0^\infty G_{xx}(f) df = \sigma_x^2 \quad (1.26)$$

To build up an average spectrum of a series of different time records, a number of autospectral density functions can be averaged so that any spurious noise be removed from the overall spectrum. For the case of n_b records of data, each of length T , this process is defined by:

$$G_{xx}(f) = \frac{2}{n_b T} \sum_{b=1}^{n_b} |X_b(f, T)|^2 \quad (1.27)$$

Each block of data may either be chosen to be a full time record, as recorded, or alternatively records may be split into a series of blocks and the resulting average spectrum calculated. The latter process results in a larger number of blocks being used to create an average, potentially reducing spurious noise, at the expense of lower-frequency resolution. In addition to the ASD, the cross-spectral density (CSD) can be useful in determining the relationship between two signals. It is commonly used as a precursor to the calculation of transfer functions, such as those described in Section 1.4.5. Unlike the ASD, the CSD is a complex function, with X^* the complex conjugate of X . For the case of n_b records of data, each of length T , the CSD is defined by:

$$G_{xy}(f) = \frac{2}{n_b T} \sum_{b=1}^{n_b} X_b^*(f, T) Y_b(f, T) \quad (1.28)$$

1.4.2.3 Turbulence Intensity

The intensity of the turbulent velocity fluctuations measured at a point can be described using a standard deviation value. For a given analysis period of N samples, the mean value of the flow velocity is subtracted from the instantaneous total flow velocity to determine the fluctuating component. The RMS of the fluctuations over this sampling period is calculated, giving the standard deviation. This process is defined

1. INTRODUCTION AND AIMS

for the x -component of the measured flow velocity:

$$\sigma_x = \sqrt{\frac{1}{N} \sum_{i=1}^N (u_{x,i} - \overline{u_x})^2} \quad (1.29)$$

Alternatively, a spectral approach can be adopted using the square-root of the variance, as shown by Equation 1.26.

Commonly, the standard deviations are normalised with respect to the mean resultant flow speed calculated over the same sampling period and reported as a percentage. These resulting component values of turbulence intensity are described by:

$$I_x = \frac{\sigma_x}{\overline{u}} \quad I_y = \frac{\sigma_y}{\overline{u}} \quad I_z = \frac{\sigma_z}{\overline{u}} \quad (1.30)$$

with the overall bulk turbulence intensity given by the vector combination of these values and given by:

$$I = \sqrt{I_x^2 + I_y^2 + I_z^2} \quad (1.31)$$

Note that the definition of bulk turbulence intensity varies between authors, with the RMS of the individual intensity components a commonly used alternative.

1.4.2.4 Turbulence Length Scale

The unsteady environment experienced by a moving vehicle is a combination of different factors that are described earlier in this section. These generate an ensemble of gusts of a range of different sizes and fluctuation intensities. One approach to characterise this environment is through the use of a spectral distribution describing the levels of energy at each fluctuation frequency. An alternative approach is to collapse this information into a single value providing a comparative measure of the average size of a wind gust. This quantity is known as turbulence length scale, and can be used

to characterise the average gust size in the full range of scales. This has the advantage of being a convenient single-value comparative measure, although care must be taken since much of the flow information is lost in calculating this value.

There are different methods available to compute the length scale parameter, notably the autocorrelation and von Kármán methods, described by ESDU 74030 (1976) and von Kármán (1948) respectively. The autocorrelation method determines a characteristic time scale of the turbulence by determining the time period it takes for the measured velocity to become uncorrelated. This time scale is then converted into a length scale through the use of Taylor's Hypothesis. The von Kármán approach takes a non-dimensional power spectra of the wind velocity components and fits a spectra defined by von Kármán (1948) using a least-squares regression. The turbulent length scale that results in the best fit of this spectrum is given as the resulting characteristic length scale. The basis of this method is the assumption that the oncoming turbulent flow field fits that of a von Kármán spectral distribution. Figure 1.25, reproduced from Wordley (2009) shows the relationship between various von Kármán spectra and the equivalent values of turbulence intensity and length scale.

Both methods can be used to characterise the average length scale of oncoming flow turbulence, with authors such as Schröck et al. (2009a) using the von Kármán method and Lindener et al. (2007) using the autocorrelation method. Wordley (2009) compared the two methods and found that the autocorrelation method tended to give lengths of around twice those calculated using the von Kármán method. Therefore comparisons between length scales determined by different authors should be treated with care.

The autocorrelation method was used in this work and follows the method defined by ESDU 74030 (1976). This involves first calculating the autocovariance function of

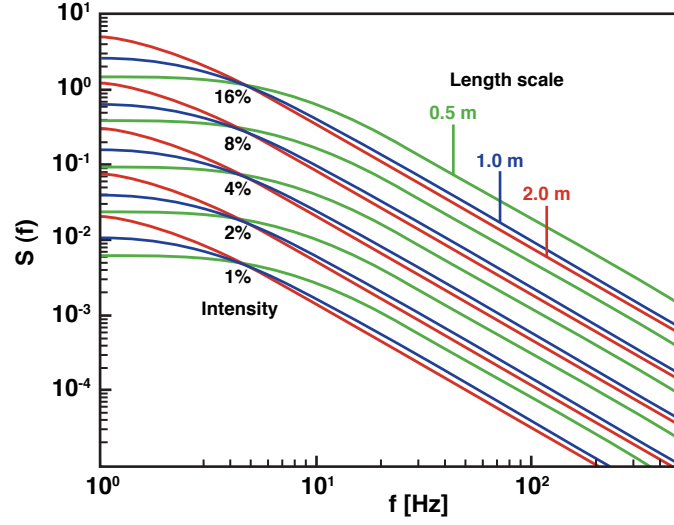


Figure 1.25: Example power spectra with equivalent turbulence intensities and von Kármán length scales, from Wordley (2009)

the three measured velocity components, according to:

$$C_{xx}(\tau) = \overline{u_x(t) \cdot u_x(t + \tau)} \quad (1.32)$$

This describes the autocovariance function calculated for the x -component of velocity, although the y and z -components follow the same form. The autocovariance function is then normalised by the respective variance at $\tau = 0$ to form the autocorrelation function, again shown for the x -component of velocity:

$$\rho_{xx}(\tau) = \frac{C_{xx}(\tau)}{\sigma_x(0)^2} \quad (1.33)$$

At small values of τ , the autocorrelation function will be close to unity since the measured signals are well correlated, i.e. there is a strong causal relationship between the signal at $t = 0$ and $t = \tau$. As τ becomes larger, this correlation will decrease since the causal relationship between a gust at $t = 0$ and $t = \tau$ will tend to zero. At a

value of zero, there is no correlation between the original signal and that at $t = \tau$ later, indicating that the original measured gust has passed downstream. To evaluate the characteristic time scale for these turbulent fluctuations, the appropriate autocorrelation function is integrated up until the point where the correlation function reaches zero, at $\tau_{\rho=0}$, as shown by:

$$T_x = \int_0^{\tau_{\rho=0}} \rho_{xx}(\tau) \, d\tau \quad (1.34)$$

Taylor's Hypothesis can be used to determine the characteristic component turbulent length scale, from the characteristic time scale, relating the temporal and spatial domains. This states that, provided the bulk flow speed \bar{u} is much greater than the turbulent fluctuations in the flow, the turbulence field can be considered to be frozen in space and convected past a point with a speed \bar{u} . Hence Taylor's Hypothesis gives:

$$L_x = T_x \bar{u} \quad (1.35)$$

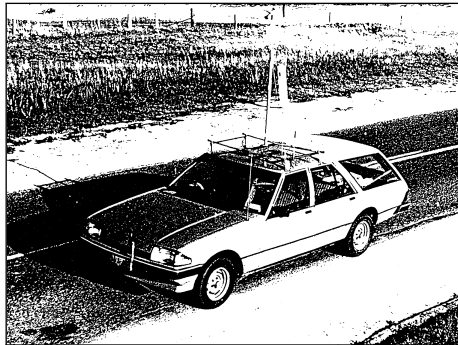
The Hypothesis was shown to be valid for scales of atmospheric turbulence generally less than 250 m through substantial research by a number of authors, including Lappe and Davidson (1963) and Powell and Elderkin (1974). However it is important to note that these studies were focussed on atmospheric turbulence rather than the unsteady flow as experienced by a ground-based vehicle.

1.4.3 The Unsteady Environment as Experienced by a Vehicle

Early work using a vehicle to collect and assess the unsteady on-road environment included that of Watkins (1990), also summarised by Watkins and Saunders (1995, 1998) and Watkins et al. (1995). This work compared turbulence intensities collected from a moving vehicle with a predictive model, taking data collected from a fixed site and translating it to what would be experienced by a moving vehicle. To collect the mov-

1. INTRODUCTION AND AIMS

ing vehicle data, a mast-mounted hot-wire anemometer was used, fixed at a height of 1.9 m above the vehicle, which travelled at 100 km h^{-1} (27.8 ms^{-1}). Two 40 km stretches of road were chosen, described as open terrain with well scattered obstructions. Turbulence intensities were found to vary depending on the degree of roadside aerodynamic obstructions and ranged from $I_x = 2.5\%$ to 5% and $I_y = 2\%$ to 10% in the longitudinal and lateral directions respectively. The model showed that wind tunnel tests at higher yaw angles should be conducted at greater turbulence levels, since under highway conditions, higher yaw angles can only be generated by inherently turbulent larger crosswinds. This is particularly significant from a wind noise perspective, since this condition combines not only yawed flow, leading to an increase in the level of wind noise through increased flow separation, but also fluctuations, leading to wind noise modulation.



(a) On-road



(b) Model-scale

Figure 1.26: Mast-mounted probe, from Watkins (1990)

Saunders and Mansour (2000) also investigated the unsteady environment as experienced by a moving vehicle. A four-hole pneumatic probe was used, mounted 0.73 m in front of a vehicle, 0.5 m above the height of the ground. Testing took place on two test tracks, in Australia and Dearborn, MI, in a range of different wind conditions. The effect of following another vehicle was also investigated. It was found that on open

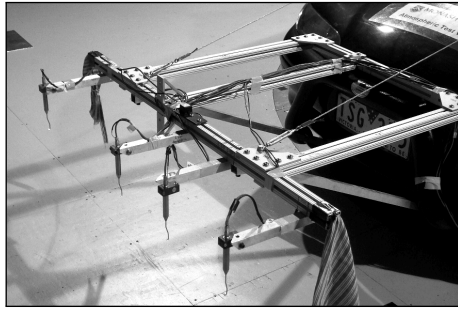
roads in light winds, turbulence intensities ranged from $I_x = 2\%$ to 3% and $I_y = 1\%$ to 2% in the longitudinal and lateral directions respectively. Autocorrelation length scales ranged from between 2 and 17 m. Turbulence intensities measured behind another vehicle were measured to range from $I_x = 10\%$ to 25% and $I_y = 6\%$ to 15% , with a separation distance of between 15 m and 4 m respectively. It was also noted that the presence of an upstream vehicle within approximately three vehicle lengths substantially increases the measured turbulence intensity, whilst significantly reducing the turbulence length scale. Finally, it was suggested that when investigating aeroacoustics in a wind tunnel, the presence of a vehicle upstream offers the opportunity to measure wind noise in a turbulent airflow. Such passive methods of turbulence generation in the wind tunnel environment are discussed in Section 1.4.7.1.

In addition to Watkins and Saunders and Mansour, a number of other authors have measured the unsteady on-road environment when assessing vehicle dynamics or aeroacoustics. These investigations are discussed in more detail in Section 1.4.6. However, a significant disadvantage of using these studies to characterise the unsteady on-road environment is that the oncoming flow tends to be measured in ways that minimise their impact on cabin noise or the flow around the vehicle. Therefore they tend to be compromised in fully capturing the on-road environment. In addition, these studies have also tended to focus on a limited range of on-road conditions and therefore do not form a complete set of data relating to the varied range of conditions that can be experienced by a vehicle. Watkins and Cooper (2007) later states that whilst this turbulence can significantly affect vehicle aerodynamic response, not enough information was known to fully characterise it.

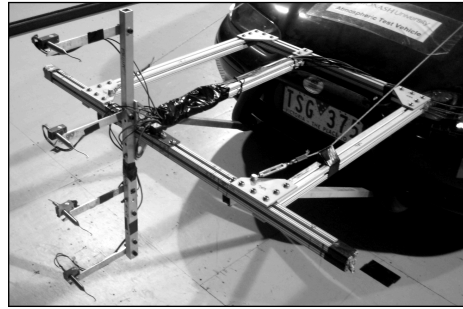
This was answered through the work of Wordley (2009), which incorporates the additional publications of Wordley and Saunders (2008) and Wordley and Saunders (2009) and forms the current definitive work on the unsteady on-road environment

1. INTRODUCTION AND AIMS

as seen from the perspective of the vehicle. This research involved collecting on-road data under a range of different traffic conditions, environments and weather conditions using a rake of four-hole pneumatic probes mounted in front of the vehicle as shown by Figure 1.27. Since the purpose of the work was to solely collect oncoming flow data, a large mounting structure could be used. This was positioned 1 m from the front of the vehicle to reduce the effect of the vehicle body on the probe measurements, although even at this spacing, the decrease in measured free-stream velocity was of the order of 10 %.



(a) Horizontal configuration



(b) Vertical configuration

Figure 1.27: Front-mounted probe rake, from Wordley (2009)

Two probe rakes were used, to investigate both horizontal and vertical spatial turbulence correlations. As the instrumented vehicle travelled along the road the probe rake moved, particularly in the vertical (z) direction. This relative motion was captured using accelerometers and the measured flow velocities were corrected. On-road data were collected under a range of conditions, with a summary of the turbulence intensities and length scales measured in these environments shown in Figure 1.28. Both von Kármán and autocorrelation length scales are presented.

These results highlight that different terrains and on-road conditions can considerably change the unsteady conditions experienced by a vehicle on-road. These range from low intensity, larger length scales experienced in smoother terrain, to the higher

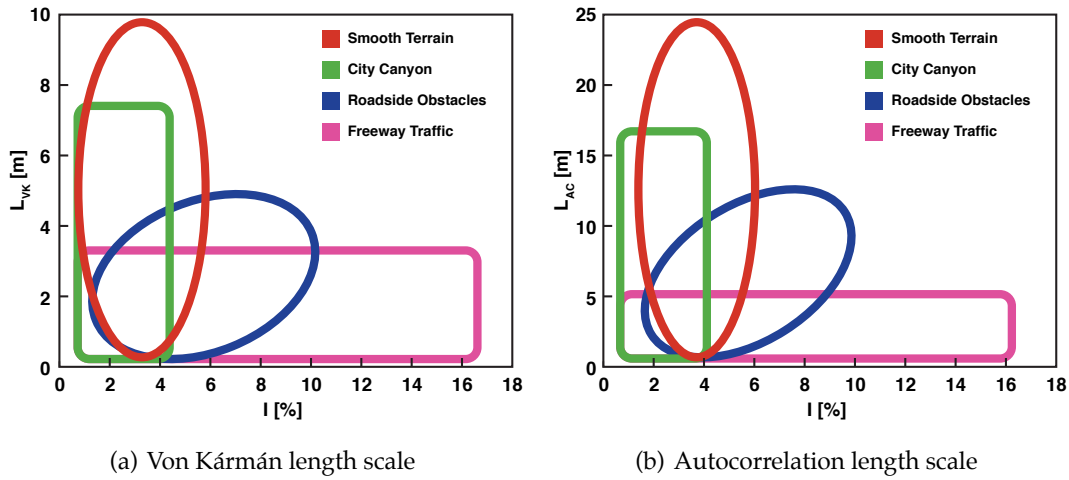


Figure 1.28: Turbulence conditions in different on-road environments, modified from Wordley (2009)

intensity, short length scales experienced in closer proximity to the wakes of other road vehicles. The measurements by Watkins (1990) took place in an environment comparable with those of the *roadside obstacle* environment of Wordley and the intensity measurements are consistent with this. Likewise, the intensity and autocorrelation length scale measurements of Saunders and Mansour (2000) on a test track, both in isolation and in the wake of another vehicle, are consistent with those of Wordley in both a smooth and freeway environment respectively.

The measurements were also presented in the spectral form of an ASD. Figure 1.29 shows these results in the lateral (cross-flow) direction, although the longitudinal direction is similar. Here, the nomenclature used to describe the ASD is S , which is equivalent to the form G_{VV} used throughout this thesis.

The wide band encapsulates the spectra for all of the measured on-road environments, highlighting the range of scales experienced on-road. The higher frequency roll-off is synonymous with the spectra of the natural wind environment. The objective of the work was to capture the range of conditions as experienced by a vehicle

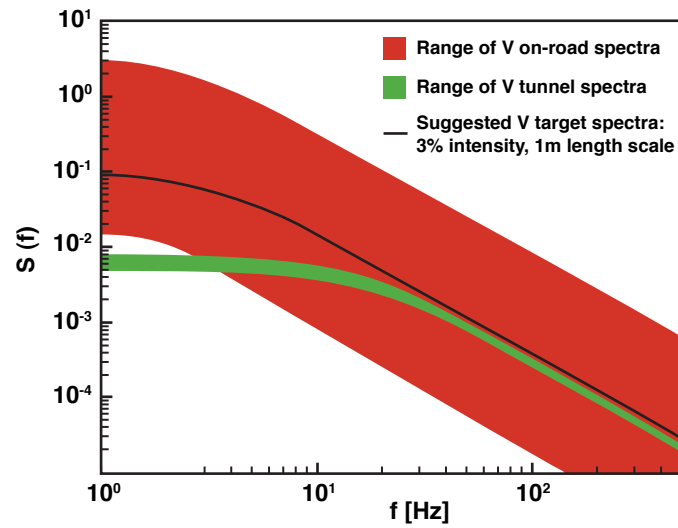


Figure 1.29: On-road cross-flow spectra, from Wordley (2009)

on-road and compare these conditions to those experienced in a full-scale automotive wind tunnel. Targets were then proposed based on these findings for the modelling of turbulence in automotive wind tunnels. Such simulation of unsteadiness is discussed further in Section 1.4.7.1.

Wojciak et al. (2010) used a similar data collection approach, focussing on isolated extreme crosswind events. Turbulence intensities were found to increase from 1–3% to 7% during the course of the gust event, with inferred gust length scales ranging from 2–200 m, with scales of 10–80 m of greatest importance.

1.4.4 Characterisation of the Vehicle's Response To Unsteadiness

When a vehicle drives through the unsteady on-road environment, it experiences a spectrum of fluctuations of different sizes and energies. How a vehicle responds to these may be frequency dependent, such that the vehicle behaves differently when subjected to either larger or smaller fluctuations in the wind.

1.4.4.1 Quasi-steady Limits

A vehicle can be said to have a quasi-steady response if the vehicle responds in the manner it would under steady conditions. That is, the behaviour of vehicle, be it in terms of flow field surface pressures or cabin noise, is independent of the rate of change of the flow field. For instance, a vehicle subjected to yawed flow that is changing sufficiently slowly will experience the same side force as would be measured at the same instantaneous yaw angle under steady conditions. As the yaw angle fluctuates with increasing frequency, the side force experienced at a particular instantaneous yaw angle will deviate from the corresponding steady measurement. At this point, the vehicle is no longer responding in a quasi-steady manner.

To characterise the interaction of transient fluctuations with an object in a non-dimensional form, the quantity *reduced frequency* is sometimes used. This is defined by

$$\begin{aligned} k &= \frac{2\pi fd}{u} \sim \frac{\text{time-scale of convection}}{\text{time-scale of unsteadiness}} \\ &= \frac{2\pi d}{\lambda} \sim \frac{\text{length-scale of object}}{\text{length-scale of unsteadiness}} \end{aligned} \tag{1.36}$$

and is a function of the oncoming flow speed u , the frequency of the oncoming unsteady fluctuations f and a length d characterising the size of the object under consideration. This relationship can also be defined using the wavelength of the unsteady fluctuation λ . Note that a number of definitions of reduced frequency exist, including that defined by Equation 1.36 divided by both 2 (for instance Bearman and Mullarkey (1994)) and 2π ; the latter more commonly known as the Strouhal number.

Reduced frequency is effectively a ratio of how long the unsteadiness lasts for to the time taken for this unsteadiness to convect over the object under consideration. It can also be thought of in terms of relative size, with fluctuations much larger than

1. INTRODUCTION AND AIMS

the object taking a correspondingly longer convection time, leading to a quasi-steady response. Conversely, smaller unsteady fluctuations will lead to a non-quasi-steady response. It is generally assumed, for instance by He (1996), that the flow will be quasi-steady at reduced frequencies less than 0.1 and will not be quasi-steady at reduced frequencies greater than 1. These limits are shown overlaid onto the crosswind spectra as presented by Wordley (2009). The equivalent length scale ratio has also been added.

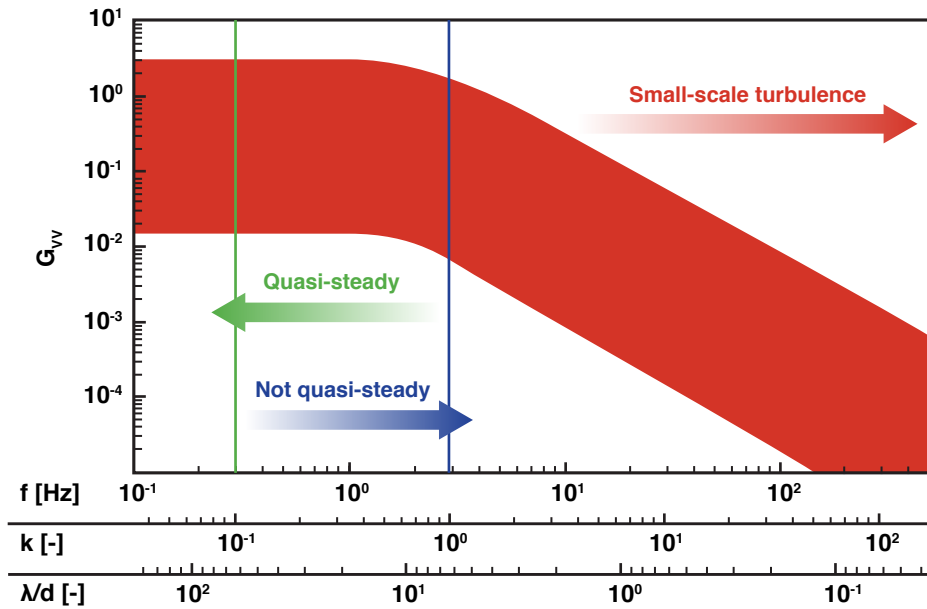


Figure 1.30: Expected bounds for vehicle quasi-steady response

The values of reduced frequency and length scale ratio are based on a vehicle travelling at 100 km h^{-1} (consistent with Wordley) and a characteristic length based on the square-root of a vehicle frontal area $\sqrt{A_f} = 1.5 \text{ m}$. Based on the reduced frequency limits, the flow around the vehicle will have sufficient time to fully develop in response to transients with wavelengths 60 times larger than the vehicle, whereas the flow field will not develop sufficiently to transients 6 times smaller than the vehicle to match that experienced under steady-state conditions.

It should be emphasised that these quasi-steady bounds are guidelines. In particular, owing to the various sizes of geometry around a vehicle, the flow around certain components may be quasi-steady, whereas around others it may not be. For instance, since the door mirrors are much smaller than the vehicle itself, the flow around the mirrors may be behaving in a quasi-steady manner, whereas the flow around the entire vehicle may not be. This therefore has implications for aerodynamics and aeroacoustics in that for a given level of unsteadiness, the aeroacoustic and aerodynamic responses may differ in their behaviour to transient fluctuations.

As the scales become smaller, the energy contained within these fluctuations becomes correspondingly reduced and this is illustrated by the high-frequency roll-off in the measured wind spectrum. These fluctuations will have a decreasing significance on the response of the vehicle as the scales become smaller. For instance, it would be imagined that transient unsteadiness of scales of the order of 1 cm would have little effect on the side forces of a vehicle, although it is likely that this small-scale turbulence will have a greater effect on aeroacoustics than aerodynamics. In summary, behaviour of the flow can be crudely separated into the following regions:

Quasi-steady region: Long length scales; vehicle responds as predicted using steady methods.

Non-quasi-steady region: Vehicle does not respond in manner predicted through steady methods; energies large enough to lead to significant vehicle response.

Small-scale turbulence region: Short length scales; energies sufficiently low to not affect vehicle, or effects imperceptible.

1.4.5 Quantifying the Response

The aerodynamic admittance is commonly used to quantify the aerodynamic response of a vehicle to unsteadiness. This approach originated in the aeronautical field by von Kármán and Sears (1938) and was extended into the field of wind engineering by Davenport (1961), describing loads on a building due to turbulent wind. The admittance is a frequency-dependent function that describes the behaviour of an output variable to a given set of input conditions. Typically, output variables are aerodynamic coefficients, such as the side force or yaw moment coefficients. An example is given by:

$$\chi(f)^2 = \frac{G_{cc}(f)}{\left(\frac{dc}{d\psi}\right)^2 G_{\psi\psi}(f)} \quad (1.37)$$

where the input and output variables are c and ψ respectively, with corresponding spectra G_{cc} and $G_{\psi\psi}$.

The differential term is determined under steady-state conditions ($f = 0$) and thus the admittance should tend to unity as $f \rightarrow 0$. However, as noted by Sims-Williams (2011), the results presented by many authors fail to demonstrate this. An admittance equal to unity is indicative of a quasi-steady response, where the ratio of output to input signal magnitudes is equal to those obtained under steady conditions. An admittance greater than unity indicates that the response is greater than that predicted by a quasi-steady approach, with admittances below unity indicative of a reduced response. At higher frequencies, the admittance function generally falls to zero, since for example these smaller fluctuations become increasingly less effective in producing a side force and yaw moment on the vehicle. An example of this was noted by Howell (2002, 2004) who found, during a theoretical investigation of ride quality for an SUV, that the unsteady wind input could cause a lateral force magnification on the vehicle at

low frequencies (an admittance greater than unity) but this effect became insignificant for frequencies greater than 2 Hz.

The aerodynamic admittance is closely related to the frequency response function, also commonly known as a transfer function. This is a more general representation of the relationship between the input and output of any linear system. The definition of the transfer function $H(f)$, with equivalent inputs and outputs to the aerodynamic admittance of Equation 1.37, is given by:

$$|H(f)|^2 = \frac{G_{cc}(f)}{G_{\psi\psi}(f)} \quad (1.38)$$

The key difference between the aerodynamic admittance and the magnitude of the transfer function is that the transfer function omits the zero-frequency ‘correction’ term. Thus depending on the sensitivity of the outputs of the system to the inputs under steady state conditions, a quasi-steady response may not be indicated by a unity transfer function.

Equation 1.38 does not illustrate the complete transfer function since it is not complex and therefore describes only the information of the magnitude change with no information given to changes in phase. This can only be determined through the use of the cross-spectral density $G_{c\psi}(f)$, which itself is a complex function. This form is given by:

$$H(f) = \frac{G_{c\psi}(f)}{G_{\psi\psi}(f)} \quad (1.39)$$

1.4.5.1 Techniques Assuming Quasi-Steady Behaviour

Quasi-steady techniques form the basis of the majority of aerodynamic and aeroacoustic testing taking place in wind tunnels. For instance it is common for a wind tunnel test to take place at a series of yaw angles and flow speeds, with the behaviour of the

1. INTRODUCTION AND AIMS

vehicle on-road inferred from these results. Indeed, it is the validity of this inference that forms the basis of this thesis.

One quasi-steady approach that extends these discrete measurements into a form more applicable to the conditions experienced on-road is through the calculation of wind-averaged drag. This is a method of not only assessing the drag coefficient of a vehicle at zero yaw, but by assessing an averaged drag from the range of yaw angles caused by the variation in the oncoming wind speed and direction. In the 1970s this became a popular method, particularly in assessing the fuel economy of trucks. The development of a wind-averaged drag coefficient $c_{D,wa}$ is discussed by Howell (2000), with the form given by Ortega and Salari (2004) based on the geometrical relationships between the wind and vehicle velocity vectors as:

$$c_{D,WA} = \frac{1}{\pi} \int_0^\pi c_D(\psi) \left(1 + 2 \left(\frac{u_{Wind}}{u_{Veh}} \right) \cos \phi + \left(\frac{u_{Wind}}{u_{Veh}} \right)^2 \right) d\phi \quad (1.40)$$

The variables are defined as per Figure 1.6, with the wind-averaged drag a function of $c_D(\psi)$, the drag coefficient at yaw angle ψ ; vehicle speed u_{Veh} ; and the average wind speed u_{Wind} blowing from direction ϕ . This simplified definition assumes that the wind can originate from any direction with equal probability and that the vehicle is symmetrical. How these quantities relate to the vehicle are shown in Figure 1.31, reproduced from the earlier Figure 1.6. More involved definitions including the use of probability distributions of yaw and wind speed are discussed by Cooper (1976), Ingram (1978) and others. However, the precise definition of these distributions will vary between different road environments and therefore the choice of probability distribution is not trivial.

Ingram (1978) found that even a relatively simple form of wind-averaged drag was a satisfactory improvement to simply assessing a zero-yaw drag value. Drag measure-

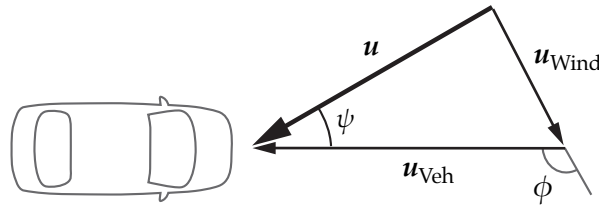


Figure 1.31: Wind, vehicle and resultant flow vectors relative to the vehicle

ments are primarily linked to fuel consumption and therefore CO₂ emissions. Fuel consumption is averaged over a relatively long period of driving and therefore a simplified wind-averaged model of the on-road wind conditions, based on a quasi-steady assumption may be sufficient to capture the differences between wind tunnel data and on road. Cabin noise in a vehicle and a passenger's perception of it is affected more by faster, transient events, and therefore a form of wind-averaged cabin noise may not be sufficient to fully capture a customer's perception of noise inside the cabin.

An alternative technique was adopted by Howell (2002, 2004) who provided an estimate of unsteady lift and yaw loading to a vehicle. Steady-wind tunnel aerodynamic coefficients were obtained in the wind tunnel and combined with a von Kármán wind spectrum to generate a theoretical response spectrum of a vehicle to these unsteady loads.

An aeroacoustic method based on the quasi-steady assumption is a cabin noise simulation technique developed by Krampol et al. (2009a,b). This technique involved creating a database of vehicle cabin noise for a number of different classes of vehicle. These were tested in an aeroacoustic wind tunnel at a range of different yaw angles and flow speeds, so that a database of noise samples was created. Using example flow data, these recorded samples were stitched together based on instantaneous resultant velocity and yaw angle, with cross-fading used to blend the samples together. To validate the procedure, the test vehicle was placed in the collector of the wind tunnel,

1. INTRODUCTION AND AIMS

with a vehicle placed in the nozzle to act as a turbulence generator. The oncoming flow field was measured from the test vehicle and this provided the example flow data, from which the cabin noise could be synthesised. Cabin noise in the test vehicle was also recorded, although not simultaneously with the flow data. Jury testing was used to assess the technique to determine the optimum stitching frequency and probe measurement location. It was found that a probe mounted on the front bumper combined with a sample frequency of 10 or 15 Hz provided the best results. It should be noted that no data was collected on-road and whilst this technique is not limited solely to wind tunnel studies, no comparison was made against the increased levels of unsteadiness found in the on-road environment. The limitations of the quasi-steady assumption forming the basis of this technique were also not assessed.

1.4.6 Assessing Vehicle Response Directly

Perhaps the most obvious approach to measure the response of a vehicle to the transient conditions on-road is to drive the vehicle in these conditions and measure the response. Like any assessment made under operating conditions, the vehicle should be measured under a sufficiently large range of wind conditions to capture the full range of unsteadiness that a vehicle may experience. Also, measurements on-road must take place at a late stage in the design process, when the vehicle is in an operable state. Wind tunnel testing has the advantage that non-functional models can be used, with measurements also generally being more controlled and repeatable. However, these advantages can be outweighed with the challenges of being able to simulate the full range of unsteady conditions that may be experienced on-road. On-road measurements are the only method in which the vehicle can truly experience these real-world conditions.

A number of studies have been completed comparing wind tunnel data with the

on-road environment. These include studies completed by Lawson et al. (2003, 2007, 2008) who compared surface pressure distributions of a mid-sized hatchback and an SUV in both the steady wind tunnel and on the road, focussing later on the A-pillar region. It was found that the wind tunnel matched the on-road time-averaged centreline and sideglass pressure profile reasonably well, but noted that the A-pillar flow structure on-road was more complex. Later work focussing solely on the A-pillar region found that whilst the oncoming flow yaw angle was the dominating factor influencing the sideglass pressure distribution, fluctuations in the pressure profile were larger than due to the yaw angle changes alone. In a similar study, Gilhome and Saunders (2002) and Saunders (2003) compared door pressures on-road and in the steady wind tunnel. The door pressure and sideglass pressure tappings are shown in Figure 1.32. It was found that the peak pressures on road were larger than that predicted by the wind tunnel, however average door pressures measured in the wind tunnel were higher than on-road. Flow structures around the A-pillar are important from a cabin noise perspective, whereas door pressures are more relevant to driving dynamics and leak noise.



Figure 1.32: Side door pressure tappings, from Gilhome and Saunders (2002)

A study by Mayer et al. (2007) assessed how the unsteady wind environment af-

1. INTRODUCTION AND AIMS

affected yawing moment on a full-size vehicle. Pressure tapings were installed over the side of a vehicle to determine the yawing moment exerted on the vehicle by the wind. A probe to measure the oncoming flow was positioned on a frame ahead of the vehicle, as shown in Figure 1.33. Testing took place on roads in the North of Germany and also in the Pininfarina wind tunnel both with and without active turbulence generation.



Figure 1.33: Probe mounted ahead of windscreen, from Mayer et al. (2007)

To compare the results obtained in both the wind tunnel and on-road, aerodynamic admittance functions were determined. These were used to assess the effect of body modifications on the stability of a vehicle under transient conditions. The measured yaw moment admittance is shown by Figure 1.34. The data were originally presented as a function of an alternative definition of reduced frequency, being a factor of 2π smaller. The results presented here have been adjusted so that the reduced frequency is consistent with that defined by Equation 1.36, with the characteristic length based on the total length of the vehicle. Results were also compared to those obtained by Cooper (1981), whose work is later described in Section 1.4.7.2.

The band of measured data was defined as being one standard deviation either side of the mean response. The data follows the results of Cooper (1981) reasonably

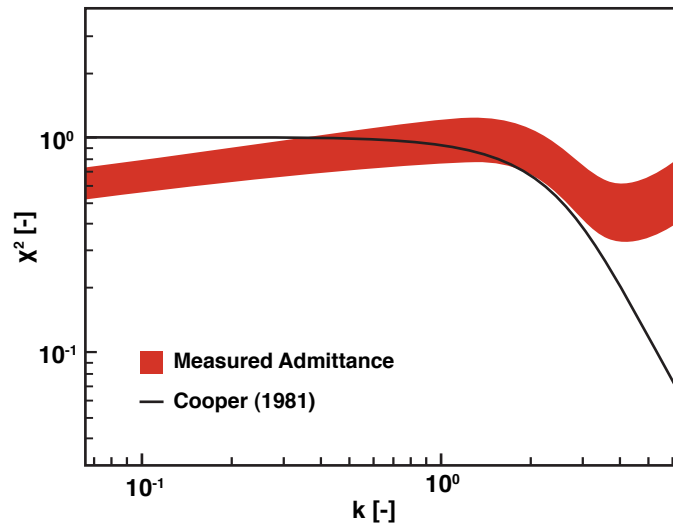


Figure 1.34: Yaw moment admittance, modified from Mayer et al. (2007)

well, with the maximum admittance and therefore vehicle yaw response at reduced frequencies between 1 and 2. It was noted that this tends to coincide with the eigen-frequency (natural frequency) of a vehicle and suspension system. Deviations from the results of Cooper occur at both extremes of the measured frequency range. The increase in admittance at higher frequencies is unusual, although noted to be consistent with Bearman and Mullarkey (1994), since it would be expected that the vehicle would respond more weakly to the smaller-scale unsteadiness on-road. The admittance was also shown to not equal unity at low frequencies.

A few aeroacoustic studies have taken place comparing wind tunnel data with the on-road environment. An early study by Zimmer et al. (2001a) assessed the effects of modifications to the A-pillar geometry of a vehicle on surface pressures and cabin noise. It was noted that improvements made in the wind tunnel were not discernible on-road, owing to engine and tyre noise effects. However, on-road testing took place in still conditions, where traffic and other vehicle wakes were avoided. More importantly, on-road testing took place at 100 kph and at these speeds it is unlikely that

1. INTRODUCTION AND AIMS

wind noise would be sufficiently dominant. Watkins et al. (2001) also compared on-road aeroacoustic data with that of the wind tunnel, using a roof-mounted probe and an acoustic head, as shown by Figure 1.35. It was noted that the time-averaged data compared between the two environments was similar and that temporal-based approaches, such as a modulation analysis were more appropriate to differentiate the effects of the onset turbulence from that of the steady flow.

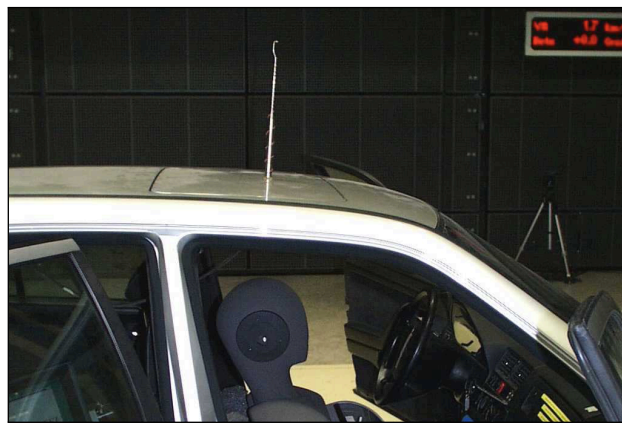


Figure 1.35: Roof-mounted probe, from Watkins et al. (2001)

An extensive study was carried out by Lindener et al. (2007), incorporating a wide range of techniques, comparing why the noise heard in the traditional smooth flow wind tunnel was different to that heard on-road. Cabin noise measurements were recorded in both the steady flow conditions of the Audi AWT and the controlled unsteady conditions of the Pininfarina AWT. These were compared against cabin noise recorded on-road under a range of conditions. A psychoacoustic study was also carried out to assess important features of the cabin noise. To measure the flow around the vehicle, both a front bumper-mounted probe, shown in Figure 1.36, and a second probe mounted near the A-pillar were used. An acoustic head was placed in the cabin to measure cabin noise.

It was found that using the turbulence generation system of the Pininfarina wind



Figure 1.36: Front-mounted probe, from Lindener et al. (2007)

tunnel, conditions that simulated the important features of the vehicle's cabin noise could be generated. However, a comparison of time-averaged data showed little difference in cabin noise response between results in the Pininfarina tunnel with or without active turbulence generation. This mirrors the findings of Lawson et al. (2008), in that it is important to look beyond the time-averaged data in assessing the differences in vehicle behaviour between steady and unsteady environments.

Using the well-known power relationship between flow speed and sound pressure level, for instance as shown by:

$$\Delta \text{dB}_{\text{SPL}}(u) = 10 \log \left(\frac{u}{u_{\text{Ref}}} \right)^{5.5} \quad (1.41)$$

a prediction of the instantaneous cabin noise can be made. The power relationship as used by Lindener et al. is presented in Equation 1.41, based on a power of 5.5. Recall that a pure dipole sound source scales with flow speed raised to the sixth power, implying that the relationship chosen here implies dipole-dominated behaviour, with a minor contribution from monopole sources.

By taking a reference speed u_{Ref} and corresponding SPL, the increase in cabin noise $\Delta \text{dB}_{\text{SPL}}(u)$ from this baseline level was then predicted. On-road, only the wind com-

1. INTRODUCTION AND AIMS

ponent of the overall cabin noise follows this power relationship. Sources such as the powertrain and tyres do not follow this relationship and can dominate certain frequency ranges of the cabin noise. Therefore, for this relationship to be useful using on-road data, an octave band dominated by wind noise was chosen; in this instance the 4 kHz octave band. The results of the flow speed dependent prediction for this octave band are shown by Figure 1.37.

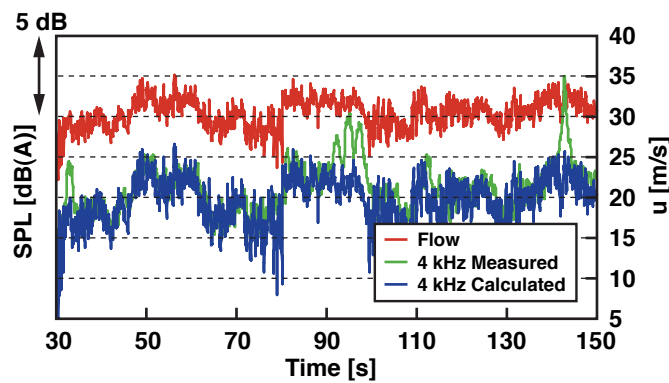


Figure 1.37: Wind noise prediction of 4 kHz octave band, modified from Lindener et al. (2007)

Generally, the prediction correlates well with the cabin noise measured on-road, with the major fluctuations of the measured noise captured by the prediction. There are notable deviations between the measured and predicted traces at 90 and 140 s, which are due to sounds not correlated with the oncoming flow speed. These may include the noise of other road vehicles, impacts on the road surface or other noises in the cabin. Alternatively, these deviations are likely to be caused by fluctuations in the oncoming flow yaw angle. These fluctuations would tend to increase the amount of leeward flow separation with a subsequent increase in cabin noise. These significant deviations are not captured by a predictive model only utilising the a speed dependent power relationship. In addition, it is clear when comparing the traces that the fluctuations caused by the longer flow speed transients are captured well by the prediction, however it is difficult to determine how successfully the faster transients are

captured. Figure 1.38 shows the relationship between cabin noise modulation and oncoming flow turbulence.

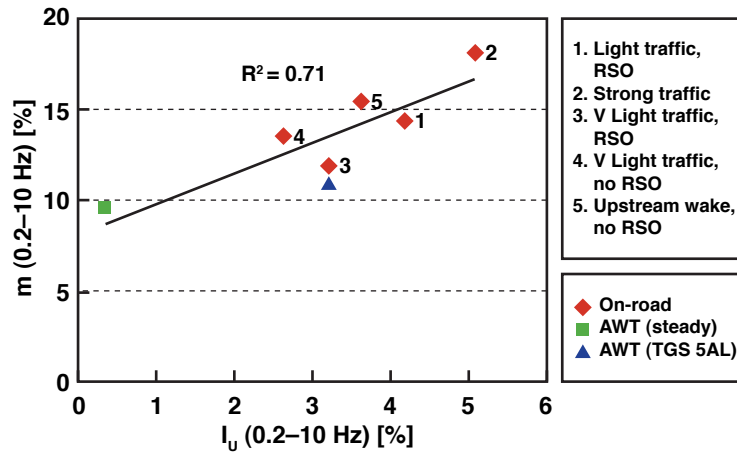


Figure 1.38: Cabin noise modulation and oncoming flow turbulence, from Lindener et al. (2007)

A total of five different road conditions are plotted, under different traffic and roadside obstacle (RSO) conditions. The correlation between cabin noise modulation and longitudinal turbulence intensity is relatively good, with $R^2 = 0.71$, indicating that modulation in the cabin noise is closely related to turbulent fluctuations in the onset flow, albeit for a specific range of noise and modulation frequencies. What is also shown is that the 5AL mode of the Pininfarina turbulence generation system produces similar modulation and turbulence intensity to that of on-road light traffic, although the modulation is not significantly different to that experienced in the wind tunnel under steady flow conditions.

Coastdown testing is another method of directly assessing aerodynamic performance by driving a vehicle on road. Typically this technique is used to assess the drag coefficient of a vehicle, particularly when assessing the overall resistance to be used as an input for a dynamometer to assess fuel consumption. A vehicle is driven to a certain speed and then allowed to decelerate naturally by placing the vehicle in

1. INTRODUCTION AND AIMS

a neutral gear. By accounting for mechanical losses, the time taken for the vehicle to decelerate can be used to determine the aerodynamic forces acting on the vehicle and hence the drag coefficient. This has to be done in still air, or alternatively the wind can be measured using an anemometer and corrected for. A typical set-up is shown by Figure 1.39, with the anemometer positioned in front of the vehicle.

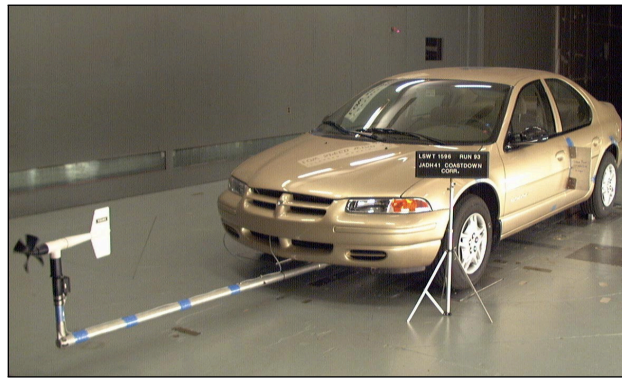


Figure 1.39: Example of an anemometer used in coastdown testing, from Walter et al. (2001)

The primary use for coastdown testing is to assess total resistance of a vehicle for the determination of fuel economy when combined with dynamometer tests. This technique is also occasionally used for larger vehicles that cannot fit in a wind tunnel, from Walter et al. (2001), and was also a common method used prior to ground simulation becoming more widespread in wind tunnels, from Howell et al. (2002). In addition to simply being used to assess the drag of a vehicle, investigations have been carried out using coastdown techniques, such as those by Bratschitsch et al. (2004) and Bischof et al. (2005), assessing aerodynamic changes to the floor of a vehicle. Work by Bischof (2008) also used a coastdown method to assess the dynamic response of a vehicle to on-road gusts. It was found that the longitudinal vehicle response to unsteadiness reached a maximum at 1.25 Hz; equivalent to a reduced frequency of unity, based on vehicle length, or wavelengths of unsteadiness approximately five times the length of

the vehicle. This response was also noted to coincide with the natural frequency range of the vehicle's suspension system.

1.4.7 Assessing Vehicle Response Indirectly through Simulation

1.4.7.1 Simulation of Wind Vector Relative to Vehicle

To take advantage of the controlled and more repeatable conditions experienced in the wind tunnel compared to on-road, an alternative approach is to simulate the effects of the unsteady onset flow through the use of turbulence generation systems. These systems are generally placed upstream of the test section in a wind tunnel and can be used to generate a particular range of scales through either passive or active means.

The work of Wordley (2009) concluded with recommendations for the scales which such generation systems should aim to simulate. Using on-road data collected under a range of conditions, autospectral density functions were fitted to these measured spectra. The chosen approach was to match the mid-to-high frequency range, whilst accepting as a necessary compromise a lower level of energy in the low frequency range than found on-road, owing to the difficulties in generating the larger length scales in existing wind tunnels. The target spectra are shown in Figure 1.40.

The equivalent turbulence length scales and intensities are, for the longitudinal and lateral direction, 1 m and 3 % respectively, with values of 0.5 m and 2 % for the vertical direction.

Whilst it is these spectra that currently form the most complete set of targets for turbulence generation systems, since they are based on averaged on-road data, they dilute the potentially important impact of less common but more extreme conditions. In addition, the work considered only what was measured on-road, but not whether all frequencies are equally important in affecting the vehicle response.

The work concludes by stating that it is anticipated that a combination of passive

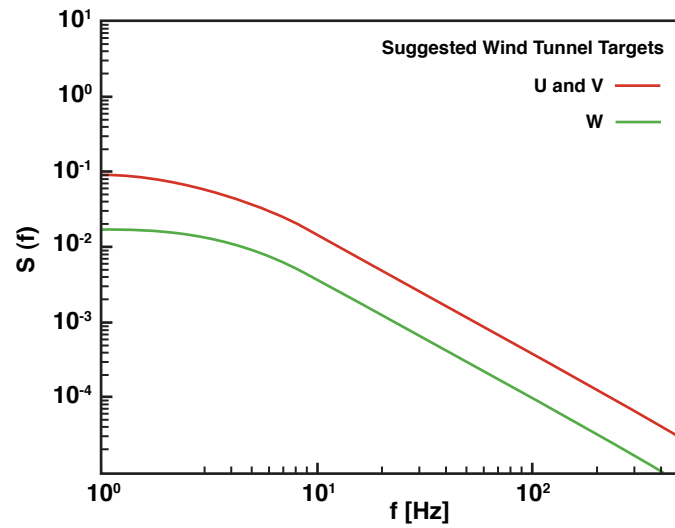


Figure 1.40: Wind tunnel turbulence targets, from Wordley (2009)

and active means will be required to produce this range of scales, with passive elements contributing to an increase in the broadband content, with active elements used to increase the energy of the low-to-mid frequency range.

Passive Methods

Passive systems involve using stationary obstructions placed in the flow upstream of the working section. These create turbulent wakes which are then carried downstream toward the working section of the tunnel. The use of grids and bars to generate turbulence has been used for many years in the field of turbomachinery, examples of which are summarised by Roach (1987) amongst others. Wind engineering studies also commonly use blocks to simulate the turbulence generated by various terrains and buildings.

Similar methods have been applied to automotive testing, including the work of Watkins (1990), where flat grids positioned normal to the flow were used to generate turbulence, as shown by Figure 1.41. In later work, Watkins and Cooper (2007)

noted that flat grids generally offered an improvement over bars since they were less Reynolds' number sensitive. Nguyen et al. (1997) also used grids when assessing the impact of turbulence on side forces generated on a vehicle. A narrowing of the spectrum with increased levels of turbulence was noted and it was proposed that the increased levels of turbulence breaks down the number of well defined flow structures acting at various frequencies, leaving for example dominating vortex shedding.

The disadvantage of passive approaches to turbulence generation is that the turbulence length scales are short, generally of the order of the size of the object used to generate the turbulence. For example, work by Howell et al. (2009) and Baden Fuller (2009) used grids to generate turbulence during a vehicle A-pillar study. Using 25 mm bars, length scales of up to 37 mm were generated. This therefore limits the size of length scale that can be generated without blocking the nozzle of the tunnel. In addition, owing to their static nature, length scales and intensities are fixed and cannot be adjusted.

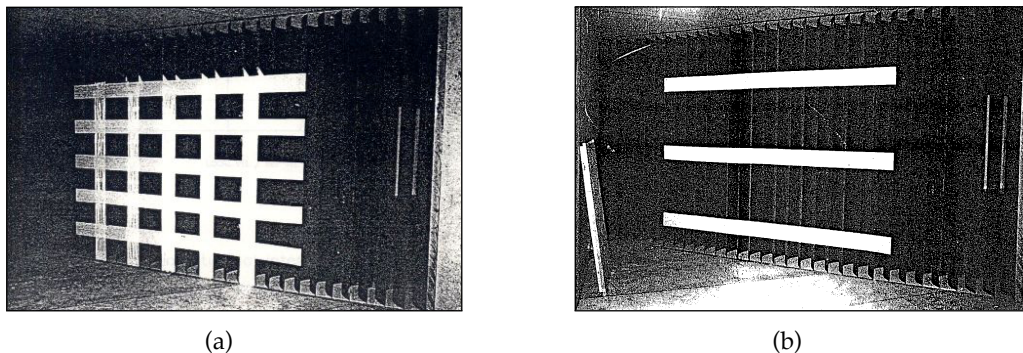
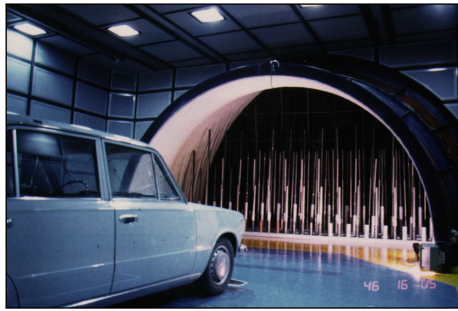


Figure 1.41: Examples of passive grids, from Watkins (1990)

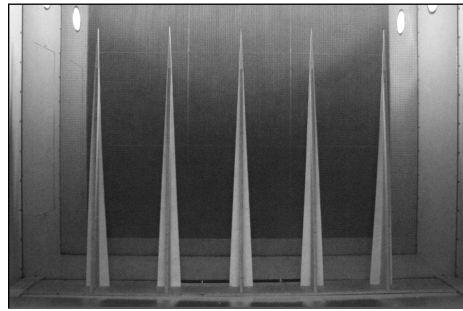
To generate a range of length scales using passive means, a number of authors have used different solutions. Prior to the installation of active aerofoils in a model tunnel, Schröck et al. (2009b) used a number of spires located in the wind tunnel's nozzle, as shown by Figure 1.42(b). These generated length scales of between 0.3–0.5 m for

1. INTRODUCTION AND AIMS

a 1/5 scale model. Another method, also used as a precursor to an active turbulence generation system installation, is the tube cascade used at Pininfarina in the late 1980s; described by Cogotti (1999) and shown by Figure 1.42(a). This involved placing an ensemble of vortex generators of varying heights and widths in the nozzle to attempt to match the boundary layer profile of the natural wind.



(a) Vortex generators, from Cogotti (1999)



(b) Spires, from Schröck et al. (2009b)

Figure 1.42: Examples of passive methods used to generate a range of scales

An alternative method of passive generation that has been used by a number of authors, including Saunders and Mansour (2000), Watkins et al. (2001), Cogotti (2001, 2003b) and Krampol et al. (2009a), is placing another vehicle within the contraction of the wind tunnel. Examples of this are shown in Figure 1.43.



(a) Watkins et al. (2001)



(b) Krampol et al. (2009a)

Figure 1.43: Examples of the use of vehicles to generate turbulence

The turbulence generated by the vehicle is convected into the working section, in-

teracting with the vehicle under test. Results suggest that turbulence intensities of the order of 10% and length scales of the order of 1 m can be generated using this approach. Whilst this is an improvement on the use of grids, there are still a number of outstanding issues. Firstly, different designs of vehicles produce different turbulent wakes and therefore the choice of dummy vehicle is not straightforward. Secondly, the wakes of other vehicles are not the only cause of turbulence experienced on the road, as discussed in Section 1.4.1. The on-road length scales measured by Wordley (2009) suggest that a vehicle traversing turbulence length scales of up to 10 m is not uncommon, especially in more rural, smooth terrain, settings. Generating turbulence length scales of this order of magnitude using passive means in a wind tunnel is not possible, unless a reduced-scale model is tested in a full-scale tunnel, thereby increasing the relative turbulence length scale, as shown by Watkins (1990).

Active Methods

The use of active means to generate turbulence is still an emerging field, with little consensus on the optimum method. This is likely to be a function of both the lack of knowledge relating to the turbulence a vehicle will experience on-road, and therefore what to model, in addition to the variety of methods that may be employed. Wordley (2009) describes two unpublished works detailing the use of both a large pendulum and flapping aerofoils upstream of the contraction. These are two examples of different methods to generate controlled levels of turbulence in a wind tunnel, as described by Mankowski et al. (2011) as drag and lift devices respectively.

Drag devices are similar to passive turbulence generation systems in that they use the wakes of bluff bodies to generate levels of turbulence. However, the turbulence generated can be altered by modifying dynamically the shape of the body and hence the wake. One particular system that has been installed and used in a number of

1. INTRODUCTION AND AIMS

different studies is the turbulence generation system (TGS) installed in the Pininfarina wind tunnel. This system and facility are summarised by Cogotti (2008) with extensive further details described by Cogotti (2002, 2003a,b,c, 2004); Cogotti et al. (2003).

The TGS uses of a number of curved, tapered vanes which can be flapped in-phase, out-of-phase and in a pseudo-random configuration, to generate a variety of different scales of unsteadiness. The TGS is shown in Figure 1.44. Whilst length scales generated by this method are generally still low when compared to what may be experienced on road, the level of control the generation system gives allows a variation in flow not possible when using a passive generation method. For example, both down-lifting and up-lifting vortex pairs can be generated, simulating the wake of different types of vehicle. Transient overtaking conditions have also been demonstrated by Carlino and Cogotti (2006).

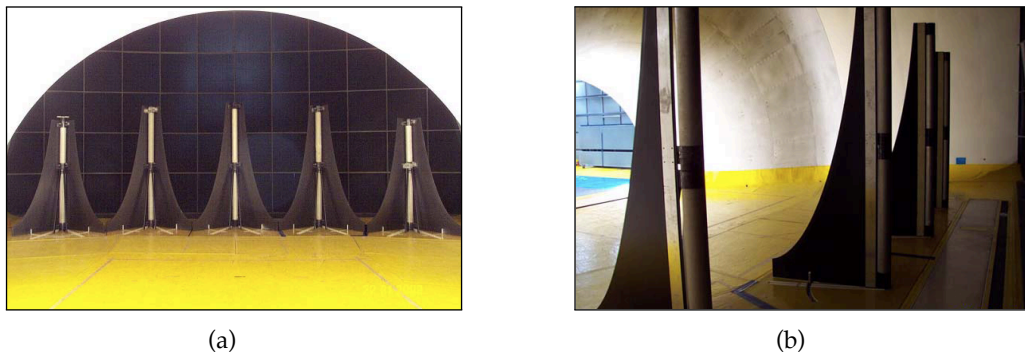


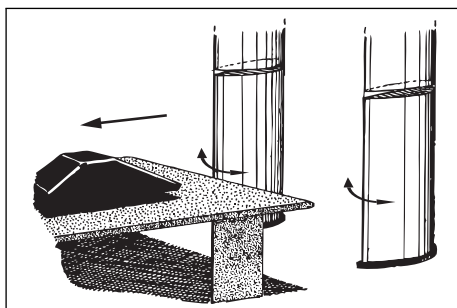
Figure 1.44: The Turbulence Generation System of the Pininfarina wind tunnel

Carlino et al. (2007) investigated the effect of the transient flow conditions as generated by the TGS on different configurations of full-scale SAE reference bodies. Scales of unsteadiness between the order of 10 and in excess of 100 vehicle lengths (λ/d) were generated. For certain configurations of SAE reference body, the yaw moment measured was up to 40% greater than that predicted under steady conditions. Smaller scales have also been assessed, including that of Maffei and Carlino (2008), who noted

that largest deviation from steady state drag measurements occurred at unsteadiness with wavelengths of less than 50% of a vehicle length ($\lambda/d < 0.5$).

The motion of the flaps is sufficiently quiet to allow acoustic measurements to be taken, with the generation system also used by Cogotti et al. (2005) in researching the booming sensation heard by passengers when side windows and sunroofs are open. It was found that unsteadiness had the effect of reducing tonal peaks whilst increasing the overall level of broadband noise.

Lift devices use aerodynamic surfaces to direct the flow, typically turning a component of the flow in the lateral, cross-flow, direction. By varying the degree and frequency of flow turning, various levels of turbulence can be generated. An early example of the use of aerofoils in turbulence generation is that of Bearman and Mullarkey (1994), who positioned aerofoils either side of a model wind tunnel nozzle which could oscillate at frequencies up to 15 Hz with a angle range of $\pm 8^\circ$. This design influenced the model-scale system described by Passmore et al. (2001), whose aerofoils could oscillate up to 18 Hz. This is shown in Figure 1.45(a) with a 1/6th scale vehicle model. The system described by Flasch et al. (2003) takes a different approach, where a single aerofoil was placed in the centre of the nozzle in a full-scale wind tunnel, allowing oscillations of up to 3 Hz. This is shown by Figure 1.45(b).



(a) Passmore et al. (2001)



(b) Flasch et al. (2003)

Figure 1.45: Examples of lift-based active turbulence generation systems

1. INTRODUCTION AND AIMS

Another use of aerofoils is described in research carried out by Schröck et al. (2011, 2009a), investigating the transient response of an idealised 20% model from the perspective of vehicle dynamics. The system, based on the work of Bearman and Mullarkey and Passmore et al. with four aerofoils positioned in the nozzle of a model-scale wind tunnel, is shown by Figure 1.46. The installation of this system followed the previously described work of the same author, Schröck et al. (2009b), using passive spires to generate a range of scales of unsteadiness. This device allowed both a greater degree of control and an increase in the range of longer-wavelength unsteadiness generated. This resulted in average lateral autocorrelation length scales increasing from 0.38 m to 0.8 m with the installation of the active generation system, over that of the passive spires.

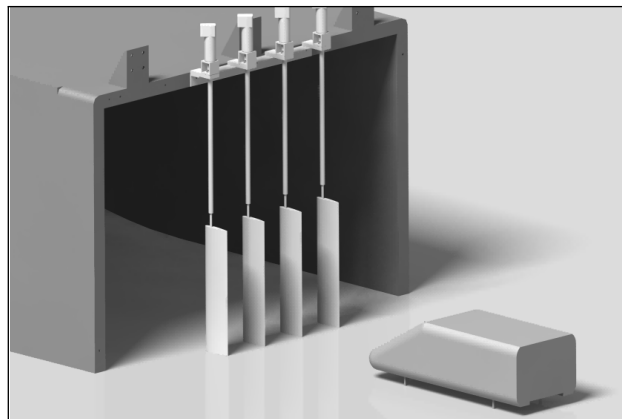


Figure 1.46: Active aerofoil gust generator, from Schröck et al. (2009a)

The work primarily focussed on assessing the transient aerodynamic response of various forms of the SAE reference body, with the work described by Schröck et al. (2009a) comparing the response of the notchback and hatchback variants to unsteady onset flows. It was found that the admittance functions of the geometries did not reach unity at low frequency. To investigate this, coherence functions were assessed to determine the degree of causality between the upstream unsteadiness and the re-

sponse of the vehicle. The notchback geometry exhibited high coherence throughout the range of frequencies tested, contrasting with the hatchback geometry with low coherence values at lower frequencies. This indicated that an additional input was also a factor in the overall vehicle response, rather than due to the upstream yaw fluctuations in the onset flow alone. Separation edges at the rear of the vehicle, such those of Figure 1.47(a), were found to improve the coherence. This indicated that self-excited unsteadiness in the low frequency range was the cause of the reduction in coherence, which the separation edges removed.

Later work described by Schröck et al. (2011) further investigated the effect of these geometry modifications. In this work the notchback SAE reference geometry was used, with both separation edges and a tail fin investigated, similar to the full-size study of Mayer et al. (2007). These modifications are shown in Figure 1.47.

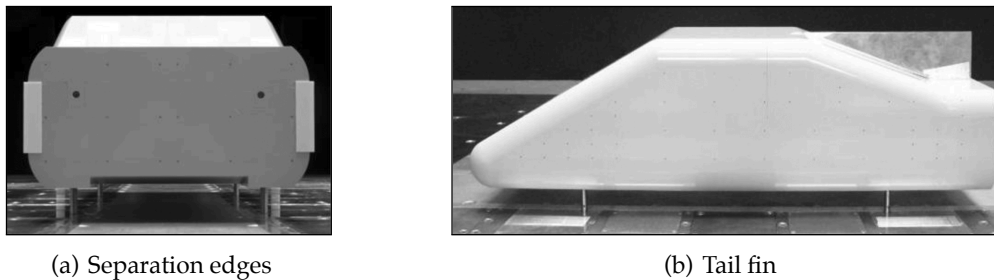


Figure 1.47: Modifications made to an SAE reference body, from Schröck et al. (2011)

It was shown that these modifications had a relatively minor impact on steady-state results, but had more significant effects on transient behaviour, particularly in the yaw moment response of the vehicle. The aerodynamic admittance functions for side force and yaw moment are shown in Figures 1.48(a) and 1.48(b) respectively. These were originally presented as a function of Strouhal number, based on vehicle wheel-base, but are shown here as a function of reduced frequency. Note that $k = 2\pi St$ according to the definition of reduced frequency used throughout this thesis.

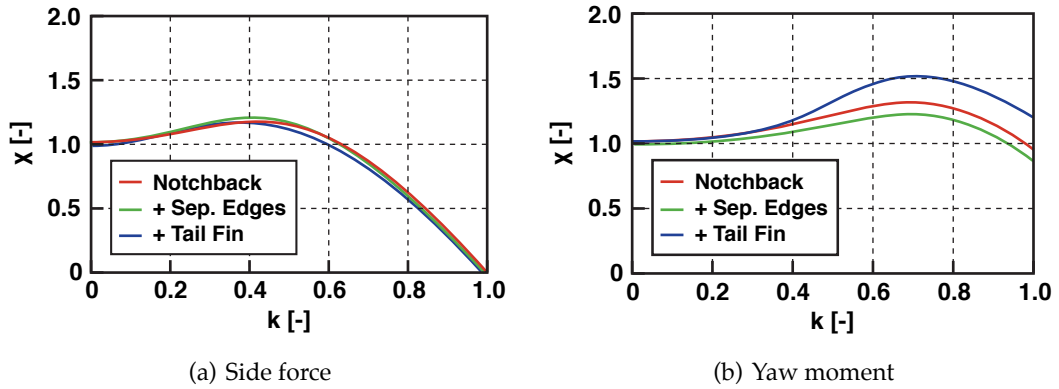


Figure 1.48: Aerodynamic admittance functions, modified from Schröck et al. (2011)

Figure 1.48(a) shows that the unsteady side force response was not affected by the geometry modifications and in all cases showed a peak 20% increase in response over quasi-steady theory for $k = 0.4$, equivalent to approximately 16 vehicle wheel-base lengths. Figure 1.48(b) indicates that both the baseline and modified vehicle geometries showed a maximum yaw moment response at $k = 0.7$, equivalent to approximately 9 vehicle wheelbase lengths. The base geometry exhibited a 30% increase in yaw moment compared to that recorded under steady conditions. Both geometry modifications showed an above-unity response at this frequency, with the tail fin increasing and the separation edges reducing the response when compared to the baseline notchback geometry. In all cases investigated, an admittance of unity was reached at low frequencies. Overall, this work highlights how relatively minor geometry modifications can have a significant effect on how a vehicle responds to unsteadiness.

In addition to lift-based active turbulence generation systems based on typical aerofoils, an example of a device that operates on the boundary between a drag and lift device is described by Knebel et al. (2010). This consists of a number of small elements, where the angle of attack can be changed. At smaller angles, the elements act as lift devices, whilst at larger angles, the flow becomes separated and acts as a

drag device. This approach attempts to bridge the gap between simulating longer and shorter length scales, although as stated by Mankowski et al. (2011), it is the intermediate scales that still provide the greatest challenges.

When assessing the response of a vehicle to isolated crosswind gusts, the typical approach is to drive a vehicle past a cross-wind generator. Results related to this method are discussed in Section 1.4.7.2. An alternative, model-scale approach is to simulate the resultant gust as would be experienced by a vehicle in motion, but by holding the vehicle stationary. In the work of Docton and Dominy (1994); Dominy and Ryan (1999); Ryan and Dominy (1998), a traversing crosswind gust was generated in a model-scale wind tunnel using a series of shutters that were operated in turn, directing a crosswind over the model. As the model first entered the crosswind, both side force and yaw moment increased above that predicted under steady conditions by between 10 and 20%. However, once the model has become immersed in the crosswind for greater than 7 vehicle lengths, the response was equivalent to that observed under steady conditions. This suggests that results assuming quasi-steady behaviour would under-predict the side force and yaw moment experienced by a vehicle under crosswind conditions.

1.4.7.2 Simulation of Vehicle Movement Relative to Wind

An alternative to simulating unsteadiness by moving the wind relative to the vehicle, is to move the vehicle relative to the wind. This has the advantage of being able to use a conventional smooth-flow wind tunnel, although introduces challenges regarding instrumentation and model motion. The maximum frequency at which a vehicle can be excited at is limited by the inertia of the vehicle and supporting structures. Therefore the technique is more suited to model-scale testing.

A range of techniques can be used to vibrate a model. Techniques and analyses

1. INTRODUCTION AND AIMS

common to structural engineering were assessed by Cooper and Larose (2002), who discussed how these techniques may be useful in measuring unsteady aerodynamic forces acting on vehicles. A common method to move a vehicle is to oscillate it about the pivot of a turntable. Many tunnels have a turntable installed to yaw a vehicle and therefore this can provide a convenient method of forced excitation. There are two disadvantages to this approach. The first being that most turntable actuators tend to operate slowly and therefore cannot reach the higher frequencies that can be experienced on-road. Secondly, as noted by both Széchenyi (2000) and Watkins and Cooper (2007), rotating a model does not capture the wind conditions as would be experienced by a vehicle on-road traversing a gust. Watkins and Cooper (2007) suggested that a combination of vehicle rotation and a turbulence generation system may provide more realistic conditions. The limitations were identified by Theissen et al. (2011) and justified by the assumption that the fundamental unsteady aerodynamic phenomena would be dominated by the changes in oncoming yaw angle, regardless whether the vehicle was affected gradually or entirely. As stated by Sims-Williams (2011), this technique can nevertheless be instructive in assessing important scales of unsteadiness.

Investigations by Lock et al. (2002, 2003) rotated a full-size vehicle at rotational speeds of $0.6^\circ/\text{s}$. Unusually, drag values seemed to lag behind what was predicted using a steady technique, leading to over and undershoots of drag by up to 10%. Yaw and side force coefficients were also larger than those recorded under steady conditions. However, a study by Flasch et al. (2003) taking place at $1^\circ/\text{s}$, showed the expected quasi-steady response.

Model-scale investigations by Passmore and Mansor (2006), Mansor and Passmore (2008) and Baden Fuller and Passmore (2010) oscillated a model using springs, with a diagram of this apparatus shown by Figure 1.49(a). Mansor and Passmore (2008)

oscillated the model at frequencies ranging from a reduced frequency of the order of 0.02 to 0.2, based on vehicle length. It was found that yaw moment magnification of up to 20% occurred throughout this frequency range, although limitations in generating higher frequencies prevented a high-frequency roll-off to be detected, where the higher frequency fluctuations have less effect on vehicle forces. Strakes mounted at the rear of the model in the work of Passmore and Mansor (2006), similar to those used by Schröck et al. (2011) were also found to reduce the magnification in dynamic yaw sensitivity.

Chometon et al. (2005) and Guilmineau and Chometon (2008) carried out a combined model-scale and CFD investigation with an idealised body using a faster turntable system, which could oscillate up to between $\pm 15^\circ$ at 2 Hz. No spectral analyses were completed, although hysteresis was noted in the pressure field particularly at the rear of the model. Investigations by Theissen et al. (2011); Wojciak et al. (2011) took place in the current state-of-the-art BMW AeroLab facility. A 50% model was oscillated about its rotational centre using actuators in a roof-mounted strut, shown by Figure 1.49(b). Oscillation frequencies between 1–4 Hz and amplitudes up to $\pm 5^\circ$ were tested. It was found that the surface pressures at the front of the vehicle remained quasi-steady, whilst over and undershoot and phase lag were recorded with the rear pressures.

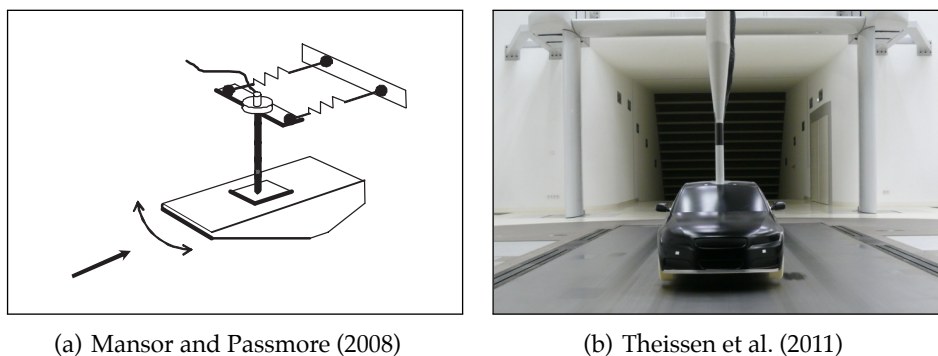


Figure 1.49: Oscillating models

How a vehicle behaves under extreme crosswind conditions is important for both a

1. INTRODUCTION AND AIMS

handling and, in the case of high-sided vehicles, an overturning perspective. As stated by Howell (2002), it is only rarely that wind strength is sufficient to create a safety problem for passenger cars, but on windy days driving can be a tiring experience.

A common method to test extreme crosswind events is through use of a crosswind generator. These devices are summarised by both Széchenyi (2000) and Hucho (1998), usually consisting of a bank of large fans positioned outside, whereby the vehicle under test is driven past experiencing a side gust. The system as described by Sedarous et al. (2007) incorporates a modular design, so that the individual fan units can be moved relative to one another. This allows testing of a vehicle in conditions where the wind direction rapidly changes, by placing fans facing in opposite directions along the test road. This system is shown in Figure 1.50.

Two forms of testing are used: open loop, where the driver applies no correction to the steering of the vehicle; and closed loop, where the driver minimises the vehicle's deviation from a straight path. As noted by work by Wagner (2003), incorporating Wagner et al. (2001); Wagner and Wiedemann (2002, 2003); Wiedemann and Wagner (2002), how a driver responds to closed-loop testing to one-off events differs from how a driver reacts under natural wind conditions. The focus of this work was to assess how a driver responded to natural gusts and be able to assess a vehicle's sensitivity to these events from the perspective of the driver. To allow this, both steering column movement and flow conditions were recorded as a driver traversed the natural wind environment. In addition, a virtual steering simulator was developed to assess how a driver responds to deviations in the course of a vehicle. Using this data, a yaw rate transfer function can be evaluated from the on-road data both with and without a driver's correction. The difference in amplitude between the peak frequencies was defined as the yaw deterioration factor and was used to assess different vehicles.

Model-scale testing allows the effect of larger, more extreme gusts on a vehicle to

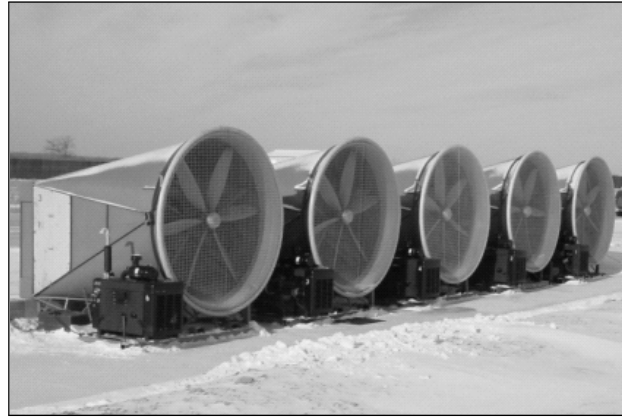


Figure 1.50: Crosswind generator, from Sedarous et al. (2007)

be investigated, as well as providing a method that can take place at an earlier stage of a vehicle's development. Typically, a model is propelled at high speed along a track past a crosswind generator. An early example of such a technique was an investigation by Cooper (1981) and further summarised by Cooper et al. (2002), during the development of a high speed train in the UK. There was concern that the low mass, tilting design may be more susceptible to overturning, particularly when on embankments. A moving model technique was implemented where a 1/5th scale model train was propelled along a track by a vehicle, to which the model was mounted to the side. Aerodynamic admittances were calculated and these were previously shown in Figure 1.34 compared to the response of a full-scale vehicle on-road, showing a decrease in admittance above reduced frequencies of unity. Studies focussed on road vehicles include work by Macklin et al. (1997), where a generic squareback model was moved by a catapult past a crosswind generator. Bars were used to increase the levels of turbulence in the crosswind, although this had little effect on the vehicle's response. This investigation continued with work by Chadwick et al. (2000), who used even more simplified models, including a flat plate normal to the crosswind and a sharp-edged box. Even though the geometries were extremely simplified, results showed that the leeward region of the body was most affected by transient conditions. The yaw mo-

1. INTRODUCTION AND AIMS

ment coefficient reached a maximum at both entry and exit from the crosswind, but only reduced at exit if the edges of the box were smoothed.

A similar study taking place in a wind tunnel by Gillieron and Noger (2004) investigated the quasi-steady response of a vehicle to side forces whilst overtaking during crosswind conditions. Idealised models were used, with one model traversed past either a single stationary model or a platoon of closely spaced models. Side forces were found to increase with overtaking speed, with the response quasi-steady when overtaking a closed spaced platoon at speeds less than five vehicle lengths per second. A CFD study of a similar setup was also introduced by Riederer (2003).

1.4.8 Key Remarks on the Unsteady Environment

- The unsteady on-road flow environment experienced by a vehicle comprises unsteady flow due to turbulence in the natural wind, unsteady wakes of other vehicles and as a result of traversing through the stationary wakes of roadside obstacles.
- This unsteady environment can be characterised using spectra or parameters such as turbulence intensity and length scale to capture the typical sizes or level of unsteadiness of turbulent gusts.
- Reduced frequency is a non-dimensional parameter that can be used to characterise the interaction of transient fluctuations with an object, for instance a vehicle. It is generally assumed that the flow will be quasi-steady (behave in the same manner as if exposed to a sequence of steady conditions) at reduced frequencies less than 0.1 and not quasi-steady at reduced frequencies greater than 1.
- Aerodynamic admittance and transfer functions can be used to quantify the re-

sponse of a vehicle to unsteadiness in the frequency domain. These are typically defined as a ratio between output and input conditions, with an admittance equal to unity indicative of a quasi-steady response, where the ratio of output to input signal magnitudes is equal to those obtained under steady conditions. At higher frequencies, the admittance function generally falls to zero, since the aerodynamic inputs of these smaller fluctuations become increasingly less effective in producing a vehicle response.

- The response of a physical vehicle to unsteadiness can either be measured under actual on-road conditions, or in the controlled, simulated environment of the wind tunnel. Unsteadiness can be produced using both passive and active generation systems, or the vehicle itself can be moved relative to a steady wind.

1.5 Summary and Objectives

1.5.1 Summary

A vehicle on the road encounters an unsteady flow due to turbulence in the natural wind, unsteady wakes of other vehicles and as a result of traversing through the stationary wakes of roadside obstacles. There is increasing concern about potential differences between the steady flow conditions used for development and the transient conditions that occur on the road, with evidence to suggest that unsteadiness in the onset flow can cause the vehicle to behave in a manner distinct from the behaviour predicted in the steady flow environment of a wind tunnel.

In particular, unsteady effects occurring in the sideglass region of a vehicle are particularly relevant to wind noise. This is a region close to the driver and dominated by separated flow structures from the A-pillar and door mirrors, which are particularly

1. INTRODUCTION AND AIMS

sensitive to unsteadiness in the onset flow. These regions are also areas where strong aeroacoustic effects can exist, in a region close to the passengers of a vehicle. The resulting aeroacoustic response to unsteadiness can lead to fluctuations and modulation at frequencies that a passenger is particularly sensitive towards.

Whilst a number of controlled techniques have been developed to simulate the unsteady environment as seen by a vehicle, many are not suited for full-scale testing (posing a challenge for aeroacoustic studies) or the transient conditions generated do not capture the full range of conditions that would be experienced on-road. Only recently has data been collected to comprehensively capture a wide range of on-road wind conditions, which these techniques hope to simulate. With the simulation of longer and shorter scales possible with active lift and passive devices respectively, future techniques may yet still struggle with simulating the more challenging, intermediate length scales seen on-road. In addition, the spatial and temporal scales required for transient aeroacoustic simulations continue to be challenging from a CFD computational expense perspective.

Measuring the response of a vehicle whilst driving on-road is therefore the only way to truly capture the full range of unsteadiness that is experienced by a vehicle during normal driving. However, this requires a fully-functioning vehicle, which may not be available at the earlier stages of a vehicle development programme, and also sufficient time to capture a wide range of wind conditions and environments.

The steady aeroacoustic wind tunnel is therefore likely to continue to be commonly used to assess the wind noise of a vehicle, along with increasing use of numerical techniques. In the work of Peric et al. (1997), a question was asked whether there was a way of using smooth flow techniques to predict wind noise measurements obtained in turbulent flow. This thesis aims to investigate this question.

1.5.2 Related Literature

This work incorporates the following conference and journal papers:

- Oettle, N. R., Sims-Williams, D. B., Dominy, R. G., and Freeman, C. M. (2013). Evaluation of the aerodynamic and aeroacoustic response of a vehicle to transient flow conditions. *SAE Int. J. Passeng. Cars – Mech. Syst.*, 6(1):389–402
- Oettle, N., Mankowski, O., Sims-Williams, D., Dominy, R., Freeman, C. M., and Gaylard, A. (2012). Assessment of a vehicle’s transient aerodynamic response. *SAE Technical Paper*, SP-2333(2012-01-0449)
- Oettle, N. R., Sims-Williams, D. B., Dominy, R. G., Darlington, C. J. E., and Freeman, C. M. (2011). The effects of unsteady on-road flow conditions on cabin noise: spectral and geometric dependence. *SAE Int. J. Passeng. Cars – Mech. Syst.*, 4(1):120–130
- Oettle, N. R., Sims-Williams, D. B., Dominy, R. G., Darlington, C. J. E., Freeman, C. M., and Tindall, P. F. (2010). The effects of unsteady on-road flow conditions on cabin noise. *SAE Technical Paper*, SP-2269(2010-01-0289)

1.5.3 Objectives

To investigate how the unsteady on-road wind environment affects the noise inside a vehicle’s cabin, this research seeks to answer the following key questions:

1. Can steady techniques predict unsteady on-road results?
2. What is the impact of on-road unsteadiness on perceived noise in the cabin?
3. Can minor geometry changes have an important impact on the transient nature of the wind noise perceived on-road?

1. INTRODUCTION AND AIMS

In answering these questions, this study primarily focussed on the front greenhouse region of a full-size vehicle, since this is a key area of aeroacoustic noise generation. Both external aerodynamic and acoustic measurements were taken combined with acoustic measurements of the noise inside the cabin. Data collection took place on road under a range of different wind conditions to accurately measure the response of the vehicle to oncoming flow unsteadiness, with steady-state measurements taking place in full-scale aeroacoustic wind tunnels.

1.5.4 Thesis Outline

This thesis is structured into the the following chapters:

Chapter 1 – Introduction and Aims

This chapter, providing an overview of existing research and introducing the work presented in this thesis.

Chapter 2 – Experimental Techniques

The various instrumentation, facilities and data handling processes are described, measuring the oncoming flow and the cabin noise, surface pressures and surface noise response of the vehicle.

Chapter 3 – The Time-Averaged Vehicle Response

This chapter focusses on comparing the aeroacoustic and aerodynamic response of the vehicle in the steady-state wind tunnel with the time-averaged results obtained on-road. The effect of minor geometry modifications were assessed. In addition, time-averaged results obtained in the unsteady conditions of the Pininfarina wind tunnel are also compared with steady results obtained in the same facility. A subjective cabin noise assessment is also made of on-road data, investigating various psychoacoustic parameters.

Chapter 4 – The Time-Resolved Vehicle Response

Using a variety of spectral techniques, this chapter assesses the transient aeroacoustic and aerodynamic response of the vehicle to unsteady fluctuations in the oncoming flow. Subjective testing also took place, assessing how changes in the steady-state response can affect perceived cabin noise of a vehicle under unsteady conditions.

Chapter 5 – Conclusions

The thesis finishes with conclusions of the research and suggestions for further work.

CHAPTER 2

Experimental Techniques

2.1 Introduction

This chapter provides details of the instrumentation, apparatus and data handling techniques used in this work. The methods used to capture the unsteady on-road flow environment are described along with the equipment used to measure the resulting aerodynamic and aeroacoustic response of the vehicle. The on-road testing locations are also detailed along with the specifications of the full-scale aeroacoustic wind tunnels used to measure the response to both steady-state and generated turbulent conditions.

2.2 Instrumentation

2.2.1 Flow Measurements

2.2.1.1 Choice of Probe Type and Location

To measure the flow over the vehicle, both the type of probe and its position must be first determined. Key considerations include the ability to capture the oncoming flow

2. EXPERIMENTAL TECHNIQUES

conditions with a sufficient range of turbulence scales and in a manner that does not affect the acoustic measurements made inside the cabin.

Probe types include pneumatic probes which directly measure oncoming flow pressure, many of which are summarised by Chue (1975). Depending on the type of probe, various data can be gathered as to the nature of the oncoming flow. One of the more simple forms of probe is the Pitot-static probe, which using a direct measurement of total and static pressure, dynamic pressure and therefore flow speed can be determined. A well-designed Pitot-static probe gives errors of less than 1% in flow speed for oncoming flow within a 15° acceptance cone of the probe axis, Massey and Ward-Smith (2005). However, this probe does not give any information as to the direction of the flow. An alternative approach is to mount the probe on one end of a weather vane, such that the probe is always turned towards the wind, as used by Kaltenhauser (2003). The angle of the vane can then be recorded to determine the oncoming flow direction.

To resolve the complete oncoming flow vector, a multiple-hole probe can be used. For instance, a three-hole probe such as used by Lawson et al. (2003) Katoh et al. (2011) can also resolve flow speed and direction in a single plane, aligned with the three holes at the tip of the probe. With the addition of either a fourth hole (for instance Wordley (2009); and Hooper and Musgrove (1997)) or fifth hole (for instance Mayer et al. (2007)), determination of flow direction in two planes is possible. This allows the three orthogonal components of flow velocity to be resolved.

Alternatively, hot-wire probes can be used. These have the advantage of having a very high frequency response, up to hundreds of kilohertz. However, they are very fragile and therefore can be problematic when used on-road where there is a strong likelihood of particle and insect impacts damaging the fine wires. These problems were encountered by Peric et al. (1997). In addition, dust build up on the wires or

films as well as atmospheric temperature fluctuations would require the probes to be frequently recalibrated. Therefore these probes are more suited to the controlled environment in the laboratory rather than the conditions on-road.

More recent advances in atmospheric laser Doppler velocimetry (LDV) and light detection and ranging (LIDAR) have allowed the possibility of the use of this technology to detect the flow conditions some distance in front of the vehicle, without the disadvantages of any supporting struts. Principally, the system involves two coherent laser beams crossing in the region under investigation. This results in interference fringes being formed and as particles in the air pass through these fringes they reflect light. The Doppler frequency shift of this reflected light is used to determine the flow conditions. This contrasts with the laboratory use of LDV and particle image velocimetry (PIV), where these particles are specifically generated for detection. The fundamental disadvantage with LDV and LIDAR systems are their limitations of temporal and spacial resolution. To resolve small length scales (<0.1 m) at higher fluctuation frequencies, these systems are generally not suitable.

Since the aim of this work was to measure and correlate the oncoming flow conditions with the noise inside the cabin, any flow measurement system should be designed and positioned in such a way that any additional noise is minimised. Options for probe mounting broadly fall into three categories, as shown by Figure 2.1.

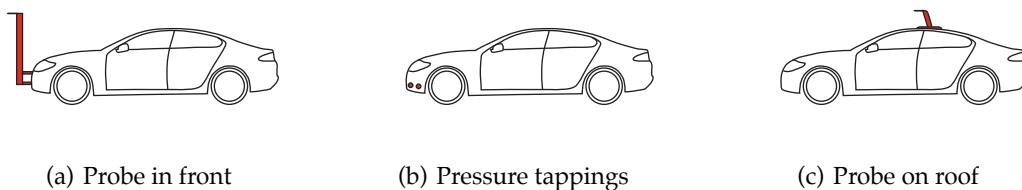


Figure 2.1: Probe mounting options

Mounting the probe in front of the vehicle, some distance away from the vehicle's

2. EXPERIMENTAL TECHNIQUES

body has been used in a number of studies. Such systems include the rake of four-hole probes located in front of the vehicle by Wordley (2009) and a single probe mounted above the front of the vehicle by Bischof (2008); Mayer et al. (2007). A number of studies have taken place where anemometers were positioned ahead of the front bumper, in a configuration commonly used during coast-down testing, such as those by Howell et al. (2002) and others including Carlino et al. (2007); Lindener et al. (2007); Saunders and Mansour (2000). Mounting the probe in this manner has the advantage that the probe measurements can be less affected by the geometry of the vehicle. However, even for the probe rake 1 m in front of the vehicle, as used by Wordley (2009), the decrease in measured flow speed from free-stream conditions was 14%. Such systems by definition require support structures which are usually large. The further these probes are mounted away from the influence of the vehicle, the larger the support structure. Also, with the probe at an increased distance from the vehicle, the measured flow conditions may become further removed from those that are influencing the response of the vehicle. Larger structures are likely to create additional noise and alter the flow over the vehicle, thus affecting both aeroacoustic and aerodynamic measurements.

Using flush-mounted pressure tappings on the front bumper of a vehicle as in Figure 2.1(b) was an approach used by Wagner (2003). This effectively uses the body of the vehicle as a large multiple-hole pressure probe. This work focused on vehicle dynamics and the effect of the unsteady on-road environment had on a vehicle's handling. During the study, vehicles of different geometries were assessed and since a probe mounted near the vehicle can be affected by the shape of a particular vehicle, an alternative flow measurement solution was sought to allow consistent flow measurement as different vehicles were compared. Whilst this approach has a number of advantages, particularly including low noise generation, one fundamental disadvan-

tage is the spacing of the tappings at the front of the vehicle. These tappings create a probe the size of the vehicle. Flow structures and turbulence scales cannot be resolved if they are smaller than the probe which measures them, and therefore this limits the resolution of the flow field under consideration. This also limits the frequency response of the system to very low frequencies, further discussed in Section 2.2.1.2.

A number of authors including Lindener et al. (2007) have mounted probes in locations where flow structures are key in generating cabin noise, such as around the A-pillar region. Whilst this technique has the potential to capture important noise-generating flow conditions, the presence of a probe in this position is likely to affect both the flow structures themselves and consequently their noise generation. Noise generation in particular is likely to be affected strongly, since minor changes in vehicle geometry can have large effects on cabin noise, from George (1990).

A compromise is to mount a probe on the roof of the vehicle. This has the advantage of measuring flow in the vicinity of the vehicle, so that the characteristic oncoming flow field can be assessed without being greatly influenced by localised vehicle geometry effects. Any noise generated is also likely to be attenuated by the roof and headlining such that the influence on the cabin noise measurements is minimised. This approach is relatively common, having been used by Peric et al. (1997); Watkins et al. (2001); Riegel et al. (2006) and Lawson et al. (2007) amongst others.

Since acoustic measurements were taken simultaneously to flow measurements, it was important that the acoustic effects of the probe and mounting were kept as low as possible. A simple approach to mount the probe to the roof would be to use a vertical tube to raise the probe above the roof of the vehicle. At 130 km/h, the Reynolds' number based on a cylinder diameter of 10 mm is $Re = 25 \times 10^3$. This results in a Strouhal number of approximately 0.21. The vortex shedding frequency for flow

2. EXPERIMENTAL TECHNIQUES

around the cylinder can then be calculated according to:

$$f_v = \frac{St u}{d} \quad (2.1)$$

From this, the shedding frequency of such an arrangement would be approximately 720 Hz. This is of the order of the note of F, one octave above middle C. Such a frequency is well within the human hearing range and therefore should be avoided. Another disadvantage of a cylindrical support is that it will tonally shed irrespective of oncoming flow direction. Helical strakes can be used to break-up the coherent shed vortices into a range of sizes, removing the tonality associated with similar-sized structures. However, reducing these separated structures as much as possible is the most effective route to reduce noise.

The chosen design of probe mounting is presented in Figure 2.2(a), showing the probe attached to the forward-swept support. By moving the probe further forward than the base, any geometry effects of the mounting system on the probe were reduced. The support was shaped with a NACA 0020 profile to inhibit tonal vortex shedding. By shaping the support in the profile of an aerofoil, shedding can be prevented at low angles of attack, since the flow around the support is attached. At higher angles of attack, under higher crosswind conditions, flow separation may occur, potentially lead to tonal shedding. During experimentation, it was found that the probe and mounting did produce a tonal noise under certain conditions. This tended to occur at the extremes of yaw, but this was only detected in the wind tunnel and not on-road. This tonal noise is clearly identifiable in the wind tunnel measurements and therefore can be accounted for.

Two rare-earth magnets were used to attach the base of the mounting to the roof of the vehicle, shown on the left side of Figure 2.2(b) These could be raised to assist with

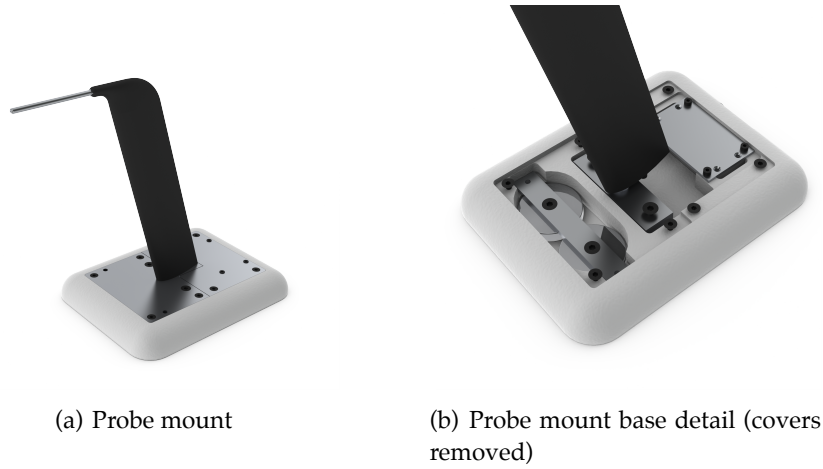


Figure 2.2: Probe mount

installation and removal, and lowered when the mounting was in position ready for testing. To further reduce the noise generation of the probe mount, tape was affixed around the base to prevent any gaps and cavities from being formed. Also, the cable exiting the rear of the probe mount was taped firmly to the rear of the vehicle to prevent any noise. The box of pressure transducers were enclosed in the base of the probe mount and are also shown in the right side of Figure 2.2(b).

2.2.1.2 Five-Hole Probes

A five-hole probe was chosen to measure the flow over the vehicle. A typical five-hole probe comprises five holes in a cruciform arrangement, shown in Figure 2.3. This also describes the numbering convention used for each of the pressure channels.

A five-hole probe can be used in two different ways. One method is to operate the probe in a *nulled* mode, where the probe is rotated about its tip, until the pressures in the opposing holes are equal (i.e. $P_1 = P_2$ and $P_3 = P_4$). At this point, the flow is acting in line with the probe. This method is suitable for time-averaged measurements and can be used when traversing a flow field in a wind tunnel environment. For in-

2. EXPERIMENTAL TECHNIQUES

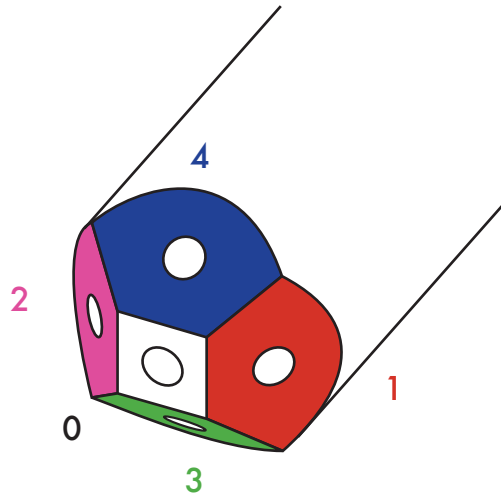


Figure 2.3: Typical five-hole probe head with numbering convention

stantaneous measurements on-road, the flow environment is constantly changing and therefore this method is unsuitable. The alternative is to fix the probe and record the pressures measured at each of the holes. After data have been collected, these pressures are then interpreted from a previously obtained calibration surface to determine details of the oncoming flow vector.

Calibration was performed using a small calibration wind tunnel, where the probe was rotated in pitch α and yaw ψ about its tip in the core of the jet. The traversing of the probe was controlled through computer-operated stepper motors. Total and dynamic pressures at the location of the probe tip were indirectly determined by first measuring the pressure upstream of the nozzle contraction and the pressure at the exit of the nozzle. These pressures were mapped to the true total and dynamic pressures, measured using a Pitot-static probe, through a nozzle calibration. This allowed the probe to be calibrated without the presence of a Pitot-static probe, which would have restricted the movement and thus the yaw and pitch range of the probe calibration. Using the

method described by Dominy and Hodson (1993), non-dimensional pressure coefficients were determined for each increment of pitch and yaw. These discrete values were stored in a table, with linear interpolation used between these values when the calibration was applied. The coefficients were defined as:

$$P_{\text{Avg}} = \frac{P_1 + P_2 + P_3 + P_4}{4} \quad (2.2)$$

$$c_{\text{Tot}} = \frac{P_0 - P_{\text{Tot}}}{P_0 - P_{\text{Avg}}} \quad (2.3)$$

$$c_{\text{Dyn}} = \frac{P_0 - P_{\text{Avg}}}{P_{\text{Dyn}}} \quad (2.4)$$

$$c_{\text{Yaw}} = \frac{P_1 - P_2}{P_0 - P_{\text{Avg}}} \quad (2.5)$$

$$c_{\text{Pitch}} = \frac{P_3 - P_4}{P_0 - P_{\text{Avg}}} \quad (2.6)$$

Two five-hole probes were used during the course of experimentation, denoted 5H50012 and 5H50015. These are shown in Figure 2.4. Specifications of these probes are shown in Table 2.1.

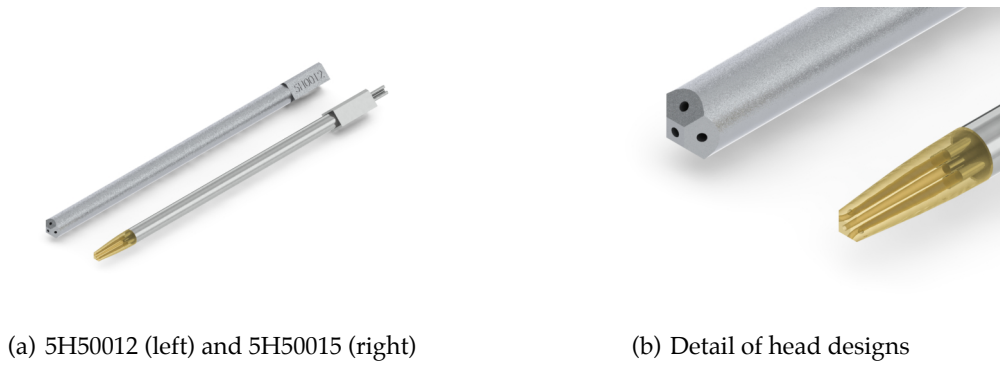


Figure 2.4: Five-hole probes used during experimentation

The head geometry for both probes was chosen to be a perpendicular pyramid,

2. EXPERIMENTAL TECHNIQUES

Property	5H50012	5H50015
Head width [mm]	6.35	3.00
Tube bore [mm]	0.91	0.91 (0.50 head holes)
Probe length [mm]	120	120
Head geometry	Perpendicular pyramid	Perpendicular pyramid
Construction	RP	RP head, SS shaft

Table 2.1: Probe specifications

since this was found to be less sensitive to deviations in the local Reynolds' number at the probe tip. This was based on the findings of Dominy and Hodson (1993), who investigated the effect of Reynolds' number upon five-hole probe calibrations. Changes in Reynolds' number were found to develop two distinct effects. The first effect results in the complete separation of the flow from the probe tip at high incidences, whilst the second effect is a lower-incidence separation bubble that can form around the tip. This bubble can extend further down the probe tip, encompassing the side holes and thus reducing the pressure measured at these points. A reduction in the measured pressure at these positions leads to a decrease in the dynamic pressure coefficient, as defined by Equation 2.4 and therefore an error in the measured flow conditions.

The Reynolds' number based on a characteristic probe tip diameter of 5 mm and a flow speed of 36.1 ms^{-1} is of the order of 15×10^3 . This is within the identified range of Reynolds' number where these effects can lead to probe measurement errors. Errors up to less than 2° are possible, although at lower yaw angles (those below 15°) these errors are much smaller, and comparable to an estimated probe mounting error of 1° . The error in measured dynamic pressure was reported to be less than 3%. These errors were considered to be acceptable for the purposes of this investigation but can be minimised by reducing the range of Reynolds' number deviation from that when the probe was calibrated. Therefore the probes were calibrated at the nominal flow speed experienced on-road so as to maximise this Reynolds' similarity.

Probe 5H50012 was the original design of probe and was used during the first phase of testing. This was constructed entirely out of rapid-prototype resin using an Objet Eden 500V 3D printer from FullCure720, an acrylic based polymer, see Objet (2009). This has the advantage of being able to readily produce a specific head geometry to relatively fine tolerances. Since spatial resolution was not important, the probe tip could be made relatively large. This allowed for larger holes at the probe tip, leading to a potentially greater frequency response. In addition, a larger tip was less vulnerable to the relatively dirty conditions on-road. The outer surface was coated with a layer of approximately 20 μm of aluminium, evaporated onto the probe. This was done with the aim of reducing the susceptibility of the material to absorb water and creep. Whilst this was not considered impermeable to moisture, it was felt that the combination of the coating and care in handling would prevent any significant geometry changes from taking place between calibrations.

Later in testing, an alternative probe design, 5H50015, was used. Instead of a full resin construction, this design had a resin head and a stainless steel tubular body. Thin-wall hypodermic tubing connected the probe head to the rear boss. This had the advantage of improving the robustness of the probe and avoiding creep issues, whilst retaining the advantages of a rapid-prototyped head. The size of the head and corresponding holes of the probe were smaller than the previous probe design, although this had little effect in the probe's frequency response.

Calibration surfaces for both probes are shown in Figures 2.5 and 2.6. These surfaces describe how the four probe measurement coefficients vary at the range of pitch α and yaw ψ angles that the probe was traversed during calibration.

Both probes were calibrated with a resolution of 2.5° in both pitch and yaw, with Probe 5H50012 calibrated to a range of $\pm 35^\circ$ and Probe 5H50015 calibrated to a range of $\pm 45^\circ$. At increased values of pitch and yaw, the probe becomes less sensitive in

2. EXPERIMENTAL TECHNIQUES

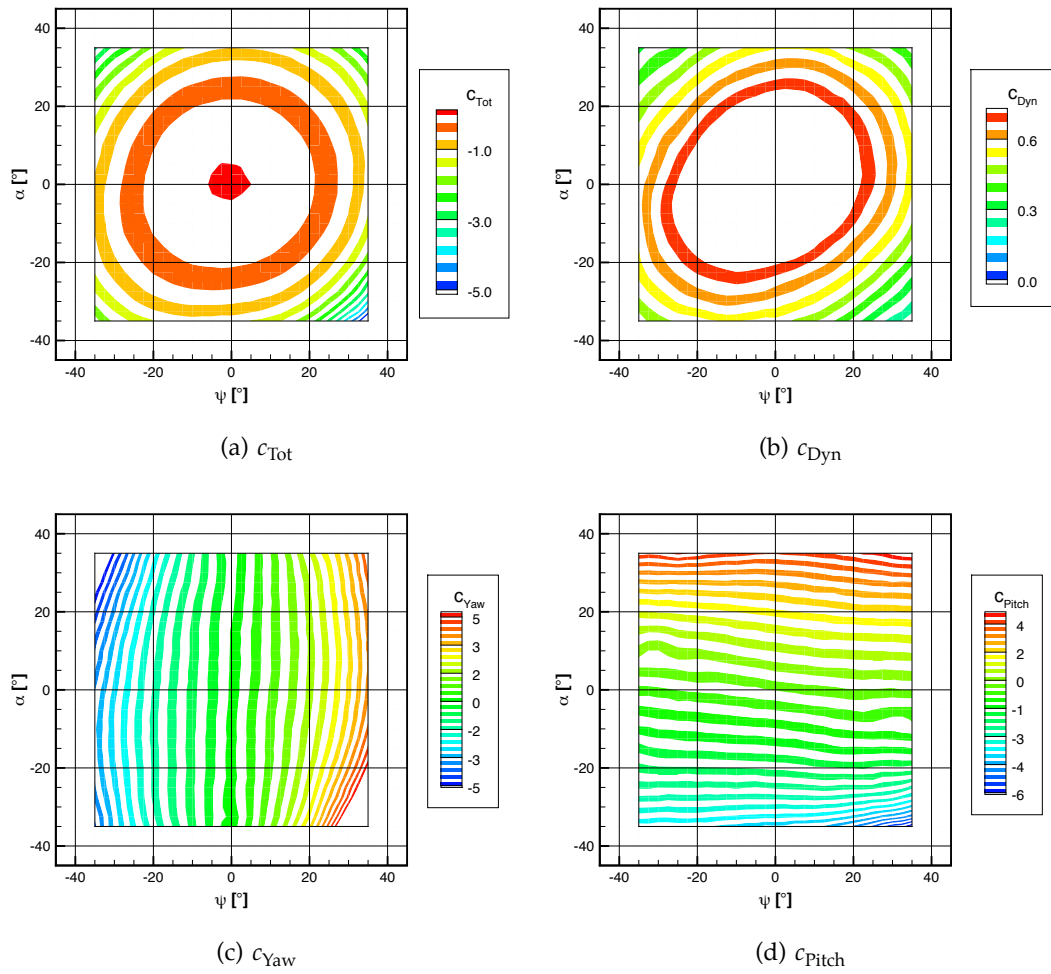


Figure 2.5: Calibration surfaces for Probe 5H50012

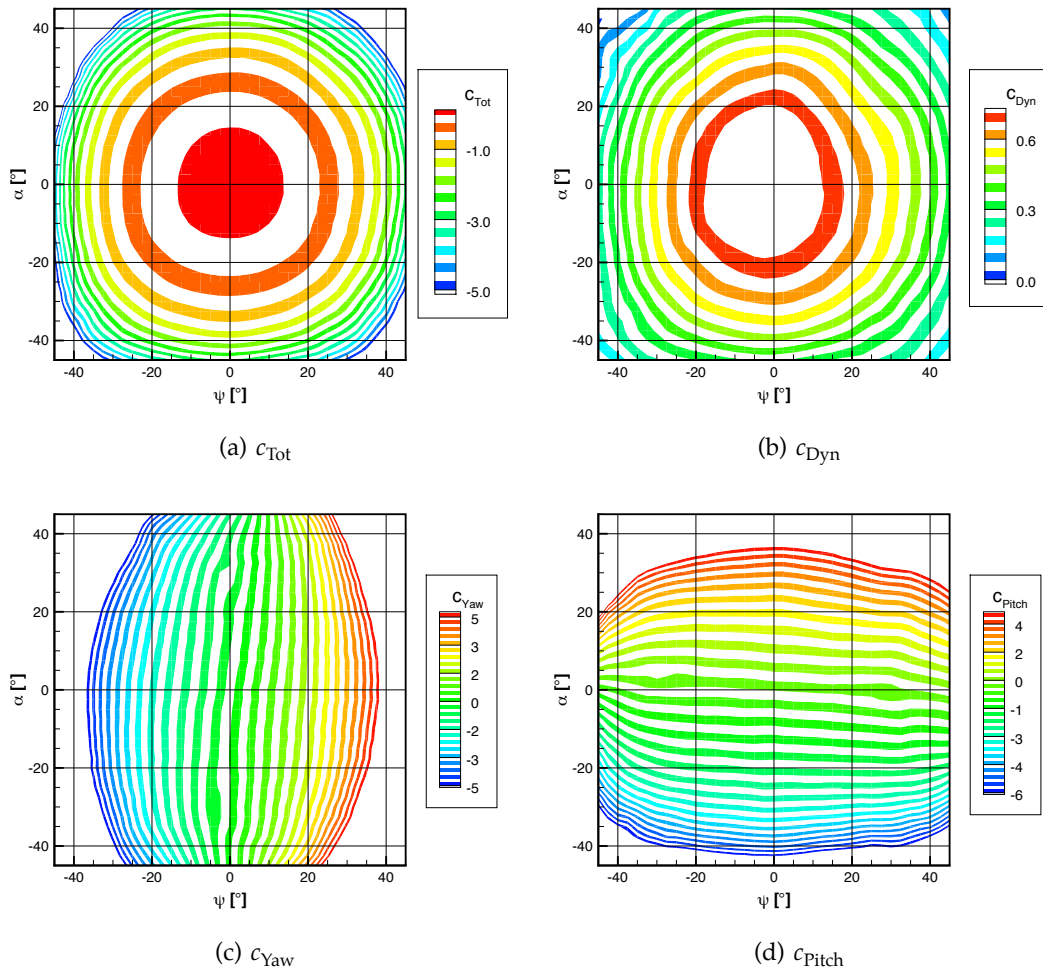


Figure 2.6: Calibration surfaces for Probe 5H50015

2. EXPERIMENTAL TECHNIQUES

resolving the oncoming flow properties, as shown by the closer spacing of the calibration contours. Since the vehicle speed is fast compared to the wind speed, the range of yaw angles experienced by the vehicle on-road was confined to within an approximate range of $\pm 20^\circ$, where the calibration contours were well-resolved.

Both of the sets of contours are plotted on the same axis range for comparison. Figures 2.5(a) and 2.6(a) plot the total pressure coefficients for each probe respectively, Figures 2.5(b) and 2.6(b) the dynamic pressure coefficients, Figures 2.5(c) and 2.6(c) the yaw coefficient, and Figures 2.5(d) and 2.6(d) the pitch coefficients.

More correctly, the probe does not measure pitch and yaw, but *attitude* (or *elevation*) and *azimuth* in a spherical coordinate system with the probe tip at the origin. However, since the probe is fixed relative to the vehicle, the oncoming flow vector is described relative to the vehicle using terms borrowed from the aerospace industry.

The use of a steady-state calibration to measure unsteady flow is only valid at frequencies of unsteadiness that are considered to be quasi-steady. An assessment of the quasi-steady limits for the probe was made using the same reduced frequency approach as introduced in Section 1.4.4.1. The definition of reduced frequency, based on probe head diameter D is given by:

$$k = \frac{2\pi f D}{u} \quad (2.7)$$

Using the assumption of He (1996) that the flow is quasi-steady at reduced frequencies below 1 to 0.1, at a nominal flow speed of 36.1 ms^{-1} and a maximum probe head size of 6.35 mm, frequencies below 90 to 900 Hz would be assumed to be quasi-steady, according to:

$$f < \frac{ku}{2\pi D} \quad (2.8)$$

The methods above describe the probe being calibrated in isolation. Alternatively, the probe can be mounted on the vehicle which is then yawed in a wind tunnel to provide calibration data. It was found that the flow around the vehicle influenced the flow measured at the probe tip. This effect was relatively small but clearly measurable, equating to an approximate increase of free-stream velocity by 14 %, when compared to the nominal road speed measured by the GPS device. Coincidentally, this is the same deviation from free-stream conditions as observed by Wordley (2009), albeit an increase rather than a decrease. To obtain this result, the vehicle was driven at constant speed in both directions on a straight single-carriageway road. The conditions were approximately still with the road speed as reported from the vehicle's cruise control of 60 mph. A total of ten runs were completed, each logging data for a period of approximately 16 seconds (8192 samples at a sample rate of 500 Hz). These results are shown by Figure 2.7.

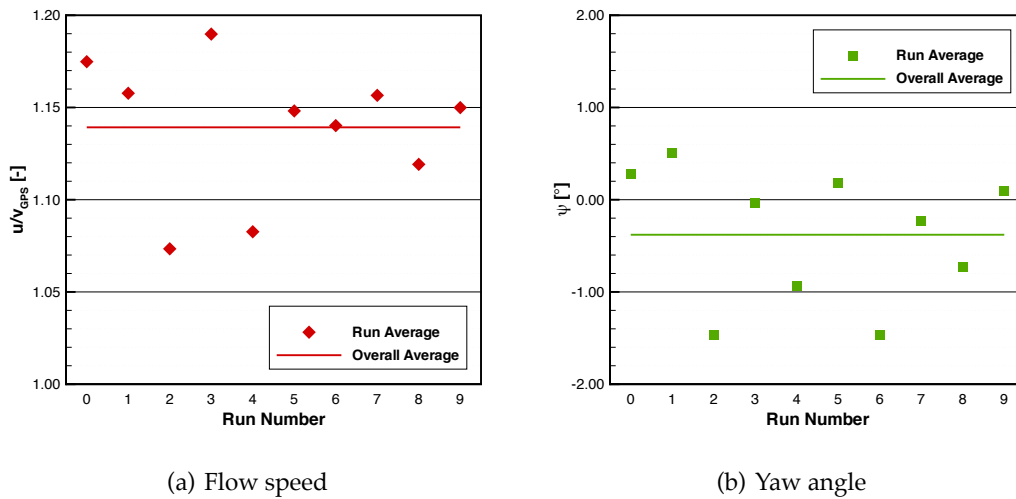


Figure 2.7: Effect of vehicle on probe flow measurement on-road

By correcting for this effect, and ensuring the dependence of the increase in flow velocity upon yaw was accounted for, the probe could measure free-stream conditions

2. EXPERIMENTAL TECHNIQUES

as opposed to the actual conditions at the probe tip. However, the investigation was focussed on seeking the differences in vehicle response between the steady-state conditions of the wind tunnel and the transitory nature of the on-road environment. Therefore it would not be appropriate to embed the steady-state aerodynamic response of the probe within an on-vehicle probe calibration, since the steady-state response may be different to the transitory response on-road. A probe calibration in isolation was thus completed, as outlined above.

2.2.1.3 Sideglass Pressures

To measure characteristics of the static pressure profile of the vehicle's sideglass, a number of flush-mounted pressure tappings were positioned in three zones. These zones are shown in Figure 2.8(a) and are areas approximately: under the influence of the door mirror wake; within the A-pillar vortex separation; and in the vortex reattachment region. These zones were based on the results of CFD simulations completed by Freeman and Gaylard (2008) and are reproduced by Figure 2.8(b). This shows vortex cores coloured by velocity magnitude, identifying the separated flow structures generated by the A-pillar and mirror wake.

A perspex sideglass was used which allowed pressure tappings to be drilled and glued into position so that the surface geometry of the sideglass was as close as possible to the original glass sideglass. The perspex was shaped on a former so that the curvature of the sideglass approximated that of the original. The window seals held the sideglass in position firmly, although aluminium tape was used around the edge to fix the perspex in place with minimal geometry disruption.

Hypodermic tube of length 15 mm, external diameter 1.24 mm and internal diameter 0.91 mm (18 gauge thinwall) were bonded in position so that the ends were flush with the outside surface of the sideglass. Internally, these were connected to individ-

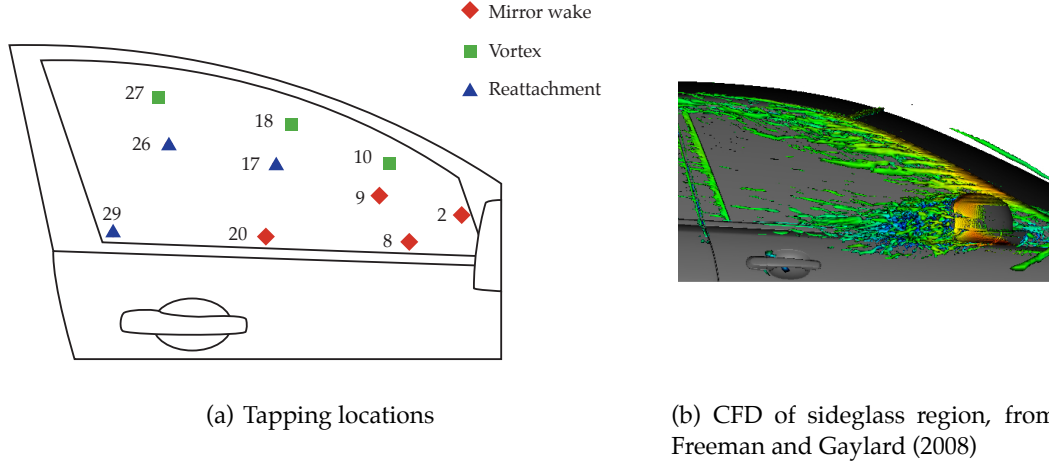


Figure 2.8: Location of pressure tapings on vehicle sideglass

ual pressure transducers by 1 m lengths of silicone Nalgene tubing, having a internal diameter of 1 mm and an external diameter of 2 mm.

The measured surface pressures P_{Tap} were reported as non-dimensional numbers in the form of a pressure coefficient. In this work, the pressure coefficient was defined based on the static and dynamic pressures measured by the five-hole probe according to:

$$c_p = \frac{P_{\text{Tap}} - P_{\text{Probe Static}}}{P_{\text{Probe Dynamic}}} = \frac{P_{\text{Tap}} - P_{\text{Probe Static}}}{\frac{1}{2}\rho u^2} \quad (2.9)$$

Defining the sideglass surface pressure coefficient relative to the roof-mounted probe pressures was the most consistent method of providing comparative data between the on-road environment and the wind tunnel, since these pressures are known with certainty in both environments. Alternative definitions using either tunnel-reported flow speed or on-road vehicle velocity do not provide such consistency. This also results in the sideglass surface pressure coefficients being independent of oncoming flow speed fluctuations measured at the probe tip, whilst remaining a function of the variation in flow structures around the sideglass region due to yaw variations in the oncoming

2. EXPERIMENTAL TECHNIQUES

flow. For the chosen definition of pressure coefficient to be valid, the five-hole probe pressures and sideglass pressures were measured to the common reference, relative to the boot of the vehicle.

2.2.1.4 Pressure Transducers

Both probe and sideglass pressures were measured using Sensortech HCLA12X5DB transducers. These measured differential pressure with a range of ± 12.5 mBar, approximately equivalent to 45 ms^{-1} dynamic pressure at sea-level defined by the ISA. The transducers were mounted in a dedicated enclosure in sets of five, with the reference pressure port common to all of the transducers. Transducers were periodically calibrated using a manometer-oil based micromanometer, with all transducers being calibrated simultaneously using the common reference pressure port. Manufacturer reported yearly drift was 0.1% of full-scale span (FSS) and thermal effects of 1% of FSS between -25 and 80 °C. Datum voltages were measured periodically during the course of a day to minimise these effects. Manufacturer reported response delay for the transducers was 0.2 ms (5 kHz), from Sensortech (2007).

On-road, the transducers were powered using the vehicle's 12 V supply. Since this supply voltage can fluctuate significantly and the transducers' output signal voltage is proportional to the input voltage, voltage regulation was required. A National Semiconductor LP2950ACZ voltage regulator was used for each set of five transducers which had an input voltage range of between 5 and 30 V. This had a manufacturer reported maximum output voltage error of 1.0% for 30 V input voltage fluctuation, from National Semiconductor (2010).

2.2.1.5 Transducer and Probe Transfer Function Correction

Whilst the pressure transducers and data logging system can operate at frequencies exceeding those required for this application, it is often the frequency response of the pneumatic components which can limit the response of the system. The effects of probe head size on the frequency response of a five-hole probe has already been discussed in Section 2.2.1.2. Typically, external pressure tappings and probes are connected to pressure transducers using tubing. Owing to compressibility effects of the air, pressure fluctuations in the measured flow field cause a mass flow of the air inside the tubing and probe. Viscosity and friction in the tubes acts against this movement and dampens these fluctuations, leading to attenuation of the signal measured by the transducers. Since the mass of the air, combined with compressibility and viscous effects create a harmonic system, resonances can also occur, driven by simple *organ pipe* theory. To reduce these effects, tubing length can be minimised, or even removed completely by embedding small transducers into probe tips or into the surfaces where pressures are to be measured. However, these viscous effects can never be eliminated due to the very nature of pressure waves leading to compression and therefore movement of air, from Tijdeman (1975).

An alternative approach is to measure these distortion effects and correct for them. The procedure used here is based on that of Irwin et al. (1979) and developed by Hooper and Musgrove (1997), Sims-Williams and Dominy (1998) and Yang et al. (2006). A diagram of the apparatus is shown in Figure 2.9. A loudspeaker was used to pressurise a small, sealed chamber, where a reference pressure transducer measured the instantaneous applied pressure. Either the tip of a probe or a hypodermic pressure tap was also connected to this chamber. The same tubing as used during experimentation connected the probe or tapping to the required number of test pressure transducers. A swept sine wave was used to operate the loudspeaker to apply the desired range of fre-

2. EXPERIMENTAL TECHNIQUES

quencies to the probe or tubing under test. Typically the sine wave was swept between 3 and 1000 Hz at a sweep rate of 1 Hz. Data were logged at 4000 Hz in 8192 sample sets.

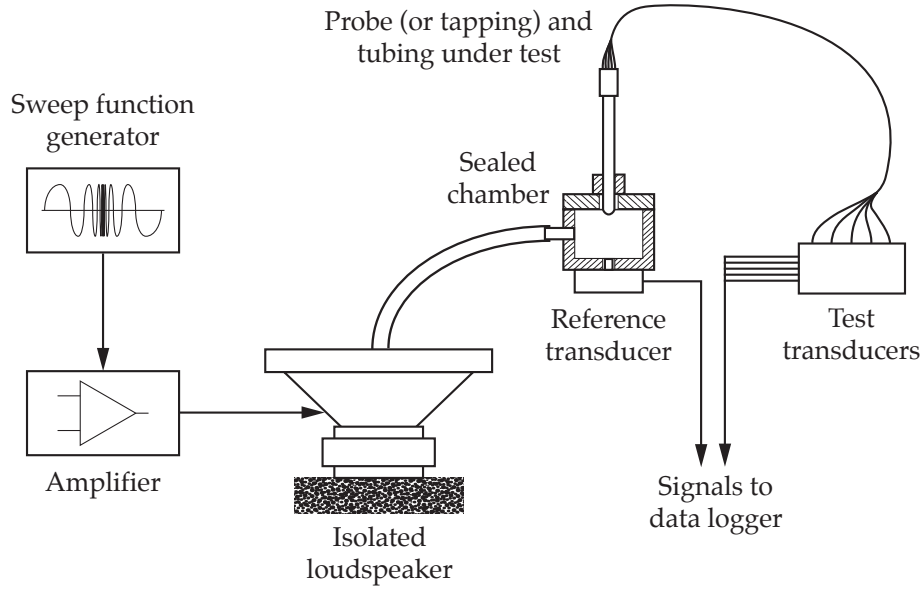


Figure 2.9: Diagram of transducer and probe transfer function correction apparatus

Fast Fourier transforms (FFTs) were taken of both the reference and measured pressure transducer signals, and a complex transfer function calculated using the definition of Bendat and Piersol (1993) as described by:

$$H(f) = \frac{G_{P_{\text{Ref}}P_{\text{Test}}}(f)}{G_{P_{\text{Ref}}P_{\text{Ref}}}(f)} \quad (2.10)$$

This definition is commonly known as the H_1 estimator in the field of vibration analysis. To create a transfer function of high accuracy, 50 sets of samples were recorded from which an average transfer function was then calculated. A Hanning window was used to reduce leakage effects when calculating the Fourier transform of a finite data set.

Figure 2.10 shows, for both amplitude and phase, the measured transfer functions

for probes 5H50012 and 5H50015. Both probes were connected to a bank of transducers with a length of 480 mm tubing, with both probes being an equal length of 120 mm, leading to an effective tubing length of the system to be $L = 600$ mm. Probe 5H50012 had larger holes at the probe tip, as detailed in Table 2.1, which is likely to explain why the transfer function has slightly less attenuation than probe 5H50015. The phase response was identical for both probes, indicating that the effective speed of sound in both systems was equal, according to:

$$a = \frac{360 \cdot Lf}{\theta} \quad (2.11)$$

where a is the effective speed of sound, L is the effective tubing length and θ is the phase angle in degrees. The resonant frequencies of the system were estimated from:

$$f = \frac{a}{4L}, \frac{3a}{4L}, \frac{5a}{4L} \dots \quad (2.12)$$

For the probe and tubing system, the first resonant frequency was 77.5 Hz. The first peak can be identified in Figure 2.10 to be approximately 65 Hz, which was lower than predicted due to viscous effects.

Figure 2.11 shows the measured transfer function for the pressure tapping and tubing. The tubing for each of the tappings was 1800 mm in length, leading to a predicted first resonant peak of 32.5 Hz. Owing to the increased viscous attenuation from the increased length of tubing, this resonant peak is not identifiable, indicating that the pressure tapping system is critically damped.

2.2.2 Data Logging

Pressure transducer voltages were recorded using a 16-bit National Instruments NIDAQmx USB-6218 data logger, with details proved by National Instruments (2009). This pro-

2. EXPERIMENTAL TECHNIQUES

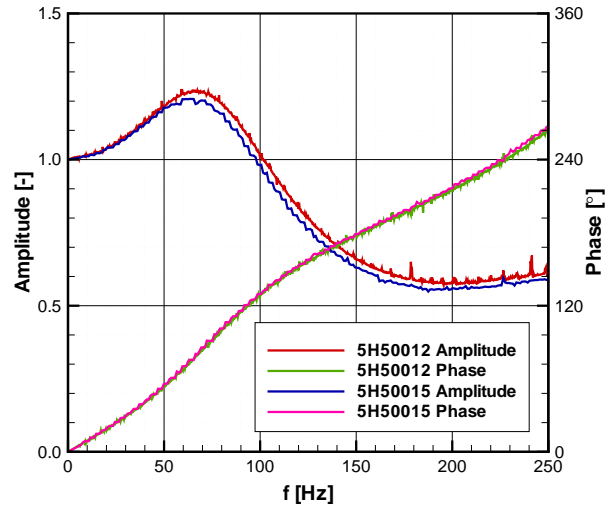


Figure 2.10: Transfer function of probe and tubing system (central hole)

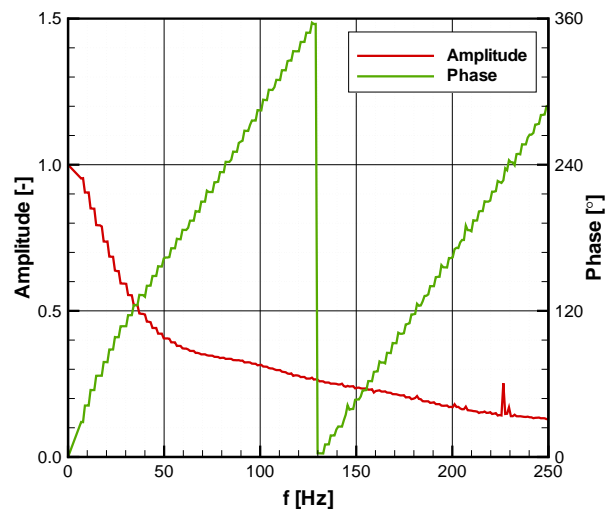


Figure 2.11: Transfer function of sideglass pressure tapping and tubing system

vided 32 analogue input channels, employed in a 16 channel differential configuration. The device also supported triggered input and digital IO capabilities. The maximum sample rate was 250 kHz. Control of the data logger was through DAQmx C routines, integrated within the control software, detailed later in Section 2.2.4. The 16 analogue input channels allowed three sets of five pressure transducers to be logged simultaneously, therefore allowing a five-hole probe and ten sideglass pressure tapings. Additional inputs and outputs specific to on-road testing were also recorded. These are described later in Section 2.2.2.2.

Logging took place at 500 Hz nominally for 16384 samples, leading to logging times of 32.768 s. Occasionally, longer times were recorded, for instance in the Pininfarina wind tunnel with the TGS operational, although the sample rate remained at 500 Hz and the number of samples were always of the form $N_s = 2^n$ where $n \in \mathbb{N}$, to ensure that all data could be used in calculating FFTs.

2.2.2.1 Filtering

To avoid any erroneous results as a result of aliasing, 250 Hz low-pass filters were used between the pressure transducers and the data logger. These removed frequency components above the Nyquist frequency $\frac{f_s}{2}$ of the logging system. The filters were of a second-order RLC type, trimmed so that they formed a matched set. In reality, a portion of the signal above the Nyquist frequency will be sampled and therefore alias. If this frequency f , where $f > \frac{f_s}{2}$, is present, it will alias at frequency:

$$f_{\text{Alias}} = \frac{f_s}{2} - \left(f - \frac{f_s}{2} \right) = f_s - f \quad (2.13)$$

However, the energy of these aliased signals will be increasingly low when compared to the level of the signal of interest and therefore have a minimal impact of the quality of the signal.

2. EXPERIMENTAL TECHNIQUES

2.2.2.2 Specific On-Road Instrumentation

Testing on-road has a number of additional challenges when compared to testing in the wind tunnel. Most significant is that the vehicle is in motion and therefore all logging equipment must be powered and controlled inside the vehicle. To assist with this, a range of additional instrumentation specific to on-road testing was used.

The triggered input of the data logger was used so that logging could be controlled without the need to directly control the data logging computer. This also allowed the driver to choose to start data logging when traffic conditions were favourable. To further assist the driver in identifying the status of the data logging equipment, a bank of eight LEDs were installed on the dashboard of the car in sight of the driver. These were connected to the digital output ports of the data logger. Four of the indicators were used to relay the status of the GPS signal in addition to the three levels of data logger status: logging program activated, waiting for trigger and logging. The remaining four indicators displayed, in binary format, the number of the run in each logging batch. The data logging software was configured so that the program waited for a trigger at the end of each run, until the specified number of runs in a batch were completed. This allowed multiple runs to be recorded without having to return to the controlling computer, reducing that number of stops the driver had to make in the vehicle to check and restart the system.

Up to four channels were used to record data from event switches, located in the vehicle's cabin. Each switch was assigned to a particular on-road event including when noticeable wind noise was heard and when a run was aborted due to changes in vehicle speed or other factors. Recording these events assisted with identification of unsuitable runs from the large amount of on-road data collected. Each switch was a momentary single-pole, double-throw (SPDT) type. This switched between the five volt output from a voltage regulator located within the switch enclosure and the zero

volt vehicle ground. Finally, a digital video camera was positioned on a tripod between the two front seats of the vehicle. This recorded all on-road testing data and the data logger status indicators were within its field of vision, allowing the run number to be identified from the recorded video.

2.2.3 Acoustic Measurements

Acoustic measurements using both an acoustic head and surface microphones were controlled by a HEAD Acoustics SQLab front-end, which acted as a data logger for both the acoustic head in the cabin and the surface microphones on the sideglass. This was controlled using a laptop running HEAD Acoustics ArtemiS X software. When only an acoustic head was used, this was directly connected to the laptop via a USB connection. In all cases, the acoustic data was recorded at 48 kHz.

2.2.3.1 Synchronisation

Since this work concerns the instantaneous correlation of flow and noise events, as opposed to time-averaged data, it is important that both the flow and noise data-logging systems were synchronised. Therefore, a common trigger was used for both the flow-logging NIDAQmx system and the sound-logging SQLab system. Two systems were used,: an audio trigger during the first on-road measurement campaign, and a combined electronic and audio trigger during the second campaign. The electronic trigger switched between 0 V ground and 5 V through a 555 chip-based de-bounced circuit to ensure that multiple triggers did not occur due to bouncing. Both flow and noise systems were configured to start logging on the rising edge of the trigger signal. Both systems ceased logging after a specified number of samples (NIDAQmx) or time (SQLab) and after a pause of a few seconds returned to a primed state, ready to accept a trigger signal to record a further data set. This status was relayed to the cabin of the vehicle

2. EXPERIMENTAL TECHNIQUES

via the logging status indicators.

To mitigate against a loss of synchronisation, an audio trigger was also used. This was also the sole synchronisation method at times when electronic synchronisation of logging systems was not possible. For instance, during 2009 testing where the external trigger-accepting SQLab was not used, and also at Pininfarina where the cabin noise logging system was also not able to accept a triggered input. To synchronise the flow and noise logging systems, a 2 kHz tone was generated which was recorded by the cabin noise logging system. This tone was also recorded by the camera. At the point when logging commenced, the tone was silenced. This tone was clearly identified on the noise data and the data synchronised accordingly. The response time between the triggered signal and the 2 kHz tone being silenced was assessed and found to be of the order of 0.02 s.

2.2.3.2 Cabin Noise

A HEAD Acoustics HMS III acoustic head was used to measure the vehicle cabin noise on-road. This device contained two HDM I.0 digital artificial head microphones, each with a frequency response of between 3 Hz and 20 kHz, with a transmission error of ± 0.1 dB. The nominal dynamic range of the microphones was 118 dB, with selectable calibration factors between 84 and 144 dB_{SPL} in 10 dB_{SPL} increments. The head was powered using a rechargeable internal DC supply. Full details can be found in the datasheet, published by HEAD Acoustics NVH Division (1998).

The head was positioned in the front passenger seat of the vehicle, as shown in Figure 2.12. The position of the front seat was consistent for each vehicle and each set of testing, with the seat positioned at middle of its travel in a fully upright position. The vehicle ventilation system was also switched off with the vents closed. The head was secured using the seat belt to prevent any self-induced noise caused by movement

of the head. Equalisation was applied to the signals recorded by the head, taking into consideration a diffuse-field environment and whether the head was fitted with a torso, from HEAD Acoustics NVH Division (2006). In the Pininfarina aeroacoustic wind tunnel, the same model of heads were used, with an additional head positioned in the driver's seat.



Figure 2.12: Acoustic head installed in front passenger seat

In the Ford aeroacoustic wind tunnel, Cortex Mk I heads were used, positioned in both front seats of the vehicle. The same diffuse-field equalisation was used. These heads had a slightly different transfer function to the HEAD Acoustics heads, primarily isolated above 10 kHz. However, the resulting impact on measured cabin noise spectrum was small compared with the differences in spectrum between the two wind tunnels and particularly between the wind tunnel and on-road.

2. EXPERIMENTAL TECHNIQUES

2.2.3.3 Surface Noise

To measure the combined hydrodynamic and acoustic pressure fluctuations on the surface of the vehicle, three B&K 4949 10 mm surface microphones were used. The frequency response of each microphone was between 5 Hz and 20 kHz with a transmission accuracy of ± 1 dB between 10 Hz and 10 kHz. The dynamic range was between 30 and 140 dB_{SPL}. Each microphone had an external diameter of 10 mm and a thickness of 2.5 mm. Full details can be found in the datasheet, published by Brüel & Kjær (2006). These were positioned on the passenger sideglass in positions corresponding to three of the surface pressure tapings on the opposite (driver's side) sideglass, as shown by Figure 2.13.

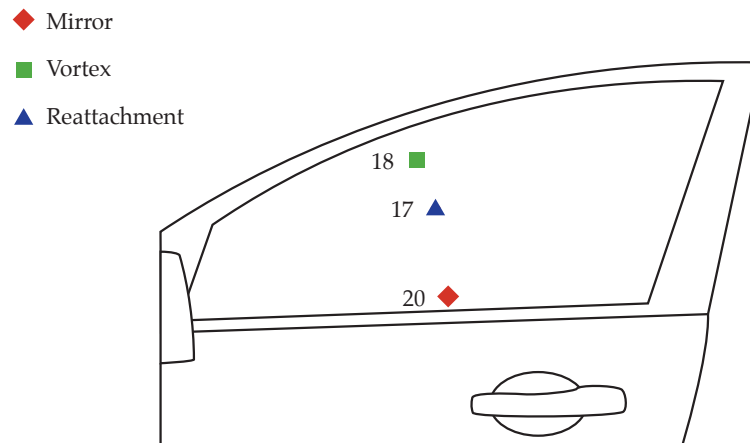


Figure 2.13: Location of surface microphones on vehicle sideglass

Aluminium adhesive tape was used to attach the microphones using their mounting pads to the surface of the sideglass, as shown in Figure 2.14(a). Cables entered the vehicle through the lower door seal and connectors between the microphone wires and extension cables were positioned behind the door handle to reduce any significant noise-inducing geometry modifications to the vehicle, as shown in Figure 2.14(b). The microphone wires were taped to the sideglass downstream to also reduce measurement-

induced noise.



(a) Detail of microphone attachment



(b) Detail of taping routes

Figure 2.14: Images of surface microphone attachment to sideglass

2.2.4 Software Integration

The data logging system was controlled through a program written in the C programming language. This was called LogVoltsGPS and was an extended form of the existing LogVolts program available as part of the *Durham Software for Windtunnels* package. The program used National Instruments NIDAQmx APIs to interface with the data logger and a virtual RS232 port to interface with a Bluetooth GPS receiver. A schematic of the basic functions of the program are shown in Figure 2.15. The GPRMC line is a standard GPS data line containing the basic location and speed data, including position, speed, heading and time.

An abridged example of the data output from LogVoltsGPS, in Tecplot ASCII format, is shown in Figure 2.16.

This shows the raw data recorded, prior to any processing including the interpolation of noise data onto the frequency of the flow data. Raw variables included the extracted data from the GPRMC line from the GPS device, converted into SI units. These variables comprised: latitude, longitude, vehicle speed (v), vehicle heading (β),

2. EXPERIMENTAL TECHNIQUES

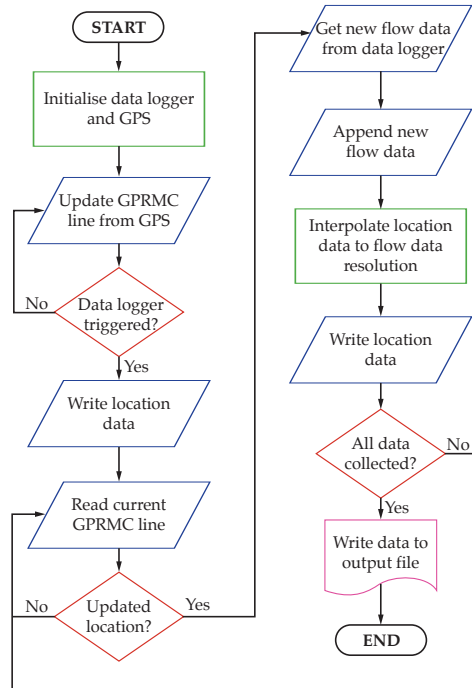


Figure 2.15: Schematic of LogVoltsGPS

```

Title = "LogVoltsGPS - A1(Q) J61 s/bound"
Variables = "Time (s)", "Latitude (deg)", "Longitude (deg)", "GPSVelocity (m/s)", "GPSHeading (deg)", "GPSDate (DDMMYY)", "GPSTime (HHMMSS.SSS)", "SH0Volts", "SH1Volts", "SH2Volts", "SH3Volts", "SH4Volts", "DataStatus"
#PAtm(Pa) TAtm(K) = 101089.383200 290.160000
#Datus= 0.000000 0.000000 0.000000 0.000000 0.000000 0.000000 2.237122 2.241462 2.240666 2.238140 2.241259
Zone.T = "Set 0", I=16384, J=1, K=1, F=POINT
0.000000 54.717967 -1.520113 29.554982 159.369912 190609.000000 150000.000100 3.128403 1.925569 2.795599 2.471825 2.470038 0.000000
0.002000 54.717718 -1.519947 29.554982 158.490000 190609.000000 150001.000000 3.117870 1.880800 2.824568 2.465100 2.461479 0.000000
0.004000 54.717717 -1.519946 29.555583 158.487770 190609.000000 150001.003464 3.079355 1.841274 2.836747 2.478596 2.425509 0.000000
0.006000 54.717717 -1.519945 29.556264 158.485540 190609.000000 150001.006969 3.065530 1.841298 2.856827 2.464771 2.422964 0.000000
0.008000 54.717716 -1.519945 29.556945 158.483310 190609.000000 150001.010453 3.061659 1.842944 2.837735 2.493410 2.395971 0.000000
0.010000 54.717715 -1.519944 29.557626 158.481080 190609.000000 150001.013937 3.119516 1.835622 2.864399 2.415064 2.494068 0.000000
0.012000 54.717714 -1.519944 29.558307 158.478850 190609.000000 150001.017422 3.117870 1.809039 2.870982 2.421318 2.482546 0.000000
0.014000 54.717713 -1.519943 29.558989 158.476620 190609.000000 150001.020906 3.078038 1.822864 2.855511 2.446666 2.447653 0.000000
0.016000 54.717712 -1.519943 29.559670 158.474390 190609.000000 150001.024390 3.079355 1.792250 2.882833 2.458845 2.420002 0.000000
0.018000 54.717711 -1.519942 29.560351 158.472160 190609.000000 150001.027875 3.088572 1.823523 2.856169 2.457199 2.433498 0.000000
0.020000 54.717711 -1.519941 29.561032 158.469930 190609.000000 150001.031359 3.114578 1.869937 2.821276 2.439424 2.475304 0.000000
  
```

Figure 2.16: Example of data output from LogVoltsGPS

date and absolute time. Voltages from each of the data logger channels were also recorded, with the five pressure transducer channels for a five-hole probe also shown in Figure 2.16. In addition, a *Datastatus* variable was also recorded, which was used in error handling. Additional channels were included when surface pressures were recorded.

2.2.5 Schematic of Overall Logging System

Figure 2.17 describes the layout of the instrumentation described in Section 2.2. Figure 2.17(a) shows the layout of the apparatus for the 2009 set of testing, including a five-hole probe, event switches and the acoustic head directly connected to the controlling laptop. Figure 2.17(b) shows the layout for the 20010 set of testing, incorporating additional pressure transducers for sideglass measurements and surface microphones controlled though the dedicated audio datalogging front-end.

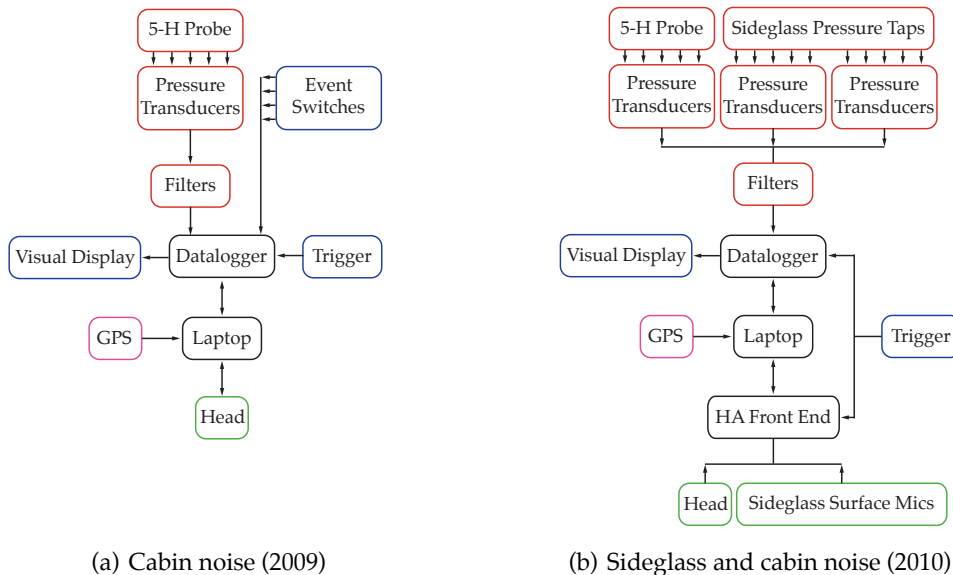


Figure 2.17: Schematic of overall logging system

2. EXPERIMENTAL TECHNIQUES

2.2.6 Terminology

When presenting data collected using the acoustic heads, the data recorded by each ear channel is referred to by the channel name. The names of these channels are listed in Table 2.2 and corresponding positions are shown in Figure 2.18. The acronym used to differentiate each channel contains information on both the head position and ear microphone used.

Channel Name	Description
LHLE	Left head, left ear
LHRE	Left head, right ear
RHLE	Right head, left ear
RHRE	Right head, right ear

Table 2.2: Acoustic head channel names

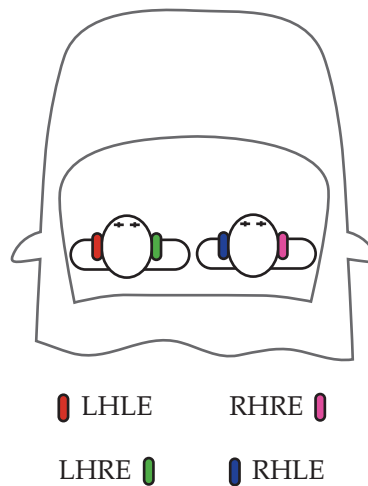


Figure 2.18: Acoustic head channel names and positions

The test vehicles were all right-hand drive and therefore only the left head was used on-road, positioned on the front passenger seat. In the wind tunnels, both heads were used, since there is no requirement for a driver to be seated in the vehicle.

Borrowing nautical terms, the side of the vehicle that turns to face the wind is known as the windward side, with the side facing away from the wind is known as the leeward side. The surface microphones were positioned on the left side of the vehicle, whilst the pressure tassings were positioned on the right side. Therefore, under negative yaw conditions, the surface microphones and head on the left side of the vehicle will be in a leeward flow condition, whereas the pressure tassings and right head will be adjacent to a windward flow condition. This information is shown diagrammatically in Figure 2.19.

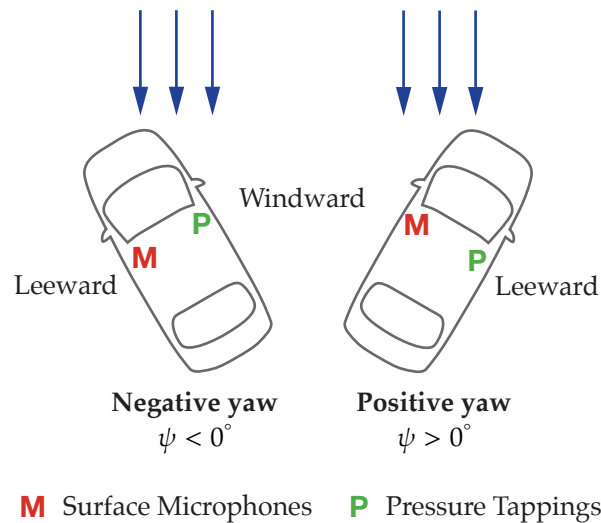


Figure 2.19: Vehicle at yaw with positions of external instrumentation

2.3 Apparatus

2.3.1 Vehicles

2.3.1.1 Specification

A Jaguar XF was used throughout this research. This vehicle is typical of a European three-box luxury saloon. The XF replaced the S-Type in Jaguar's product range and

2. EXPERIMENTAL TECHNIQUES

has a drag coefficient $c_D = 0.29$ and a frontal area $A_f = 2.33 \text{ m}^2$, from Gaylard (2008).

A publicity image of the 2010 XF is shown in Figure 2.20.



Figure 2.20: Jaguar XF © Jaguar Land Rover

2.3.1.2 Geometry Modifications

During the various phases of testing, different models of this vehicle were used. The differences between these geometries are summarised in Table 2.3. On-road testing with the Geometry 1 vehicle took place during the first testing campaign using an XF powered by a 2.7 litre V6 petrol engine. For the second on-road campaign, testing took place using a 3.0 litre V6 diesel-powered vehicle. This was a Geometry 2 vehicle, which was then modified for Geometry 3 testing.

Name	Short Name	Mirrors	Bonnet	Sideglass
<i>Internal Investigation</i>				
Geometry 1	Geo1	Baseline	Baseline	Glass
Geometry 2	Geo2	Modified	Baseline	Glass
<i>External Investigation</i>				
Geometry 1 (perspex sideglass)	Geo1 SG	Baseline	Baseline	Perspex
Geometry 2 (perspex sideglass)	Geo2 SG	Modified	Baseline	Perspex
Geometry 3 (perspex sideglass)	Geo3 SG	Modified	Modified	Perspex

Table 2.3: Summary of all vehicle geometries used

The vehicle geometries used can be broadly divided into two categories: those used when investigating effects on the cabin noise of the vehicle; and those used when investigating effects on the flow structures and noise generation around the sideglass of the vehicle. Geometry modifications were used to assess how minor geometry changes were able to affect the sensitivity of the vehicle to changes to the oncoming flow, and hence whether the engineer has to ability to modify the unsteady response of a vehicle.

For the cabin noise investigation, Geometry 1 vehicle testing took place in 2009, prior to the availability of the Geometry 2 mirror modification. This vehicle was an unmodified production vehicle with standard mirrors, bonnet and glass sideglass. Geometry 2 vehicle testing took place the following year, in 2010, also using an unmodified production vehicle. The design of the mirrors were updated from those of the Geometry 1 vehicle, with the differences shown in Figure 2.21.

The mirror cap and body were the same for both mirror designs, with the modification restricted to solely the stem and sail assembly. The sail is the triangular section which mounts the mirror to the body of the vehicle. The modification resulted in a reduction in the size of the mirror wake adjacent to the sideglass. Figure 2.21(b) shows the side profile of the mirror and how the stem was thinned and smoothed to reduce the air disturbance in the mirror region. Figure 2.21(d) shows how the mirror was moved downwards slightly, reducing the area of sideglass that the flow around the mirror can influence. Finally, Figure 2.21(f) show how the mirror was moved away from door by approximately 15 mm, increasing the gap between the mirror housing and the sideglass. A visual comparison between the two vehicle geometries used for the cabin noise measurements is shown in Figure 2.22.

The sideglass investigation took place at the same time as the Geometry 2 cabin noise investigation and used the same Geometry 2 vehicle. To measure the surface

2. EXPERIMENTAL TECHNIQUES

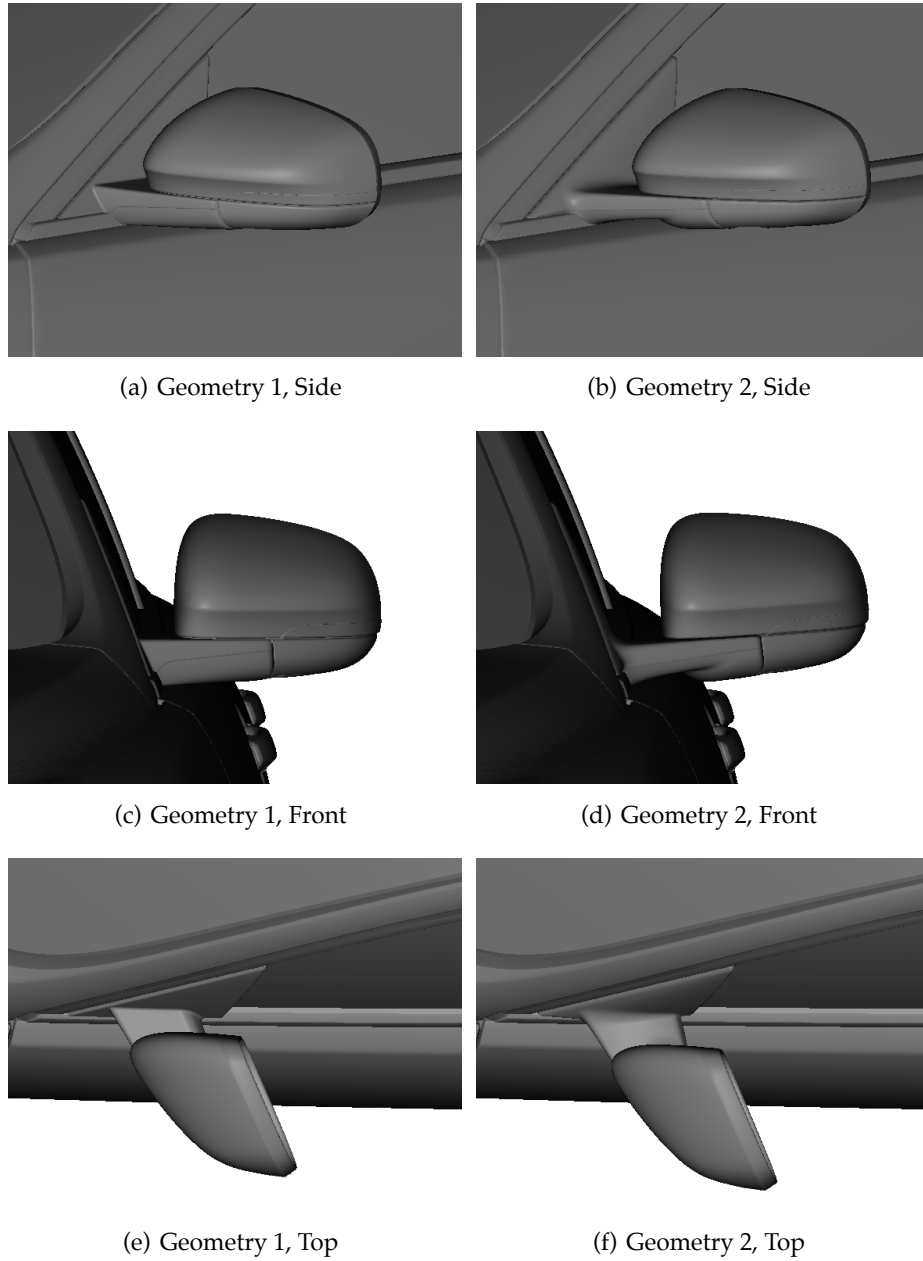


Figure 2.21: Comparison of Geometry 1 and 2 door mirrors

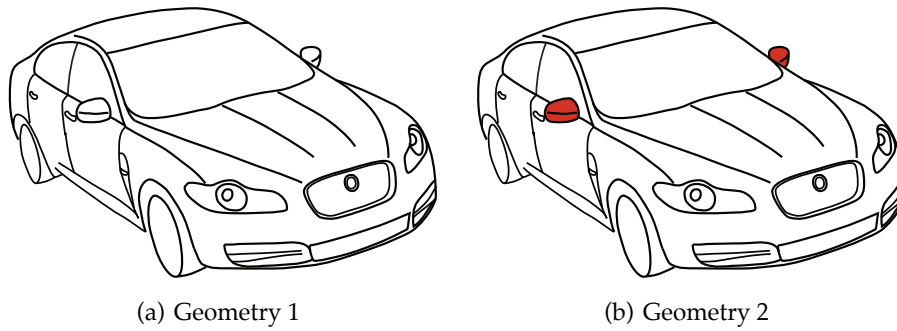


Figure 2.22: Vehicle geometries used for cabin noise measurements

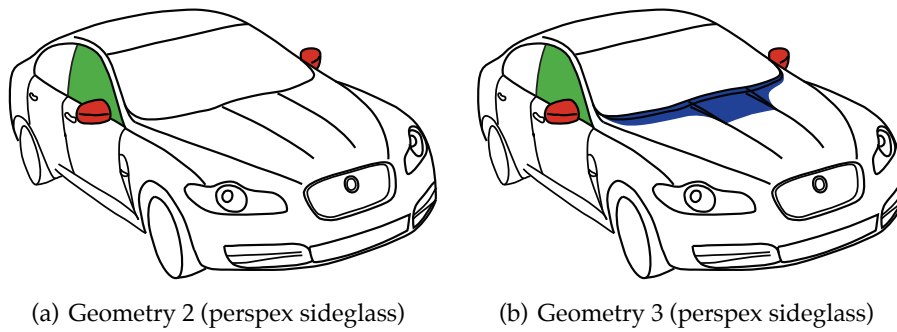


Figure 2.23: Vehicle geometries used for sideglass measurements

pressure field of the sideglass, the standard glass sideglass was replaced by a perspex sideglass, complete with drilled surface pressure tapings. Full details of the modified sideglass are described in Section 2.2.1.3. The Geometry 3 vehicle was the same as the Geometry 2 vehicle, with the addition of a bonnet kicker which increased the height of the rear lip of the bonnet by approximately 15 mm. The effect of the kicker was to reduce the amount of the wiper structure visible above the bonnet line and therefore reduce the size the vortices shed from the edge of the wiper blades and arms, similar to the work of Zaccariotto et al. (1997). The kicker was manufactured from a series of pieces of rapid-prototype resin and fixed in place using tape. The leading edge of the kicker was blended to the existing bodywork using modelling clay. An overall image is shown in Figure 2.24(a), with the detail of the blending shown in Figure 2.24(b). A

2. EXPERIMENTAL TECHNIQUES

visual comparison between the two vehicle geometries used for the cabin noise measurements is shown in Figure 2.23.

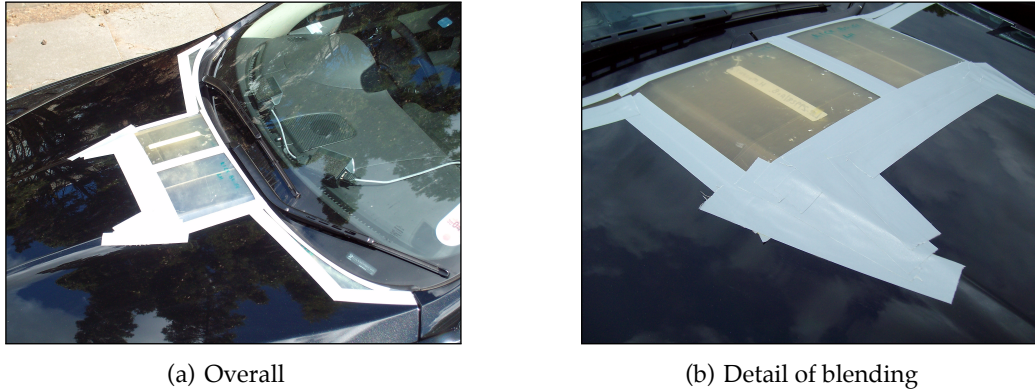


Figure 2.24: Images of bonnet kicker and attachment to existing bonnet

2.3.2 On-Road Testing

Road testing took place on UK dual-carriageways, encompassing a range of different wind conditions. The road surface included both hot-rolled and coarse chip asphalt, as typically experienced by a vehicle. A variety of wind conditions were chosen in order to capture the range of yaw angles that would be experienced on the road. These included high-yaw conditions experienced during particularly windy days. Traffic conditions were varied during the course of experimentation, although data collection was usually performed in light traffic as it was in these conditions that a constant speed could be most frequently held. In addition to passing vehicles, a range of different roadside obstacles were passed during data collection including crash barriers, trees, signs and bridges. Additional testing took place on both the test track at Jaguar Land Rover's Gaydon facility and on a straight section of single-carriageway road near Durham. The vehicle geometry configurations tested during both of the on-road testing campaigns are summarised by Table 2.4.

Name	Short Name	On-road Campaign
Geometry 1	Geo1	1
Geometry 2	Geo2	2
Geometry 2 (perspex sideglass)	Geo2 SG	2
Geometry 3 (perspex sideglass)	Geo3 SG	2

Table 2.4: Summary of vehicle geometries tested on-road

During on-road testing, a large number of 33 second runs were collected using each vehicle configuration. Owing to the nature of on-road testing, a proportion of these runs were rejected at times when a run was interrupted, particularly when a constant speed could not be held for the duration of a run.

On-road testing took place on motorways in the North of England, typically in the vicinity of Durham. This section of road was not only located near the University, but also provided a range of different terrain and corresponding localised oncoming wind conditions. Some sections of road contained a range of different roadside obstacles, whereas other sections of road were more open and susceptible to strong crosswinds. Images of these varied conditions are shown in Figure 2.25.



(a) Roadside obstacles



(b) Open terrain (© 2012 Google)

Figure 2.25: Typical on-road conditions

Logging GPS data not only allowed the vehicle speed to be recorded, but also the location of the vehicle and direction of travel. The location and direction of travel

2. EXPERIMENTAL TECHNIQUES

for each run and vehicle configuration are presented by Figures 2.26 and 2.27, for the vehicle geometries corresponding to the cabin noise and external investigations respectively.

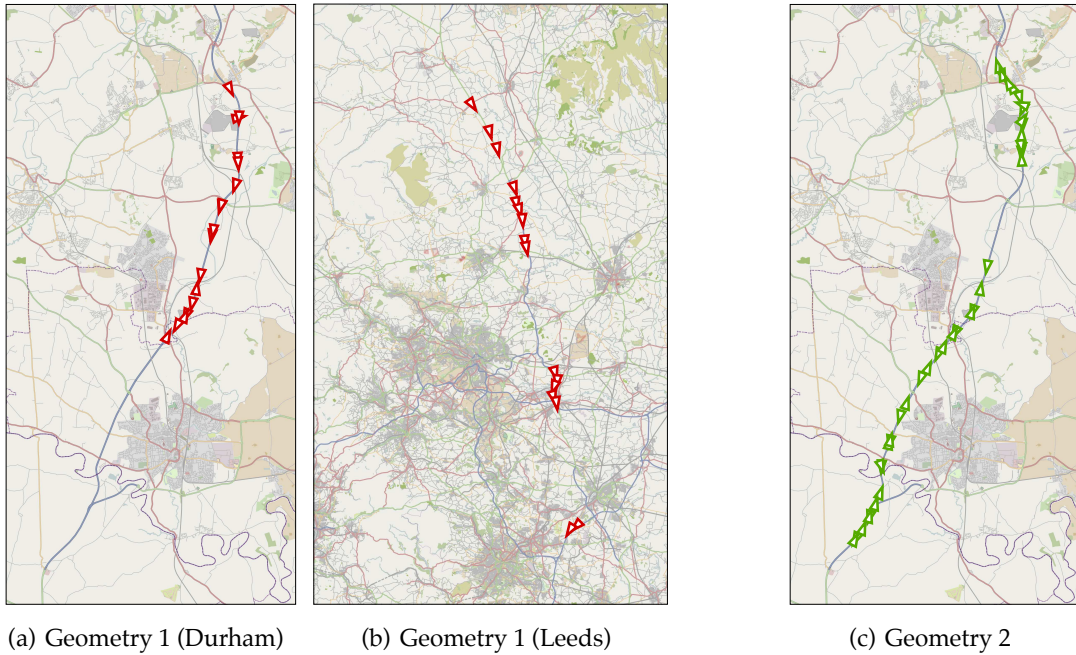


Figure 2.26: Testing locations for Geometry 1 and 2 vehicles (Map data © OpenStreetMap contributors, CC BY-SA)

2.3.3 Wind Tunnel Testing

Two full-size aeroacoustic wind tunnels were used during the course of this research: The Ford of Europe tunnel in Merkenich, Cologne, Germany; and the Pininfarina tunnel in Turin, Italy. Descriptions of the facilities and vehicles tested during these two testing campaigns are summarised in the following sections.

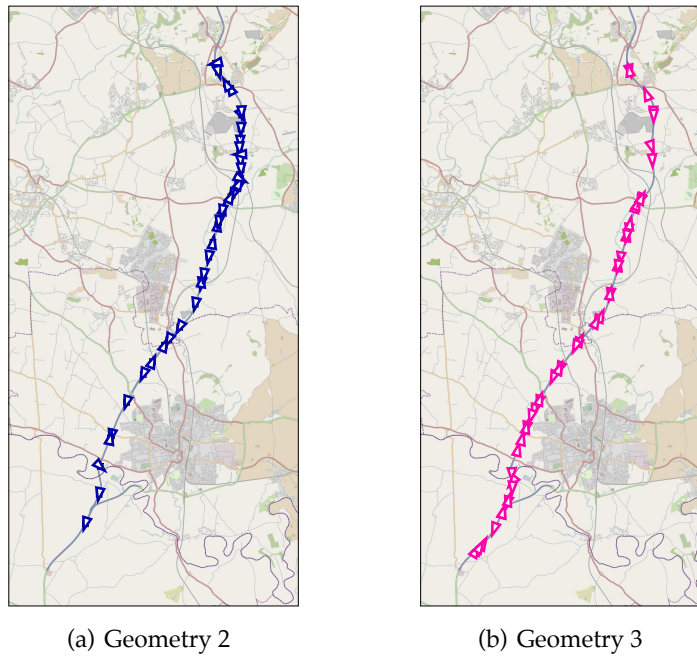


Figure 2.27: Testing locations for Geometry 2 and 3 vehicles (perspex sideglass)
(Map data © OpenStreetMap contributors, CC BY-SA)

2.3.3.1 Ford Wind Tunnel

The Ford tunnel was of a three-quarter open, closed-return Göttingen configuration. The tunnel was commissioned in 1984 and became acoustically treated in 1994. An image of the vehicle in the tunnel test section is shown in Figure 2.28(a), whilst a diagram detailing the tunnel configuration is shown in Figure 2.28(b), as taken from Hennig et al. (2010).

Testing at the Ford wind tunnel took place at an earlier stage of the research, when only vehicle Geometry 1 was available. This single geometry is summarised in Table 2.5.

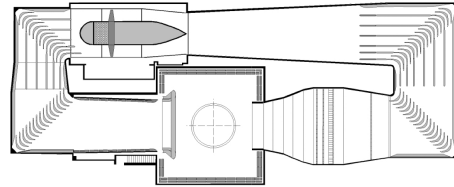
Name	Short Name
Geometry 1	Geo1

Table 2.5: Summary of vehicle geometries tested in the Ford AWT

2. EXPERIMENTAL TECHNIQUES



(a) Vehicle under test



(b) Diagram of tunnel layout, Hennig et al. (2010)

Figure 2.28: Ford of Europe Wind Tunnel

2.3.3.2 Pininfarina Wind Tunnel

Like the Ford wind tunnel, the Pininfarina tunnel was also of a three-quarter open type, but of a return not easily classified as either fully open or closed. The tunnel was originally built as an open-return type, but with the enclosing building not being large compared to the tunnel. Therefore the space between the tunnel and building acts as a non-ducted return leg. Later, to increase both the tunnel speed and the aeroacoustic performance, an additional thirteen fans were added on the return leg as described by Cogotti (2006). Therefore the tunnel is best described as being of a hybrid or semi-open type, since the return leg is not ducted as is the case in a true Göttingen tunnel. A sectional view of the tunnel showing this configuration is shown in Figure 2.29(b) as taken from Cogotti (2003a), whilst an image of the vehicle in the test section is shown in Figure 2.29(a).

Taking place at a later stage in the research, testing at the Pininfarina wind tunnel involved both internal and external investigation configurations of vehicle Geometries 1 and 2. These vehicle geometries are summarised in Table 2.6.

As described in Section 2.3.1.2, the difference between vehicle Geometries 1 and 2 is

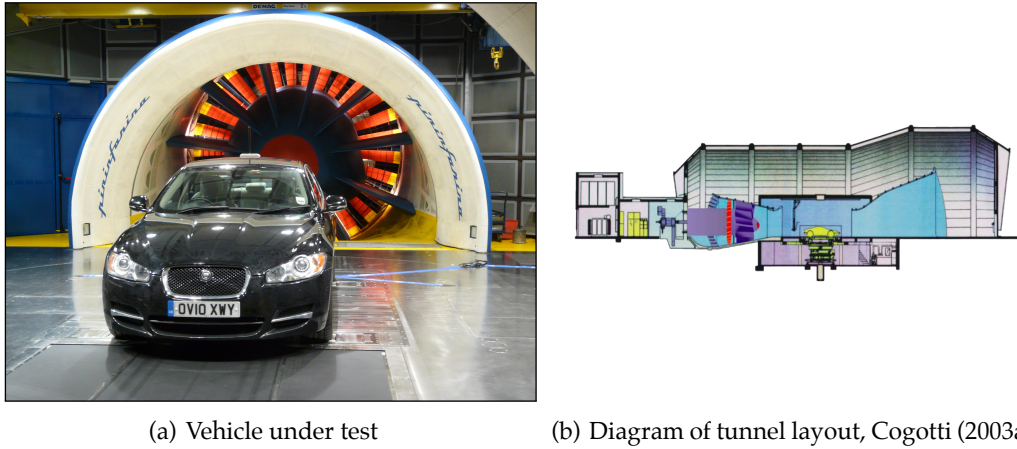


Figure 2.29: Pininfarina Wind Tunnel

Name	Short Name
Geometry 1	Geo1
Geometry 2	Geo2
Geometry 1 (perspex sideglass)	Geo1 SG
Geometry 2 (perspex sideglass)	Geo2 SG

Table 2.6: Summary of vehicle geometries tested in the Pininfarina AWT

a design change to the mirror stem. To test both configurations of vehicle, a Geometry 2 vehicle was used, with the mirror assembly changed to that of a Geometry 1 vehicle. These mirror assemblies are shown in Figure 2.30.

Aside from the differences in tunnel configuration, the significant difference between the tunnels is the turbulence generation facility (TGS) offered at Pininfarina. This allows the generation of controlled levels of turbulence and is described in detail in Section 1.4.7.1 of this thesis. An image of the TGS at the time of testing is shown in Figure 2.31(a).

A total of five TGS modes were chosen and summarised in Figure 2.31(b). These comprise two pseudo-random modes which were recommended by Pininfarina to simulate the broad-band turbulence conditions experienced during highway driving

2. EXPERIMENTAL TECHNIQUES

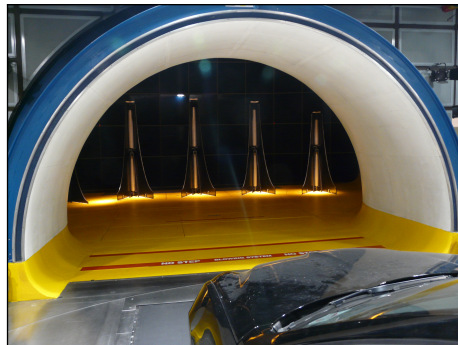


(a) Geometry 1 mirror assembly in position



(b) Geometry 2 mirror assembly in isolation

Figure 2.30: Images of the mirror configurations as tested at the Pininfarina AWT



(a) TGS upstream of the vehicle

Mode	Description
3BL	Strong traffic
5AL	Moderate traffic
4D1.0	1 Hz dynamic gust
4D0.4	0.4 Hz (2.5 s) dynamic gust
4D0.2	0.2 Hz (5.0 s) dynamic gust

(b) Description of TGS modes used

Figure 2.31: TGS as used during testing

in both strong and moderate traffic conditions. Three additional modes were also chosen to simulate a dynamic gust through the opening of the TGS flaps in turn. These modes were also explored by Lindener et al. (2007), who found that the 5AL mode more closely represented very light traffic conditions with roadside obstacles when testing on an Autobahn in the North of Germany.

2.3.3.3 Tunnel Comparison

A comparison of the two tunnel specifications is shown in Table 2.7. Data relating to the Ford tunnel was published by Volkert and Kohl (1987), whilst the Pininfarina tunnel data was published by Cogotti (2006).

Property		Ford	Pininfarina
Maximum speed (with car)	ms^{-1}	52	70
Average turbulence intensity	%	$< 0.5^a$	0.26^b
Nozzle area	m^2	23.75	11.00
(Blockage ratio ϕ)	(-)	(0.10)	(0.21)
Nozzle width	m	6.0	4.80
Nozzle height	m	4.01	2.80
Nozzle contraction ratio	-	4.0 : 1	6.5 : 1
Test section length	m	10.3	8.0
Fan motor power	MW	2	3.2^c

^a Data unavailable, measured value from vehicle roof

^b Up to 8% with TGS

^c Total for all fans, including main 2.1 MW fan and 13 additional fans

Table 2.7: Specifications of wind tunnels

Aerodynamic Performance

To compare the aerodynamic performance of both wind tunnels, the vehicle instrumented with the roof-mounted probe was positioned in the test section and yawed in 2.5° intervals between $\pm 20^\circ$ with the tunnel set to a constant speed of 130 km h^{-1} . The probe reported flow speed and yaw angle were recorded and compared against the nominal values as set by the wind tunnel. Figure 2.32 shows this data for the Ford tunnel. Both probe reported yaw ψ and the resultant probe speed versus tunnel speed ratio $u_{\text{Res}}/u_{\text{AWT}}$ are plotted against the wind tunnel turntable yaw ψ_{AWT} . Error bars relate to a single standard deviation above and below the mean over the course of the standard 33 s logging time.

Comparing the constant nominal tunnel speed with that measured by the probe at zero yaw, there was a significant increase in flow speed of approximately 14% as the flow travelled over the vehicle to the probe. This increase in speed was due to the flow accelerating as it curves around the top of the windscreen. As the vehicle was yawed, this increase in speed became larger, owing to the increased flow curvature and therefore acceleration as the flow passed over the A-pillar region. This speed increase

2. EXPERIMENTAL TECHNIQUES

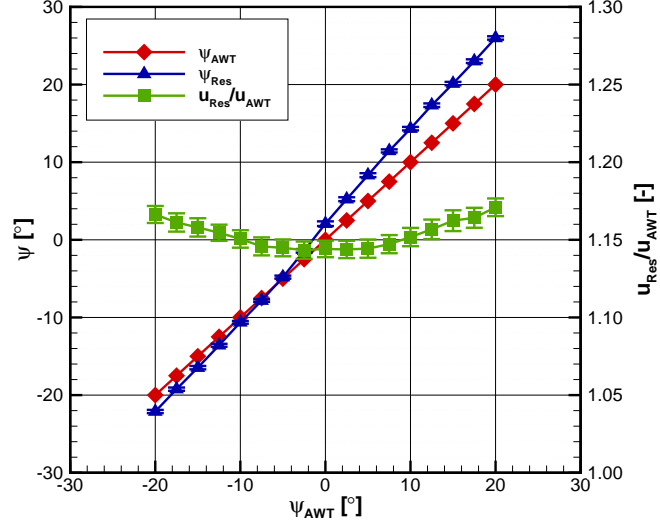


Figure 2.32: Ford AWT: Error of roof-mounted probe measurements (Geometry 1)

was consistent with the results obtained on-road, presented in Figure 2.7.

Comparing the turntable yaw angle with the yaw angle measured at the probe tip, both an offset and a stretching of the turntable yaw were measured by the probe. The yaw measured at the probe with the turntable at zero yaw is of the order of 2° . This is likely to be due to a combination of probe and mounting misalignment on the roof of the vehicle and to a lesser extent, misalignment of the vehicle on the turntable. The latter effect was investigated by Walter et al. (2005) who found that vehicle alignment uncertainty should be aligned to within $\pm 0.15^\circ$ using laser alignment sheets for the vehicle yaw to be contained within its uncertainty band for vehicle force measurements.

As the vehicle was yawed, the probe-measured yaw increased relative to the actual vehicle yaw, indicating that there was increased acceleration in the lateral flow direction (u_y) compared to the longitudinal direction (u_x), deflecting the flow. Taking into account the offset, there was consistent stretching of the measured yaw angle in both the positive and negative direction, indicating that the steady-state probe mea-

surements did not appear to be affected by any asymmetry in either the door mirrors or windscreen wipers.

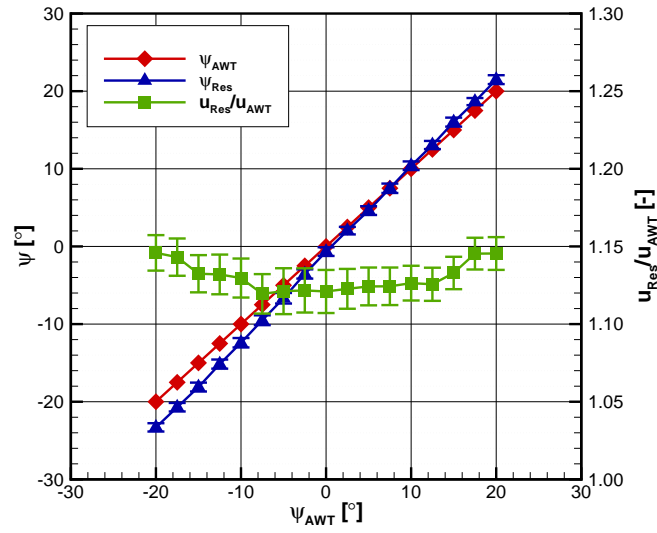
Figure 2.33(a) shows the equivalent data collected at the Pininfarina wind tunnel using vehicle Geometry 1. Data for vehicle Geometry 2 is also reported in Figure 2.33(b). Again, error bars are based on a single standard deviation.

Both vehicle geometries showed similar behaviour compared to the data obtained for the Geometry 1 vehicle in the Ford wind tunnel. The yaw angle offset was different in the two wind tunnels owing to the variation in probe positioning and vehicle position on the turntable. However, the same yaw offset was recorded between the two geometries of vehicle, reinforcing that the offset was due to a combination of probe and vehicle positioning, rather than an asymmetric vehicle geometry effect.

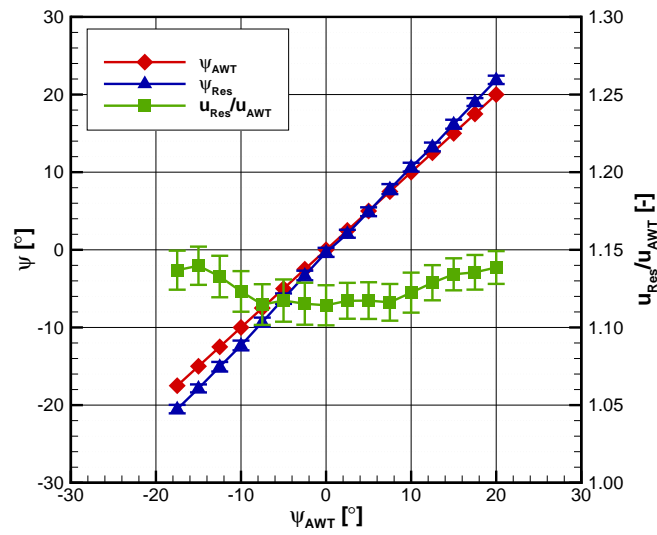
The increase in velocity measured by the probe compared to the nominal tunnel speed was less at Pininfarina than at the Ford tunnel. There was also increased uncertainty in these measurements. Since the geometry of the vehicles in both tunnel tests was nominally the same (with the exception of the small mirror-stem modifications between Geometry 1 and 2), it is unlikely that the reduction in flow speed increase was due to the differences in the vehicles. More likely, this was due to a nozzle blockage effect, where the presence of a body in a wind tunnel can affect the measured flow speed.

In a closed-wall wind tunnel, the presence of a body in the test section reduces the area through which the air can pass and thus, through the principles of continuity, the wind speed around the vehicle increases. However, in open-section tunnels, such as those of Ford and Pininfarina, the opposite effect can occur. As the jet exits the nozzle and passes around the body of the vehicle, a degree of jet over-expansion can occur, leading to a larger effective area through which the air passes and thus leads to a reduction in the flow speed in the vicinity of the vehicle. Wind tunnel blockage

2. EXPERIMENTAL TECHNIQUES



(a) Vehicle Geometry 1



(b) Vehicle Geometry 2

Figure 2.33: Pininfarina AWT: Error of roof-mounted probe measurements

effects, of which nozzle blockage is only a single component, is a large topic in itself and the various methods and effects are summarised by Wickern (2007).

Two methods are commonly used to measure the flow speed in an open-section wind tunnel: the plenum method and the nozzle method. The nozzle method involves taking the pressure difference at two different cross sections of the nozzle. This pressure difference is multiplied by a calibration factor determined in the empty tunnel to obtain the dynamic pressure. Using this method, the volume flux in the tunnel is kept constant for all blockage conditions. This is the only method available for use in closed section tunnels. The plenum method involves taking the pressure difference between a position upstream of the nozzle and the plenum chamber (test section). This has the effect of keeping the velocity of the jet boundary constant for all blockage conditions. In an open-section tunnel at a low blockage condition, both methods deliver the same results.

There is no consensus as to which method is most suitable for a particular open-section tunnel. However, larger tunnels tend to use the plenum method, with smaller tunnels using the nozzle method, from Hucho (1998). Both the Ford and Pininfarina wind tunnels use the nozzle method to determine tunnel speed and this is stated in the EADE wind tunnel correlation report by Hennig et al. (2010). From Table 2.7, the blockage ratio of the vehicle in the Pininfarina wind tunnel is relatively high at 21%, whilst the Ford wind tunnel is lower at 10%. Therefore, even though the pressure difference through the nozzle will nominally give the same dynamic pressure for both tunnels, the flow speed in the vicinity of each vehicle was likely to be different, owing to the difference in blockage ratio between the tunnels. With a higher blockage ratio, the jet expansion will increase leading to a greater velocity reduction. It is this effect which was likely to cause the reduced speed increase over the roof of the vehicle in the Pininfarina wind tunnel.

2. EXPERIMENTAL TECHNIQUES

However, since the flow speed over the vehicle was directly measured using the roof-mounted probe, the indicated tunnel speed was not required in any further analysis contained within this thesis.

Acoustic Performance

As discussed in Section 1.3.5.1, it is important for the level of tunnel background noise to be lower than that of the noise of the vehicle within the spectral region of interest. Otherwise, the noise of the vehicle may be masked by the noise of the tunnel. In the absence of comparable tunnel background noise data, a convenient method to compare the acoustic performance of the tunnels is to test the same vehicle under the same flow conditions and measure the cabin noise. Figure 2.34 compares the third-octave spectra of the cabin noise for the Geometry 1 vehicles measured in the Ford and Pininfarina wind tunnels. The tunnel speed was 130 km h^{-1} and turntable yaw was 0° . Values reported were recorded from the front passenger, outer ear (LHLE) position.

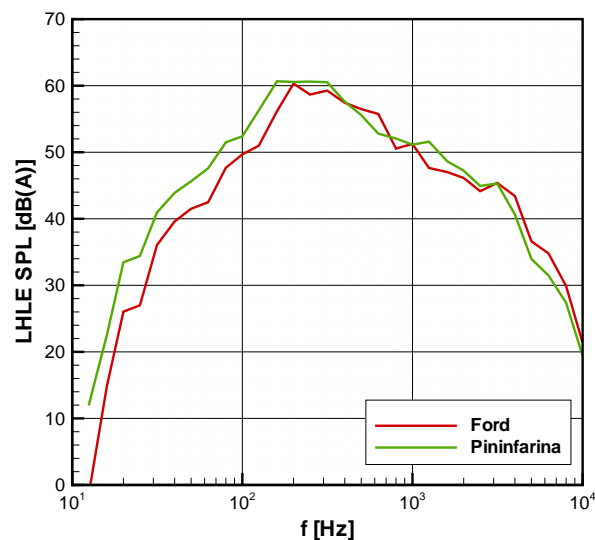


Figure 2.34: Comparison of third-octave tunnel spectra

The overall spectra from both tunnels was relatively consistent, particularly above 200 Hz. The vehicle in the Pininfarina tunnel showed an increased level of the order of 5 dB(A) at lower frequencies, which may be a feature of the tunnel background noise. As shown by Cogotti (2006), the addition of the thirteen-fan drive system to the Pininfarina wind tunnel, whilst increasing tunnel top speed and reducing overall background noise, caused a slight increase at low frequencies.

The two vehicles geometries tested in each of the tunnels had nominally the same external shape. However, it is likely that the sealing performance between the vehicles may have been subtly different, which may have caused a difference in the cabin noise spectra due to the noise generated by these leak paths. The vehicles were tested in an 'on-road condition,' where joints and sealing lines were not taped. Therefore this may be a cause of the small spectral differences in level between the two tunnels at higher frequencies. However, the cabin noise performance of the vehicle in both tunnels was comparable, particularly in the higher frequency region most important to wind noise.

2.4 Data Handling

Prior to further analysis, the raw aerodynamic and acoustic data was processed using a series of software tools. For the aerodynamic data, the recorded voltage outputs from the pressure transducers were read into a series of software routines written in the C programming language. The procedures for both the five-hole probe and side-glass data are described in the following sections, along with a section describing the processing of the subjective jury testing data.

2. EXPERIMENTAL TECHNIQUES

2.4.1 Five-Hole Probe Data

ApplyCal Takes the output voltages recorded by the five probe pressure transducers and applies the transducer calibration to convert to pressure.

TFCorrect Applies the inverse of the experimentally measured transfer function of the probe and tubing system to the measured pressures.

Apply5HCal Converts the five probe pressure channels into the four non-dimensional probe pressure coefficients. Using the experimentally determined calibration surfaces, these are converted into the dimensional flow conditions, including the three orthogonal velocity components.

CalcTurbRolling Takes the velocity components and determines the turbulence properties including autocorrelation length scale and intensity. A rolling average approach was chosen, determining the properties from a window of data. The window size chosen was 2048 samples, equal to 4.096 seconds at a sampling frequency of 500 Hz. The reduced frequency for this time period is $k < 0.1$ and therefore both quasi-steady and unsteady fluctuations can be captured.

2.4.2 Sideglass Pressure Data

ApplyCal Takes the output voltages recorded by the sideglass pressure transducers and applies the transducer calibration to convert to pressure.

TFCorrect Applies the inverse of the experimentally measured transfer function of the tubing system to the measured pressures.

CalcCp Converts the corrected sideglass pressure measurements to the non-dimensional form of c_p , using the static and dynamic pressures as recorded by the roof-mounted probe.

2.4.3 Acoustic Data

The raw sound pressure data were processed using the HEAD Acoustics ArtemiS software. This was used to determine both sound pressure level and various psychoacoustic parameters. Since sound pressure level is calculated using the RMS values of the raw sound pressure, according to Equation 1.4, a finite window of data must be used in its calculation. The size of this window was chosen to equal 2 ms ($f = 500$ Hz) such that the time period of calculated SPL matched that of the logging frequency of the flow data. Loudness, articulation index and sharpness were calculated according to methods outlined in Section 1.3.7, but are also summarised in Table 2.8.

Psychoacoustic Parameter	Method
Loudness	According to ISO532:1975 (1975), diffuse field
Articulation Index	According to Van Ligten (1982)
Sharpness	According to Fastl and Zwicker (2007)

Table 2.8: Methods used in calculating various psychoacoustic parameters

2.4.4 Subjective Testing

The two jury testing methods of a paired comparison and ranking were used in this research, each serving a different purpose. Both of these methods were introduced in Section 1.3.7.4. The paired comparison was used after dividing up a continuous cabin noise time-history into a series of blocks that were individually assessed. This allowed both flow and cabin noise events during the course of an on-road testing run to be correlated with the subjective response of wind noise *annoyance*. Ranking was later used to subjectively assess various cabin noise samples. The methods used are outlined in the following sections.

2. EXPERIMENTAL TECHNIQUES

2.4.4.1 Paired Comparison

When two sound files are assessed in a simple paired comparison, one of the samples will be perceived as being more annoying than the other and given a marker. After the complete set of these pairs have been compared, the markers are then totalled for each sample, providing a relative annoyance index. Typically, a paired comparison is used to analyse a discrete set of sound samples, recorded in a range of different conditions. In this case, the sound samples were taken from a continuous time history to assess how the subjective response of wind noise annoyance changes with cabin noise over the course of a recording.

The time history was selected from a series of on-road data using a Geometry 1 vehicle. This was chosen since it had few additional noise sources that may distract a participant, such as changes in road surface or the sound of passing vehicles. In addition, the wind conditions were relatively strong and modulating wind noise could be heard clearly in the recorded data.

To create a paired comparison jury test of this form, the recorded audio file was first divided into a series of equal-duration blocks. This provided subjective data at the mid-point of each block. For N such blocks of duration t , it follows that the duration of the sound file T_{File} is:

$$T_{\text{File}} = Nt \quad (2.14)$$

For a given total sound file length, T_{File} , the temporal resolution is dependant on the length of t chosen and the corresponding number of samples N . To improve this resolution, t can be reduced, with a resulting increase in N . This increases the time taken to run the experiment, since the number of comparisons is dependant on the number of sound samples. As previously discussed, for a paired comparison where all combina-

tions of these audio blocks are compared, the total number of combinations is shown by:

$${}^N C_2 = \frac{N!}{2!(N-2)!} = \frac{1}{2}N(N-1) \quad (2.15)$$

Therefore, if N increases, the number of pairs will increase with the power 2. For a modest increase in the resolution of the data, this can result in a much larger increase in experimental time.

An alternative method is to repeat the paired comparison using an additional set of N blocks of audio, offset by $t/2$. This doubles the resolution of the responses, or alternatively gives the same resolution for a smaller number of blocks. This method is shown graphically in Figure 2.35. By defining $N_{\text{set}} = N/2$, the resulting number of combinations is shown by:

$$2^{N_{\text{set}}} C_2 = N_{\text{set}}(N_{\text{set}} - 1) = \frac{1}{4}N(N-2) \quad (2.16)$$

In comparing the two methods, it can be shown that in using the offset method, experimental time can be at least halved. Therefore, it was this method that was adopted in this study.

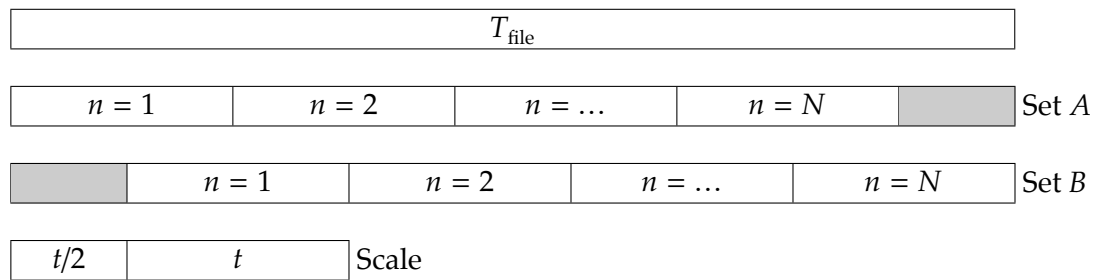


Figure 2.35: Alternative offset method in dividing the sound file

To estimate the time taken for testing, it was assumed that an equal amount of time was used for the silence between each pair of samples as the time taken to hear a single sample. A shorter period of time was chosen between the samples in a pair than

2. EXPERIMENTAL TECHNIQUES

the length of time between pairs. In the longer period of time between sample pairs, a sound file containing an introduction of a numerical value was included to help participants identify the sample pairs. Each pair therefore had a duration of $T_{\text{Pair}} = 3t$, depicted by Figure 2.36. For an investigation using the offset method, the total time taken to evaluate is given by Equation 2.17.

$$T_{\text{Test}} = \frac{1}{4}N(N-2)T_{\text{Pair}} = \frac{3}{4}N(N-2)t \quad (2.17)$$

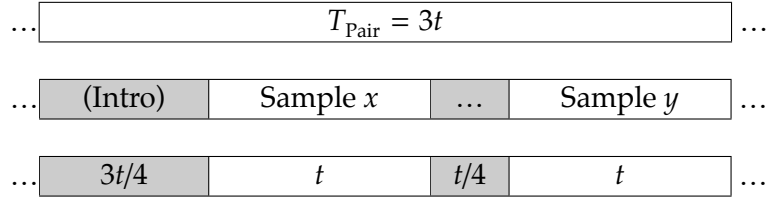


Figure 2.36: Relative lengths of sound samples within a comparative pair

The combined flow and audio data used in this investigation had a duration of 38 seconds. It was decided that a sample length, t , should be 4 seconds. This was a compromise between the sample being long enough to capture fluctuations and modulation in the noise, whilst being short enough for the participant to remember the characteristics of the noise before hearing the second sample of the pair. This is also sufficiently long for quasi-steady fluctuations to be captured. From Equation 2.14, 38 seconds of audio data was analysed, split into $N_{\text{Set}} = 9$ overlapping blocks, each of $t = 4$ seconds. Therefore resulting time taken for a participant to be tested was $T_{\text{Test}} = 14$ minutes, 24 seconds.

To determine the order in which the samples were played to a participant, a random number table was used, from Rich (2001). The ascending combinations of set A followed by set B were assigned a random number. These random numbers were

then arranged in ascending order, therefore randomising the order in which a sample pair would be heard during the course of the experiment. As can be shown in Table 2.9, the first sample is always a block taken at an earlier point in time from the audio file. To give both earlier and later blocks an equal chance of being heard first within a comparative pair, in any pair assigned an odd random number, the order of samples was reversed.

First Sample	Second Sample	Set	RAND
1	2	A	10097
1	3	A	37542
1	4	A	08422
⋮	⋮	⋮	⋮

First Sample	Second Sample	Set	RAND
1	4	A	08422
2	1	A	10097
1	3	A	37542
⋮	⋮	⋮	⋮

Table 2.9: Randomisation of sample pairs

Once the order of samples had been determined, the pairs were combined into a continuous audio file separated by an audible numerical value. This was then played to each participant in turn who recorded their responses as the test was in progress. A pair of closed-back headphones were used to listen to the samples and care was taken to ensure the output level was the same for each participant.

To assess the reliability of the responses given by each participant, an evaluation of respondent consistency was made. During the course of a paired comparison investigation, a participant may contradict themselves. For example, sample *a* could be considered more annoying than sample *b*. Further into the test, sample *b* could then be considered more annoying than *c*. If later, *c* is then thought to be more annoying

2. EXPERIMENTAL TECHNIQUES

than a , a *circular triad* is formed. Depending on the manner of the test, a degree of inconsistency is to be expected. Since the various samples of in-cabin noise are generally very similar, complete consistency was unlikely.

The degree of consistency of a particular participant was assessed according to:

$$\zeta = 1 - \frac{24d}{N_{\text{set}}^3 - N_{\text{set}}} \quad (2.18)$$

where d is the number of circular triads and ζ is the coefficient of consistence. This form of the equation applies only for odd values of N_{set} . Recall that $N_{\text{set}} = 9$ for this study.

For this experiment, there are a possible $N_{\text{set}}C_3 = {}^9C_3 = 84$ combinations for each set A and B . To calculate d , a program was written to evaluate each possible circular triad and check for circularity. After the value of ζ was found for each of the sets, the value was then averaged for both sets to form an overall coefficient. This value was between 0 and 1, where 1 represents complete consistency. A low value of ζ is an indication of either poor differentiation of the samples by the participant or the samples being too difficult to differentiate.

To collect, process and analyse the data, routines written in the C programming language were used. These are described below:

CollectPairedCompResults Reads an address file, containing the order of sound samples that were played to each participant. The program then proceeded through each pair in turn and asked the participant which sample they found the most annoying. The response data was then combined with the address data and written to an output response file.

CalcPairedComp Took response data from **CollectPairedCompResults** and with information of the duration of each sample, a time history of the participants rel-

ative annoyance to each of the sounds was then created. The coefficient of consistency was also calculated.

2.4.4.2 Ranking

Ranking was completed later in the research, comparing various simulated cabin noise samples. The testing approach adopted was one used by Jaguar Land Rover. This approach, whilst being less rigorous than a paired comparison approach, allows a greater number of samples to be assessed, or alternatively a shorter test time allowing a greater number of participants. Whilst the sounds samples were generated by the author, the testing took place at Jaguar Land Rover in the controlled environment of an equalised listening suite.

The test was controlled by a graphical interface comprising a slider bar and control button to play each sound. The participant proceeded through the list of sounds, and adjusted the corresponding slider bar to best characterise their response. The extremes of the slider bar were *least annoying* and *most annoying*. The slider had a minimum score of 0 (most annoying) and a maximum score of 100 (least annoying), with a resolution of 1. The test allowed the respondents to listen to the sounds multiple times to ensure that they were satisfied with their responses.

To process the data, each of the respondents scores were normalised such that the lowest ranked score r_{Min} was adjusted to equal 0, the highest score r_{Max} adjusted to 100 and the other scores being linearly interpolated between these limits, according to:

$$\hat{r} = \left(\frac{100}{r_{\text{Max}} - r_{\text{Min}}} \right) (r - r_{\text{Min}}) \quad (2.19)$$

where r is the original score and \hat{r} is the normalised score.

The scores of each of the respondents were then averaged for each sound sample

2. EXPERIMENTAL TECHNIQUES

to determine an overall score of \bar{r} , with confidence intervals used to characterise the reliability of the average. To assess the quality of the responses of a particular participant, the coefficient of determination R^2 was calculated between the participant's data and the overall averaged data.

CHAPTER 3

The Time-Averaged Vehicle Response

3.1 Introduction

The conventional steady-flow aeroacoustic wind tunnel is generally used during the development of a vehicle. The vehicle is assessed at a range of discrete conditions of both flow speed and yaw angle, with the behaviour of the vehicle in the on-road unsteady environment inferred from this steady-state response. This chapter aims to compare the results obtained in these two quite different environments from a time-averaged perspective. As throughout this thesis, the response of the vehicle is focussed on the overall cabin noise and the external pressure fluctuations in the sideglass region.

The range of flow conditions experienced by the test vehicles on-road are initially presented and compared with those generated by the Pininfarina Turbulence Generation Systems (TGS). Subjective results used to determine the key acoustic parameters to capture the wind noise in the cabin are then presented. Three key measurements of the vehicle response are assessed: the noise inside the cabin, as heard by a passenger; the surface pressure distribution in the sideglass region, to determine key flow structures; and the surface noise on the sideglass, to measure the differences in noise

3. THE TIME-AVERAGED VEHICLE RESPONSE

generation made between modifications to the vehicle geometry. In each case, the steady-state results obtained in the aeroacoustic wind tunnel are compared against the time-averaged results obtained on-road using a range of averaging techniques, with an assessment made of the accuracy of the wind tunnel in capturing the time-averaged vehicle response. In addition, time-averaged results of the unsteady conditions produced by the Pininfarina TGS are compared with both results obtained in the same facility under steady conditions and the on-road environment.

3.2 Data Averaging

Time-averaged data collected under steady conditions at the wind tunnel was taken at discrete values of flow speed and yaw angle and averaged over the logging time. This contrasts with the on-road environment where the flow conditions were fluctuating continuously.

By simply plotting the instantaneous values of yaw angle measured by the probe against the corresponding level of noise inside the cabin, the relationship between yaw angle and cabin noise may be seen. However, since there was a wide spread of both flow conditions and resulting cabin noise on-road, any relationships are likely to be very difficult to determine. Therefore, to provide time-averaged data of a form which was comparable to that obtained in the wind tunnel, an averaging technique was adopted that split the nominally continuous data (albeit sampled discretely) into a series of discrete categorised *bins*. Each of the variables contained within this bin was then averaged to provide characteristic data for that particular condition. Figure 3.1 shows the *bin-averaging* method graphically, using yaw angle as the conditional variable.

In this example, the instantaneous value of oncoming flow yaw angle is read for

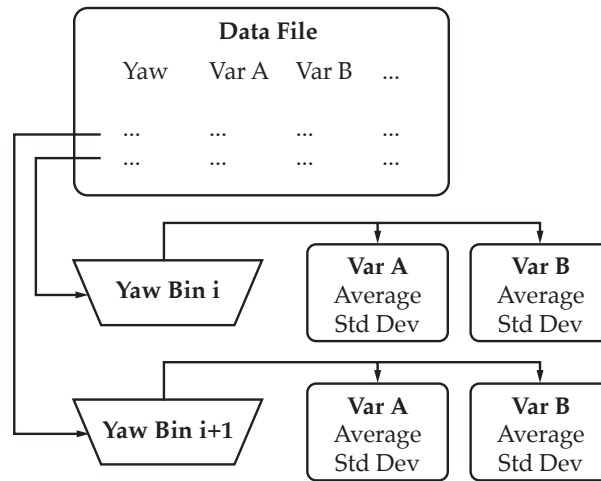


Figure 3.1: Bin-averaging process

each data line to determine which bin that particular data line should be assigned to. This process is continued for each subsequent measured yaw angle, with the corresponding data lines being assigned to a bin for that particular yaw angle range. Once this is complete, the data for each variable in each bin is then averaged to provide a characteristic value for that particular yaw angle. This process is not restricted to a single conditional variable, allowing multiple variables to be used to define the various bins. A total of three different sets of bins were used in this research and these are listed below:

All bins: To capture the behaviour of the vehicle over the complete range of flow speeds and yaw angles as experienced on-road, a total of 255 bins were created. The yaw angle range captured by these bins extended between $\pm 20^\circ$ in 2.5° intervals; the same yaw interval as used by the wind tunnel turntable. The flow speed ranged between $28\text{--}56\text{ ms}^{-1}$ in 2 ms^{-1} intervals. It should be emphasised that on-road the oncoming flow velocity was not deliberately varied; the bins captured the range of natural variation in the resultant velocity (made up of a vector combination of the vehicle velocity and the natural wind veloc-

3. THE TIME-AVERAGED VEHICLE RESPONSE

ity). The mid-points of each of these bins are shown in Figure 3.2(a) with the boundaries of each bin also shown.

Constant ψ : To simulate the conditions that would be experienced in a wind tunnel at a straight-ahead position with a varying tunnel speed, a set of bins were created at a fixed yaw angle of 0° . For consistency with the other bin-averaged data, the bin width of yaw remained at 2.5° , such that the bin width was $\psi = 0^\circ \pm 1.25^\circ$. The flow speed increments and range were also the same as with the **All bins** set. These bins are shown graphically in Figure 3.2(b). Recall that the vehicle on-road travelled at a constant speed $u_{\text{veh}} = 36.1 \text{ ms}^{-1}$, so that the flow speed variation is due to the external wind alone.

Constant u_{Res} : Likewise, to simulate the conditions that would be experienced in a wind tunnel at constant flow speed as the vehicle was yawed, a set of bins were created at a fixed nominal flow speed. This was set at the speed measured by the probe at the nominal tunnel test speed. This took into account the increase in free-stream flow speed when measured by the probe. Again, for consistency with the other bin-averaged data, the bin width of this flow speed remained at 2 ms^{-1} , with the yaw angle increments and range the same as with the **All bins** set. These bins are shown graphically in Figure 3.2(b).

It is important that the range of bins fully captures the range of flow speeds and yaw angles experienced on-road. Likewise, it is also important the the range of conditions in the wind tunnel is also representative of those on-road, since ultimately the bins are defined based on the tunnel turntable yaw resolution. To assess this, the bin-average technique was completed on the entire collection of on-road measured flow data, using the full extent of bins. Figure 3.3 shows the proportion of data collected by each bin, with both the height and the colour shading describing the probability of a

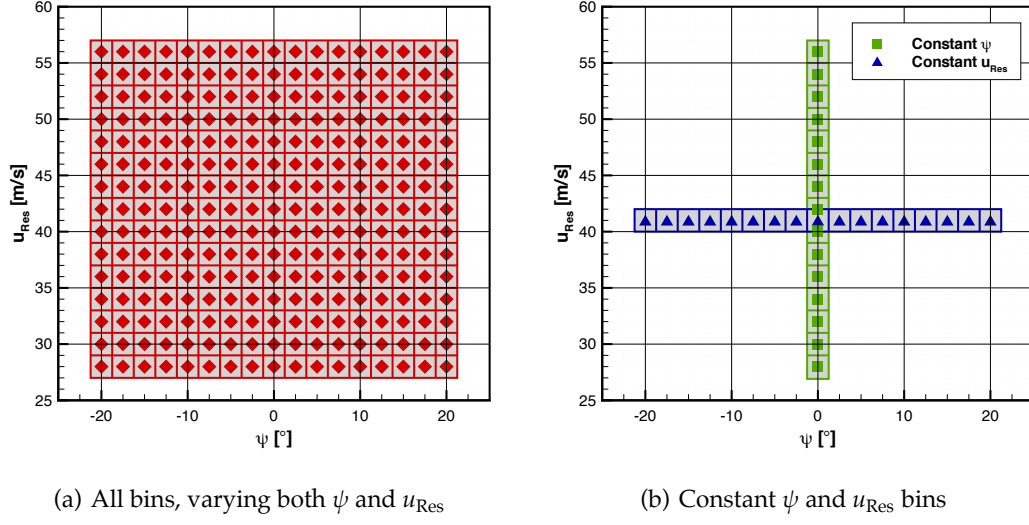


Figure 3.2: Sets of bins used to average the on-road data

line of data falling into a particular bin.

This shows that the majority of data falls in the centre of the yaw angle and flow speed range of the bins, with the outer extremes of these conditions containing a very small amount of data. This indicates that the range of bins chosen is suitable for capturing the full range of flow conditions as experienced by the vehicle on-road.

3.3 Flow Conditions

3.3.1 On-Road

It is widely considered, for instance by Cooper and Watkins (2007), that the variation in wind speed u_{Wind} at a particular measurement point is normally distributed, following a Gaussian distribution i.e. $P(U_{Wind}) = \mathcal{N}$. It may also be assumed that the wind direction onto the vehicle ϕ is uniformly distributed, with an equal likelihood of arriving from any direction, such that $P(\Phi) = \mathcal{U}$. Since the yaw angle of the oncoming flow onto the vehicle ψ and the resultant flow speed u are a function of only wind speed

3. THE TIME-AVERAGED VEHICLE RESPONSE

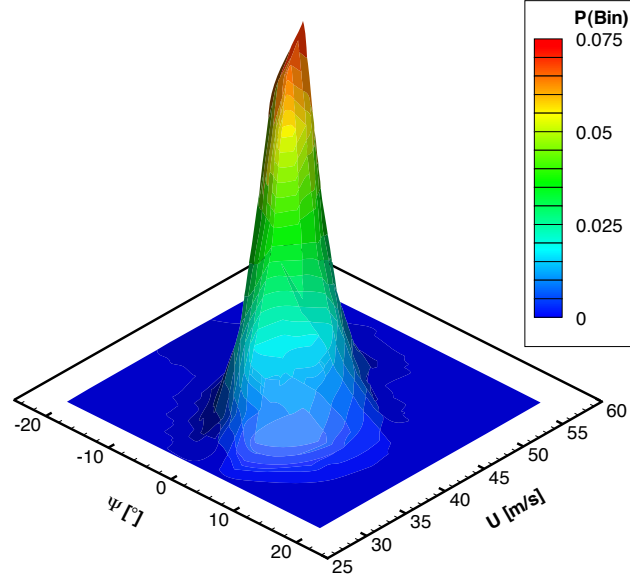


Figure 3.3: Distribution of on-road data between each of the bins

and direction at constant vehicle speed (see Figure 1.31), it follows that the probability of yaw angle and resultant flow speed onto a vehicle will also be normally distributed, according to:

$$P(U), P(\Psi) = P(U_{\text{Wind}} \cap \Phi) = \mathcal{N} \quad (3.1)$$

Figure 3.4 shows the probability distributions for both flow speed u and yaw angle ψ as measured by the roof-mounted probe. The data comprises all of the the data collected on-road, for all configurations of vehicle geometry. In addition to the measured probability, a normal (Gaussian) distribution is also plotted, as defined by:

$$f(x) = \frac{1}{\sqrt{2\pi\sigma^2}} e^{-\frac{(x-\mu)^2}{2\sigma^2}} \quad (3.2)$$

To fit the normal distribution to the data, the values of the mean μ and standard deviation σ of the on-road collected data were used. Figure 3.4(a) shows the measured distribution of resultant flow speed. This distribution closely follows a normal distri-

bution, indicating that the resultant flow speed data collected on-road is reasonably representative of what would be expected under normal driving conditions, with no bias towards particularly high or low wind conditions. These would lead to a skewed distribution, weighted toward either high or low resultant flow velocities.

Figure 3.4(b) shows the distribution of yaw angle, which does not show the same normal distribution as either flow speed, or as predicted. The bias towards zero yaw angles was also present in the on-road data presented by Carlino et al. (2007). This implies that the distribution of wind direction relative to the vehicle is not uniform. This would suggest that there was a greater chance for the prevailing wind direction to be aligned with the direction of travel of the vehicle rather than from any other direction. This may either be due to macro-scale weather conditions at the time of measurement, or more likely to be due to the channeling effect of the wind as it passes along the road. Embankments either side of the road or lines of trees would all assist the wind in following the direction of the road. Since these are the wind conditions as would be experienced by a vehicle on-road, removal of these trends was not undertaken.

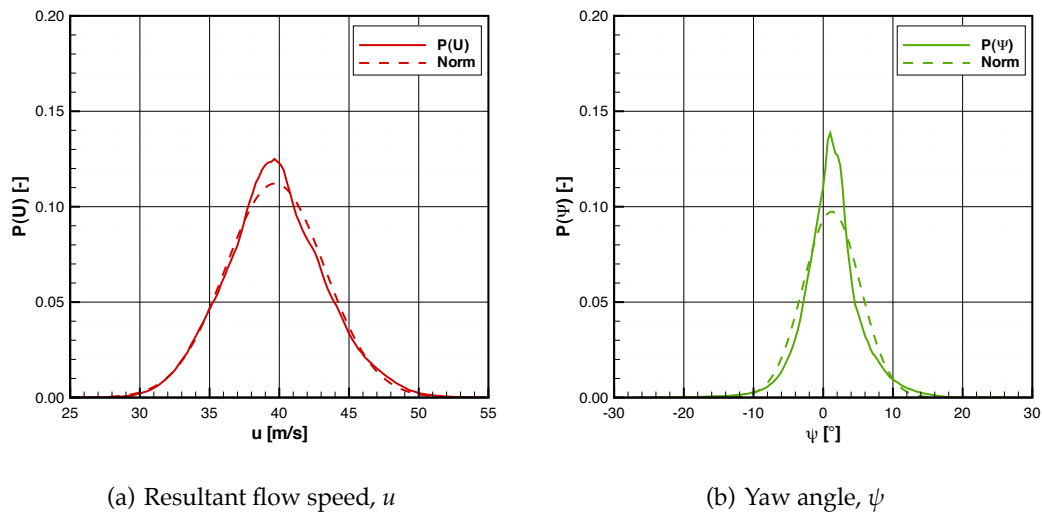


Figure 3.4: Probability distributions of on-road flow conditions

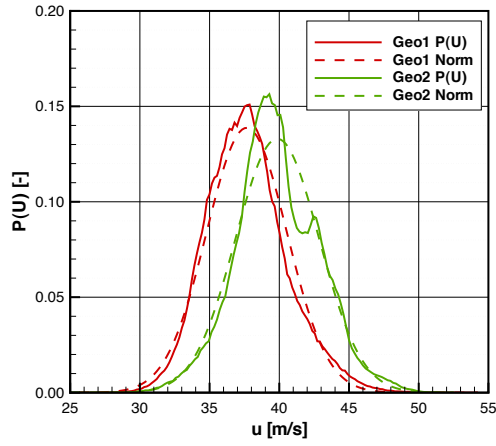
3. THE TIME-AVERAGED VEHICLE RESPONSE

Figure 3.5 shows the probability distributions of flow speed and yaw angle as experienced by each vehicle configuration. The distributions are relatively consistent for each measurement campaign, with an approximately normal distribution of flow speed and a distribution of yaw angle more weighted towards zero. Two anomalies of note include the bimodal distributions of flow speed experienced by the Geometry 2 vehicle and the yaw angles experienced by the Geometry 3 SG vehicle. These indicate the presence of a prevailing wind speed or direction over the course of testing. It is also possible that the slight shifts in average yaw angle may be due to a probe offset.

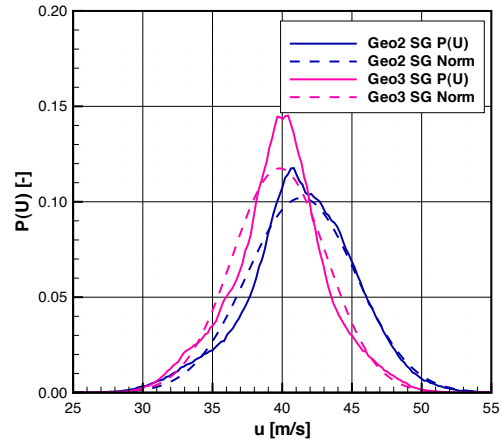
Figure 3.6(a) shows the range of turbulence intensities I and length scales L as experienced on-road. The length scales and intensities are similar in the longitudinal and lateral directions, with mean values of approximately 7 m and 4 % respectively. Vertical length scales remained constant under the range of on-road wind conditions. These data are also presented superimposed onto Figure 3.6(b), which identifies the range of turbulence conditions as experienced in different on-road environments in Australia by Wordley (2009). The data presented by this thesis appears to show the greatest similarity to that collected under 'roadside obstacle' conditions. Note that the freeway conditions as described by Wordley are quite different to those in the UK, with fewer roadside obstacles in a flatter terrain environment, generally leading to longer turbulent length scales experienced by a vehicle.

Figure 3.7 shows these conditions as experienced by each vehicle configuration. Again, the conditions are relatively consistent for each vehicle geometry. The Geometry 2 vehicle generally experienced lower turbulence intensities than the other vehicles, whilst at the same time also experiencing a smaller range of yaw angles.

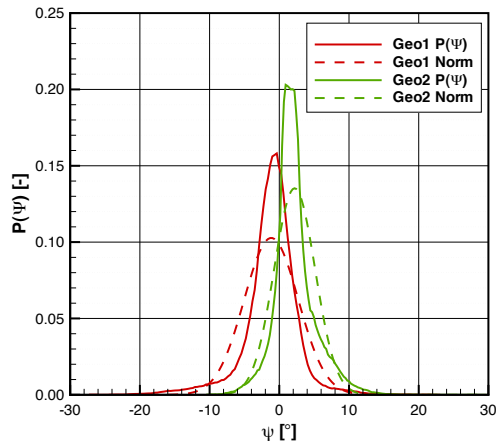
Watkins (1990) derived a mathematical model to predict the turbulence intensities experienced by a moving vehicle, using fixed-site wind data. This model predicted that the turbulence intensity experienced by a vehicle would be greater at higher yaw



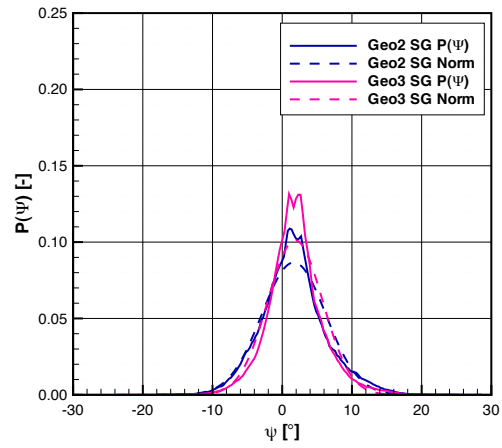
(a) Geometries 1 and 2, u



(b) Geometries 2 and 3 SG, u



(c) Geometries 1 and 2, ψ



(d) Geometries 2 and 3 SG, ψ

Figure 3.5: Probability distributions for individual vehicle geometries

3. THE TIME-AVERAGED VEHICLE RESPONSE

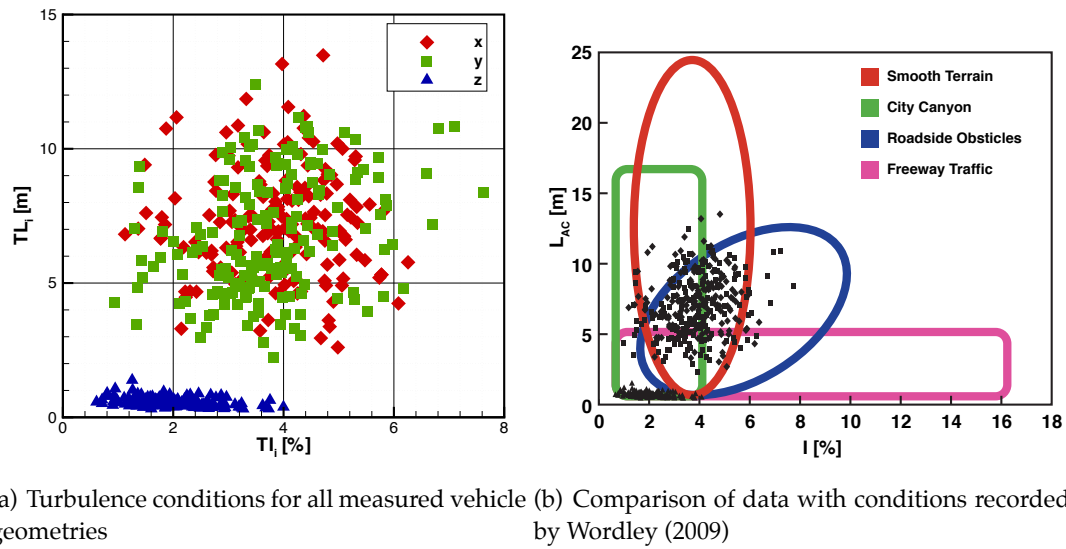


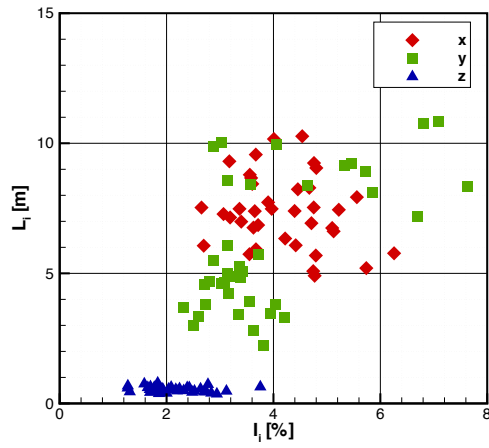
Figure 3.6: Turbulence conditions measured on-road

angles, since these high yaw angles can only be generated through the action of inherently turbulent crosswinds. To test this theory, the complete set of measured on-road flow data were processed using the constant speed bin-average technique to determine how the measured turbulence intensity relates to yaw angle. The resulting data is shown in Figure 3.8.

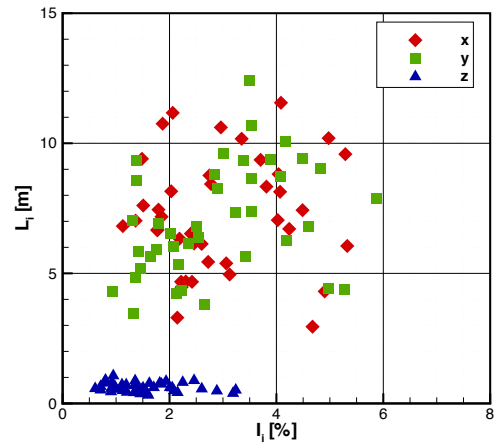
This data shows a clear relationship between turbulence intensity and oncoming yaw angle. Turbulence intensities increase by up to 50% at the extremes of measured yaw angle, indicating that the crosswind component of the oncoming flow vector provides a significant amount of the turbulent fluctuations experienced by a vehicle on-road.

3.3.2 Pininfarina Turbulence Generation System

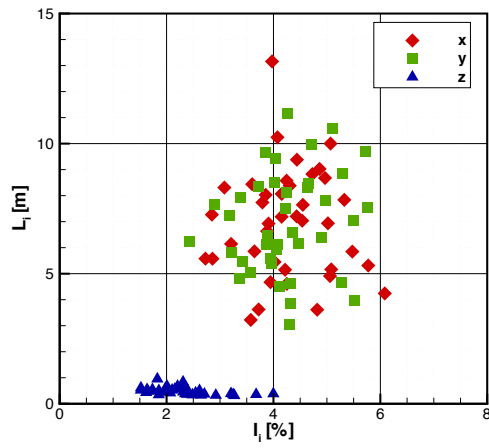
The range of yaw angles generated by the TGS in the Pininfarina wind tunnel were also measured using the roof-mounted probe. As introduced in Section 2.3.3.2 a total of five TGS modes were used, comprising two pseudo-random modes and three



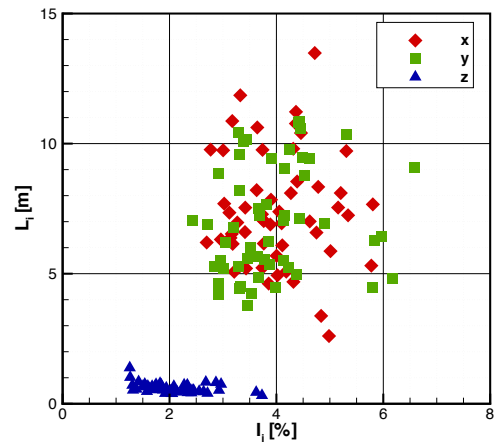
(a) Vehicle Geometry 1



(b) Vehicle Geometry 2



(c) Vehicle Geometry 2 SG



(d) Vehicle Geometry 3 SG

Figure 3.7: On-road flow turbulence conditions reported by each vehicle geometry

3. THE TIME-AVERAGED VEHICLE RESPONSE

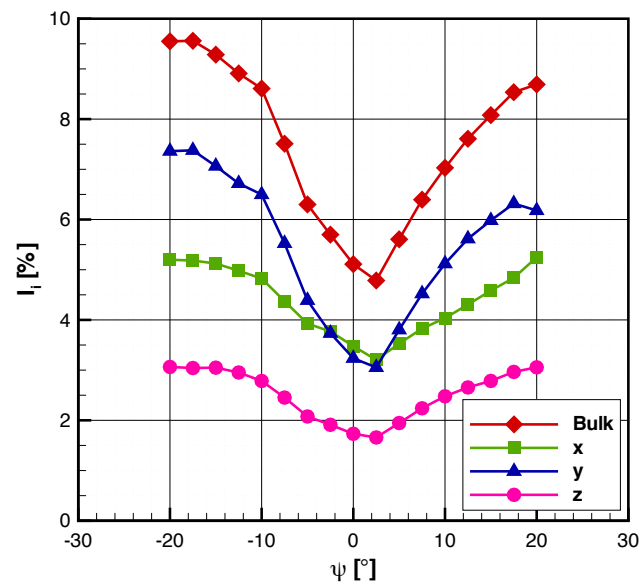


Figure 3.8: Relationship between yaw and turbulence intensity

dynamic yaw modes. The pseudo-random modes 3BL and 5AL aimed to simulate strong and moderate traffic conditions respectively, whilst the dynamic yaw modes 4D1.0, 4D0.4 and 4D0.2 opened the flaps in turn to continuously simulate gusts at 1, 0.4 and 0.2 seconds respectively. The probability distributions of yaw angle measured by the vehicle for these modes are shown in Figure 3.9. Since the three dynamic modes create the same yaw angle variation, with only the fluctuation frequency differentiating the modes, these modes are combined in a single plot in Figure 3.9(a). A normal distribution is also plotted, defined using the same mean and standard deviation as the measured data.

The distribution of yaw angles as generated by the TGS is narrower than that experienced on road, with the TGS yaw angles predominantly confined to a range of between $\pm 5^\circ$. Conversely, the yaw angles experienced on-road were regularly observed to exceed $\pm 10^\circ$. However, the shape of the distributions match those observed on-road, in that they show a stronger bias towards zero yaw than the normal distribution. The

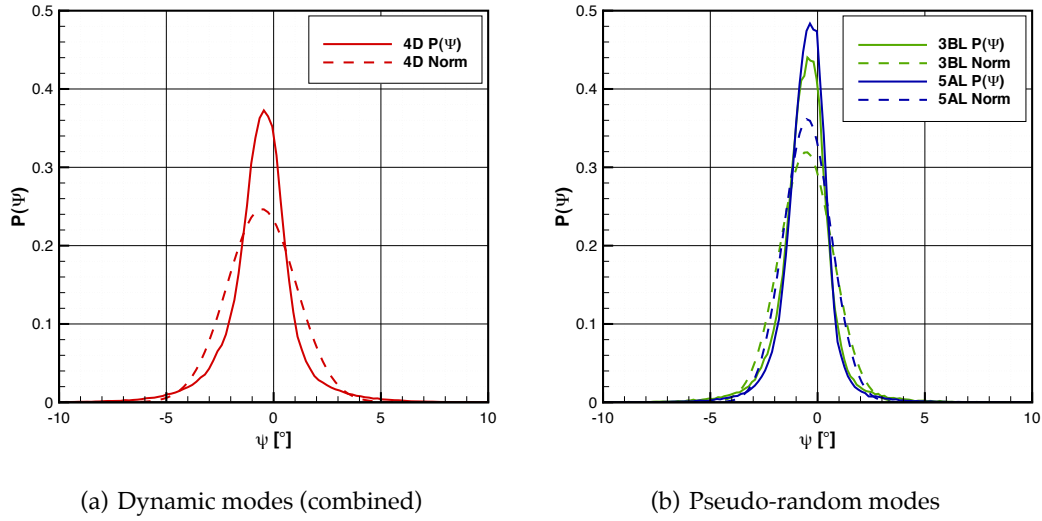


Figure 3.9: Probability distributions of yaw generated by the Pininfarina TGS

yaw angle range generated by the pseudo-random modes is also reduced when compared to that generated by the dynamic modes. The generated turbulence conditions of autocorrelation length scale and turbulence intensity are also plotted for the various TGS modes, for each of the component directions, in addition to a comparison with the zero-yaw, no TGS case. These results are shown in Figure 3.10, with the different symbol shapes differentiating the components, whilst the shading styles differentiating the various TGS modes.

Both the turbulence length scales and intensities are generally much lower than those experienced on-road. For all TGS modes, and also when the TGS is off, the length scales are consistently of the order of 1 metre. The exception to this is the lateral turbulence length scale being of the order of 4 metres. An explanation for this is that this may be a function of the nozzle width of the tunnel, with the probe measuring lateral jet instability. This is likely to be small, given the correspondingly small level of turbulence intensity. The length scales measured for the dynamic TGS modes are, whilst short, comparable to those measured by Lindener et al. (2007), as are the turbu-

3. THE TIME-AVERAGED VEHICLE RESPONSE

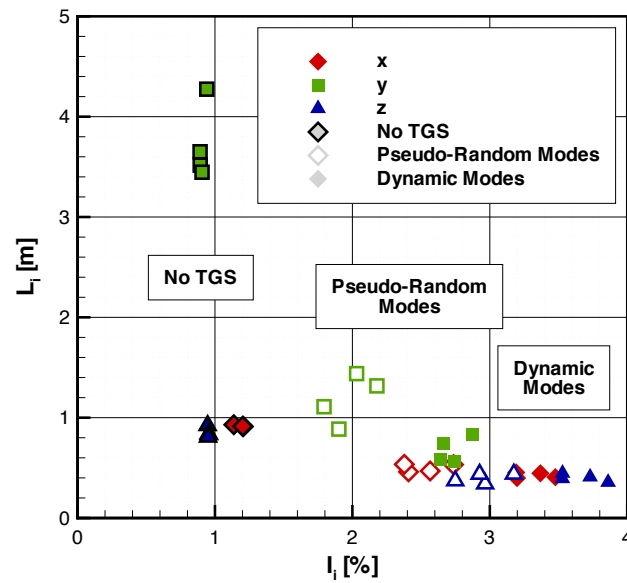


Figure 3.10: Turbulence conditions as generated by the Pininfarina TGS

lence intensities. However, for the pseudo-random modes, Lindener et al. measured length scales of up to 4 metres for the 3BL mode and up to 6 metres for the 5AL mode, compared to between 0.5 and 1.5 metres as shown by the figure.

These reduced values are likely to be due to the combination of turbulence generation and probe measurement location, with the turbulent fluctuations as generated by the vanes not fully reaching the height of the probe positioned on the roof. Lindener et al. used a probe mounted on the front bumper of the vehicle and therefore this may have captured the fluctuations more directly, before they traversed over the body of the vehicle to the roof. For consistency with on-road data, the same 4 second rolling window was used to calculate the turbulence properties. This is likely to affect the measurements, particularly for the 4D0.2 mode since the fluctuation frequency is 5 seconds. However, the similar length scales were measured for all of the dynamic modes, implying that this measurement is more likely to be affected by probe position rather than through data processing.

3.4 Cabin Noise

3.4.1 Subjective Cabin Noise Assessment

Subjective testing took place on a 38 s sample of on-road cabin noise data. The objective of this test was to determine how the noise inside the vehicle cabin was perceived and which acoustic measurement parameters were suited to capturing this psychoacoustic response. A temporally-resolved paired comparison technique was used, as described in Section 2.4.4.1, allowing subjective data to be collected with a resolution of 2 s.

A total of 11 respondents were asked to compare the series of sound samples and determine which they found the most *annoying*. Once every combination of pairs of samples had been compared by an individual, a normalised subjective index was generated for each sample. This summed the number of times a respondent had ranked that particular sample as more annoying and normalised this value such that it lay between 0 and 100. An index of 100 symbolised that the sample had been ranked as the most annoying in all comparisons, whilst 0 symbolised that the sample was never ranked as the more annoying of a pair.

This procedure was completed for each respondent with the subjective time histories averaged and confidence intervals calculated. This overall subjective response is shown by Figure 3.11(a), with the error bars defined by the 95% confidence intervals.

Whilst the confidence bands are relatively wide in places, the key features of the trace include a low level of annoyance at the beginning of the trace, rising to a wide peak at 12 s, before falling to a minimum at 20 s. The response then rises sharply after this point, before remaining at a moderate level. Two response quality indicators were used to assess each of the participants of the study. The coefficient of determination R^2 was assessed in correlating an individual's response to that of the overall average response, whilst the coefficient of consistence ζ was also used to assess how consistent

3. THE TIME-AVERAGED VEHICLE RESPONSE

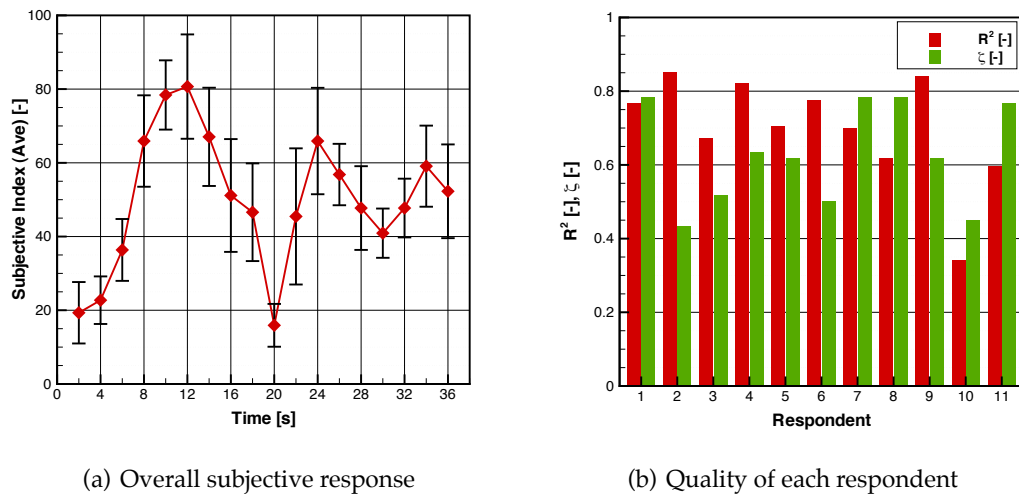


Figure 3.11: Generation of subjective index to cabin noise annoyance

the responses of an individual were in differentiating the various sound samples.

A high value of ζ indicates that a respondent could clearly discern differences between each of the samples and rank the samples in a consistent manner. High values of R^2 indicate that the responses of an individual to a particular sounds being annoying is consistent with the view held by the entire group. For instance, respondent 1 shows high levels of ζ and R^2 , indicating that they are good at differentiating between the sounds and that their view on an annoying sound is consistent with the group. Participant 2 shows consistency with the group, although a low consistency in differentiating the sounds. Participant 11 shows the opposite, in being able to differentiate the various sounds consistently, although has a generally different view on what they considered to make a sound annoying.

When asking the respondents to compare sounds based on cabin noise annoyance, it was up to the participants to determine which particular features of the noise they considered to be annoying. Whilst the cabin noise time history was selected owing to wind noise being clearly present, since the noise was collected on-road, a number of

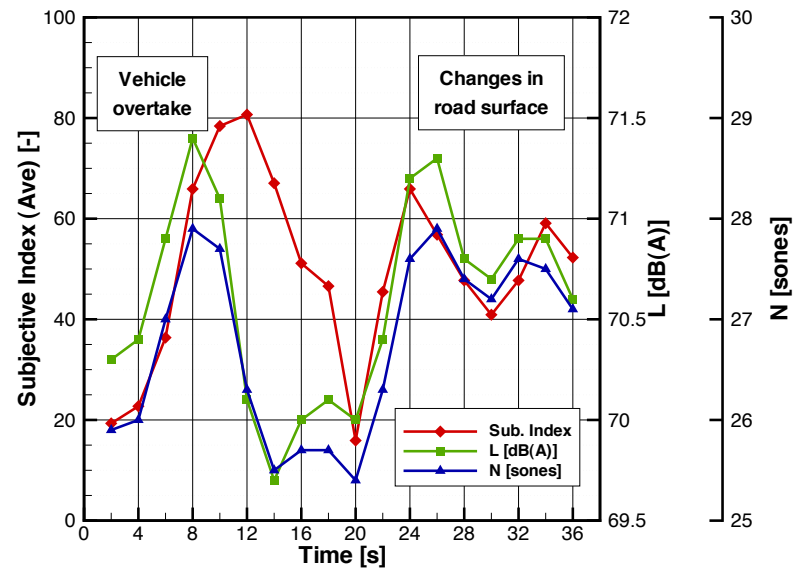
other noise events can also be heard. These sounds, in addition to wind noise, can be seen to affect the subjective response of the participants.

Figure 3.12 plots the subjective index against a number of acoustic and psychoacoustic parameters. Whilst the more formalised correlation coefficient R^2 may be useful in assessing correlation between the subjective response and the various psychoacoustic parameters, comparing the traces in time domain can provide information as to how the various metrics respond to different on-road events.

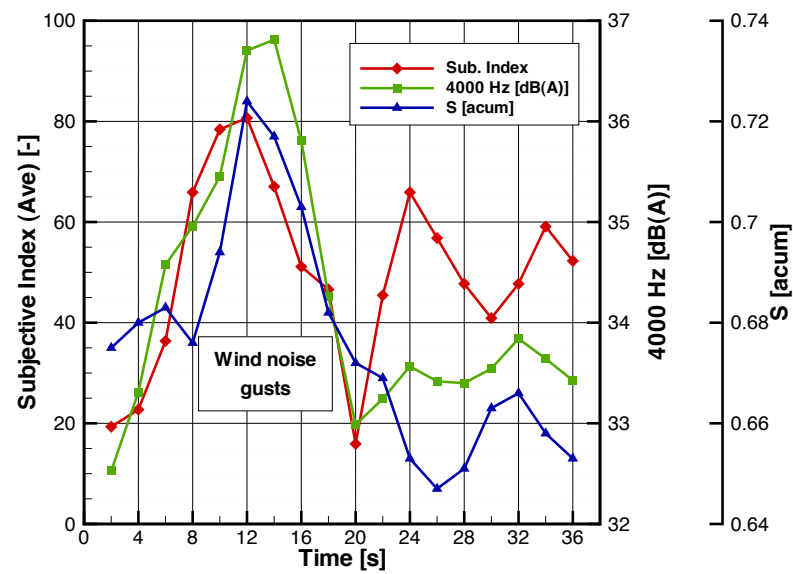
Figure 3.12(a) plots the subjective index against loudness N , measured in sones, and sound pressure level L , measured in dB(A). Firstly, this shows that there is a good correlation between A-weighted SPL and loudness for noise heard inside the cabin. These metrics also correlate well against the subjective index at the beginning of the time history and also at the end. The sound of a vehicle overtaking the test vehicle caused an increase in both loudness and the annoyance index. Later, the increase in both loudness and annoyance index occurred during a significant change in road surface, where a smoother surface changed to a coarser one.

Figure 3.12(b) shows the relationship between the subjective index and measurement parameters more focussed on the higher frequency content of the cabin noise. It has previously been shown that sharpness S and the 4 kHz third-octave band correlate well with wind noise, as shown by Helfer and Busch (1992) and Lindener et al. (2007) respectively. These parameters are shown against the subjective index and tend to correlate well with the increase in annoyance recorded between 4 and 20 s. The peaks of the higher-frequency content of the cabin noise occur after the peaks of loudness, and the higher frequency maximum occurs at a time where wind noise gusts are clearly heard. These gusts are likely to be caused by the turbulent wake of the passing vehicle. Later in the time history, the 4 kHz band shows little response to changes in the road surface, with sharpness showing some response, likely to be due to frequencies associated with road noise below 4 kHz.

3. THE TIME-AVERAGED VEHICLE RESPONSE



(a) SPL (L) and Loudness (N)



(b) 4 kHz third-octave band and Sharpness (S)

Figure 3.12: Assessment of subjective index against psychoacoustic metrics

In summary, a small-scale paired comparison was completed to assess the subjective response towards an example cabin noise time history, typical of that recorded on-road. This has shown that the 4 kHz third-octave band is a useful parameter to characterise a passenger's response to wind noise gusts, whilst remaining relatively independent of other typical on-road noise events such as changes in road surface. Loudness can also be approximated through the use of A-weighted SPL, giving an indication of the overall sound level in the cabin.

3.4.2 Steady Wind Tunnel

3.4.2.1 Relationship Between Cabin Noise and Flow Speed

Figure 3.13 shows the variation of cabin noise with tunnel speed, collected at the Pininfarina wind tunnel for the Geometry 1 vehicle, in an untaped configuration as would be on-road. The wind tunnel was nominally set at 100 km h^{-1} and increased up to 160 km h^{-1} in 10 km h^{-1} increments, with the vehicle in a zero-yaw ($\psi = 0^\circ$) position. Figure 3.13(a) shows the third-octave spectra variation with this increasing tunnel speed. The overall A-weighted sound pressure level at each tunnel speed was also determined and shown plotted against the probe-measured resultant flow speed (u_{Res}) in Figure 3.13(b).

The overall shape of the third-octave spectra are similar for each tunnel speed, indicating that an increase in flow speed leads to a broadband level increase without a change in pitch. Therefore fluctuations in the oncoming flow speed, such as those experienced on-road, lead to an amplitude modulation of the cabin noise. By investigating by how much the sound pressure level of the cabin noise varies with an increase in flow speed, information on the dominating source of the noise can be found. In Section 1.3.3, the three principle aeroacoustic noise generation mechanisms were introduced, the level of each scaling with a different power relationship for flow speed. By deter-

3. THE TIME-AVERAGED VEHICLE RESPONSE

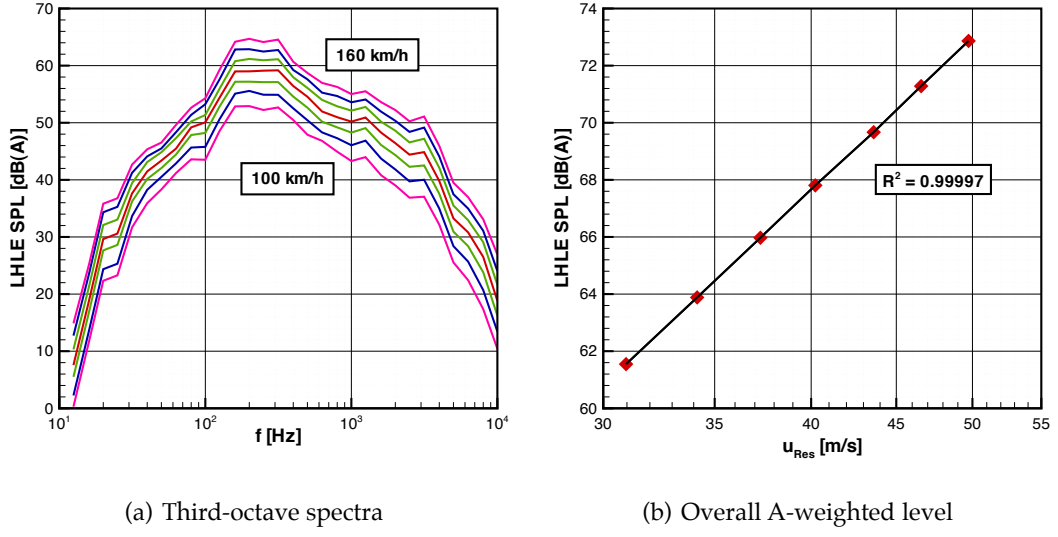


Figure 3.13: Steady AWT cabin noise at various wind tunnel speeds (Geometry 1)

mining this power relationship, the key aeroacoustic noise generation mechanism can be identified.

The logarithmic relationship between SPL and flow speed is shown in Figure 3.13(b). The probe resultant speed u_{Res} is plotted on a logarithmic axis, linearising this relationship. A regression line is shown plotted from this linearised data, with the coefficient of determination R^2 indicating strongly correlated data. Through the relationship:

$$\Delta \text{SPL} = 10 \log \left(\frac{u_{Res,2}}{u_{Res,1}} \right)^n \quad (3.3)$$

the power relationship between SPL and flow velocity can then be determined, giving the power relationship:

$$\text{SPL} \propto u^{5.50} \quad (3.4)$$

Monopole sound sources are proportional to flow speed raised to the fourth power, whilst dipole sources are proportional to flow speed raised to the sixth power. Monopole sources tend to result from leaks, for example, those in the door seals, whereas dipole

sources result from flow interacting with solid boundaries. Noise generated from body gaps can also generate noise which is proportional to flow speed raised to the fourth power, as described by Wickern and Brenberger (2009a). Near the A-pillar region, it is expected that dipole sound sources dominate and this is shown by Equation 3.4. Since the power relationship is less than six, this indicates that a minor component of the cabin noise is due to monopole sources, such as leaks or gaps in the body panels. Whilst there is no reason why this empirical power should be universal between different vehicles, this value is consistent with that determined by Lindener et al. (2007) in an investigation using multiple premium vehicles. This implies that the value may remain relatively constant between vehicles, particularly in the premium vehicle sector.

This power law relationship investigation can be extended to determine the dominating noise sources for each third-octave frequency band. Similar investigations have taken place by Wickern and Brenberger (2009b) and Peng (2007). The power parameter in this work is termed the *source index*, which provides information as to the nature of the aeroacoustic source. By undertaking a linear regression between the variables $10 \log u_{\text{Res}}$ and cabin SPL L , the source index n is equal to the regression slope coefficient. This process is undertaken for each third-octave band, with the results shown in Figure 3.14.

These results show that dipole sound sources dominate much of the frequency range. There is greater influence from monopole sources between 50–100 Hz and at frequencies greater than 5 kHz quadrupole sources dominate. Since pure dipoles have a source index of exactly 6, the range of source indices present implies that each frequency band is comprised of a range of different acoustic sources. Peng (2007) used a similar approach to determine the nature of external sound sources on different regions of a vehicle sideglass. The source behaviour determined in a regions close to the

3. THE TIME-AVERAGED VEHICLE RESPONSE

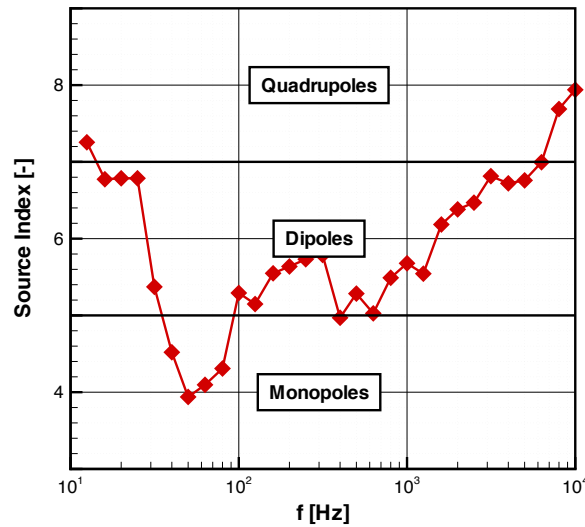


Figure 3.14: Nature of noise sources in AWT (Geometry 1)

A-pillar most closely resembles the results presented by Figure 3.14, indicating that the noise measured inside the cabin is strongly influenced by flow structures in this region.

The relationship between cabin noise and flow speed is revisited later in Section 3.4.3.1 where it is used to isolate the flow-speed dependent wind noise from the flow-speed independent road and powertrain noise measured on-road in the vehicle cabin.

3.4.2.2 Relationship Between Cabin Noise and Vehicle Geometry

The vehicle was tested in the Pininfarina wind tunnel to assess the relationship between cabin noise and the modifications made to the mirror between vehicle Geometries 1 and 2. To isolate the effect of this change from other noise sources, the same baseline vehicle was used with only the mirror assembly changing between tests. This reduced the impact of variations in cabin noise spectrum due to sealing and other differences that are difficult to control between vehicles.

Figure 3.15 plots cabin noise data for both outer ear positions: LHLE for the left

(passenger) position and RHRE for the right (driver) position. Each pair of bars compares the overall cabin noise for the Geometry 1 and Geometry 2 vehicle configurations. The cabin noise attributes assessed comprise overall SPL, loudness and articulation index.

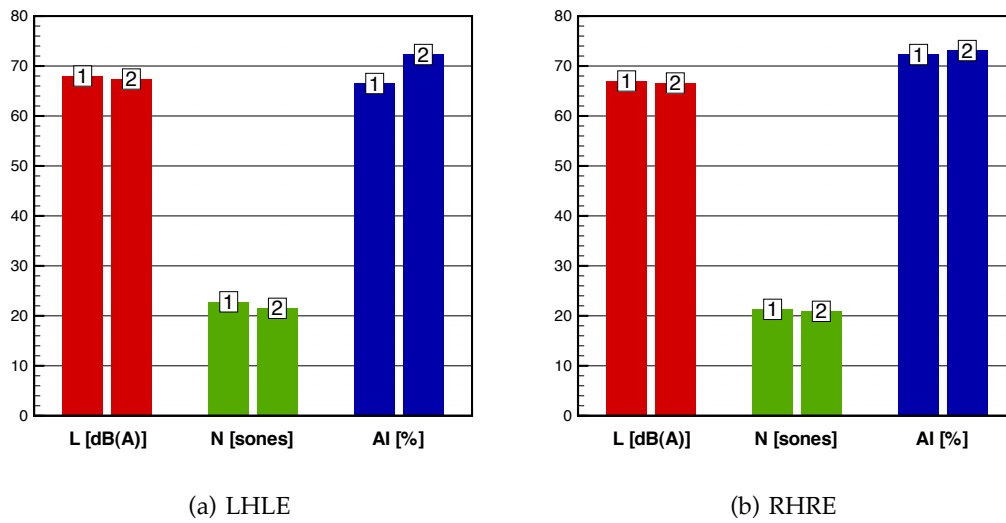


Figure 3.15: Steady AWT (Pininfarina) variation of cabin noise at $\psi = 0^\circ$ between Geometry 1 and 2

The LHLE position in Figure 3.15(a) shows an improved cabin noise performance for all attributes with the modification made to the mirror stem design. Both the SPL and loudness are reduced, with an increase in AI indicating reduced speech disruption. The Geometry 2 modification reduced the level of asymmetry between the LHLE and RHRE side of the vehicle, with the noise measured at both microphone positions similar for the Geometry 2 case.

On the passenger (LHLE) side of the vehicle, the channel between the mirror body and the side of the vehicle converges, leading to an increased flow speed in the vicinity of the sideglass. An increase in flow speed tends to lead to a corresponding increase in wind noise. The Geometry 2 modification increases the distance between the mirror

3. THE TIME-AVERAGED VEHICLE RESPONSE

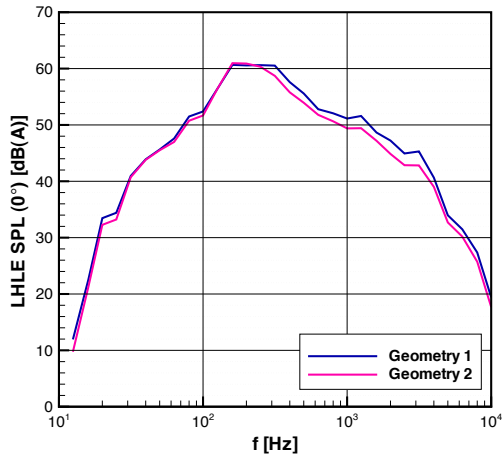
body and the vehicle compared to Geometry 1, reducing the effect of this convergence on flow speed.

The third-octave spectra of cabin noise for both vehicle geometries and microphone positions are shown in Figure 3.16. The spectra for the LHLE and RHRE positions are plotted in Figures 3.16(a) and 3.16(c). The difference between these spectra relative to the Geometry 1 configuration are plotted in Figures 3.16(b) and 3.16(d) for the LHLE and RHRE channels respectively, such that negative (green) changes in SPL indicate quieter performance in the Geometry 2 configuration.

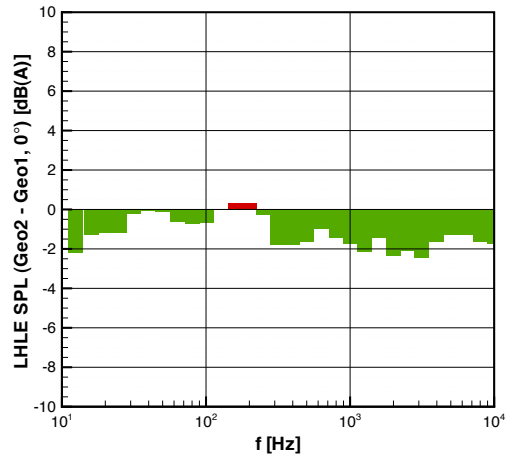
This again shows that the Geometry 2 modification over Geometry 1 primarily affects the LHLE side of the vehicle. This improvement is principally limited to frequencies about 300 Hz. Higher frequencies, especially those above 1000 Hz, are particularly important from a wind noise perspective in real-world conditions. Masking from other sources such as the tyres and engine is reduced in this frequency range, so that wind noise is more clearly discernible from the other vehicle sound sources. The geometry modifications are also shown to have little spectral effect on the RHRE position, with relatively minor variations limited to the higher and lower extremes of the frequency range.

3.4.2.3 Relationship Between Cabin Noise and Yaw Angle

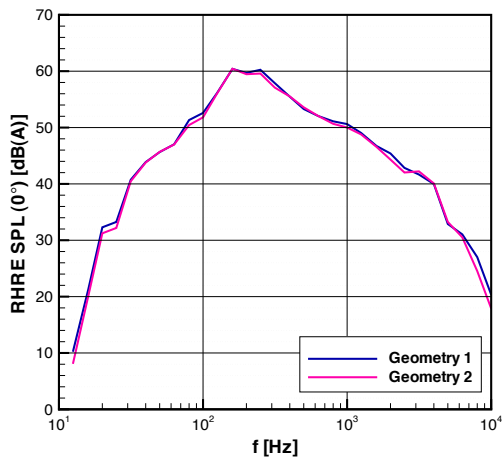
By turning the vehicle in the wind tunnel, the steady-state cabin noise response to yawed oncoming flow conditions can be assessed. Figure 3.17 shows how the overall SPL varies as the vehicle is yawed. Both mirror geometries are compared in Figures 3.17(a) and 3.17(b) respectively, with the cabin noise recorded by each of the acoustic head channels displayed. The vehicles were yawed using the wind tunnel turntable between $\psi_{\text{AWT}} = \pm 20^\circ$ in 2.5° increments, with the yaw values reported measured using the roof-mounted probe. Recall from Figures 2.18 and 2.19 that the left



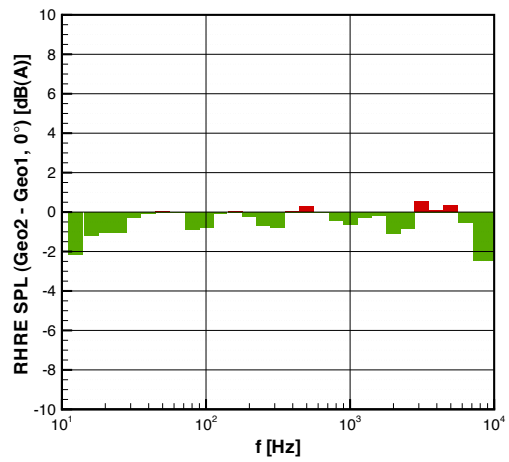
(a) Third octave spectra (LHLE)



(b) Difference in spectra (LHLE)



(c) Third octave spectra (RHRE)



(d) Difference in spectra (RHRE)

Figure 3.16: Steady AWT (Pininfarina) variation of third-octave cabin noise at $\psi = 0^\circ$ between Geometry 1 and 2

3. THE TIME-AVERAGED VEHICLE RESPONSE

side of the vehicle is in a leeward flow condition at negative yaw, with the right side in a leeward condition at positive yaw.

Leeward flow condition for cabin noise — *aide-memoire*:

On the **left** of the ψ -axis, the **left** head is leeward, whereas on the **right** of the ψ -axis, the **right** head is leeward.

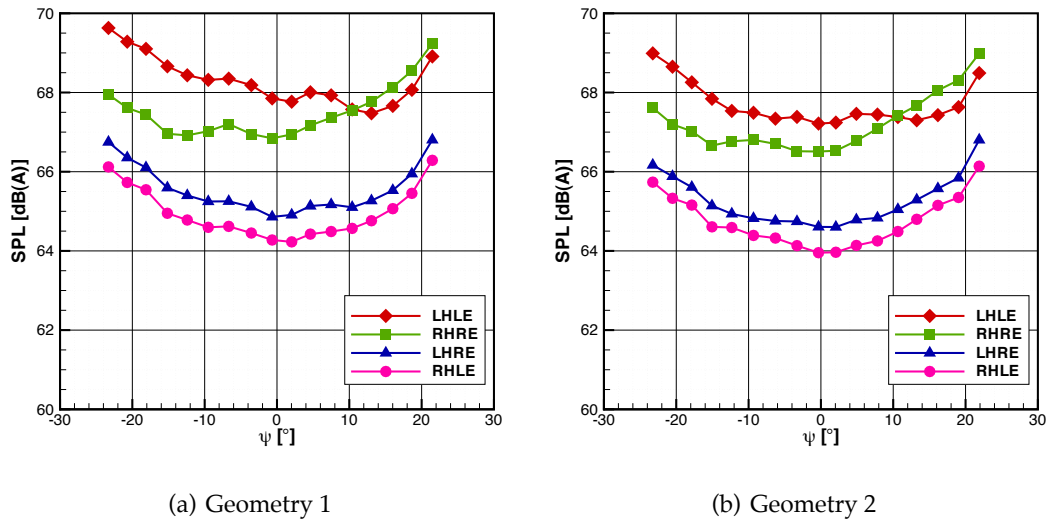


Figure 3.17: Steady AWT (Pininfarina) variation of overall SPL at yaw

At extremes of yaw angle, the overall level is greater owing to the noise generated by the separated flow structures, particularly those around the A-pillar. This is particularly the case for noise measured by the outer ears, which show an increase in SPL over that of the inner ears. Under leeward conditions there is greater flow separation, leading to an increase in size of the A-pillar vortex, as noted by Watkins (1999). This leads to a greater amount of aeroacoustic noise generation. This is identified by the data, where the ear adjacent to the leeward condition measures a greater SPL than the windward case. The inner ears show greater symmetry as they are positioned more

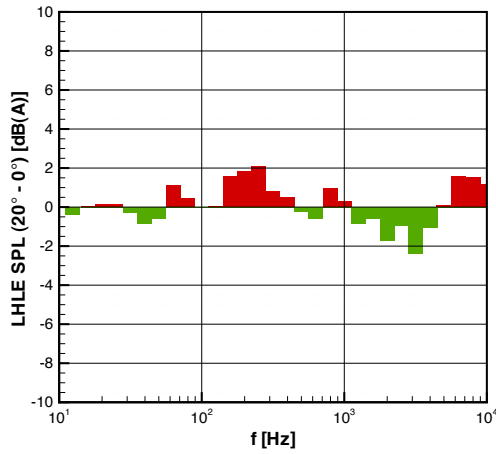
towards the centre of the cabin and thus measure the leeward separated noise increase from both sides of the vehicle.

As noted previously, the Geometry 1 vehicle has a higher cabin noise SPL than the Geometry 2 vehicle and this is the case throughout the yaw range. Also previously shown is that the mirror on the left side of the vehicle, adjacent to the LHLE channel, shows the greatest difference between Geometry 1 and Geometry 2. This difference is clearly shown in the LHLE channel between $\psi = \pm 10^\circ$ of Figure 3.17, where the Geometry 1 mirror shows a steeper decreasing trend of SPL with increasing yaw, whereas the Geometry 2 mirror shows a relatively flat response in SPL between this yaw range. This yaw sensitivity of the Geometry 1 mirror is likely to be heard by the vehicle occupants in the form of gustiness in windy conditions as the oncoming yaw angle fluctuates.

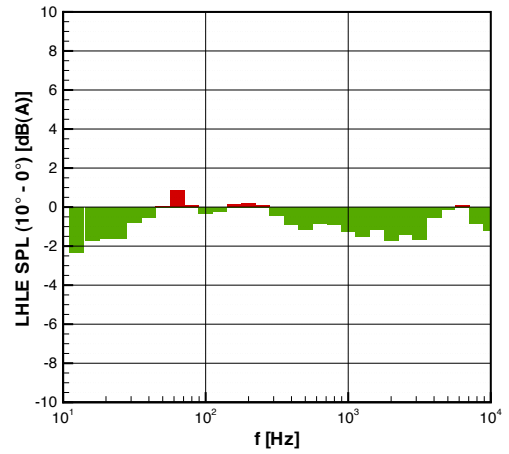
The change in the third-octave spectra at various turntable yaw angles from the zero-yaw case are shown in Figures 3.18 – 3.21. Whilst data were collected at 2.5° intervals, for clarity four key angles are displayed: $\psi_{AWT} = 20^\circ, 10^\circ, -10^\circ$ and -20° . To allow the same flow condition to be compared on each side of the vehicle, the data relating to these four angles are ordered with the two windward graphs appearing at the top, followed by the two leeward graphs at the bottom. Thus for the LHLE data, the top figures show the positive yaw angle condition, whilst for the RHRE data, the top figures show the negative yaw angle condition. Figures 3.18 and 3.19 show the variation in cabin noise spectra at yaw for the LHLE and RHRE channels respectively.

In the maximum leeward yaw case, both the LHLE (Figure 3.18(d)) and RHRE (Figure 3.19(d)) channels measure the largest noise increase, owing to the larger separated flow structures from the A-pillar and mirror generating greater amounts of noise. This primarily affects frequencies above 100 Hz. For the LHLE case, there is also an increase in the lower frequency range. This is likely to be a more general effect not isolated to

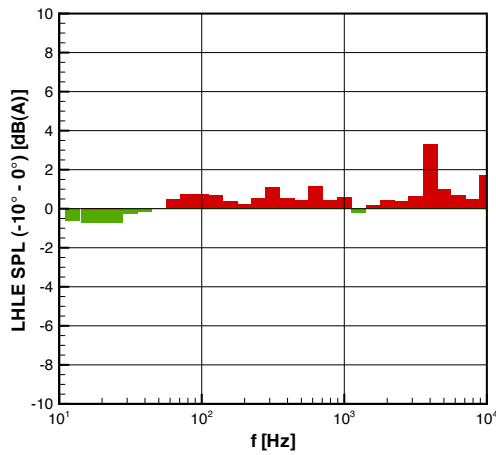
3. THE TIME-AVERAGED VEHICLE RESPONSE



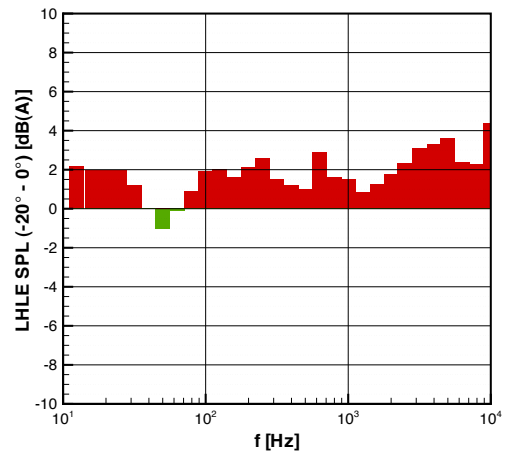
(a) $\psi = 20^\circ$ (windward condition)



(b) $\psi = 10^\circ$ (windward condition)

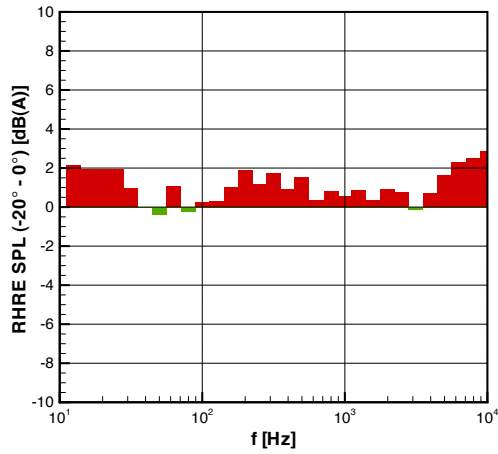


(c) $\psi = -10^\circ$ (leeward condition)

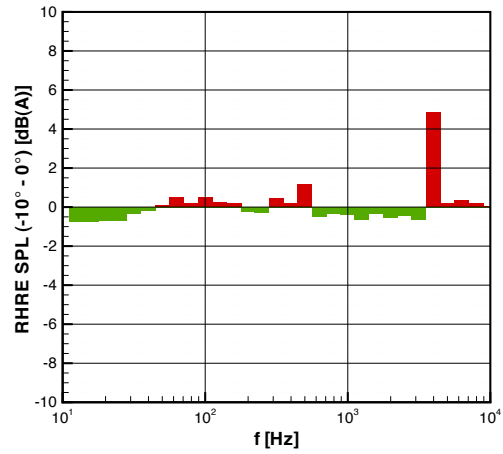


(d) $\psi = -20^\circ$ (leeward condition)

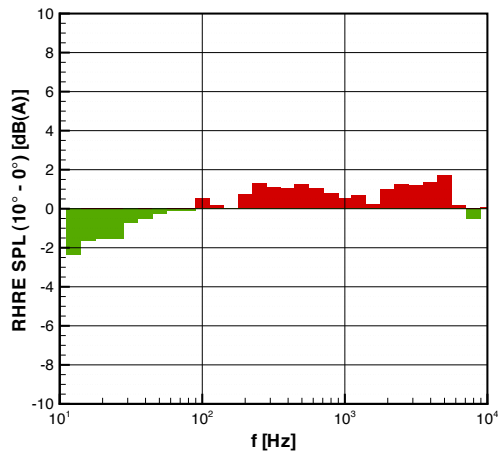
Figure 3.18: Steady AWT (Pininfarina) variation of LHLE cabin noise spectra at yaw (Geometry 1)



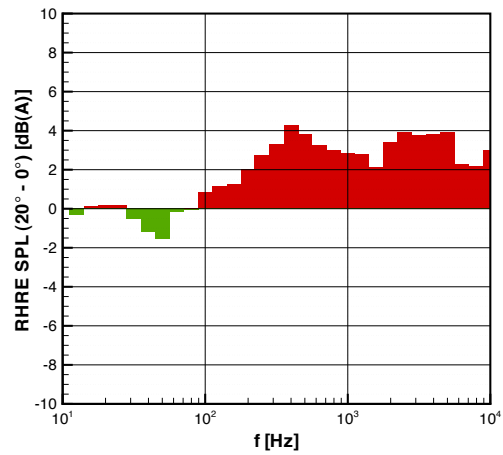
(a) $\psi = -20^\circ$ (windward condition)



(b) $\psi = -10^\circ$ (windward condition)



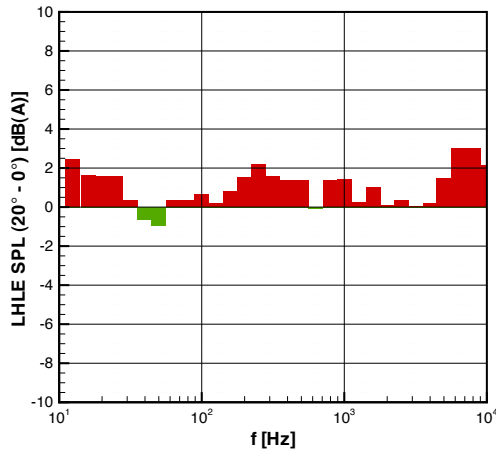
(c) $\psi = 10^\circ$ (leeward condition)



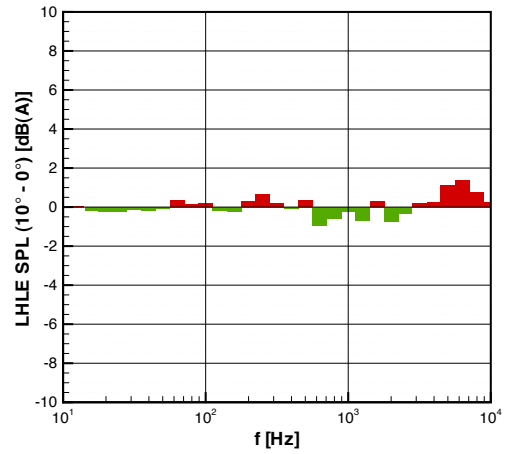
(d) $\psi = 20^\circ$ (leeward condition)

Figure 3.19: Steady AWT (Pininfarina) variation of RHRE cabin noise spectra at yaw (Geometry 1)

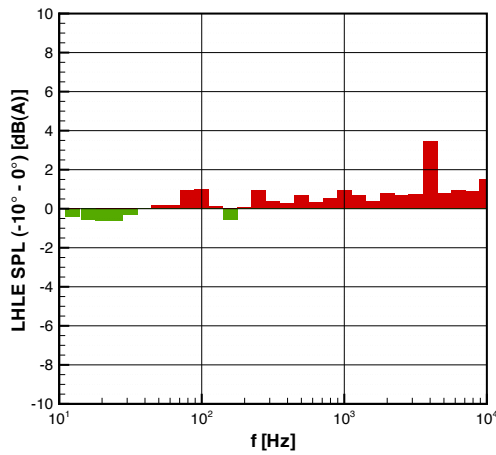
3. THE TIME-AVERAGED VEHICLE RESPONSE



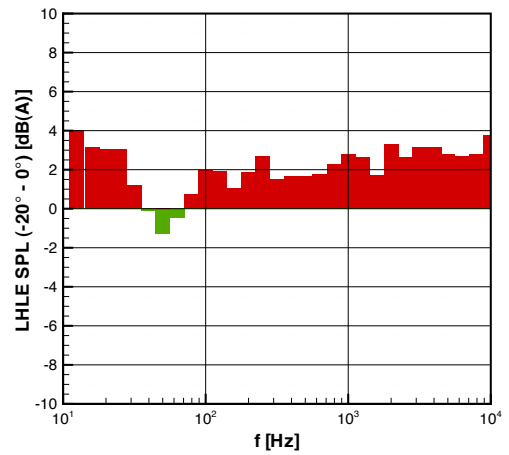
(a) $\psi = 20^\circ$ (windward condition)



(b) $\psi = 10^\circ$ (windward condition)

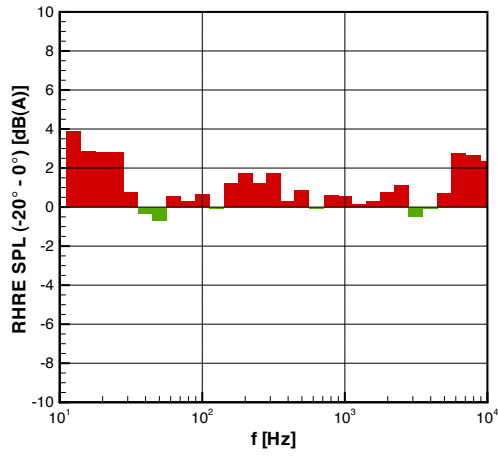


(c) $\psi = -10^\circ$ (leeward condition)

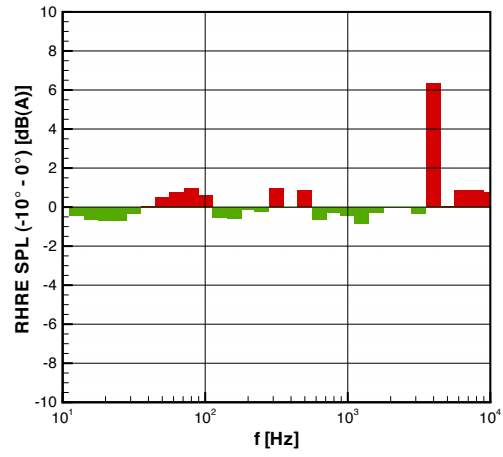


(d) $\psi = -20^\circ$ (leeward condition)

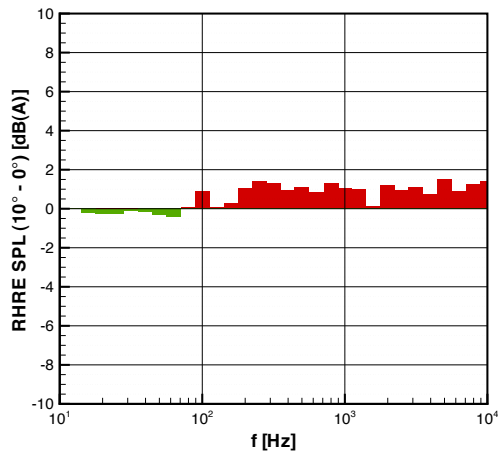
Figure 3.20: Steady AWT (Pininfarina) variation of LHLE cabin noise spectra at yaw (Geometry 2)



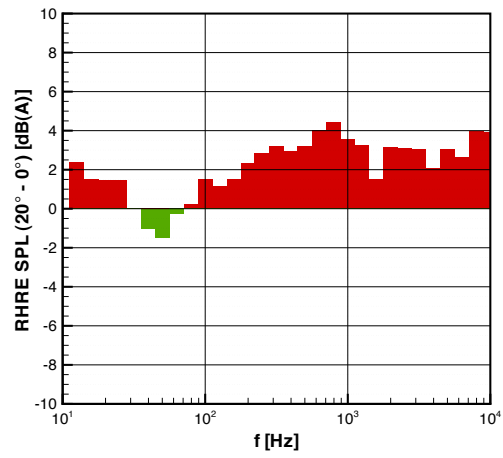
(a) $\psi = -20^\circ$ (windward condition)



(b) $\psi = -10^\circ$ (windward condition)



(c) $\psi = 10^\circ$ (leeward condition)



(d) $\psi = 20^\circ$ (leeward condition)

Figure 3.21: Steady AWT (Pininfarina) variation of RHRE cabin noise spectra at yaw (Geometry 2)

3. THE TIME-AVERAGED VEHICLE RESPONSE

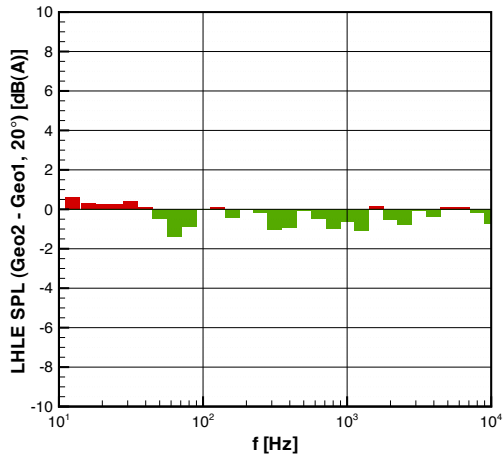
the sideglass, since it is also measured at the same yaw angle of $\psi_{\text{AWT}} = -20^\circ$ by the RHRE channel, as shown in Figure 3.19(a). The effect of the roof-mounted probe and mounting can also be seen at $\psi_{\text{AWT}} = -10^\circ$ for both channels, shown by Figure 3.18(c) for the LHLE channel and Figure 3.19(b) for the RHRE channel. This produces a clear tonal peak at 4 kHz, although this is not seen at $\psi_{\text{AWT}} = 10^\circ$.

The main difference in the Geometry 1 mirror between the left and right side of the vehicle occurs at the $\psi_{\text{AWT}} = 10^\circ$ windward condition. The mirror adjacent to the RHRE channel, shown by Figure 3.19(b), remains at a fairly constant level from zero-yaw, whereas the LHLE channel under the same flow conditions, shown by Figure 3.18(b), becomes quieter. As discussed earlier, this sensitivity of the mirror on the left side of the vehicle to yaw angle is likely to be perceived negatively by passengers.

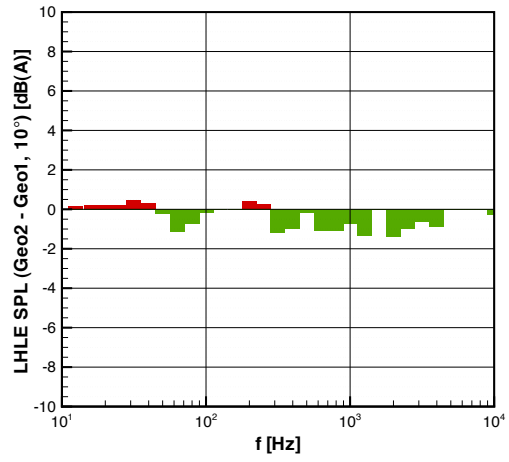
Figures 3.20 and 3.21 show the same yaw sensitivity data for the LHLE and RHRE channels respectively for the Geometry 2 mirror modification.

Previously it was shown that at zero-yaw, the Geometry 2 mirror modification only significantly affected the acoustic performance of the mirror on the left side of the vehicle, adjacent to the LHLE acoustic head channel. At yaw, this behaviour is the same, with only minor differences in spectra between the Geometry 1 and Geometry 2 mirror designs for the RHRE channel, as shown in Figures 3.19 and 3.21 respectively. The Geometry 2 mirror makes the largest difference at $\psi_{\text{AWT}} = 10^\circ$, as shown by Figure 3.20(b), with the spectra behaving much more similarly to the mirror on the opposite side of the vehicle, in that it is relatively insensitive to yaw angle changes. The overall affect of the Geometry 2 modification is that it reduces the yaw sensitivity to wind noise, making the aeroacoustic performance of the vehicle more symmetric to oncoming flow yaw angle. This is summarised by Figures 3.22 and 3.23, which compare the different mirror designs on the LHLE and RHRE channels respectively.

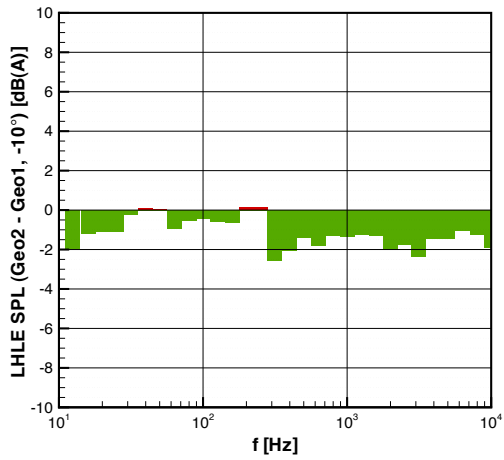
The Geometry 2 mirror results in a lower SPL at all yaw angles and (with some



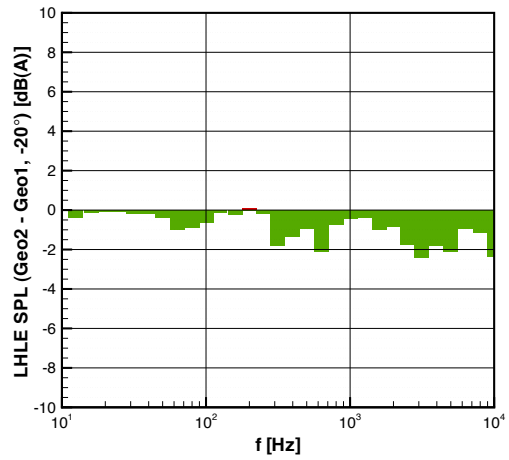
(a) $\psi = 20^\circ$ (windward condition)



(b) $\psi = 10^\circ$ (windward condition)



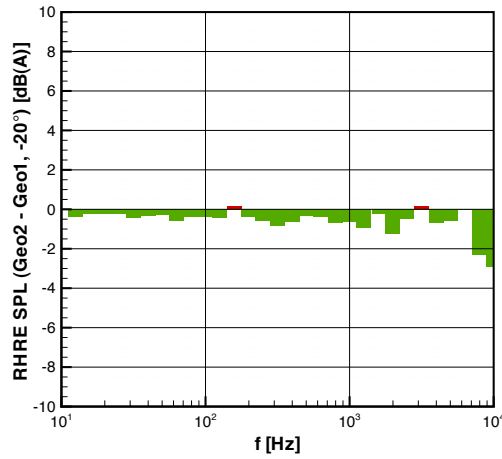
(c) $\psi = -10^\circ$ (leeward condition)



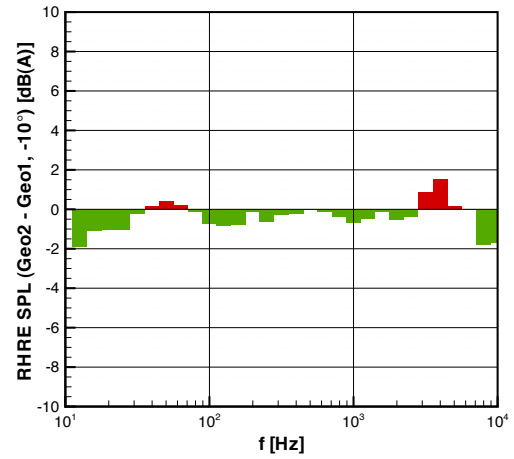
(d) $\psi = -20^\circ$ (leeward condition)

Figure 3.22: Steady AWT (Pininfarina) variation of LHLE cabin noise spectra at yaw between Geometry 1 and 2

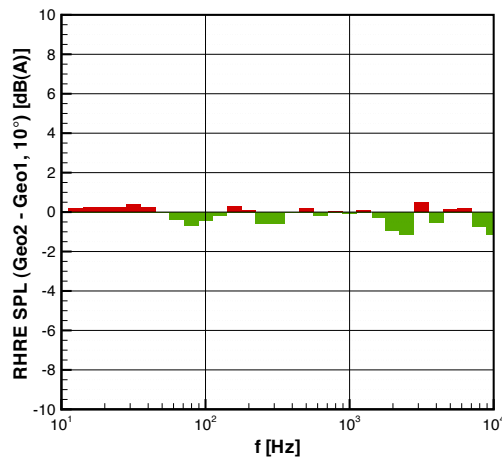
3. THE TIME-AVERAGED VEHICLE RESPONSE



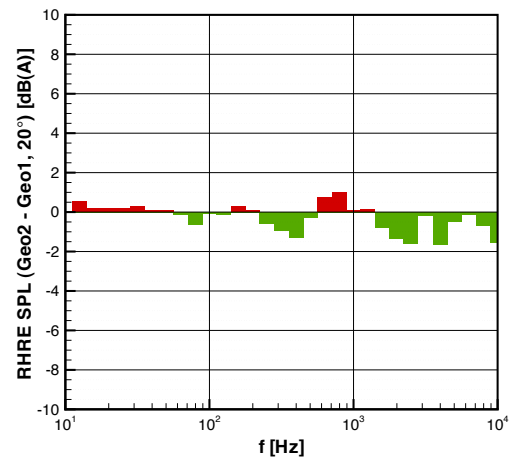
(a) $\psi = -20^\circ$ (windward condition)



(b) $\psi = -10^\circ$ (windward condition)



(c) $\psi = 10^\circ$ (leeward condition)



(d) $\psi = 20^\circ$ (leeward condition)

Figure 3.23: Steady AWT (Pininfarina) variation of RHRE cabin noise spectra at yaw between Geometry 1 and 2

minor exceptions) throughout the frequency range when compared to the Geometry 1 mirror. This reduction in SPL has a greater effect on the left side of the vehicle, on the passenger (LHLE) position, particularly under leeward wind conditions, as shown by Figures 3.22(c) and 3.22(d). The geometry modification has less of a significant effect under windward conditions and also on the driver (RHRE) position.

Overall, the Geometry 2 mirror modification has the effect of reducing both cabin noise and also the sensitivity of this noise to changes in oncoming flow yaw angle. For changes in yaw angle occurring at a fluctuation frequency sufficiently slow so that they can be considered quasi-steady, this will result in a reduction in cabin noise modulation due to unsteadiness in the oncoming flow direction.

3.4.3 On-Road

To measure the cabin noise response to the unsteady on-road flow conditions, both vehicle Geometries 1 and 2 were driven with an acoustic head positioned on the front passenger seat. This was on the left side of the vehicle and therefore only the LHLE and LHRE channels were recorded.

3.4.3.1 Relationship Between Cabin Noise and Flow Speed

To determine the relationship between cabin noise and flow speed on-road, the on-road data was processed using the bin-average technique. This isolated data points with a nominal zero yaw ($0^\circ \pm 1.25^\circ$) and divided this data into a series of bins based on resultant flow speed u_{Res} at intervals of 2 ms^{-1} . The result of this process used on a Geometry 1 vehicle is shown in Figure 3.24, along with the results obtained in the AWT with a similar Geometry 1 vehicle.

The regression line plotted through the on-road data shows a good correlation of $R^2 = 0.98$, indicating a strong relationship between SPL and flow speed. However, the

3. THE TIME-AVERAGED VEHICLE RESPONSE

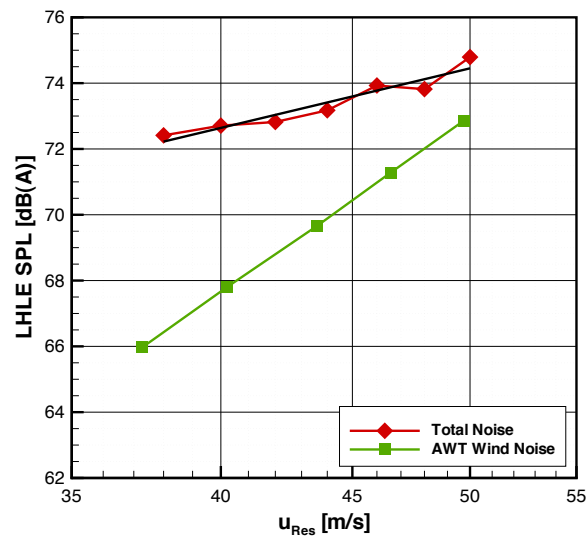


Figure 3.24: On-road and AWT overall SPL at various flow speeds (Geometry 1)

power relationship is much lower at 2.26 compared to that determined in the AWT of 5.5.

The on-road SPL plotted is the overall noise heard inside the cabin, which is not solely due to aeroacoustic sources as is the case with the AWT data, but also contains noise from the powertrain and tyres on the road. These additional effects are dependent on vehicle speed but independent of flow speed. Therefore, for a vehicle traveling at constant speed, these noise sources will be approximately constant. The addition of these constant components to the wind noise will have the effect of modifying the power relationship between overall cabin noise and flow speed, since the addition of decibel scales is non-linear.

The presence of these other noise sources within the on-road cabin noise makes it difficult to meaningfully compare it to the noise measured in the wind tunnel. However, based on the assumption that the other noise sources are independent of flow speed, a technique was developed to estimate the level of these other sources of noise. This allows the wind noise contribution to be isolated from these other sources, allow-

ing the wind noise SPL measured on-road to be compared against the SPL of the wind tunnel data.

A second assumption was also made; that the sensitivity of the wind noise SPL to flow speed remained the same on-road as it was in the wind tunnel. The combination of this known power relationship together with the constant SPL contribution allows the wind noise SPL to be estimated from the overall cabin noise. By adjusting the SPL of the constant SPL contribution, the sensitivity of the wind noise contribution to flow speed can be set to equal 5.50, the same as determined in the wind tunnel. The SPL of this constant contribution is the estimate of the level of other noise sources that make up the overall cabin noise. The level of the wind noise SPL can then be compared against the wind tunnel data.

Using the the summative relationship of SPL components, shown previously by Equation 1.6, the relationship between overall cabin noise level $L_{\text{Cabin}}(u)$ and the aeroacoustic $L_{\text{Wind}}(u)$ and other source contributions L_{Other} is:

$$L_{\text{Cabin}}(u) = 10 \log \left(10^{\left(\frac{L_{\text{Wind}}(u)}{10}\right)} + 10^{\left(\frac{L_{\text{Other}}}{10}\right)} \right) \quad (3.5)$$

This relationship can be rearranged such that the aeroacoustic SPL is shown as a function of the overall cabin noise and the other source contributions, as shown by:

$$L_{\text{Wind}}(u) = 10 \log \left(10^{\left(\frac{L_{\text{Cabin}}(u)}{10}\right)} - 10^{\left(\frac{L_{\text{Other}}}{10}\right)} \right) \quad (3.6)$$

As stated previously, the overall cabin noise and aeroacoustic sources are a function of flow speed u , whereas the other sources are assumed to remain constant. The increase in aerodynamic noise as the flow speed increases from u_1 to u_2 can be described as $\Delta L_{\text{Wind}}(u)$, which is the difference between $L_{\text{Wind}}(u_2)$ and $L_{\text{Wind}}(u_1)$. Equation 3.6 can be

3. THE TIME-AVERAGED VEHICLE RESPONSE

substituted into this to form the relationship:

$$\Delta L_{\text{Wind}}(u) = 10 \log \left(\frac{10^{\left(\frac{L_{\text{Cabin}}(u_2)}{10}\right)} - 10^{\left(\frac{L_{\text{Other}}}{10}\right)}}{10^{\left(\frac{L_{\text{Cabin}}(u_1)}{10}\right)} - 10^{\left(\frac{L_{\text{Other}}}{10}\right)}} \right) \quad (3.7)$$

There is also another solution to the aeroacoustic sound level increase, based on the assumption that the sensitivity of the wind noise SPL to flow speed remains the same on-road as it was in the wind tunnel:

$$\Delta L_{\text{Wind}}(u) = 10 \log \left(\frac{u_2}{u_1} \right)^{5.50} \quad (3.8)$$

This relationship can then be substituted into Equation 3.7 to solve for L_{Other} , using the on-road measured total cabin noise $L_{\text{Cabin}}(u)$ at two different flow speeds u_1 and u_2 . Once L_{Other} is known, the aeroacoustic contribution to the overall cabin noise $L_{\text{Wind}}(u)$ can be determined using the relationship in Equation 3.6.

The results of this process are shown in Figure 3.25, comparing the measured on-road total cabin noise and AWT data to the calculated contributions using this method.

The contribution of the other noise sources was found to be $L_{\text{Other}} = 71.4 \text{ dB(A)}$. This resulted in an on-road wind noise contribution that matches the wind tunnel data fairly well, with a slight under-estimate of the order of 1 dB(A). Therefore, through the use of a simple power relationship with speed (likely to be reasonably constant for many vehicles) and assuming that the other on-road noise sources are independent of flow speed, a good estimation of the wind noise component of the overall SPL heard inside the cabin can be found.

This process has been demonstrated for the overall SPL, however is equally applicable to individual third-octave frequency bands to build up an estimate of the spectral contributions to the overall cabin noise measured on-road. Using the source indices

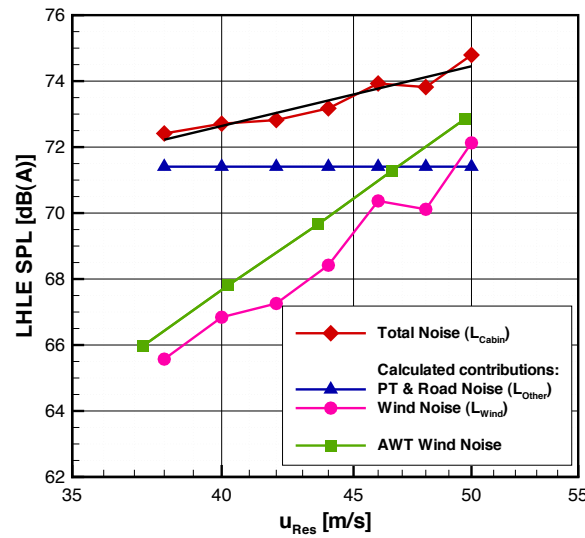


Figure 3.25: Calculated on-road sound source contributions (Geometry 1)

calculated for each third-octave band, previously presented by Figure 3.14, the same process was followed to determine the SPL of the constant noise sources for each corresponding band. The SPL of these other sources was then subtracted from the overall cabin noise, determined at the same nominal flow speed as measured in the wind tunnel, to determine the wind noise SPL at each frequency band. This was repeated for all third-octave bands to build up an entire wind noise contribution spectrum. The results of this process are shown in Figure 3.26, which also compares the calculated contributions to the wind noise measured in the AWT.

When comparing the calculated contributions from both the wind noise and other sources, the level of the wind noise dominates over the powertrain and road noise at frequencies above 2 kHz, as indicated on the figure. This cross-over point is consistent for both the calculated wind noise contribution and the wind noise as measured in the AWT. Indeed, at the higher frequencies above 1 kHz, the on-road calculated wind noise contribution closely follows that measured in the wind tunnel.

There is greater error between the measured and calculated wind noise contribu-

3. THE TIME-AVERAGED VEHICLE RESPONSE

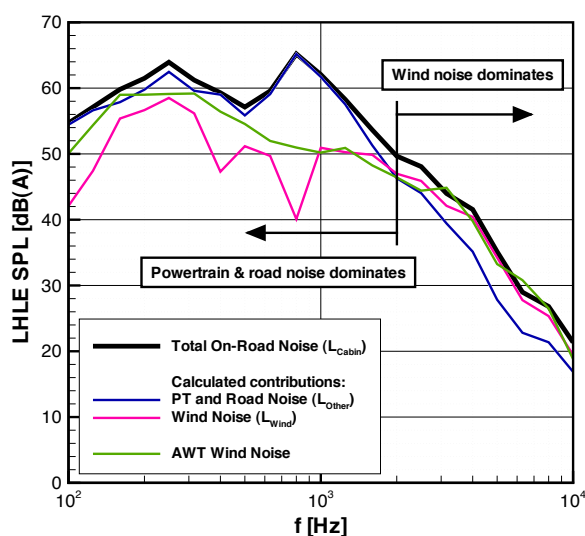


Figure 3.26: Calculated third-octave on-road sound source contributions (Geometry 1)

tions below 1 kHz, particularly when the other noise sources dominate the overall noise measured in the cabin. For instance at 800 Hz the road noise dominates, leading to the wind noise component being heavily masked, such that it is difficult to measure any relationship between the cabin noise and oncoming flow speed for this frequency band.

To investigate the frequencies in which there is the greatest error in calculating the wind noise contribution, the correlation between the level of each third-octave frequency band and flow speed was assessed using the coefficient of determination R^2 . Frequency bands with a high value of R^2 indicate that there is a strong relationship between flow speed and SPL, leading to an accurate determination of the wind noise contribution. Bands with a low value of R^2 indicate that there is a weak correlation between flow speed and SPL, implying that the cabin noise at this frequency is dominated by sound sources that are not affected by wind noise, such as the powertrain and tyres. The R^2 values for each third-octave frequency band are presented by Figure 3.27.

The figure shows that for frequencies above 2 kHz there is a very good correlation

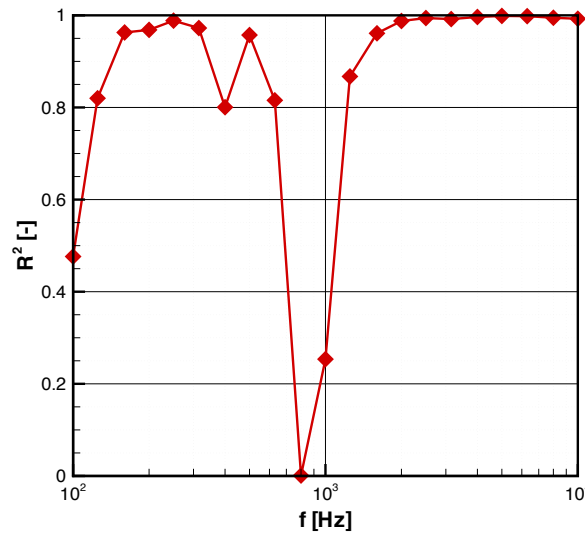


Figure 3.27: Calculated R^2 of third-octave on-road sound source contributions (Geometry 1)

between the overall on-road cabin noise and oncoming flow speed. This frequency range coincides with the range where the overall noise is dominated by wind noise, shown in Figure 3.26 and results in the strong correlation. There is also strong correlation between 200-300 Hz, which is another region where the wind noise dominates also shown in Figure 3.26, particularly at 250 Hz.

At frequencies where the cabin noise is completely dominated by road noise, such that there is no discernible relationship between flow speed and noise, including where the noise is constant for any flow speed, the R^2 value will be very close to zero. This is the case at 800 Hz. When the slope between the cabin noise and flow speed relationship is very low, there is a much greater error in determining the level of the wind noise contribution responsible for the relationship between overall noise and flow speed. This leads to errors in the spectral prediction of the wind noise contribution, particularly noticeable at 400 and 800 Hz in Figure 3.26. At frequencies where the relationship between flow speed and cabin noise is more defined, the technique is much more successful.

3. THE TIME-AVERAGED VEHICLE RESPONSE

Since the technique provides insight into the levels of wind and other road noise sources, it can also be used to determine at which flow speed the wind noise sources in a particular frequency band will start to dominate over the other noise sources. The criteria used was the flow speed required to increase the wind noise such that the SPL of the wind noise contribution matched that of the constant contribution from the other on-road sources. The speed required for each third-octave band is shown in Figure 3.28.

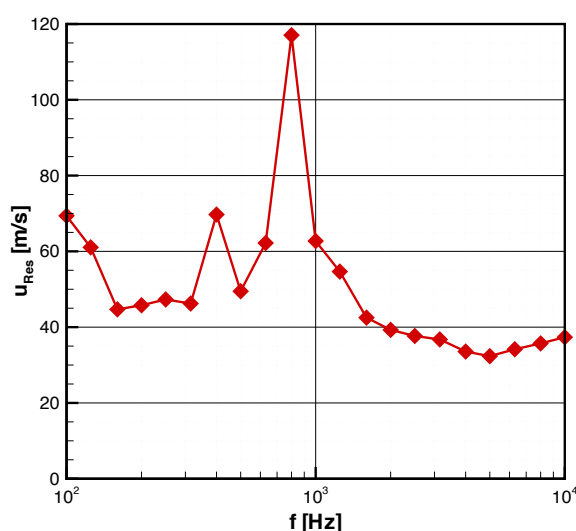


Figure 3.28: Flow speed when third-octave wind noise dominates other sound source contributions (Geometry 1)

The nominal oncoming flow speed measured by the probe for the vehicle travelling at 130 km h^{-1} was approximately 40 ms^{-1} . This shows that at this vehicle speed, the overall cabin noise is dominated by aeroacoustic sources through a large proportion of the frequency range. At frequencies dominated by the road-noise sources, such as those centred around 800 Hz, these other sources are so strong that they will always dominate, since the flow speed required for the wind noise to dominate is unrealistically high.

Therefore, using the dipole dominated flow speed relationships for cabin noise determined in the wind tunnel, the relative contributions of both the wind noise and other on-road sound sources to the overall noise measured on-road was determined. This has shown that for this particular vehicle travelling at 130 km h^{-1} , the wind noise dominates the cabin noise at frequencies above 2 kHz, with the road noise particularly dominating at frequencies centred at 800 Hz.

3.4.3.2 Relationship Between Cabin Noise and Yaw Angle

As when assessing the relationship between cabin noise and flow speed on-road, the bin-average technique was used with the bins based on yaw angle at constant flow speed. The yaw angle bins ranged between $\pm 20^\circ$ and divided the data into 2.5° intervals, the same resolution used when yawing the vehicle on the turntable in the AWT. The flow speed interval was set to equal the nominal flow speed measured in the Pininfarina wind tunnel at zero yaw, with a range of $\pm 1 \text{ ms}^{-1}$.

Figure 3.29 shows the results of this process for overall A-weighted SPL for both Geometry 1 and Geometry 2 vehicles. Both acoustic head channels are displayed: the LHLE channel adjacent to the passenger sideglass and the LHRE channel facing the centre of the vehicle. Also displayed are the equivalent overall SPL data obtained in the Pininfarina AWT. Note that the range of yaw angles reported for each of the vehicle geometries differs, since the range of yaw angles experienced by each vehicle on-road is a function of the conditions at the time of testing. In cases where insufficient data points existed to generate a reliable average, these points were excluded.

The overall SPL data collected in the AWT and on-road differ considerably and this is the case for both vehicle geometries. In the AWT, the measured cabin noise is solely due to aerodynamic sources, whereas on-road the cabin noise is comprised not just of wind noise, but also sources such as the powertrain and tyres. As shown previously by Figure 3.26, the road noise in particular dominates parts of the spectrum.

3. THE TIME-AVERAGED VEHICLE RESPONSE

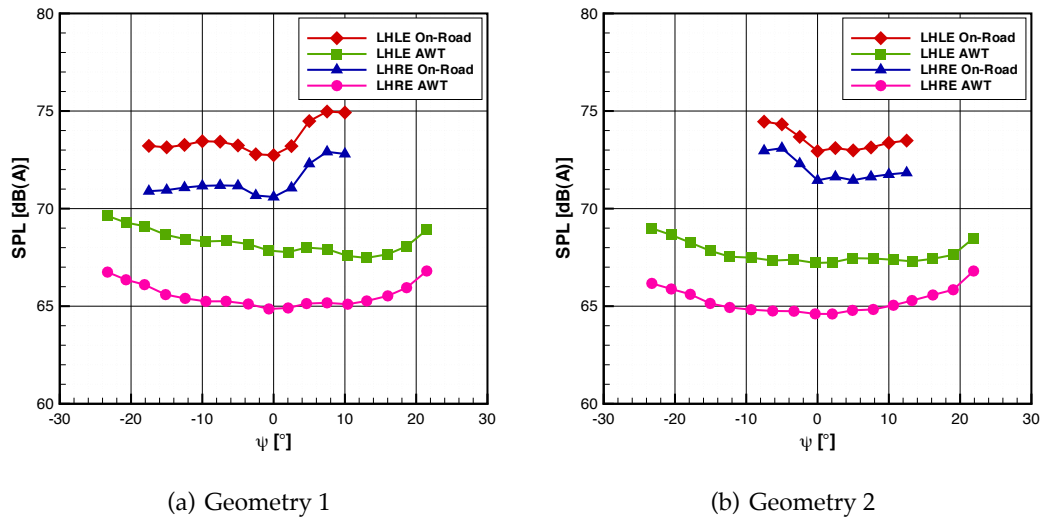


Figure 3.29: On-road variation of overall SPL with yaw, compared with equivalent AWT data

This will have a large effect in changing the overall SPL measured between the two environments.

In addition to the differences in measured data between the AWT and on-road, there are also significant differences between the behaviour of the two vehicle geometries, with vehicle Geometry 1, shown in Figure 3.29(a) seemingly behaving in the opposite fashion to vehicle Geometry 2, shown in Figure 3.29(b). If these differences were due to aeroacoustic sources this result would be very significant, since the behaviour in the wind tunnel between the geometries is very similar. Since the sensitivity of on-road cabin noise to changes in yaw angle is the same for both the outer LHLE and inner LHRE channels, it is unlikely that the origin of the noise changes is in the sideglass region, so is likely to be due to less directional sources, such as road noise. To investigate this further, the overall SPL and 800 Hz third-octave band are shown in Figure 3.30, for the LHLE channel for both vehicle geometries. This band has previously been shown to be dominated by road noise sources.

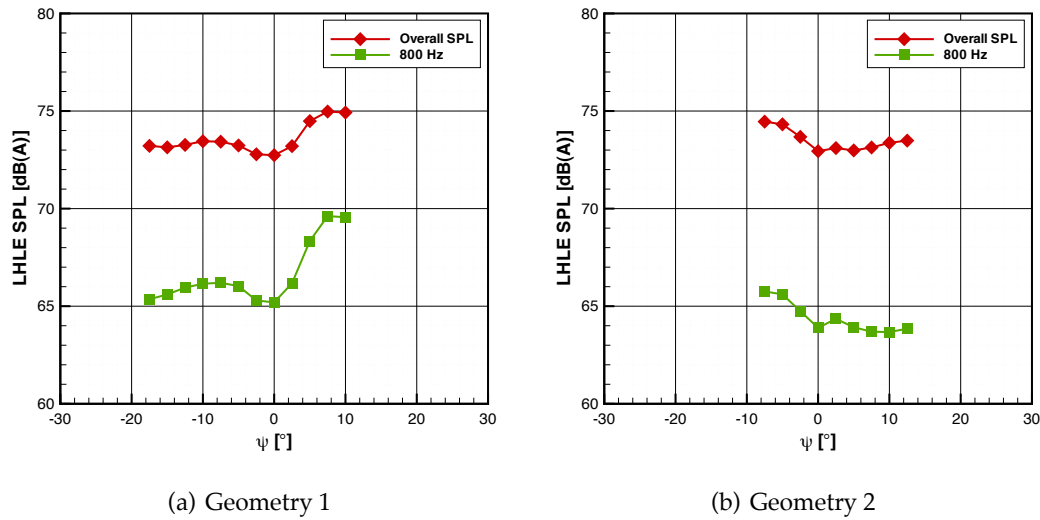


Figure 3.30: On-road variation of overall and 800 Hz third-octave band SPL with yaw

The 800 Hz third-octave band in both vehicle geometry cases follows the yaw behaviour of the overall SPL very closely. This indicates that the overall SPL is dominated by road noise sources, such that apparent variations in road noise with yaw dominate the overall yaw sensitivity. Since there is likely to be no relationship between the level of road noise and oncoming flow yaw angle, the relationships shown in Figure 3.30 are an artefact solely of the road surface and the oncoming flow conditions at the time of on-road data collection. This is the reason as to why there is no consistent relationship between the two vehicle geometries.

Figure 3.31 compares the higher frequency cabin noise behaviour with yaw angle. These frequencies were shown in Figure 3.27 to correlate well with variations in the oncoming flow, indicating that they are dominated by aeroacoustic sources.

The relationship between the 2, 4 and 8 kHz bands and yaw angle between the two vehicle geometries is much more similar, in particular showing the expected increase in level under leeward conditions, where the LHLE channel is adjacent to a region of flow separation. As is consistent with data from the AWT, the Geometry 2 vehicle

3. THE TIME-AVERAGED VEHICLE RESPONSE

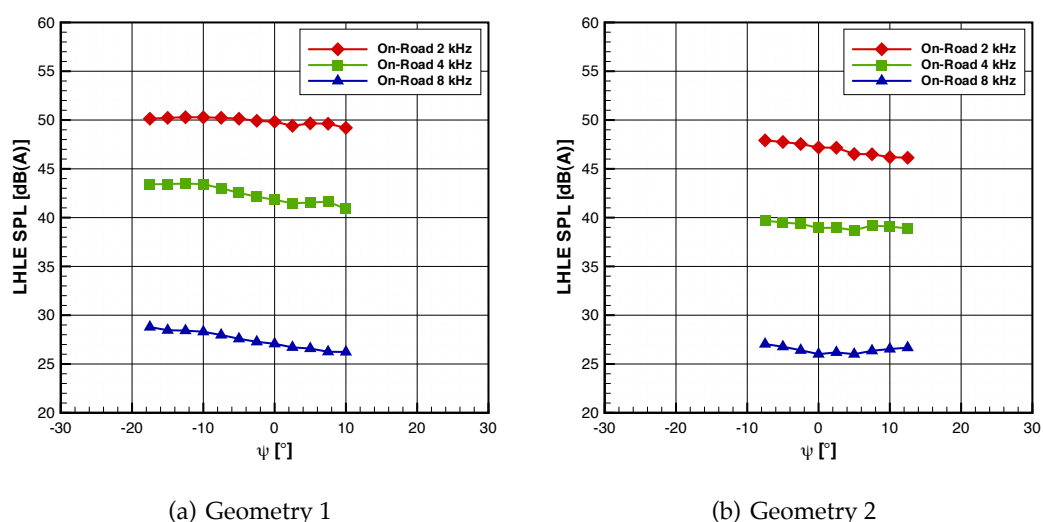


Figure 3.31: On-road variation of 2, 4 and 8 kHz third-octave bands with yaw

modification results in a reduction in the overall level compared to the Geometry 1 vehicle. Figure 3.32 presents the equivalent data as measured in the AWT for both geometries and the same third-octave channels.

The sensitivity of the higher-frequency third-octave bands to oncoming flow yaw angle is similar between the AWT data and that obtained on-road, with both traces showing approximately the same characteristics. The main exception to this is the tonal 4 kHz probe mount noise, clearly detected in the AWT at both $\pm 10^\circ$, whilst not being so clear in the on-road data. This is likely to be due to increased levels of small-scale, free-stream turbulence disrupting the tonal flow structures shed from the mount. The relative difference in level between the vehicle geometries in the two environments is also captured. On-road, the 2 kHz band is approximately 2–3 dB(A) greater than that measured in the AWT, indicating that road noise sources have some effect in this spectral band. Indeed, from Figure 3.26, at 2 kHz the estimated wind noise and road noise contributions to the overall cabin noise are equal. The combination of two equal-SPL sources will result in a 3 dB increase owing to logarithmic addition and

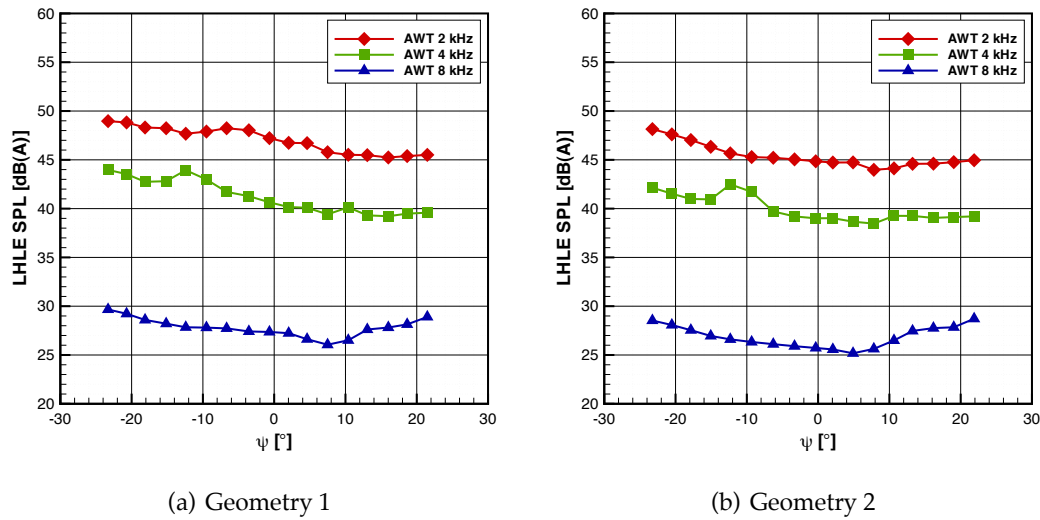


Figure 3.32: AWT (Pininfarina) variation of 2, 4 and 8 kHz third-octave bands with yaw

therefore it is likely that additional road noise sources are likely to be the cause of this offset. For the 4 and 8 kHz bands where other on-road noise sources are low, this offset is much smaller with the AWT able to predict both the overall characteristics and levels of the wind noise response of the cabin noise to yaw with accuracy.

3.4.4 Unsteady Wind Tunnel

The effect of increased levels of oncoming flow unsteadiness on cabin noise was assessed in the Pininfarina wind tunnel, using the TGS with the vehicle at zero yaw. Figure 3.33 shows cabin noise data collected for both Geometry 1 and 2 vehicles for each of the TGS modes used. In addition, these values are compared with the cabin noise of the vehicle without the TGS in operation.

For both the LHLE and RHRE channels, adjacent to the passenger and driver's sideglass respectively, it is shown that by increasing the levels of unsteadiness in the oncoming flow, the cabin noise SPL is raised by approximately 1 dB(A), with little

3. THE TIME-AVERAGED VEHICLE RESPONSE

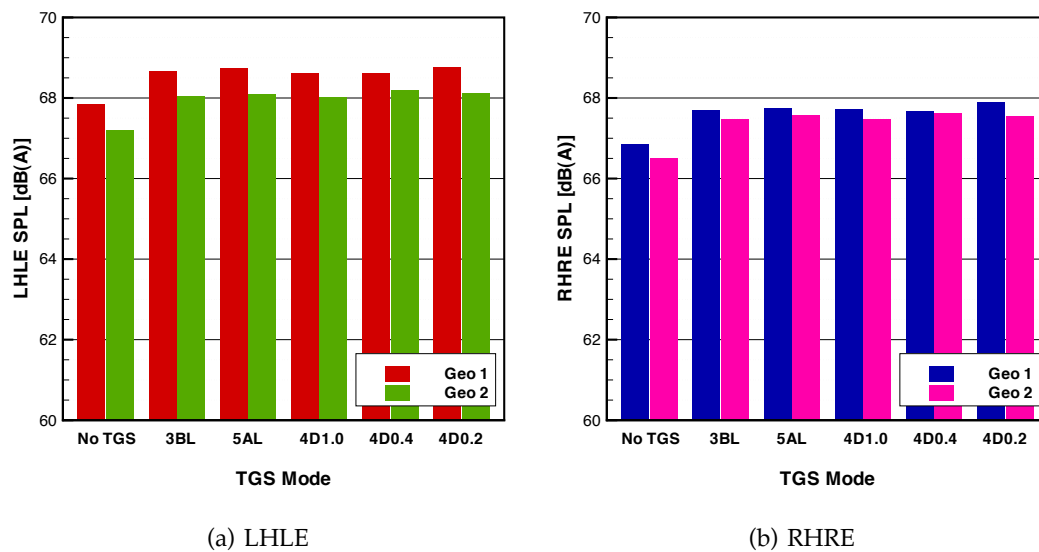


Figure 3.33: Variation in cabin noise between vehicle geometries at various TGS modes

differentiation between each of the TGS modes. It should be noted from Cogotti (2008) that the operational noise of the TGS is well below the background noise of the wind tunnel. As previously shown, the Geometry 2 modification to the mirrors results in a reduced cabin noise, and this is also the case when the TGS was in operation. The mirror modification reduces the cabin noise more significantly on the passenger side of the vehicle, again as previously shown. There is an equal cabin noise increase on both sides of the vehicle when the TGS is in operation.

Figure 3.34 shows the equivalent data for the 4 kHz third-octave band, which is dominated by wind noise sources on-road.

The 4 kHz third-octave band follows the same general behaviour of the overall SPL, with the increased levels unsteadiness generated by the TGS producing increased noise. However, for the 4 kHz band, this increase is less significant, leading to an increase of less than 0.5 dB(A) for the LHLE channel, with the RHRE channel recording a slightly larger increase. This increase due to oncoming unsteadiness is fairly insignificant compared to the large difference between the two vehicle geometries. Overall

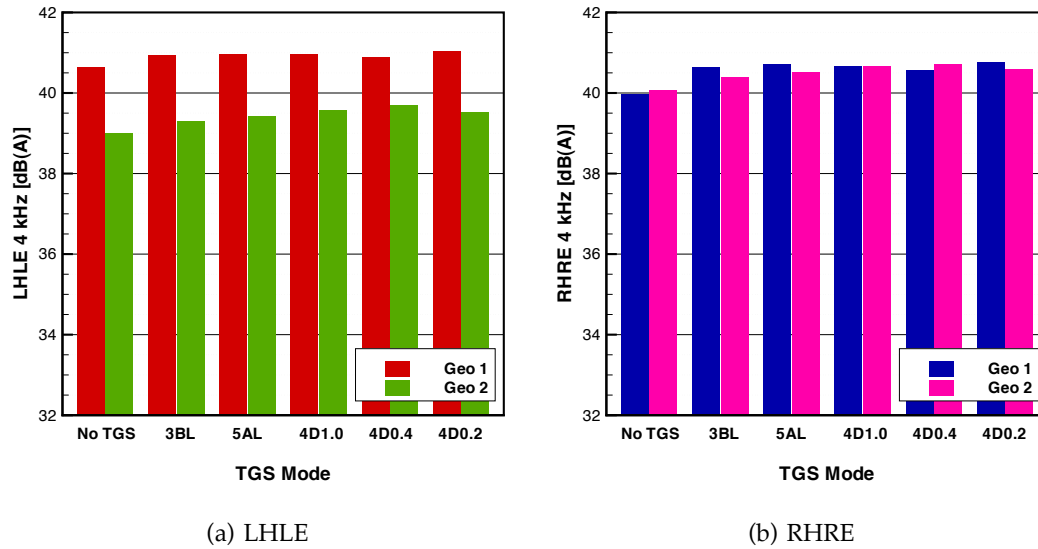


Figure 3.34: Variation in 4 kHz cabin noise between vehicle geometries at various TGS modes

the different in cabin noise performance between the two mirror designs is the same with or without the TGS under zero-yaw conditions.

3.5 Surface Pressures

As introduced in Section 2.2.1.3, a total of ten flush-mounted pressure tappings were installed on the driver's sideglass, on the right side of the vehicle. Vehicle Geometries 1 SG and 2 SG were assessed in the Pininfarina AWT, whilst vehicle Geometries 2 SG and 3 SG were assessed on-road. Since each of these vehicles had the instrumented perspex sideglass in place, hence the SG suffix, no cabin noise measurements were recorded. The pressure tappings were spread over the sideglass, covering regions nearest the mirror wake, the A-pillar vortex and the vortex reattachment region, as shown previously by Figure 2.8(a)

3. THE TIME-AVERAGED VEHICLE RESPONSE

3.5.1 Relationship with Flow Speed

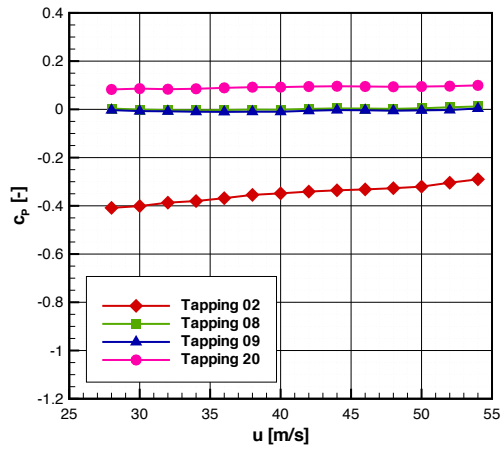
The measured surface pressures were reported as the non-dimensional coefficient, c_p , originally defined by Equation 2.9 and repeated here for convenience:

$$c_p = \frac{P_{\text{Tap}} - P_{\text{Probe Static}}}{P_{\text{Probe Dynamic}}} = \frac{P_{\text{Tap}} - P_{\text{Probe Static}}}{\frac{1}{2}\rho u^2} \quad (3.9)$$

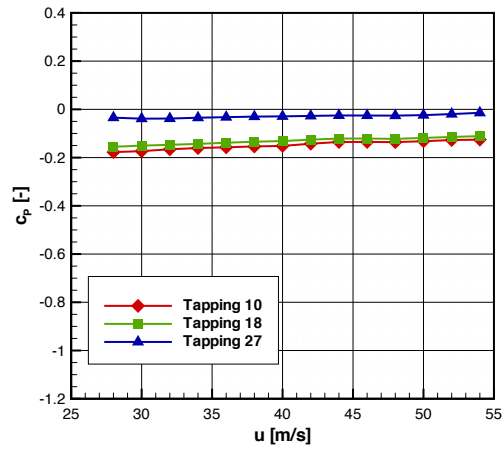
Defining c_p using the oncoming flow conditions measured by the probe allows consistency when comparing the different environments of the AWT and on-road, rather than using definitions based on nominal wind tunnel speed or vehicle speed. By normalising the measured pressures using probe-reported dynamic pressure, the sideglass surface pressure coefficients should be independent of oncoming flow speed fluctuations, whilst remaining a function of the variation in flow structures around the sideglass region due to yaw variations.

To assess the independence of c_p to oncoming flow speed, the same bin-averaged technique was used as that used to assess the relationship between cabin noise and oncoming flow speed for on-road data. The same bin boundaries were used, each at $\psi = 0 \pm 1.25^\circ$ and u increasing in steps of 2 ms^{-1} . The variation of the surface pressure coefficients with flow speed are presented by Figure 3.35, divided into the three main sideglass regions.

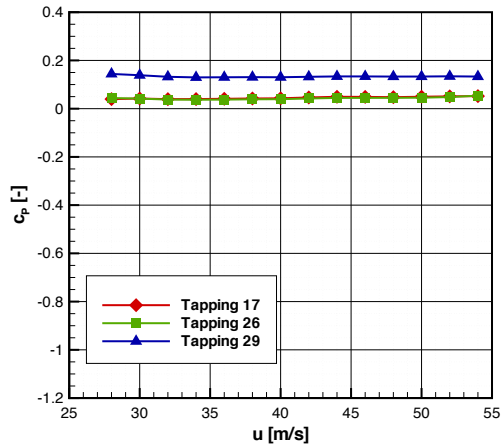
The c_p values for the pressure tapplings in the vortex reattachment and mirror wake regions remain constant with an increase in flow speed. The exception to this is Tapping 2 which, like the tapplings positioned in the the A-pillar vortex region, have a slightly reduced value of c_p at slower flow speeds. This implies that at higher Reynolds' numbers, the proportional flow speed increase in the vicinity of these tapplings is not as great than at lower Reynolds' numbers. These four tapplings are all located close to the A-pillar vortex and this is likely to be the main cause of the non-linear behaviour.



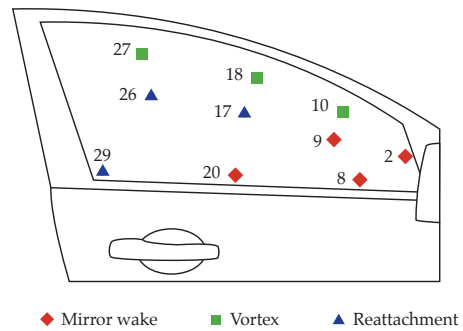
(a) Mirror wake region



(b) A-pillar vortex region



(c) Vortex reattachment region



(d) Tapping locations

Figure 3.35: On-road sideglass pressure characteristics (Geometry 2)

3. THE TIME-AVERAGED VEHICLE RESPONSE

3.5.2 Steady Wind Tunnel

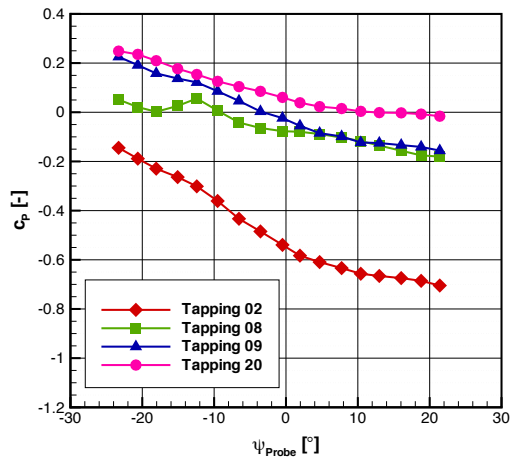
The variations in the surface pressure profile with yaw angle were assessed in the Pininfarina AWT for both vehicle Geometries 1 SG and 2 SG. Since the pressure tappings were installed on the right sideglass, adjacent to the driver, positive oncoming yaw angles result in a leeward flow condition on the sideglass whereas negative yaw angles are windward. The results obtained for a Geometry 1 SG vehicle are shown in Figure 3.36, separated into the various sideglass flow regions.

In the mirror wake region, shown by Figure 3.36(a), each of the tappings exhibit relatively similar behaviour with changes in yaw angle, with a gradually decreasing c_p with increasing yaw angle in the windward flow condition ($\psi < 0^\circ$). There is an anomaly in this behaviour with Tapping 8, with an increase from this trend at approximately -10° . Under positive yaw, leeward, conditions the c_p traces tend to flatten, indicative of a region of flow separation.

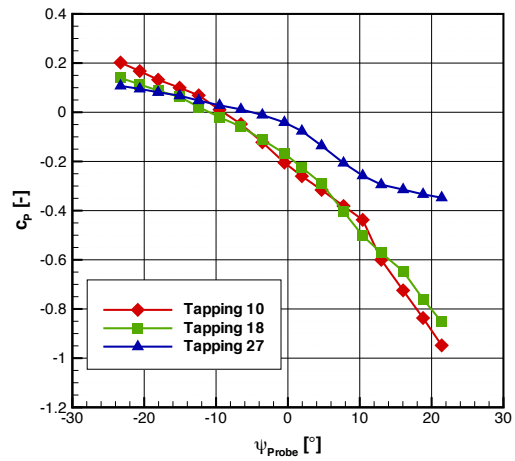
The A-pillar vortex region also shows a continuously decreasing c_p at increasing yaw angles, transcending both windward and leeward flow conditions, shown by Figure 3.36(b). The non-linearity of this decrease is consistent with that of longitudinal vortices, such as the non-linear vortex lift generated by delta wings.

The tappings further away from the mirror wake and A-pillar, as shown by Figure 3.36(d), behave in a largely similar manner to the tappings in the mirror wake region, however with a reduced sensitivity to changes in yaw. Again, there is a decrease in c_p with increasing yaw angle under windward conditions with a separation plateau evident under windward conditions. In an exception to this, Tapping 26 continues to decrease non-linearly at higher yaw angles, exhibiting behaviour similar to that of the A-pillar vortex region, indicative of a change of size and position of the A-pillar vortex.

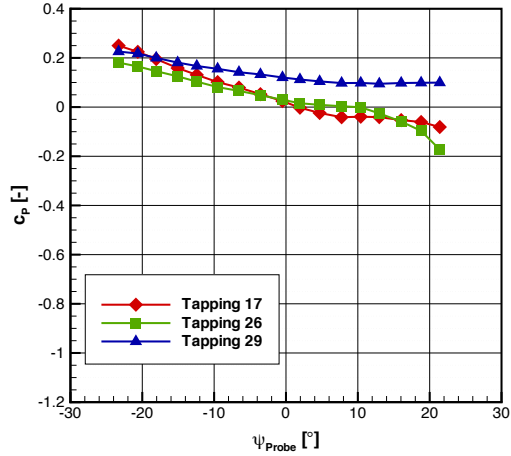
Figure 3.37 shows similar data for the Geometry 2 SG vehicle modification. To recap, this modification involved changing the mirror stem such that it was more aerodynamically profiled and the mirror was positioned further from the sideglass.



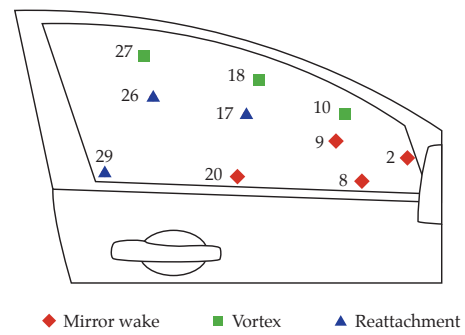
(a) Mirror wake region



(b) A-pillar vortex region



(c) Vortex reattachment region



(d) Tapping locations

Figure 3.36: Steady AWT sideglass pressure characteristics (Geometry 1 SG)

3. THE TIME-AVERAGED VEHICLE RESPONSE

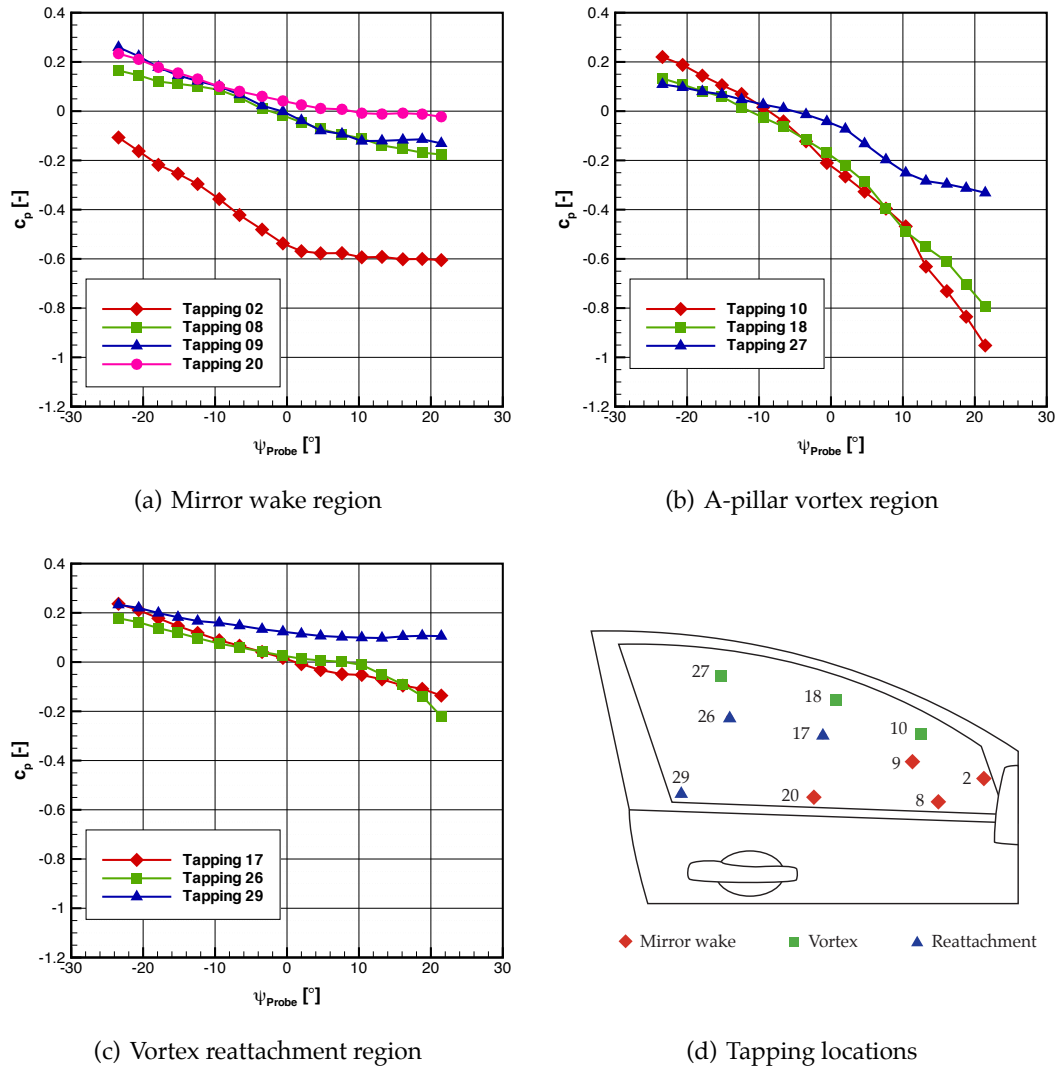


Figure 3.37: Steady AWT sideglass pressure characteristics (Geometry 2 SG)

The main differences between the two vehicle geometries are confined to the mirror wake region, perhaps unsurprisingly since the geometry modification was limited to this region. Other regions nearer the A-pillar and further downstream of the mirrors are largely unaffected by the geometry modification, such that the dominating A-pillar geometry is unchanged.

For the mirror wake region in Figure 3.37(a), the flow separation plateaux under leeward, positive yaw conditions are much more clearly defined than for the Geometry 1 vehicle. This transition from a decreasing c_p to a constant value is clearly defined for Tappings 2, 9 and 20. This behaviour implies that the flow structures in this region remain constant when changes in yaw angle occur at higher positive yaw values. This yaw insensitivity may result in a reduced fluctuation in noise on the sideglass as the oncoming yaw angle changes when compared to the Geometry 1 SG vehicle.

The most significant difference in surface pressure between the two vehicle geometries is at Tapping 8, which for the Geometry 2 SG vehicle closely follows the behaviour of Tapping 9. The discontinuity at $\psi = -10^\circ$ for the Geometry 1 SG vehicle is also not present. This measurement position is closest to the mirror stem and therefore the change in behaviour is likely to be driven by changes to this geometry.

3.5.3 On-Road

On-road, the sideglass instrumented vehicle Geometries 2 SG and 3 SG were assessed. The bin-averaged technique was again adopted based on the same yaw intervals as in the AWT. Whilst the c_p values are relatively independent of flow speed, as shown by Figure 3.35, to minimise any flow speed effects the bins were also defined at constant speed, as with the on-road cabin noise yaw assessment. Figure 3.38 shows the variation in c_p with oncoming flow yaw angle for the Geometry 2 SG vehicle on-road.

In the mirror region, as shown in Figure 3.38(a), the behaviour of Tapping 2 on-

3. THE TIME-AVERAGED VEHICLE RESPONSE

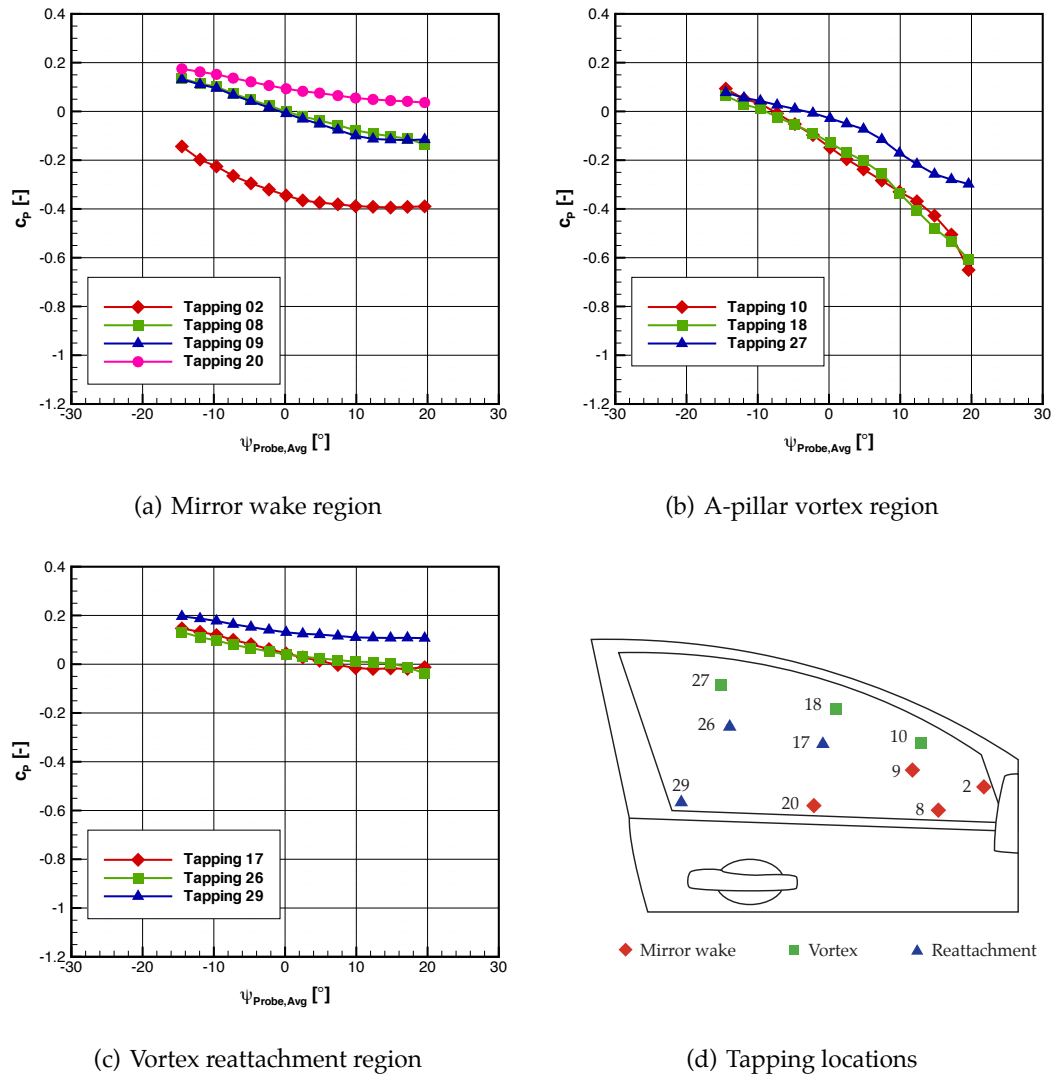


Figure 3.38: On-road sideglass pressure characteristics (Geometry 2 SG)

road is similar to that as measured in the AWT, but with an overall c_p offset increase of 0.2. Tapping 20 also has an offset, although this is smaller at approximately 0.1. Tappings 8 and 9 show very similar behaviour to the wind tunnel, indicating that the offsets are likely to be a real phenomenon as opposed to an systematic shift across all of the measurements. The decrease in the Tapping 2 characteristic with increasing yaw is more gradual than measured in the AWT, with the transition to the sharp separation plateau not as clearly defined. However, the c_p reaches a constant value at a similar yaw angle, indicating that the separation occurs under similar flow conditions.

The on-road A-pillar vortex region characteristics show a strong correlation with the AWT, with small differences occurring at the extremes of yaw angle, particularly shown by Tapping 10. In the AWT this characteristic falls away more sharply with increasing yaw angle above 10° , whereas on-road this decrease is more smooth. Likewise the on-road characteristics in the vortex reattachment region are smoother, particularly the steeper decrease in c_p at higher yaw angles is not as clearly identified as in the AWT. Tapping 29, exhibiting more flat behaviour, is indistinguishable from the data obtained in the AWT.

The bin-averaging process accepts on-road data with a yaw angle within a specified range, with the bin width used throughout this thesis of $\Delta\psi = 2.5^\circ$. This width was chosen since it allowed consecutive bins resulting in an overall yaw resolution equal to that measured in the AWT. Narrower bins would lead to fewer data being used in the averaging process and thus increasing variation, whilst wider bins would reduce the yaw resolution of the measured characteristics. In the AWT no bin-averaging process is required and therefore the results presented are those obtained at discrete 2.5° intervals. On-road, the data is continuous with the bin-averaging process averaging 2.5° windows of this data. This inevitably leads to a degree of ‘smoothing,’ resulting in sharp changes of c_p being less defined on-road than in the AWT.

3. THE TIME-AVERAGED VEHICLE RESPONSE

Vehicle Geometry 3 SG was also assessed on-road, with this geometry nominally the same as Geometry 2 SG with the rear edge of the bonnet raised by approximately 15 mm. Full details were given in Section 2.3.1.2. The aim of the modification was to reduce the amount of wiper structure visible above the bonnet line and reduce the size of any trailing flow structures that can impinge on the windscreen, resulting in noise. This data is shown in Figure 3.39.

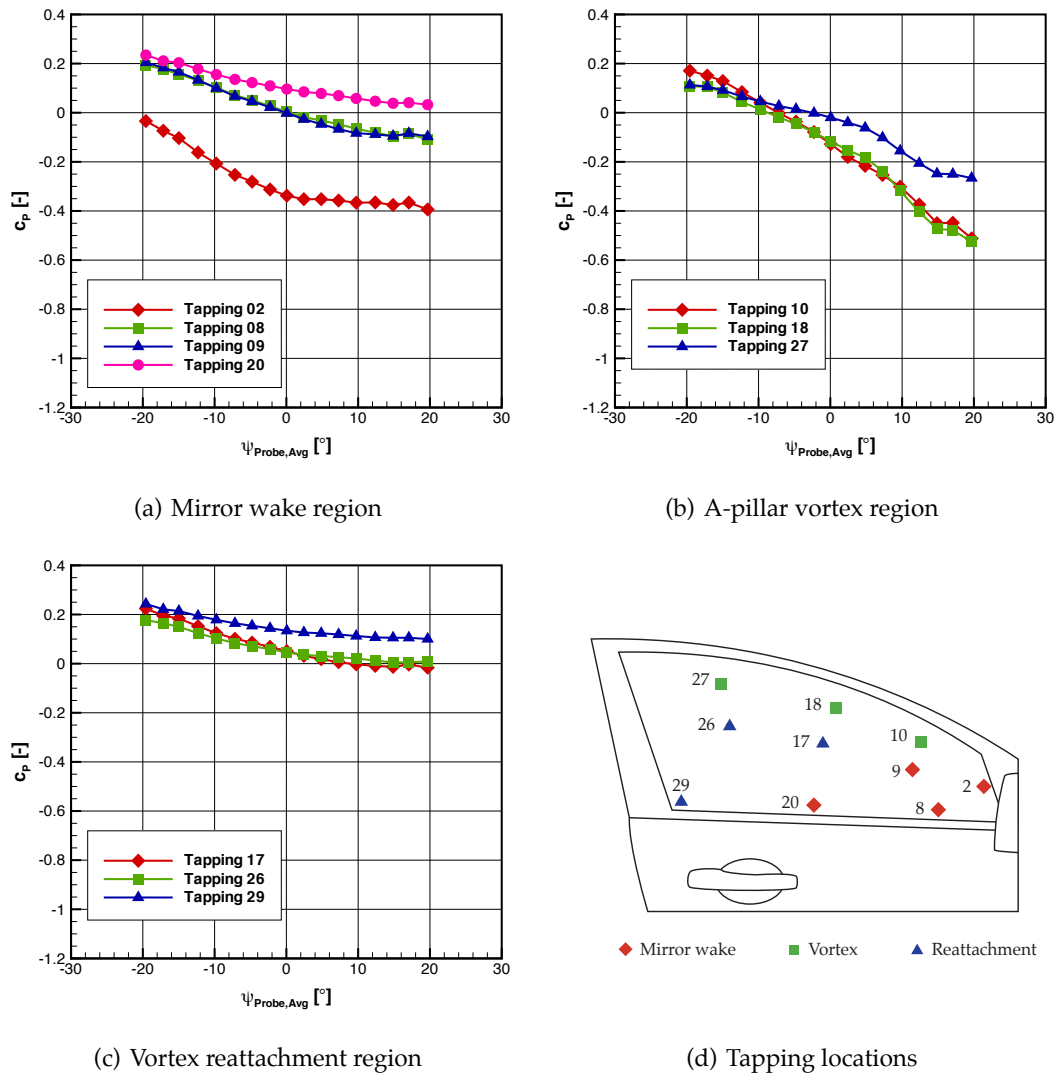


Figure 3.39: On-road sideglass pressure characteristics (Geometry 3 SG)

The variations in flow structure between the Geometry 2 SG and Geometry 3 SG vehicles are not identified by differences in the pressure coefficient characteristics, with the c_p profiles for each tapping location indistinguishable between the two vehicle geometries. Since the raised height of the bonnet affects the flow structures from the wipers, it is likely that the main differences are confined to the windscreen area. From the limited set of measurement positions on the sideglass, it would appear that any differences do not interact strongly with either the A-pillar vortex or the mirror wake, resulting in broadly similar sideglass characteristics between the geometries.

The similarity of the results also increases the level of confidence in the repeatability of the data collected on-road, with strong consistency of the data collected during separate testing days and corresponding on-road conditions.

3.5.4 Unsteady Wind Tunnel

The effect on the sideglass surface pressure distribution of increased free-stream unsteadiness was also investigated at zero-yaw in the Pininfarina AWT using the TGS. Figure 3.40 shows the variation in c_p for the Geometry 1 SG vehicle at each of the pressure tappings under the influence of the pseudo-random 3BL TGS mode, the dynamic-yaw 4D1.0 mode and with the TGS off. As previously, the pressure tappings are split into three groups, under the influence of the mirror wake, the A-pillar vortex and the vortex reattachment.

Both TGS modes result in similar effect on the sideglass c_p with no significant difference in behaviour between them. The pressure tappings that are most affected by the increase in oncoming flow turbulence are Tappings 2, 8, and 9 of the 'mirror wake' set and Tappings 10 and 18 of the 'A-pillar vortex' set. These tappings are all positioned near the front of the vehicle sideglass and are likely to more heavily influenced by the large vortex shed from the A-pillar and any shed structures from the mirror.

3. THE TIME-AVERAGED VEHICLE RESPONSE

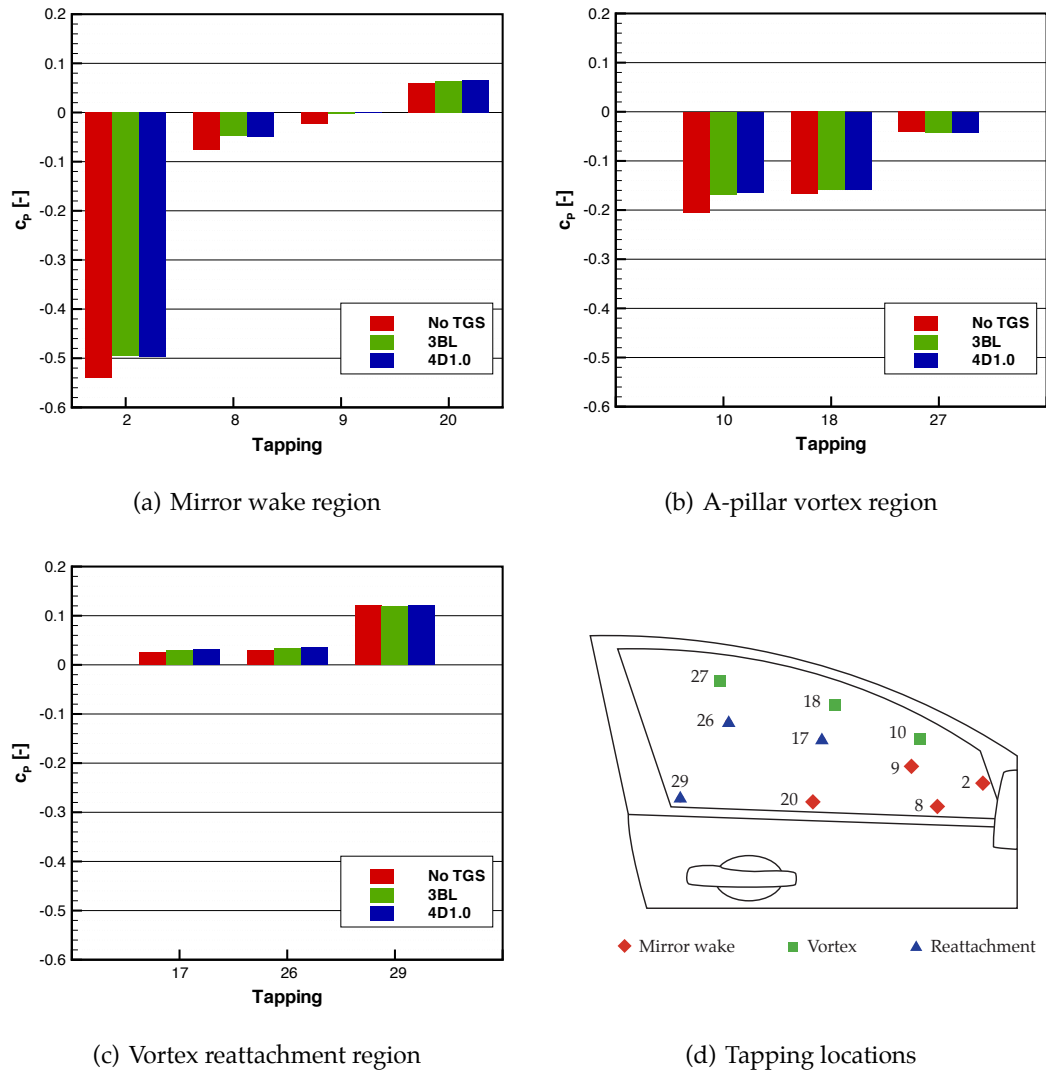


Figure 3.40: TGS sideglass pressure characteristics (Geometry 1 SG)

Tappings further away in the reattachment region are comparatively not affected by the increased levels of unsteadiness. In each of these cases, the generated unsteadiness causes a decrease in the measured c_p . This indicates a possible decrease in the strength of the A-pillar vortex, an effect observed by Vino et al. (2003) and Newnham et al. (2006) during model-scale experiments. Figure 3.41 shows the equivalent data for the Geometry 2 SG vehicle.

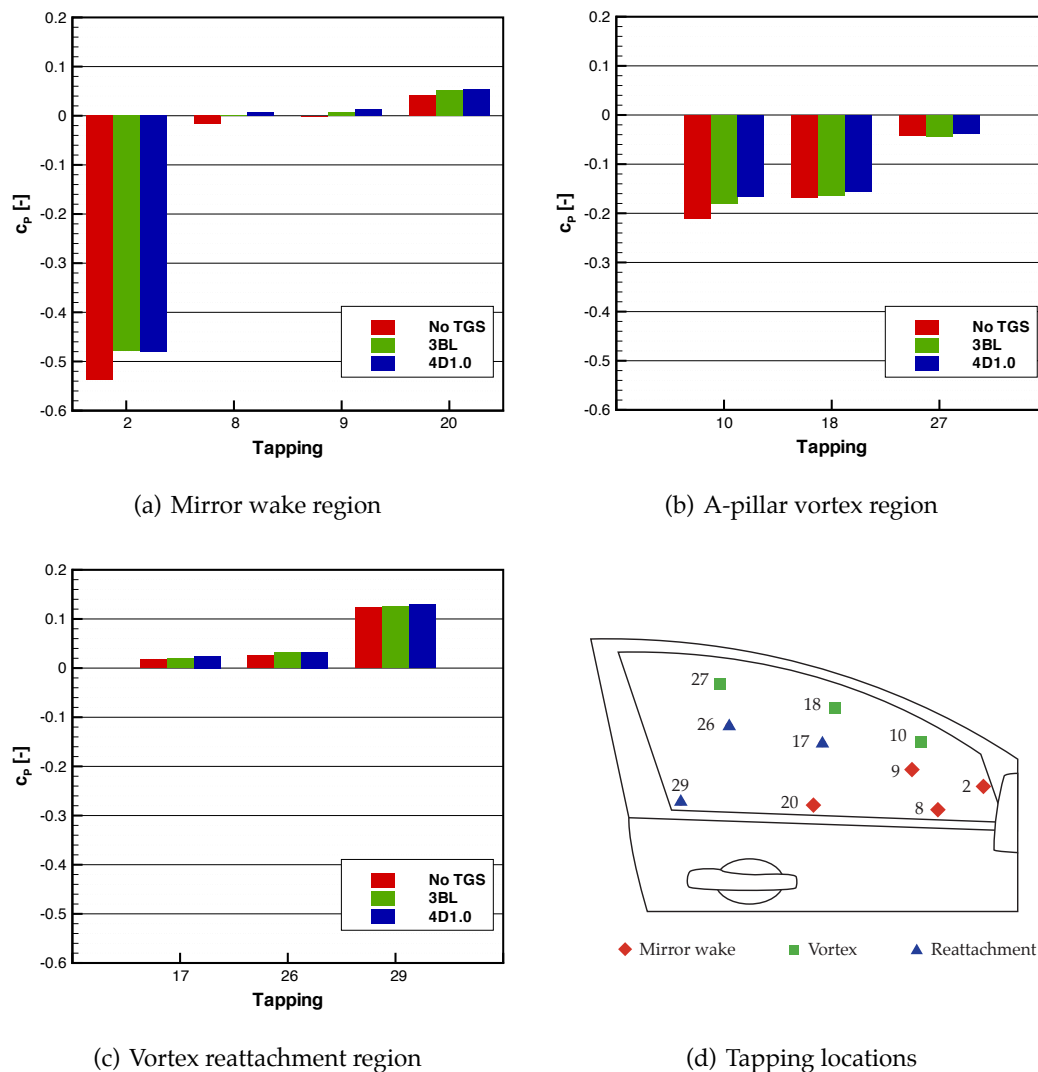


Figure 3.41: TGS sideglass pressure characteristics (Geometry 2 SG)

3. THE TIME-AVERAGED VEHICLE RESPONSE

In the mirror wake region, the c_p measured by Tappings 8 and 9 appear to be unaffected by the use of the TGS, indicating that the Geometry 2 SG mirror modification reduces the sensitivity towards fluctuations in the oncoming flow over that of Geometry 1 SG. Tapping 2 shows the same decrease in c_p as observed with the Geometry 1 SG vehicle. This tapping is positioned very close to the step of the mirror sail mounting and therefore is likely to be dominated by localised flow structures in this unchanged region, rather than the changes made to the mirror stem. In the other sideglass regions, the behaviour is unchanged from that of Geometry 1 SG, with flows in this region dominated by the unchanged geometry of the A-pillar.

3.6 Surface Noise

Three surface microphones were installed on the left, passenger sideglass of the vehicle. These were positioned to capture the range of different flows experienced by the sideglass, whilst ensuring that the microphones were arranged such that they had minimal influence over each other. As with the flush-mounted pressure tappings, vehicle Geometries 1 SG and 2 SG were assessed in the Pininfarina AWT, whilst vehicle Geometries 2 SG and 3 SG were assessed on-road.

It is important to recall that the surface microphones were positioned on the left side of the vehicle, opposite the pressure tappings. Therefore for a given non-zero oncoming flow yaw angle, the surface microphones are in a different flow condition to the tappings; either leeward or windward. A diagram of the relative positions of the surface microphones and pressure tappings at yaw was presented by Figure 2.19.

3.6.1 Steady Wind Tunnel

The variation in surface noise as both vehicle geometries were yawed in the Pininfarina AWT is presented in Figure 3.42, along with a diagram recalling the numbering and corresponding positions of the microphones.

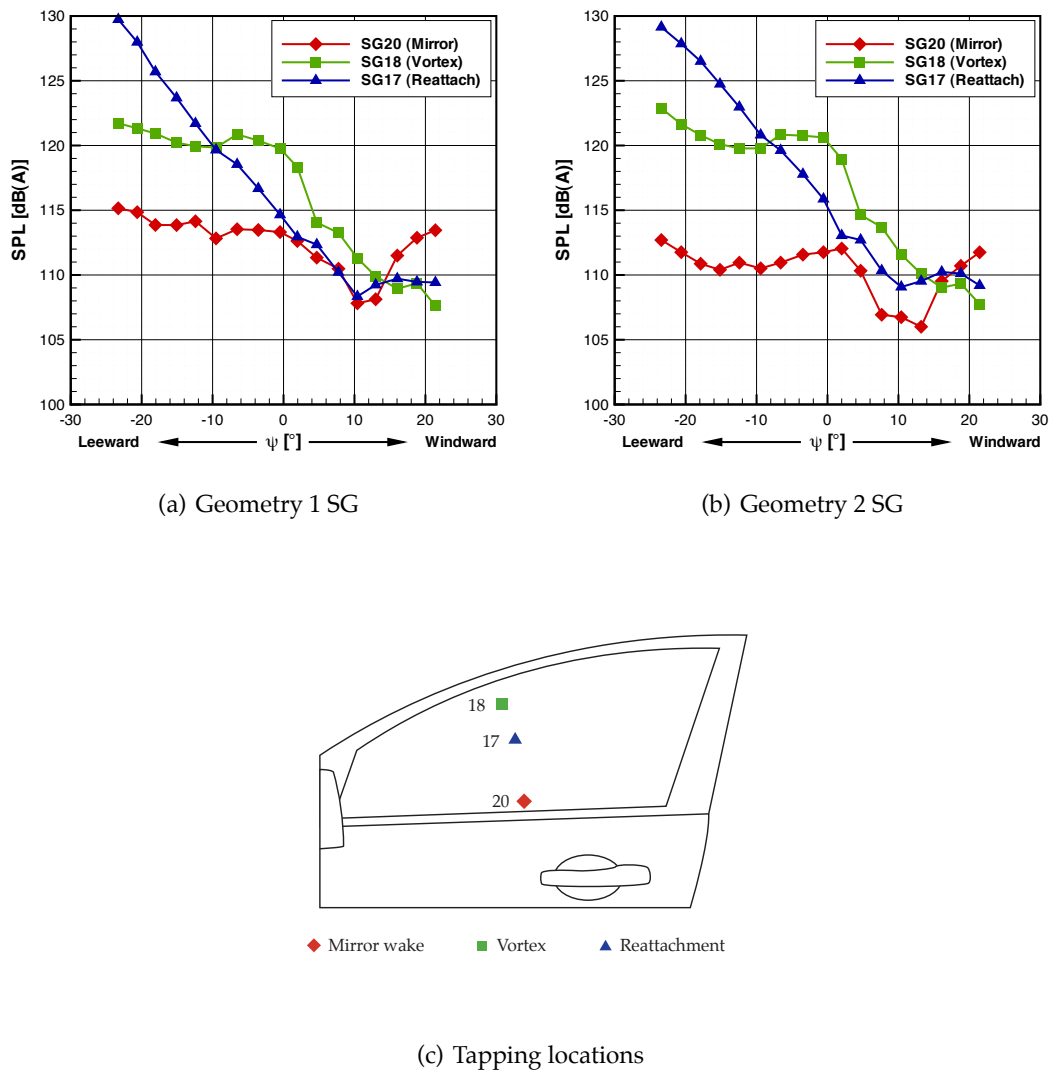


Figure 3.42: AWT (Pininfarina) sideglass surface noise characteristics

The SPL characteristics for both vehicle geometries include a number of discontinuities, rather than exhibiting a continuous change in behaviour. Both Geometry 1

3. THE TIME-AVERAGED VEHICLE RESPONSE

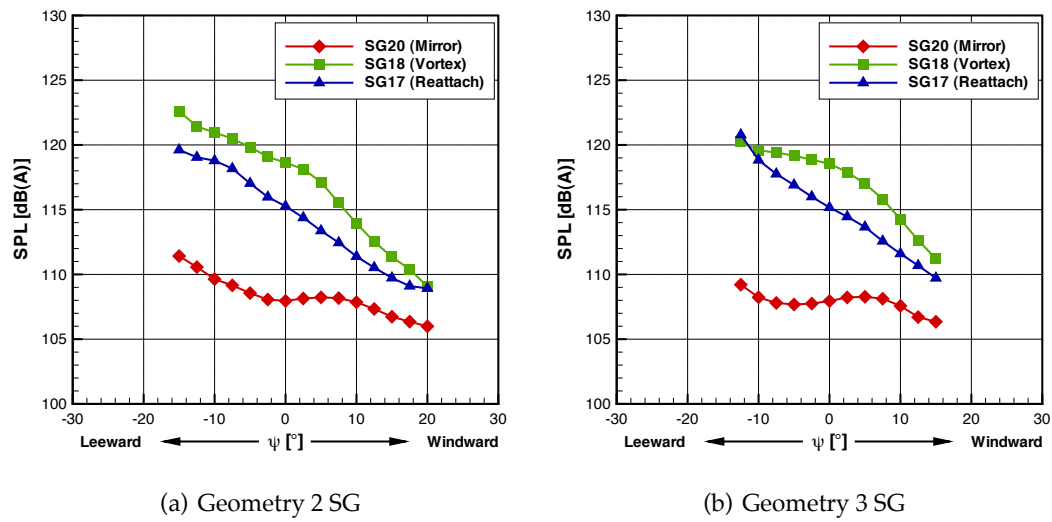
SG and 2 SG show significant discontinuities at $\psi = 10^\circ$ for both Microphones 17 and 20, which are regions away from the influence of the A-pillar vortex. To explain this behaviour under windward conditions, these microphones may be exposed to the noisier shear layer of the mirror wake or alternatively to direct oncoming flow, leading to a step-change in SPL. However, no sudden change was detected when assessing the equivalent surface pressure measurement locations in Figures 3.36 and 3.37.

Microphones 17 and 18 behaved in a very similar manner for both vehicle geometries, with even the smaller features of the characteristics being replicated. The most significant differences are shown by Microphone 20 in the mirror wake region. Since the differences in vehicle geometry were confined to a change in mirror stem design, this behaviour is perhaps expected. The general features of the characteristics are the same, including the sharp reduction in SPL at approximately $\psi = 10^\circ$, although the overall sound pressure levels for the Geometry 2 SG vehicle are reduced by approximately 3 dB(A) when compared to the Geometry 1 SG vehicle. There is also a difference in the SPL at $\psi = -10^\circ$, under leeward conditions. This reduction is also corroborated by measurements of noise inside the cabin, as shown by Figure 3.17.

3.6.2 On-Road

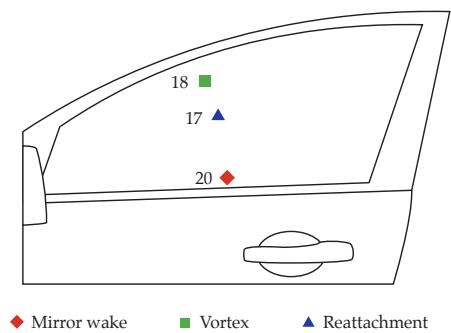
The same microphones were used on-road, capturing the differences in sideglass SPL between the Geometry 2 SG and Geometry 3 SG vehicles. The Geometry 2 SG results shown in Figure 3.43 allow a direct comparison to be made with the results obtained in the wind tunnel.

Comparing the on-road results of Figure 3.43(a) with those of the AWT in Figure 3.42(b), it is clear that the results obtained on-road do not show that same discontinuities that are present in the AWT. Overall, the general shapes of the characteristics between the two environments are similar, however there are some significant differ-



(a) Geometry 2 SG

(b) Geometry 3 SG



(c) Tapping locations

Figure 3.43: On-road sideglass surface noise characteristics

3. THE TIME-AVERAGED VEHICLE RESPONSE

ences. Owing to the averaging process adopted for the on-road data, a degree of data smoothing would be assumed to occur, however the observed differences are larger than expected from this process.

In the mirror wake region, measured by Microphone 20, the steep increase in SPL at higher positive values of yaw seen in the AWT is not present. However, the increase in SPL at zero yaw in the AWT is present on-road, although at a much smaller level. With the exception of these two features, the overall behaviour between the two environments is relatively similar. In the A-pillar vortex region, the increase in SPL in the AWT at zero yaw is present in the on-road measured data, although again at a lower level. Aside from this feature, the overall levels measured in both of the environments are generally alike, with a slight overall increase in level, likely to be caused by other sound sources on-road.

The SPL characteristic in the reattachment region shows a greater sensitivity to yaw in the AWT than on-road, although this discrepancy is not significantly different, with both SPL characteristics having a 10 dB(A) decrease in SPL between -10° and 10° . Again, the increased levels of other sound sources on-road may be the cause of the reduced sensitivity to yaw angle. There is also evidence of the higher yaw angle flattening of the SPL characteristic on-road, although occurring at a higher yaw angle than in the AWT. Overall, whilst the exact nature of the on-road SPL characteristics was not fully captured by the AWT, the larger-scale behaviour was generally fairly well represented.

Figure 3.43(b) shows the on-road surface SPL characteristics as measured on the Geometry 3 SG vehicle. At positive, windward, yaw angles the Geometry 2 SG and 3 SG vehicles are largely indistinguishable, with the differences confined to the larger leeward yaw angles. Here, the Geometry 3 SG vehicle shows a reduction in surface SPL measured by Microphones 18 and 20, although there is a slight increase in that

measured by Microphone 17. These differences are not significantly clear and may be due to measurement variations, however the difference in the A-pillar vortex region may equally be due to changes in the shed wiper structures due to the modifications made to the rear edge of the bonnet.

Previously in Equation 1.12, it was shown that surface SPL and c_p can be linked using the dipole-source relationship:

$$\begin{aligned}\Delta\text{SPL} &= 10 \log \left(\frac{u}{u_\infty} \right)^6 \\ &= 10 \log (1 - c_p)^3\end{aligned}\tag{3.10}$$

To test this relationship, the sideglass c_p characteristics as measured on-road were compared against the equivalent surface microphone measurements. The Geometry 2 vehicle was chosen, with the c_p characteristics shown in Figure 3.44(a), with the sideglass noise data shown by Figure 3.43(a). Note that whilst the measurement positions were nominally the same on the sideglass, the pressure tappings and surface microphones were positioned on opposite sides of the vehicle. Therefore for a given non-zero yaw angle, one side of the vehicle is in a leeward condition whilst the other will be in a windward condition.

From Figure 3.44(a), Tapping 18 has a $c_p < 0$ for much of the assessed yaw angle range, specifically above -10° . At $\psi = -10^\circ$, $c_p = 0$ and therefore the flow speed in the vicinity of the tapping is equal to free-stream. At increasing yaw angle, the flow speed increases such that $c_p = -0.48$ at $\psi = 15^\circ$. Using the relationship in Equation 3.10, this results in a predicted increase in SPL of 5.1 dB(A) from that measured at -10° . To compare this to the sideglass noise measured by the surface microphones, Figure 3.43(a) was used. Since the microphones were placed on the opposite sideglass, the difference in SPL between -15° and 10° was assessed, and found to be 8.7 dB(A), approximately

3. THE TIME-AVERAGED VEHICLE RESPONSE

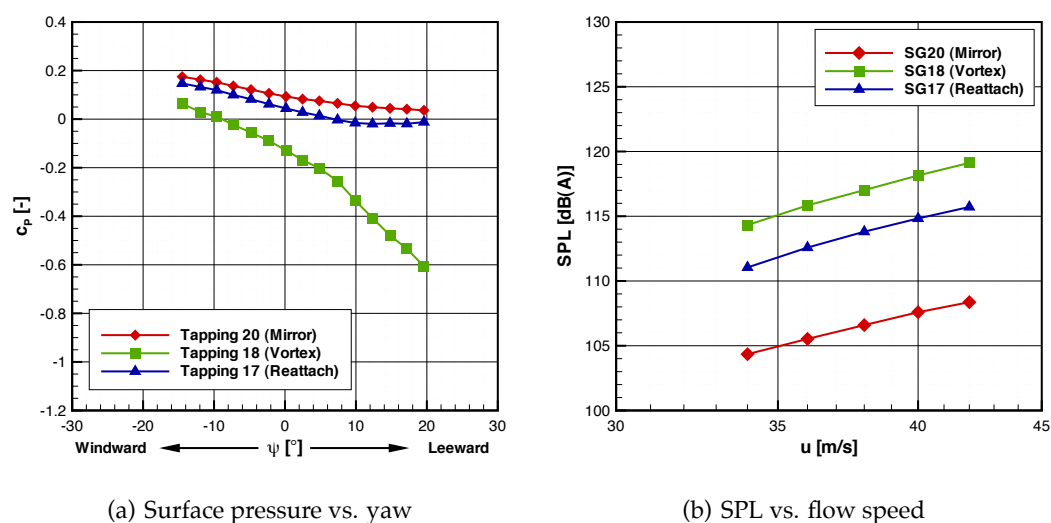


Figure 3.44: On-road surface pressure characteristics at equivalent surface microphone positions (Geometry 2 SG)

3 dB(A) greater than predicted.

The largest deviation between the predicted and measured SPL occurs between 10° and 5° windward, where there is a discontinuity in the measured surface noise. Moving towards an increased leeward flow condition, the deviation remains at 3 dB(A), indicating that the gradient of the SPL characteristic in this region is well predicted with a dipole-dominated relationship. In the windward condition, where the SPL characteristic is steeper, this relationship does not hold, implying a different power relationship due to alternative aeroacoustic sources. However, as shown by the relationship between the surface noise and oncoming flow speed, determined using the bin-averaging technique at zero yaw, the overall power relationship for Microphone 18 is 5.8, indicating that the dominating aeroacoustic sources are dipole-based.

By inferring the behaviour of the surface noise from that of the surface pressures, it should be noted that the data used to measure these different parameters were collected on opposite sides of the vehicle. For this technique to be truly valid, the geom-

etry of the vehicle would have to be symmetrical. It has been previously shown that this is not the case, owing to differences in the mirror angle and the position of the windscreen wipers. This is therefore likely to lead to differences in the measurement of both surface pressure and surface noise at comparable positions on opposite sides of the vehicle, potentially leading to errors in this technique, such as the measured 3 dB(A) deviation.

3.6.3 Unsteady Wind Tunnel

As with the steady wind tunnel assessment, vehicle Geometries 1 SG and 2 SG were evaluated in the Pininfarina wind tunnel using the TGS. Figure 3.45 shows the variation in sideglass surface noise for both vehicle geometries under the unsteady conditions generated by the 3BL pseudo-random mode and the 4D1.0 dynamic yaw mode, in addition to the TGS deactivated.

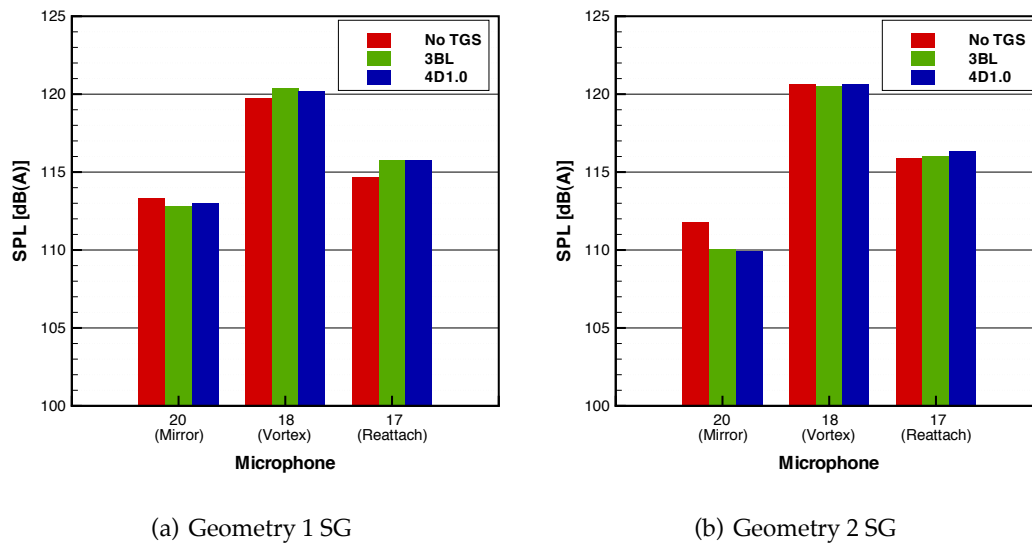


Figure 3.45: On-road sideglass surface noise characteristics

The Geometry 1 SG vehicle in Figure 3.45(a) shows relatively consistent surface

3. THE TIME-AVERAGED VEHICLE RESPONSE

noise behaviour under both steady and unsteady conditions. The reattachment region shows a small increase in SPL for both TGS modes, with the increased levels of free-stream fluctuation being translated into increased levels of fluctuation in this region. However, the Geometry 1 SG vehicle surface noise is generally not affected by the levels of unsteadiness as generated by the Pininfarina TGS.

Figure 3.45(b) shows the behaviour for the Geometry 2 SG vehicle, which in the A-pillar vortex and reattachment regions behaves in a similar manner to the Geometry 1 SG vehicle. Again, since the Geometry 2 SG modifications were limited to changes made to the mirror stem, this consistency is expected. Under steady conditions, there is a decrease in surface noise in the mirror wake region between the two geometries. However, there is an even greater decrease between the geometries under unsteady conditions. Even under the relatively low turbulence conditions as generated by the TGS compared to the conditions experienced on-road, the surface noise in the mirror region decreases. This was also observed to occur on road, although to a greater extent, as shown by the difference in zero-yaw SPL between AWT data from Figure 3.42(b) and on-road data from Figure 3.44(a).

This change in behaviour under unsteady conditions may be due to either increased levels of turbulence breaking up coherent structures shed from the mirror, although there is no evidence of any tonal noise indicative of such a condition. Alternatively, the unsteadiness may lead to a decrease in localised flow speed around the mirror stem and gap to the door, leading to a decrease in noise generation. The surface pressures measured under same conditions on the opposite side of the vehicle show a slight increase in c_p under unsteady conditions, implying a reduction in localised flow velocity and therefore a reduction in surface noise.

3.7 Summary

3.7.1 Cabin Noise

- As determined through a subjective listening study, the 4 kHz third-octave band captured the wind noise component of the overall cabin noise, with other sound sources having a negligible impact within this frequency range.
- The primary aeroacoustic sources affecting the noise inside the cabin were dipoles, indicating that the fluid interactions with the solid surfaces of the vehicle geometry dominated over other sources such as leak noise or body-gap cavity resonances.
- Using the frequency-dependent relationships between flow speed and cabin noise as determined in the wind tunnel, a technique was developed to determine the wind noise contribution to the overall cabin noise measured on-road. At the highway speeds used in this investigation, this found that aeroacoustic sources dominated the cabin noise spectra at frequencies above 2 kHz, whilst road noise dominated at frequencies centred around 800 Hz.
- By adopting a bin-averaging technique, whereby the cabin noise response of the vehicle is averaged based on the instantaneous on-road flow conditions, a representative comparison can be made between the cabin noise on-road and that measured in the aeroacoustic wind tunnel.
- Since the overall A-weighted cabin noise sound pressure level is dominated by tyre noise on-road, a comparison of the cabin noise between this and the aeroacoustic wind tunnel does not lead to a particularly useful comparison. However, by comparing third-octave bands dominated by wind noise, particularly

3. THE TIME-AVERAGED VEHICLE RESPONSE

the 4 kHz band, it was found that the time-averaged wind noise behaviour on-road correlated well with that determined in the wind tunnel.

- Both on-road and in the aeroacoustic wind tunnel, a geometry modification made to the stem of a door mirror was found to improve the cabin noise performance of the vehicle. This primarily affected higher frequencies under leeward flow conditions.
- The overall sound pressure level and the 4 kHz third-octave band component of the cabin noise were increased slightly with the generation of additional unsteadiness by the Pininfarina turbulence generation system. However, these increases were generally low, with the steady wind tunnel able to determine the same better-performing modification made to the door mirror as the unsteady wind tunnel.

3.7.2 Sideglass Surface Pressures

- The on-road time-averaged surface pressure profile of the vehicle sideglass was generally found to be similar to that obtained under the steady-state conditions experienced in the wind tunnel.
- Surface noise data obtained in the aeroacoustic wind tunnel was less consistent with the time-averaged data obtained on-road. Whilst the exact nature of the on-road surface noise behaviour was not fully captured by the AWT, the larger-scale behaviour was generally fairly well represented.
- Modifications made to the bonnet to reduce the size of any shed flow structures from the windscreen wipers had an unmeasurable effect on the surface pressure profile of the vehicle sideglass on-road. However, a small reduction in surface noise was measured under more extreme leeward flow conditions.

CHAPTER 4

The Time-Resolved Vehicle Response

4.1 Introduction

This chapter explores both the aerodynamic and aeroacoustic response of the vehicle, through measurements of both the surface pressures on the vehicle sideglass and the internal vehicle cabin noise. The analysis of this chapter contrasts with that of the previous chapter in that the time-resolved response is explored, rather than comparing the results in a steady or unsteady environment using statistically-stationary techniques. Both spectral and temporal methods were used to compare the on-road measured response with that predicted in the steady-flow environment of the wind tunnel to determine whether the vehicle responded in a manner that could be predicted using steady techniques. Again, the cabin noise and sideglass pressure fluctuations are the areas of the vehicle response that are focussed upon.

Common methods used to assess the transient response are described, followed by the introduction of a new method to linearise the non-linear aspects of both the surface pressure and cabin noise steady-state response. The surface pressure response in the sideglass region is first assessed, focussing on the different areas of the sideglass and

4. THE TIME-RESOLVED VEHICLE RESPONSE

the corresponding response. A new approach to separate the self-excited response of the vehicle from that due to external unsteadiness is also presented, allowing the overall aerodynamic response of the vehicle to be isolated, free from self-excited effects.

Various spectral approaches were assessed whilst attempting to capture the cabin noise response of the vehicle. A number of methods to simulate the quasi-steady predicted cabin noise using the steady-state response from the wind tunnel combined with measurements of the unsteady on-road environment were developed. A subjective assessment of various features of the simulated cabin noise was also completed to quantify how cabin occupants perceived fluctuations in the cabin noise.

4.2 Assessment of the Transient Response

4.2.1 Typical Admittance and Transfer Function Approaches

As previously introduced in Section 1.4.5, the aerodynamic admittance $\chi(f)$ is a common method used to quantify the aerodynamic response of a vehicle to unsteadiness in the oncoming flow. This is usually defined using aerodynamic coefficients, but there is no reason why it may not be defined in terms of aeroacoustic admittance, for example as:

$$\chi(f)^2 = \frac{G_{LL}(f)}{\left(\frac{dL}{d\psi}\right)^2 G_{\psi\psi}(f)} \quad (4.1)$$

where $G_{LL}(f)$ and $G_{\psi\psi}(f)$ are the autospectral densities of the cabin noise SPL and oncoming flow yaw angle respectively, with $\frac{dL}{d\psi}$ the steady-state sensitivity of SPL to changes in yaw angle. The ratio of the two autospectral densities is also equal to the magnitude of the transfer function squared, such that the admittance may be defined

in terms of the transfer function $H(f)$:

$$\chi(f) = \frac{|H(f)|}{\left(\frac{dL}{d\psi}\right)} \quad (4.2)$$

As f tends to zero it would be expected that the admittance would tend to unity, with the transfer function tending to the steady-state sensitivity of changes in SPL to yaw angle, as measured in the wind tunnel.

The transfer function can also be defined as the ratio of the cross-spectral density to the autospectral density and it is this definition that is shown in general terms by Figure 4.1, where the oncoming flow conditions are described by $F(t)$ and the vehicle response by $R(t)$. This outlines the approach in determining the transient response of the cabin noise of a vehicle to yaw fluctuations in the oncoming flow, based on admittance.

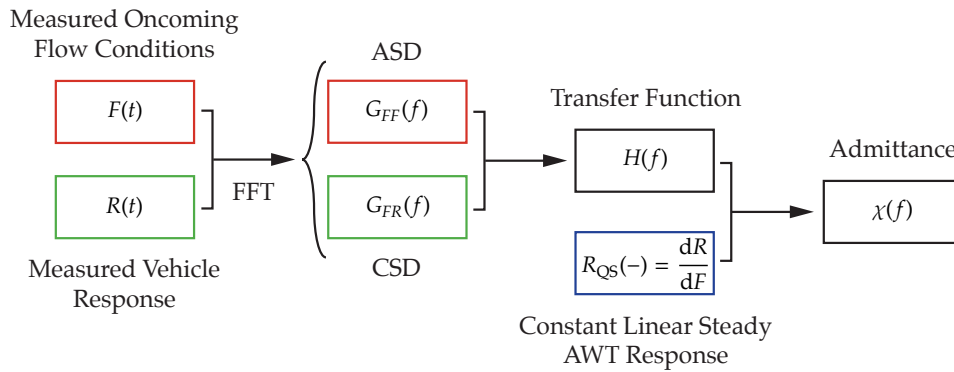


Figure 4.1: Method to determine the transient response of a vehicle via admittance

When considering an aerodynamic admittance, for instance based on a side force or yaw moment coefficient on a vehicle, the coefficients tend to vary linearly with yaw angle. Therefore, the rate of change (gradient) between the force coefficients and yaw remains independent of the particular instantaneous oncoming yaw angle, such that

4. THE TIME-RESOLVED VEHICLE RESPONSE

the correction term $\frac{dL}{d\psi}$ of Equations 4.1 and 4.2 is constant.

However, when considering localised surface pressure changes, for example the pressure at a particular point on the sideglass, the behaviour may not be linear. This is particularly noticeable in the sideglass region adjacent to the A-pillar, as shown in the previous chapter by Figures 3.36 and 3.37. This is also the case when considering the response of cabin noise to yaw angle, where it is clear that owing to the greater amount of flow separation at the extremes of yaw angle, the cabin noise at both positive and negative yaw angles is greater than at a zero yaw condition. This was shown in the AWT by Figure 3.17, highlighting that the cabin noise is strongly non-linear with yaw angle and therefore an equivalent aeroacoustic admittance approach would not be appropriate. Indeed, when determining the aeroacoustic admittance on-road, the correction term would vary depending on the range of yaw angles experienced.

Cabin noise is not only affected by variations in oncoming yaw angle, but also to fluctuations in flow speed. Typically the relationship between oncoming flow speed and cabin noise scales with flow speed raised to the power of the order of 6, as discussed in Section 3.4.2.1. Therefore, instead of a single input – single output system, a multiple input – single output system must be considered, discussed in further detail by Bendat and Piersol (1993). This does not preclude such a transfer function assessment *per se*; it is the non-linear response of cabin noise to yaw angle which provides the challenge, since it could be imagined that the logarithmic response of the cabin noise to flow speed could be successfully linearised.

Therefore an alternative spectral approach was sought to be able to assess the response of the vehicle to fluctuations in the oncoming flow when the steady-state response is non-linear.

4.2.2 An Alternative Linearised Transfer Function Approach

To assess the nature of the vehicle aerodynamic and aeroacoustic response, a simulation technique was implemented that used the vehicle response to steady flow variations measured in the wind tunnel, combined with the transient flow environment measured by the probe on the vehicle roof on-road to predict the instantaneous response. With this simulation it was then possible to compare the behaviour of the vehicle on-road to that predicted by the wind tunnel. Therefore any non-linearities in the wind tunnel steady-state characteristics are removed and converted into a continuous predicted time-history of cabin noise or external pressure fluctuations. Figure 4.2 outlines a generalised form of this process.

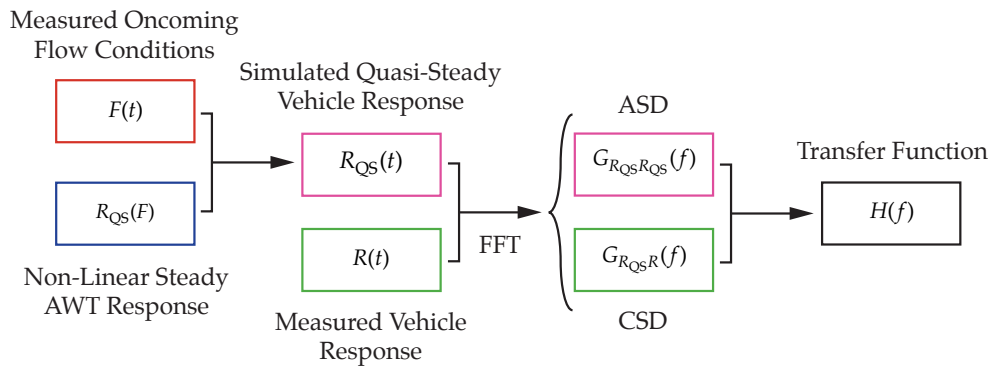


Figure 4.2: Method to determine the transient response of a vehicle via an alternative linearised approach

This results in a transfer function whereby a value of unity implies that the vehicle response to oncoming flow fluctuations is equal to that predicted in the steady environment of the AWT, *id est* the response is quasi-steady. A transfer function of greater than unity implies that the vehicle responds to a greater extent to that predicted by the instantaneous oncoming flow conditions alone, whilst a response of less than unity implies a response less than predicted under steady conditions.

It has been shown, for instance in Figure 1.48 that for the aerodynamic response

4. THE TIME-RESOLVED VEHICLE RESPONSE

of a vehicle, a transfer function of unity would be expected at lower frequencies for scales much greater than the vehicle, where the response can be considered to be quasi-steady. At higher frequencies, the vehicle response is no longer quasi-steady, although the higher-frequency, small-scale fluctuations much smaller than the size of the vehicle have a progressively decreasing impact of the vehicle response, leading to a transfer function of less than unity. In the intermediate frequency range, scales of unsteadiness may exist that are sufficiently large and of sufficient energy to influence a vehicle, but not so large that they can be considered to be quasi-steady. These effects can lead to transfer function values of greater than unity and these are sometimes associated with resonances of the vehicle suspension system in the case of vehicle forces.

The alternative linearised approach presented simplifies the analysis of the system, since multiple-input problems can be simplified to consider only a single input, avoiding the need for a multiple input – single output analysis. For instance, it has been shown that the noise inside the cabin of a vehicle is influenced by both the on-coming flow speed and yaw angle. Instead of assessing these as independent inputs to the system, these inputs were linearised to produce a single input of the expected cabin noise as determined under the steady conditions of the wind tunnel. This single input was then assessed against the single output of the measured cabin noise to determine the response of the system.

4.3 Surface Pressures

On-road testing invariably leads to increased levels of uncorrelated noise to both the input and output signals and therefore it is expected that the coherence levels measured in this environment will be much lower than those of testing undertaken in the more isolated environments of anechoic chambers (for acoustic transfer functions) or

structurally isolated conditions (for modal testing).

It is for this reason that the surface pressure data is presented initially. The cabin noise measurements recorded on-road contain acoustic content unrelated to fluctuations in the oncoming flow, such as noise from the powertrain and tyres. This leads to a reduction in the quality of the cabin noise transfer functions. The sideglass pressure measurements contain much less uncorrelated content and therefore show much clearer relationships. The cabin noise response of the vehicle is also dominated by aerodynamic fluctuations in the sideglass region and therefore presenting the surface pressure data first is a more natural chronology.

Vehicle Geometry 2 SG was used, since this vehicle was measured in both the steady environment of the Pininfarina AWT and in the unsteady conditions on-road. Once again, the pressure tappings were spread over the sideglass, covering regions nearest the mirror wake, the A-pillar vortex and the vortex reattachment region, as shown previously by Figure 2.8(a). This figure is reproduced when presenting the following results.

The following sections outline the process of i): determining the quasi-steady predicted surface pressure response; ii): comparing this to the measured on-road response in the time domain; and iii): using spectral techniques to formally assess the response of the vehicle. Figure 4.2 is used as a basis, with each step of the overall process considered separately, defined using the specific surface pressure terms.

4.3.1 Determination of the Quasi-Steady Response

4.3.1.1 Simulation Technique

To determine the quasi-steady predicted sideglass surface pressure response, a simulation technique was implemented using the steady-state c_p response to yaw angle measured in the wind tunnel, combined with the transient flow characteristics measured

4. THE TIME-RESOLVED VEHICLE RESPONSE

by the probe on the vehicle roof on-road. Each yaw angle time history $\psi(t)$ was used to simulate the steady-state response, as would be expected based on the behaviour of the vehicle in the wind tunnel, by mapping each instantaneous yaw angle measurement to a predicted c_p using the steady-state AWT response $c_p(\psi)$. This resulted in the simulated quasi-steady surface pressure response $c_{p,qs}(t)$, with this process outlined by Figure 4.3.

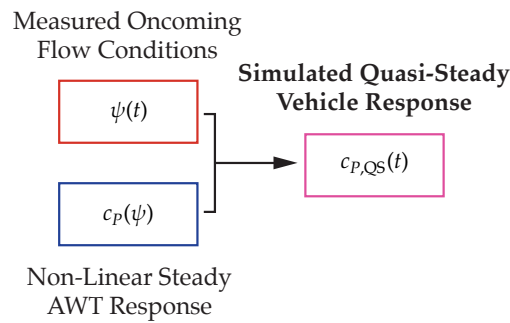


Figure 4.3: Determination of the simulated quasi-steady predicted surface pressure response

The process was completed for each of the sets of data collected on-road using the Geometry 2 SG vehicle. This generated a series of quasi-steady predicted sideglass pressure time histories, for each of the pressure tap locations.

4.3.1.2 Temporal Comparison of On-Road and Simulated Data

To compare the on-road measured sideglass fluctuations with the quasi-steady AWT predicted fluctuations, an example time history was chosen allowing a comparison to be made in the time domain. This allows a primary comparison of the measured and quasi-steady predicted data. If the surface pressure coefficient experienced in transient conditions for a particular instantaneous yaw angle matched that in the wind tunnel then the response can be described as quasi-steady. This comparison is outlined in Figure 4.4.

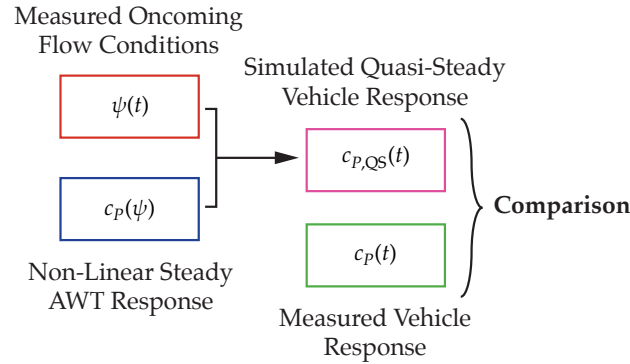


Figure 4.4: Comparison of the simulated quasi-steady predicted surface pressure response with that measured on-road

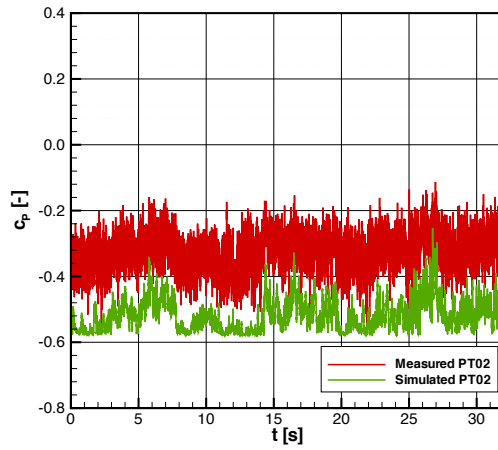
The quasi-steady simulated and on-road measured surface pressure time histories are presented in Figures 4.5–4.7 for each of the sideglass regions. Figure 4.5 presents the first set of time histories for the four pressure tappings located in the mirror wake region.

The first observation is that the agreement is generally good, with the behaviour at the lower-frequency scales that are visible in the presented time histories appearing closely quasi-steady. It is, of course, difficult to assess frequencies much higher than 1 Hz in this way and so further analysis is required to assess the vehicle response at higher frequencies.

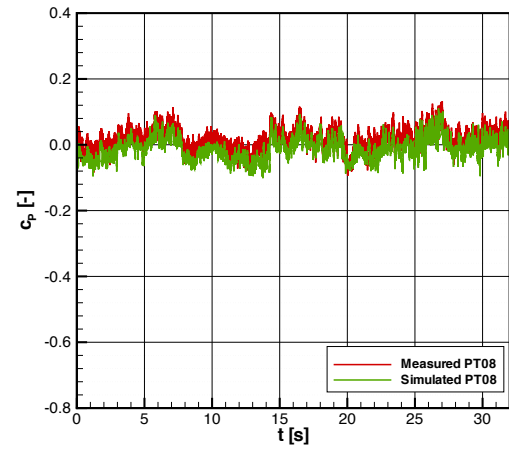
Pressure Tapping 9 in Figure 4.5(c) appears to show an excellent correlation between the measured on-road data and that predicted using the quasi-steady response in the AWT. Tappings 8 and 20 in Figures 4.5(b) and 4.5(d) respectively also show a good correlation, however with an offset between the two signals. Tapping 2 also shows an offset between the signals, but also a significant level of unsteadiness present in the on-road measured signal not predicted by the instantaneous yaw measurements and quasi-steady AWT response.

The offset between the two signals was previously identified by the steady-state

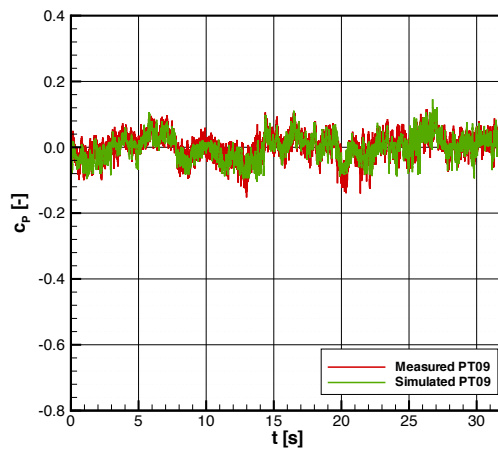
4. THE TIME-RESOLVED VEHICLE RESPONSE



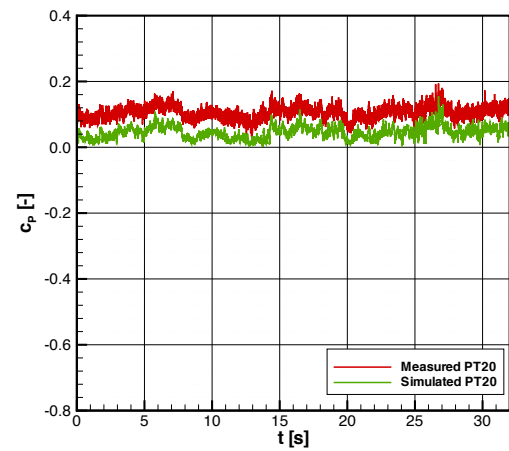
(a) Pressure Tapping 02



(b) Pressure Tapping 08



(c) Pressure Tapping 09



(d) Pressure Tapping 20

Figure 4.5: Vehicle Geometry 2 (perspex sideglass): Mirror region

and time-averaged measurements taken in the AWT and on-road respectively, shown in the previous chapter in Figures 3.37 and 3.38. This is indicative of a difference in the flow structures between the two environments, for instance a change in the size and strength of the A-pillar vortex or mirror wake. Variations in unsteadiness between the on-road surface pressure measurements and those predicted by the quasi-steady AWT response using the probe measured variations in yaw angle are indicative of a non quasi-steady response.

Figures 4.6 and 4.7 show the equivalent pressure time histories for the A-pillar vortex and vortex reattachment regions respectively.

The on-road pressure behaviour in these regions showed excellent temporal correlation, with both the overall pressure levels and low-frequency unsteadiness being captured well through the quasi-steady predicted data. Levels of unsteadiness were greater in the sideglass regions adjacent to the A-pillar, becoming progressively lower as this distance increases. The increased response to oncoming fluctuations in yaw angle was due to increased sensitivity in the flow structures to changes in yaw angle, as shown through the steady-state characteristics of Figure 3.37.

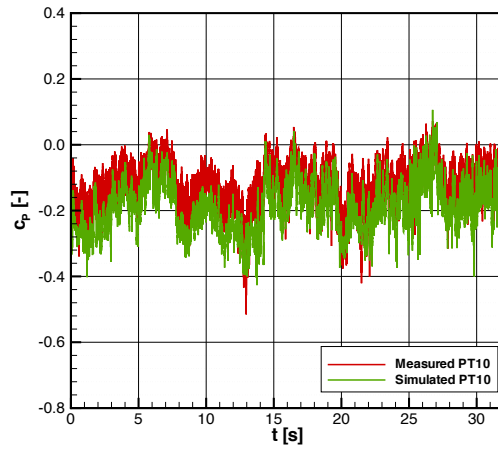
4.3.2 Assessment of the Frequency Response

4.3.2.1 Linearised Transfer Functions

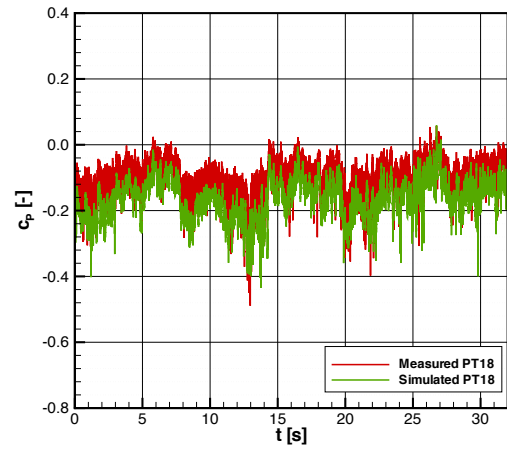
Whilst the example time traces show a generally quasi-steady response for the majority of pressure tappings, this was assessed formally through the use of transfer functions and spectral analysis. This assessed the quasi-steady response at the full range of unsteady fluctuation frequencies as measured on-road. The transfer function is defined according to:

$$H(f) = \frac{G_{c_{p,QS} c_p}(f)}{G_{c_{p,QS} c_{p,QS}}(f)} = \frac{CSD}{ASD} \quad (4.3)$$

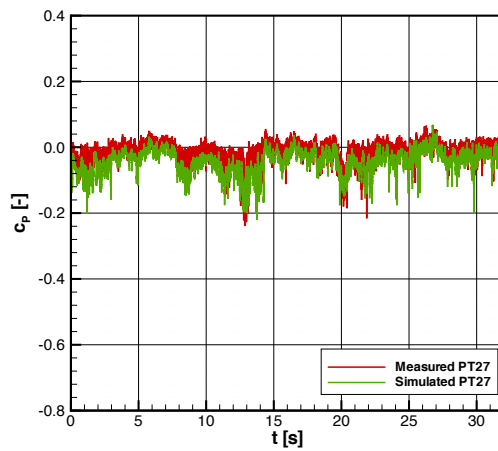
4. THE TIME-RESOLVED VEHICLE RESPONSE



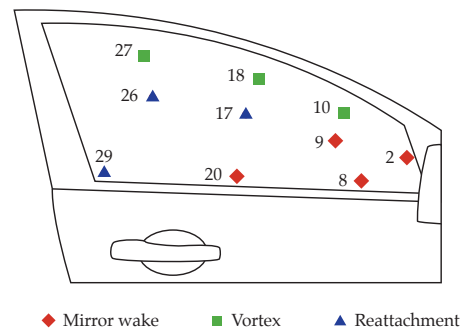
(a) Pressure Tapping 10



(b) Pressure Tapping 18

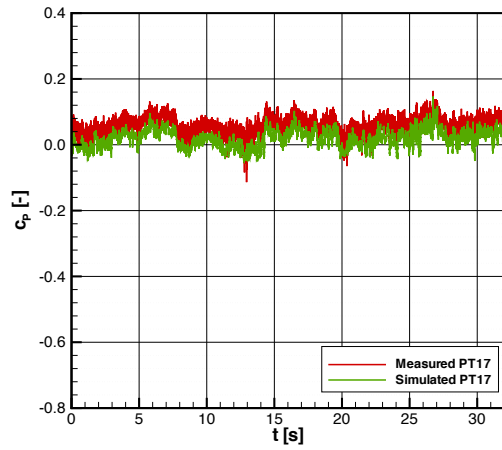


(c) Pressure Tapping 27

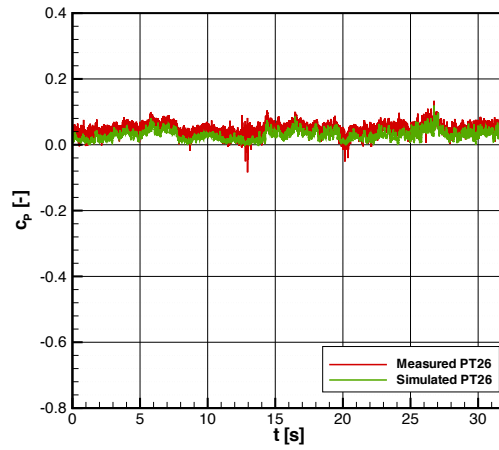


(d) Tapping locations

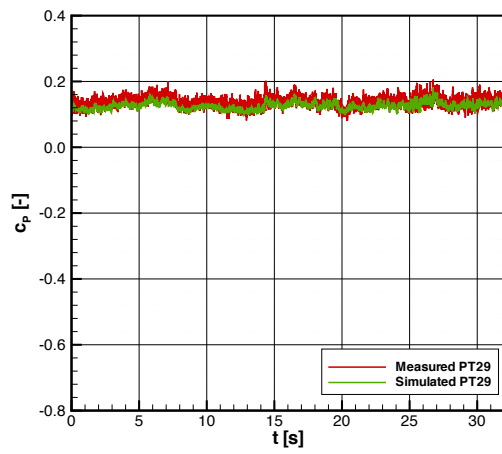
Figure 4.6: Vehicle Geometry 2 (perspex sideglass): Vortex region



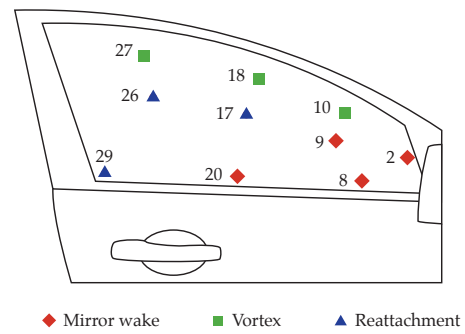
(a) Pressure Tapping 17



(b) Pressure Tapping 26



(c) Pressure Tapping 29



(d) Tapping locations

Figure 4.7: Vehicle Geometry 2 (perspex sideglass): Reattachment region

4. THE TIME-RESOLVED VEHICLE RESPONSE

and is the ratio of the cross-spectral density of the measured and quasi-steady predicted pressures $G_{c_{p,QS} c_p}(f)$ against the auto-spectral density of the simulated pressures $G_{c_{p,QS} c_{p,QS}}(f)$.

A transfer function of unity indicates that the sideglass fluctuations are as predicted in the wind tunnel. A shift in absolute c_p values between those measured on-road and those measured in the wind tunnel, such as that shown by Tapping 20 in Figure 4.5(d). would be manifested as a non-zero transfer function at low frequency (0 Hz), whilst not affecting the transfer function at higher frequencies.

To calculate the transfer functions of each of the sideglass pressure tapplings, first the auto and cross spectral densities were determined. These are presented and compared for each of the tapplings according to Figure 4.8.

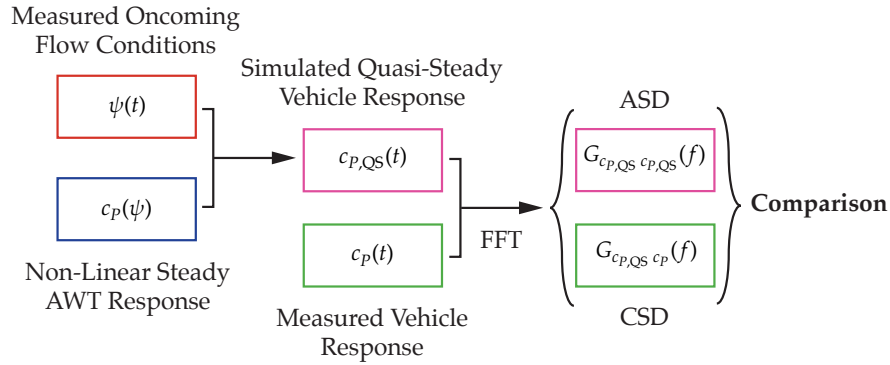


Figure 4.8: Determination of the constituent spectra for the overall surface pressure transfer function

These spectra were calculated from each 33 s time history, for the complete set of on-road measured surface pressure and flow data, with the average simulated to measured CSD denoted by $G_{SM}(f)$ and the average simulated ASD denoted by $G_{SS}(f)$. As with the previous set of temporal comparisons, the spectral data are grouped together according to the region on the sideglass to which they relate: Figure 4.9 compares the spectra in the mirror wake region; Figure 4.10 compares the spectra in the region of

the A-pillar; with Figure 4.11 comparing the spectra in the vortex reattachment region.

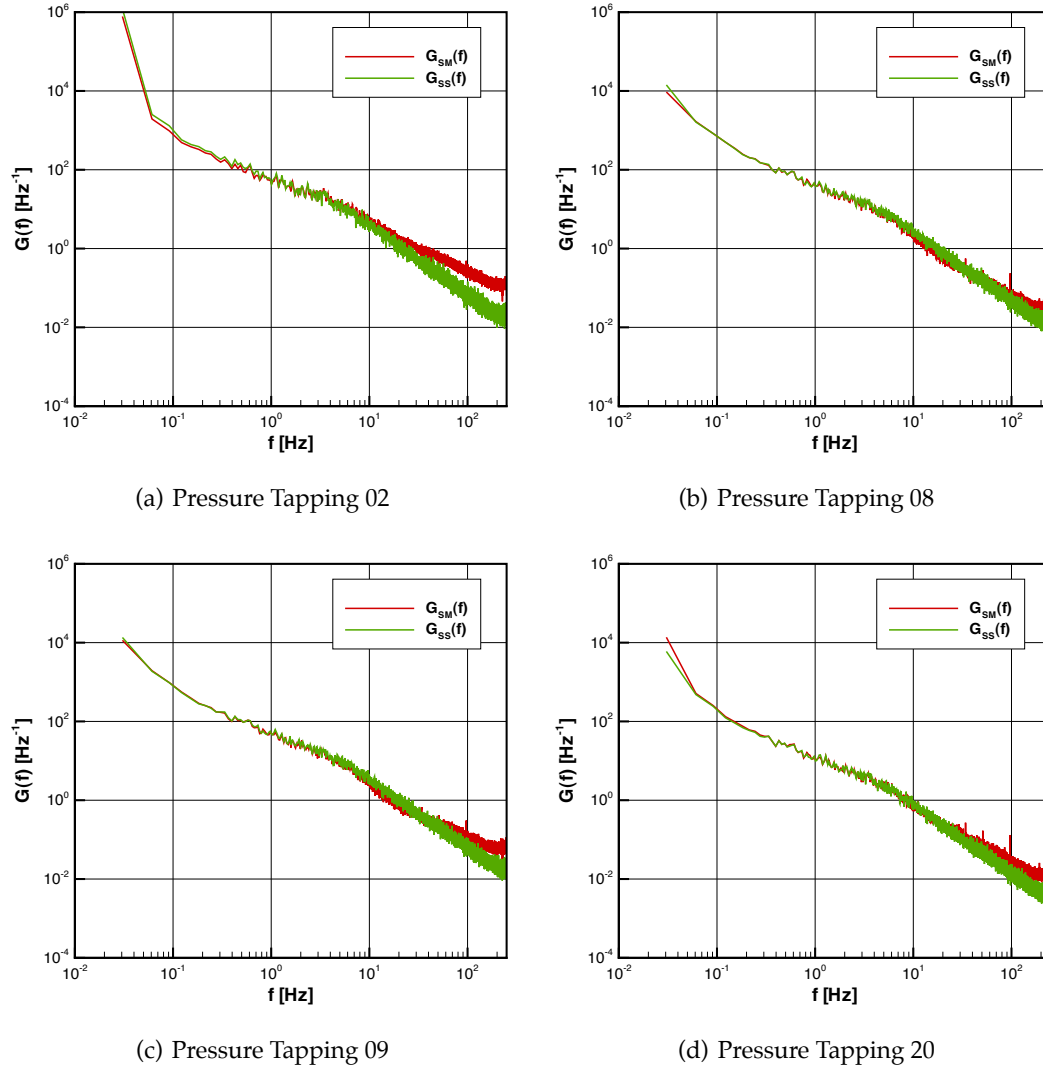
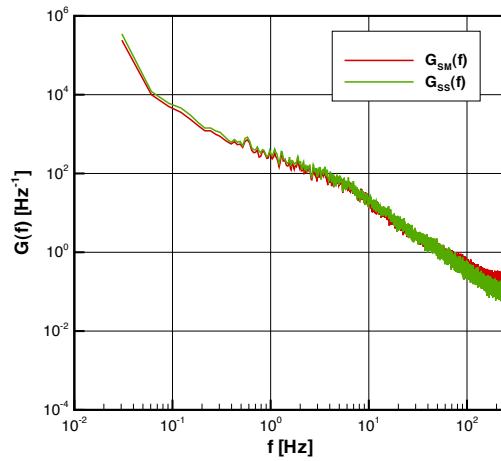


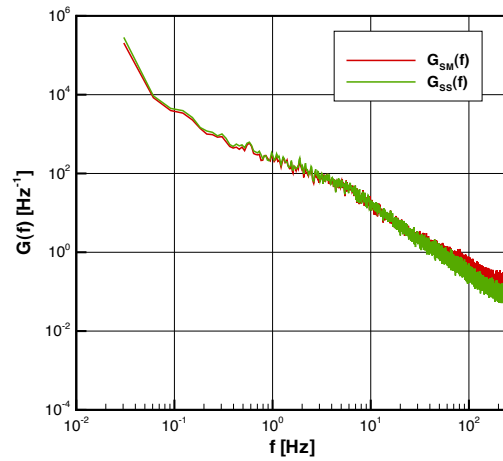
Figure 4.9: Vehicle Geometry 2 (perspex sideglass): Mirror region

The progressive roll off of spectral energy as frequency increases can be clearly seen. The two spectra can be seen to agree very closely over most of the range but at higher frequencies, the spectra tend to deviate. The extent of this deviation and the frequency where this starts to occur depends on the measurement point considered.

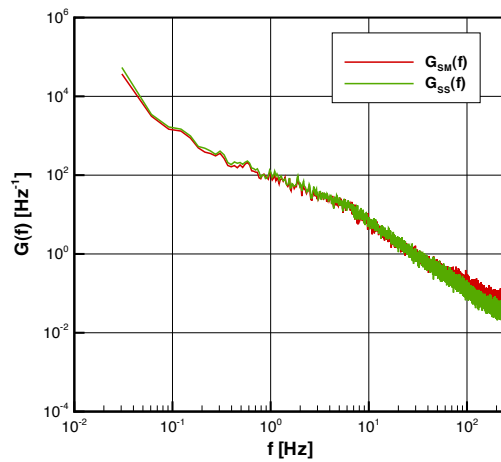
4. THE TIME-RESOLVED VEHICLE RESPONSE



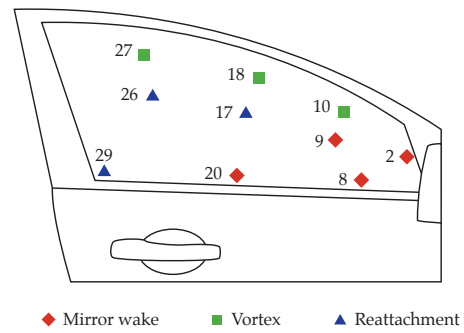
(a) Pressure Tapping 10



(b) Pressure Tapping 18

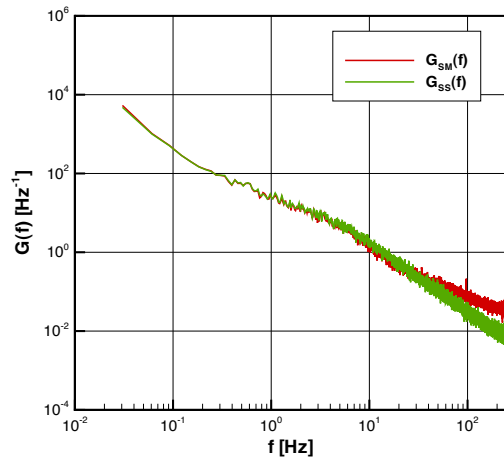


(c) Pressure Tapping 27

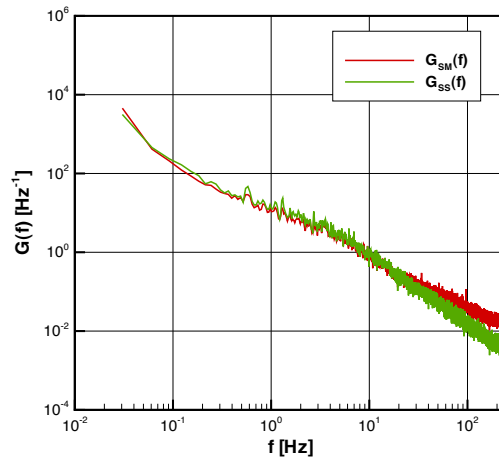


(d) Tapping locations

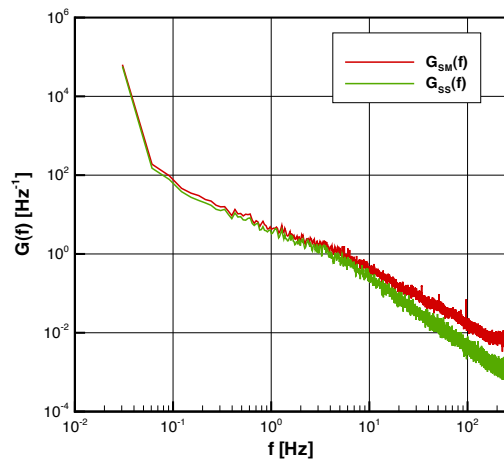
Figure 4.10: Vehicle Geometry 2 (perspex sideglass): Vortex region



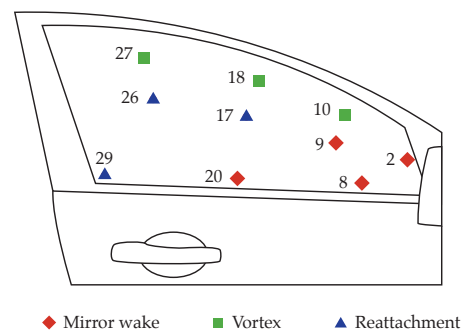
(a) Pressure Tapping 17



(b) Pressure Tapping 26



(c) Pressure Tapping 29



(d) Tapping locations

Figure 4.11: Vehicle Geometry 2 (perspex sideglass): Reattachment region

4. THE TIME-RESOLVED VEHICLE RESPONSE

For instance, the regions downstream of the mirror tend to show a greater deviation, in particular Tappings 2 and 29 (shown by Figures 4.9(a) and 4.11(c) respectively), with points closest to the A-pillar showing the least deviation.

It is the CSD term ($G_{SM}(f)$) that contains the greater energy at these higher frequencies, indicating that the unsteadiness measured on the sideglass exceeds that predicted based solely on unsteadiness in the natural wind environment. The logical explanation is that there is energy contained within the sideglass fluctuations that is due to self-excited unsteadiness in the sideglass region, for instance due to the door mirror.

Self-excited unsteadiness is unsteadiness generated through the interactions between the oncoming flow and solid structures. This can lead to coherent flow structures that are shed downstream and, in the case of the sideglass, shedding from the door mirrors can impact the glass and lead to greater levels of unsteadiness in this region than caused by the unsteady oncoming flow alone. Other solid structures of the vehicle can also lead to self-excited unsteadiness, ranging from small structures such as aeriels, see Blevins (1990), to the overall shape of the vehicle body, see Schröck et al. (2011). Various sources of unsteadiness leading to noise generation were discussed in Section 1.3.4, however in the sideglass region, the self-excited unsteadiness was dominated by shed structures primarily from the door mirrors and A-pillar region.

The quasi-steady simulations are based solely upon the measurements of the oncoming flow. These flow measurements are converted into equivalent sideglass pressures using the yaw characteristics as measured under the steady conditions of the wind tunnel. Whilst the self-excited behaviour is also present in the AWT, the averaging process in collecting the steady-state characteristic data means that, by definition, only the mean data is recorded, with the fluctuating component *averaged-out*. Therefore, this is the cause of the self-excited content being present in the on-road measured pressure data, but not in the predicted quasi-steady data.

Figure 4.12 shows the resulting transfer functions created using the averaged spectral data. These are once again separated into the three different sideglass regions.

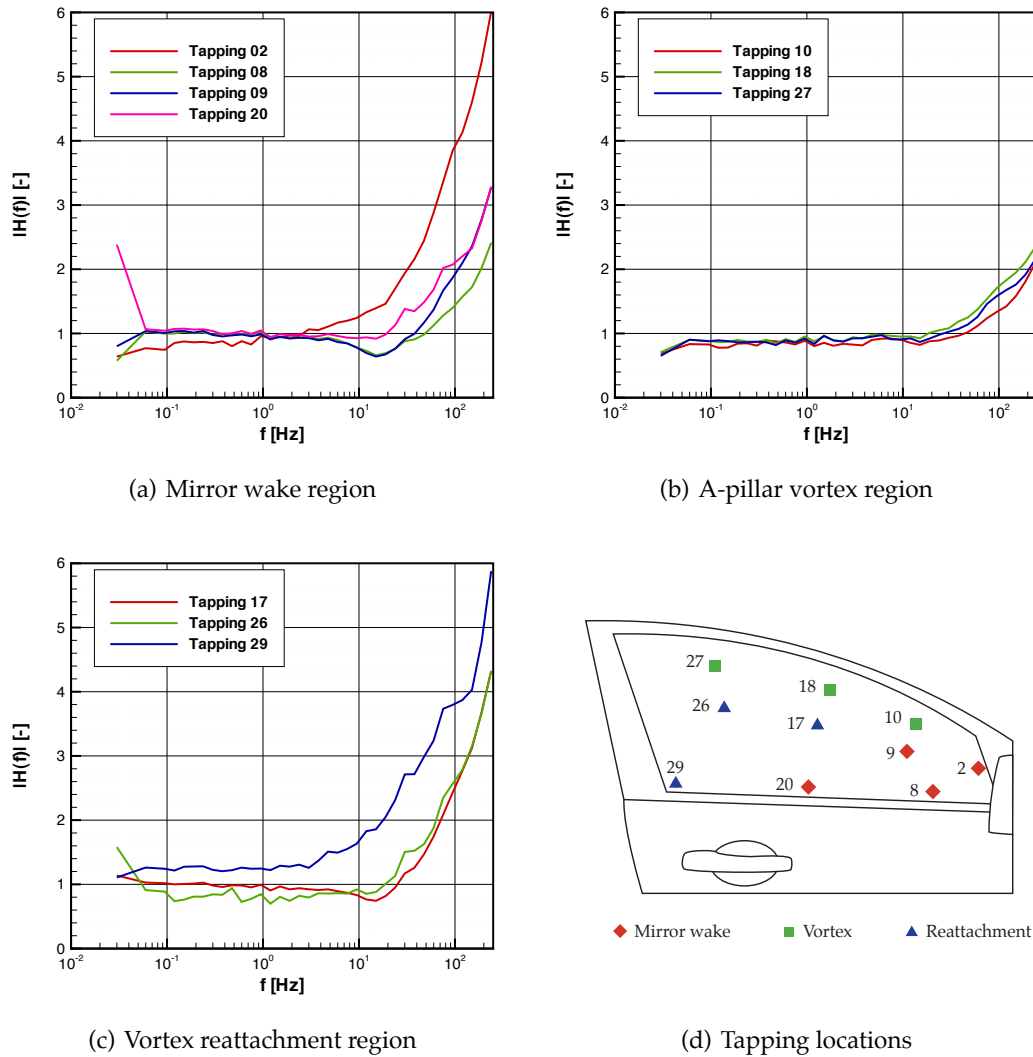


Figure 4.12: On-road to AWT sideglass pressure transfer functions (Geometry 2 SG)

At the lowest frequency point, dictated by the length of the time record ($f = 1/T$), there is generally a single non-unity point due to the steady-state difference in c_p values between the on-road averaged measurements and those obtained in the wind tunnel. The value varies; depending on the sign of the c_p values and the amount of offset, this steady-state transfer function value can either be less than or greater than

4. THE TIME-RESOLVED VEHICLE RESPONSE

unity. If the wind-tunnel-predicted average c_p value is close to zero then this can lead to a large steady-state value owing to this term being the denominator in the transfer function definition. Therefore this single steady-state value has a greater sensitivity to error and thus should be regarded with caution.

The key observation is that near-unity transfer function amplitudes are seen at frequencies up to at least 2 Hz, or reduced frequencies (based on the square-root of vehicle frontal area) of at least $k = 0.5$. This indicates that the sideglass of the vehicle exhibits a quasi-steady response over the frequency range where the majority of on-road unsteadiness is experienced. This shows that the combination of steady-state wind tunnel tests and knowledge of the unsteady wind environment, allows an accurate prediction of the surface pressures and hence transient forces that can be expected.

In some cases, such as above 2–5 Hz for Tappings 8 and 9 in Figure 4.12(a), the transfer function decreases below unity, indicating that fluctuations measured by the probe are not translated to changes in surface pressure at the sideglass. This is consistent with the fact that the reduced frequency is greater than unity and thus a quasi-steady response can no longer be expected.

Beyond 10–20 Hz the transfer functions increase rapidly above unity. While both the measured and quasi-steady predicted pressure fluctuations continue to decrease with frequency, there is more fluctuation measured on the side glass on-road than predicted based on the yaw fluctuations seen at the probe and this is attributed to self-excited unsteadiness. Tapping 2 is closely positioned to the door mirror and stem assembly, and is therefore correspondingly more affected by the self-excited flow structures being shed from the mirror. This is shown by the rapid increase in transfer function at 2 Hz. The tappings closest to the A-pillar, shown by Figure 4.12(b), appear to show the least self-excited effects owing to their location furthest away from the mirror wake.

4.3.2.2 Self-Excited Effects

In order to better understand the comparative impact of both the externally-imposed unsteadiness and self-excited unsteadiness at the various fluctuation frequencies, the behaviour of the on-road measured and quasi-steady predicted records of surface pressure were assessed in two separate frequency ranges. Using Parseval's Theorem, as outlined by Bendat and Piersol (1993), the area under the ASD is related to the variance of the data. Thus, through a summation within a specified frequency range, the standard deviation of the data between these limits can be determined.

This technique was used to compare the magnitude of the measured and quasi-steady predicted fluctuations in two different frequency ranges. An ASD for both the measured and predicted surface pressure signals was calculated for each time history. From this, the standard deviations were determined between 0.1 Hz and 10 Hz, where the behaviour was mostly quasi-steady, and in the range between 10 Hz and 250 Hz, where self-excited effects dominated. The results of this process are presented by Figure 4.13, showing how Tapping 8 behaves for each of the frequency ranges.

The lower frequency range response is shown by Figure 4.13(a), with each point corresponding to an individual on-road time history. A regression line was plotted through the points, with a guide line showing a equal ratio of on-road measured to quasi-steady predicted unsteadiness. The gradient of this line is similar to the amplitude of the transfer function, with a gradient of unity indicative of an equal measured and simulated response, and thus quasi-steady behaviour. As expected, the behaviour of Tapping 8 between 0.1 Hz and 10 Hz is therefore quasi-steady.

Figure 4.13(b) presents the corresponding data for the frequency band from 10 Hz to 250 Hz, where self-excited unsteadiness takes on increasing importance compared with externally-imposed unsteadiness. What is shown here is that the actual amount of sideglass unsteadiness has a baseline level, dictated by self-excited unsteadiness, in

4. THE TIME-RESOLVED VEHICLE RESPONSE

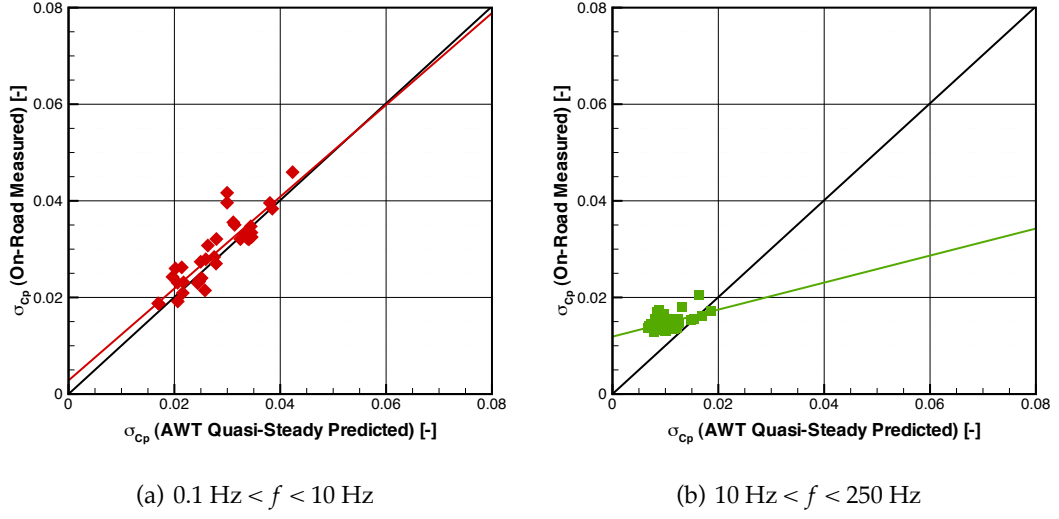


Figure 4.13: Fluctuation of c_p measured on-road against AWT quasi-steady prediction at low and high frequencies (Tapping 8, Geometry 2 SG)

addition to the the smaller dependence on external effects.

If the unsteady aerodynamic response is represented conventionally, using an admittance or transfer function, then this is equivalent to computing the slope for a family of plots such as those of Figure 4.13 at reduced frequency intervals, but in each case forcing an intercept through the origin and taking the slope to the centre of the cluster of points. This is fine for cases where almost all of the unsteadiness is caused by the external source, for instance Figure 4.13(a), but produces misleading results where there is a combination of sources of unsteadiness. A better representation is achieved by separately looking at the intercept and slope of a line through the points, as outlined.

The y -axis intercept of these lines represents the level of self-excited unsteadiness while the slope of this line represents the response of the vehicle to the externally-imposed unsteadiness. From Figure 4.13(b), the self-excited unsteadiness a little greater than 1% of the dynamic pressure, with a slope of 0.3, indicating that at these higher frequencies around 30% of the unsteadiness predicted by a quasi-steady approach due to

externally-imposed fluctuations actually gets translated through to sideglass pressure fluctuations.

4.3.2.3 Separation of External and Self-Excited Unsteadiness

This technique can be extended by determining the slope and intercept of a number of frequency bands to build up a ‘true’ transfer function, unconfused by the presence of self-excited unsteadiness. Figure 4.14 shows data from Tapping 8, but comparing the fluctuation response in narrower frequency bands. Four frequency bands were chosen, equally logarithmically spaced between 0.1 Hz and 250 Hz.

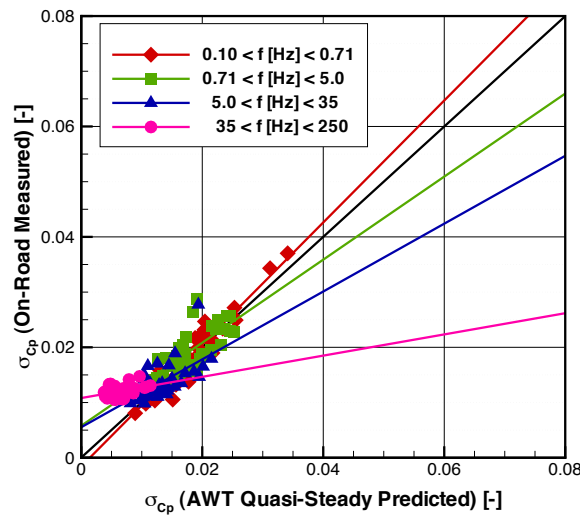


Figure 4.14: Fluctuation of c_p measured on-road against AWT quasi-steady prediction at narrower frequency range (Tapping 8, Geometry 2 SG)

At progressively higher fluctuation frequencies the gradient of the points reduces, indicating a reduction in transfer function amplitude. Simultaneously, there is an increase in the value of the y -axis intercept, as the levels of self-excited unsteadiness increase.

Through the calculation of the gradient and the intercept, two sensitivity coeffi-

4. THE TIME-RESOLVED VEHICLE RESPONSE

cients were generated, determined through linear regression. For the general case of a random sample of observations, the population regression line can be estimated by:

$$\hat{y} = b_0 + b_1x \quad (4.4)$$

where x is the value of the independent variable, \hat{y} is the predicted value of the dependent variable and b_0 and b_1 are the regression constant and coefficient respectively. These were determined using the standard regression formulae given by:

$$b_1 = \frac{\sum_{i=1}^n (x_i - \bar{x})(y_i - \bar{y})}{\sum_{i=1}^n (x_i - \bar{x})^2} \quad (4.5)$$

$$b_0 = \bar{y} - b_1\bar{x} \quad (4.6)$$

where \bar{x} and \bar{y} are the mean values of x and y respectively. In this case, x is equal to the standard deviation of the quasi-steady predicted fluctuations, with y equal to the standard deviation of the measured pressure fluctuations on-road.

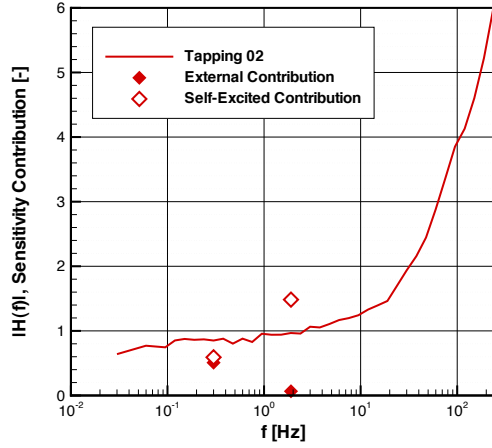
The slope of the line b_1 represents the sensitivity of the sideglass surface pressure response to external unsteadiness and is related to the transfer function amplitude, defining the external contribution sensitivity coefficient. The y -axis intercept b_0 was used to generate a coefficient representing the self-excited contribution of the overall transfer function. This was non-dimensionalised using the unsteadiness measured in the AWT under nominally steady oncoming flow conditions:

$$\text{Self-excited contribution coefficient} = \frac{b_0}{\sigma_{\text{AWT}}} \quad (4.7)$$

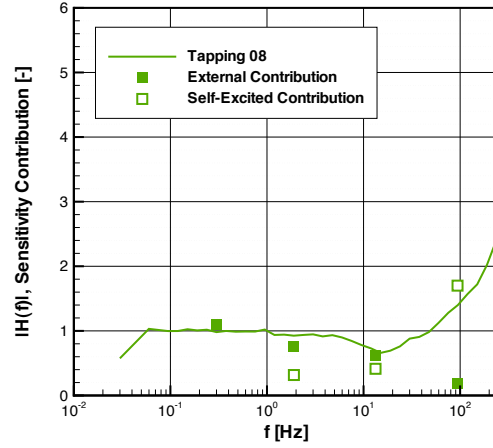
This describes the on-road self-excited unsteadiness as a proportion of the self-excited unsteadiness generated in the AWT.

Both of these coefficients are presented in Figures 4.15–4.17 along with the conven-

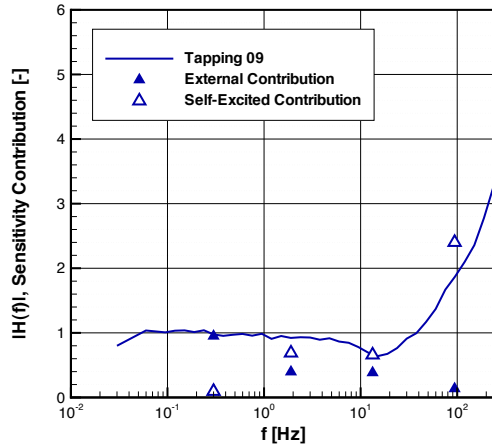
tional transfer functions for each of the sideglass pressure tapings.



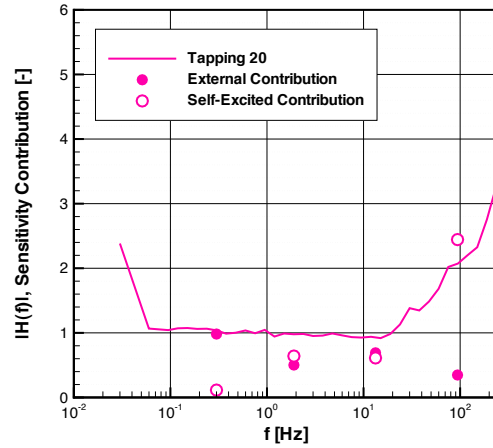
(a) Pressure Tapping 2



(b) Pressure Tapping 8



(c) Pressure Tapping 9



(d) Pressure Tapping 20

Figure 4.15: Contributions of external and self-excited unsteadiness to overall sideglass pressure transfer functions (Mirror wake region, Geometry 2 SG)

As a general observation for all of the tapplings, up until approximately 1–10 Hz, the results from the new method and the conventional transfer function tend to agree, particularly shown by tapplings in the A-pillar vortex region in Figure 4.16. Above this frequency, particularly in regions nearest the mirror wake (Figure 4.15) the new method reveals that progressively less of the energy contained within the external un-

4. THE TIME-RESOLVED VEHICLE RESPONSE

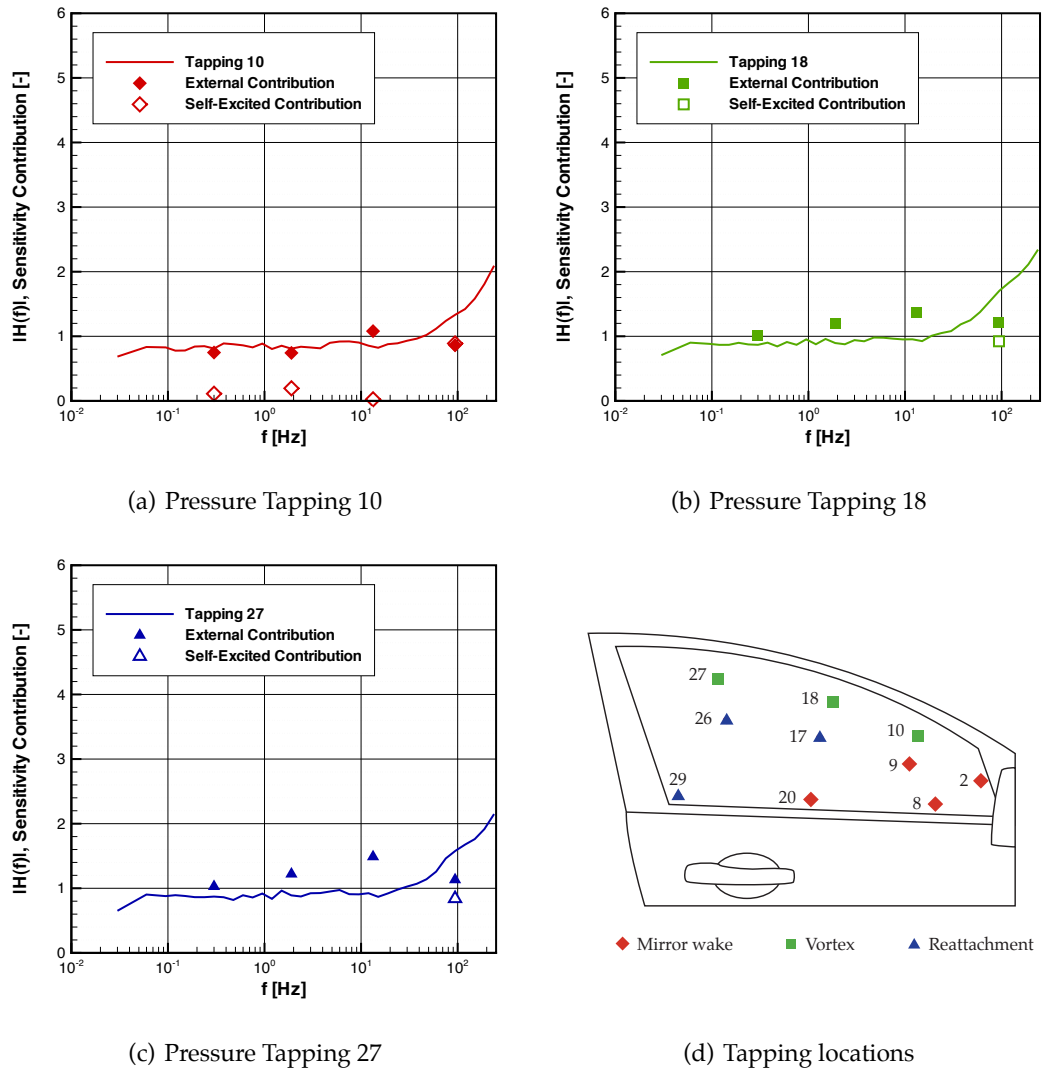
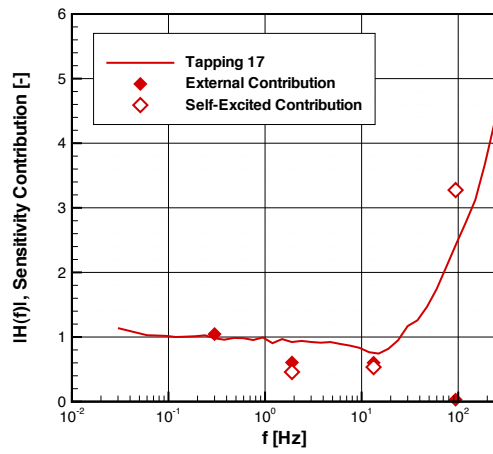
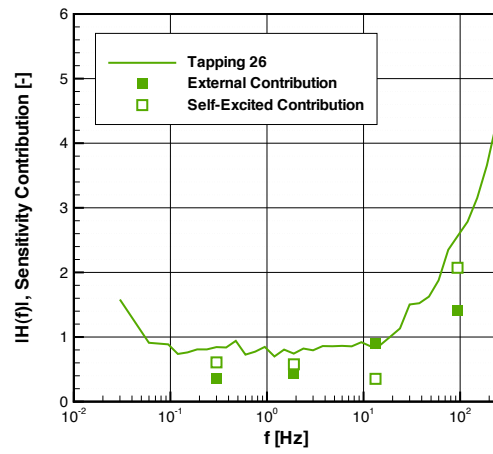


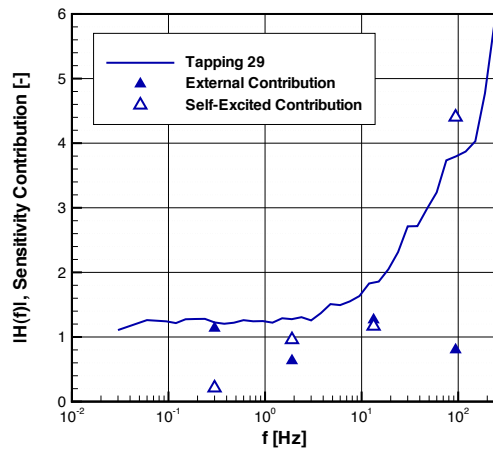
Figure 4.16: Contributions of external and self-excited unsteadiness to overall side-glass pressure transfer functions (A-pillar vortex region, Geometry 2 SG)



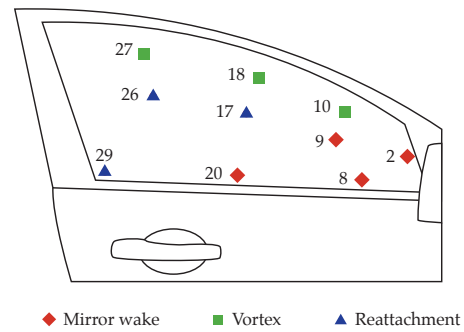
(a) Pressure Tapping 17



(b) Pressure Tapping 26



(c) Pressure Tapping 29



(d) Tapping locations

Figure 4.17: Contributions of external and self-excited unsteadiness to overall side-glass pressure transfer functions (Vortex reattachment region, Geometry 2 SG)

4. THE TIME-RESOLVED VEHICLE RESPONSE

steadiness is transmitted to unsteadiness measured on the sideglass. The method also allows extraction of the self-excited contribution to the unsteadiness. At the lowest frequency band, the self-excited contribution is generally negligible and this increases progressively showing that self-excited effects begin to dominate over externally imposed unsteadiness above about 10 Hz. Tapping 2 is the exception, shown by Figure 4.15(a), since it is dominated by the self-excited unsteadiness close to the door mirror, making it difficult to determine the relative contributions of the unsteadiness due to external or self-excited effects at frequencies above 1 Hz.

The region nearest the A-pillar is perhaps the most interesting, presented in Figure 4.16. This shows quasi-steady behaviour up to between 1–2 Hz, with the transfer function amplitude rising above unity to about 1.2 at frequencies close to 10 Hz. Based on the square root of vehicle frontal area $\sqrt{A_f} = 1.5$ m, this equates to a reduced frequency of approximately $k = 2.6$. However, for the isolated region around the A-pillar, a more representative characteristic length would be of the order of 0.1–0.2 m, leading to reduced frequencies of $k = 0.2$ –0.4. The model-scale findings of Schröck et al. (2011) also found similar behaviour when assessing the aerodynamic side force response with generated upstream turbulence, as shown previously by Figure 1.48(a). Passmore and Mansor (2006) also measured a 20% increase in yaw moment across the measured frequency range in another model-scale investigation, whereby the model was oscillated in steady upstream flow conditions.

The tappings in the vortex reattachment area, shown by Figure 4.17, tend to exhibit characteristics of the nearby, upstream, tappings in the other sideglass regions, with Tapping 17 behaving in a similar manner to Tapping 9, and Tapping 29 similar to Tapping 20. Tapping 26 is more unusual in that it does not show a high-frequency roll-off, rather the transfer function amplitude gradually increases with frequency.

4.4 Cabin Noise

To assess the cabin noise response of the vehicle to unsteady on-road flow conditions, a similar approach to the sideglass surface pressure investigation was used. To overcome the additional challenges of on-road cabin noise measurements containing acoustic content unrelated to fluctuations in the oncoming flow, such as noise from the powertrain and tyres, additional approaches were introduced to capture the cabin noise response in the most representative manner to allow a complete comparison between the two environments. Both vehicle Geometry 1 and Geometry 2 were assessed, allowing the effect of geometry modifications on the cabin noise response to also be investigated. This determined how a relatively minor change to a significant noise-producing component affects the transient behaviour. In addition, using a quasi-steady cabin noise simulation technique, the impact of transient cabin noise modulations on the wind noise perception by cabin occupants was also investigated.

4.4.1 Steady State Cabin Noise Characteristics

A similar technique was used to determine the quasi-steady predicted cabin noise response as when calculating the quasi-steady sideglass pressure response. However, there are three key differences between the pressure and cabin noise predictions. Firstly, the steady-state cabin noise response of the vehicle is a function of both flow speed and yaw angle. Conversely, the c_p characteristics are functions of yaw angle alone, since the c_p definition accounts for the variations in dynamic pressure with changes in flow speed. Therefore steady-state characteristics dependent on both flow speed and yaw angle were used.

Secondly, the cabin noise response varies depending on the specific frequency of the cabin noise considered. For instance, it is likely that the specific frequency of noise

4. THE TIME-RESOLVED VEHICLE RESPONSE

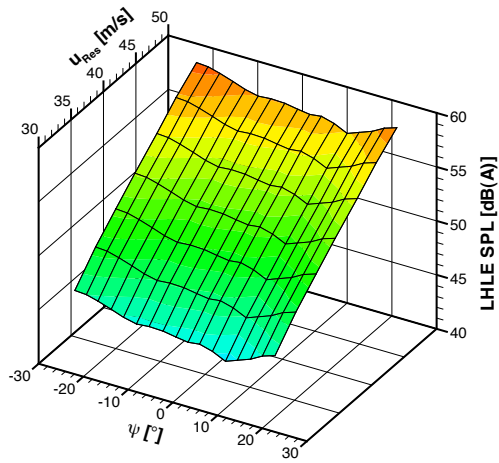
generated by the mirror stem will vary at yaw to a different extent to the noise generated by the windscreen wipers. This is because the flow is likely to separate by differing amounts at yaw for each of the geometry components. It is important to clarify here the difference between the fluctuation frequencies related to the cabin noise modulations (between approximately 0.1–250 Hz) and the frequency bands of the cabin noise itself (presented here above 800 Hz). In this work, the lower-frequency fluctuations of the higher-frequency noise-generating pressure fluctuations were considered and how they are affected by oncoming flow unsteadiness. The behaviour of each individual third-octave characteristic against that of the overall SPL characteristic is discussed later on in this section, but to fully capture the individual response of the various frequency bands, a number third-octave band characteristics were considered.

Finally, since the cabin noise is made up of various sources, including non-aeroacoustic sources on-road, the assessment of the cabin noise response over the entire cabin noise spectrum was not possible, since the quasi-steady predicted cabin noise was only able to predict the steady-state response of the wind noise component of the overall cabin noise. Therefore, cabin noise response of a range of frequency bands was explored, although the main focus was of cabin noise frequencies strongly related to wind noise, as identified previously in Figure 3.26.

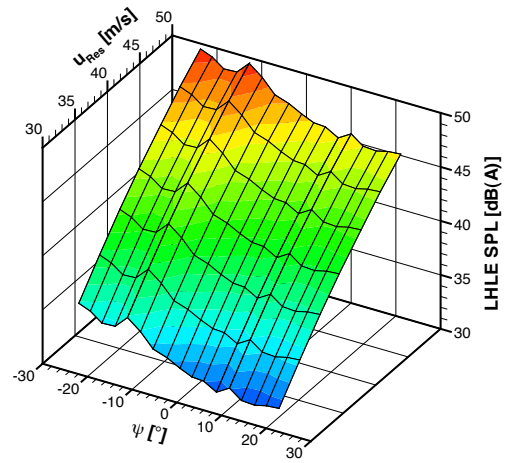
Some example third-octave cabin noise characteristics as obtained in the Pininfarina AWT are presented in Figure 4.18. These show how the different cabin noise frequency bands respond to variations in flow speed and yaw.

These are a compound surface of the yaw and flow speed cabin noise characteristics determined in the AWT, similar to those shown in Figures 3.17(a) and 3.13(b) respectively. In producing the surface, multiple yaw sweeps and a zero-yaw speed sweep were combined to produce an overall surface.

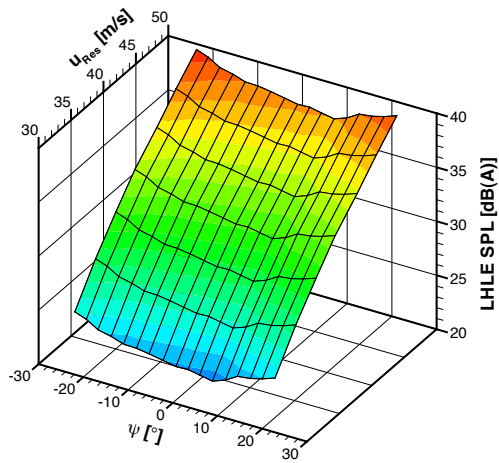
In generating a cabin noise versus flow speed characteristic in the AWT, the cabin



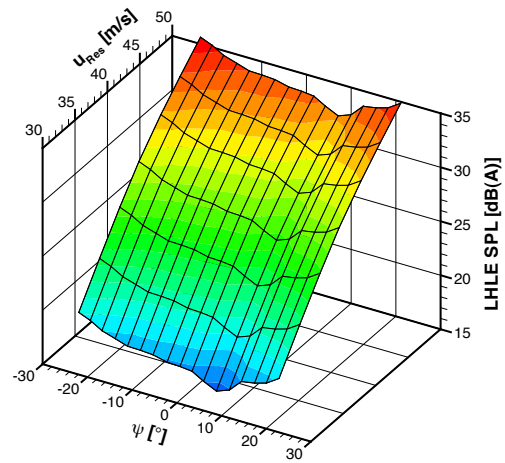
(a) 800 Hz centre frequency



(b) 4000 Hz centre frequency



(c) 6300 Hz centre frequency



(d) 8000 Hz centre frequency

Figure 4.18: Vehicle Geometry 1 AWT cabin noise third-octave characteristics

4. THE TIME-RESOLVED VEHICLE RESPONSE

noise was measured at a series of discrete flow speeds at zero yaw. When interrogating this characteristic, linear interpolation was used to determine the level of cabin noise at a particular flow speed. However, as demonstrated previously, the physical link between the flow speed and cabin noise is not linear but logarithmic. Figure 4.19 shows the overall linearly interpolated cabin noise characteristic in addition to a comparison of the linear approximation and true logarithmic behaviour of the measured overall cabin noise at zero yaw.

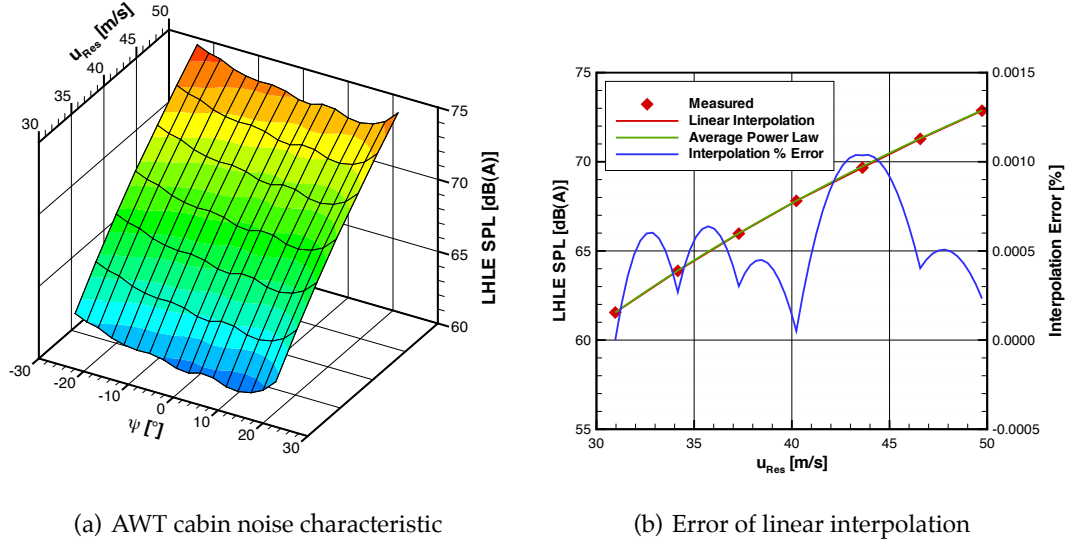


Figure 4.19: Vehicle Geometry 1 AWT cabin noise characteristic

To calculate the logarithmic relationship, the power law between adjacent measured points was determined. These were then averaged to capture the overall power relationship relative to u_{Ref} , the flow speed measured at the probe with the tunnel running at a nominal velocity of 100 kph (27.78 ms^{-1}), described by:

$$L(u) = L(u_{Ref}) + 10 \log \left(\frac{u}{u_{Ref}} \right)^{5.50} \quad (4.8)$$

The percentage error, defined as the percentage error relative to the logarithmic power

law, between the linear approximation and the logarithmic relationship is also plotted by Figure 4.19. This shows that the error is generally below 0.001% for the range of flow speeds tested. For comparison, 0.001% of 70 dB(A) is of the order of 0.001 dB(A), well within the measurement error of the apparatus, therefore indicating that the linear approximation of the flow speed and cabin noise relationship is satisfactory.

4.4.2 Assessment of the Frequency Response

4.4.2.1 Linearised Transfer Functions

A similar approach to the surface pressure data was taken for the cabin noise data. In generating the steady-state predicted cabin noise fluctuations, the AWT-predicted cabin noise characteristic for each individual third-octave band was used to determine the cabin noise fluctuation for that particular band for a given on-road measured on-coming flow fluctuation. The result of this process is shown in Figure 4.20, where a short example of an on-road time history is used to compare the measured cabin noise and the quasi-steady predicted cabin noise for the 4 kHz third-octave frequency band for the Geometry 1 vehicle.

For this data, it is shown that the predictive technique captures the overall shape of the measured time-history well, predicting the overall level and size of the larger fluctuations with relative accuracy. This indicates that not only does the predictive model work well, but also that the longer fluctuations in the measured cabin noise are indeed due to variations in the oncoming flow as measured by the roof-mounted probe. The most significant difference between the two signals is the level of higher-frequency content present in the measured on-road cabin noise, which is not present in the quasi-steady prediction. This indicates that there is a level of high-frequency fluctuations heard inside the cabin not due to fluctuations in the oncoming flow.

To further investigate this, the transfer function approach was continued, with the

4. THE TIME-RESOLVED VEHICLE RESPONSE

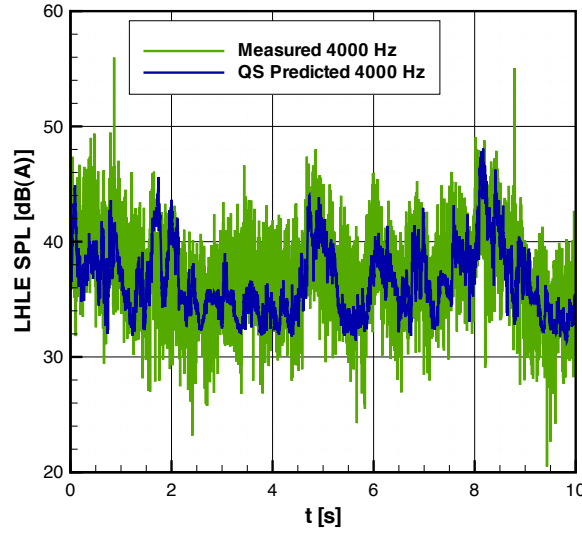
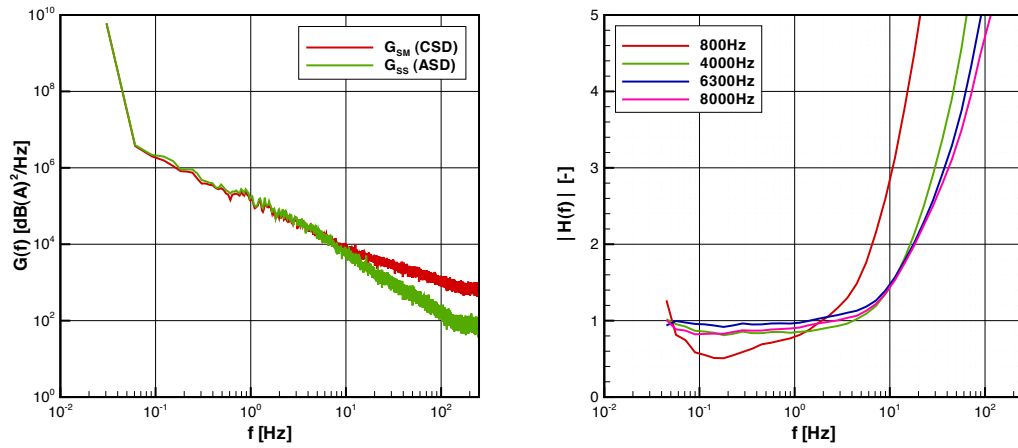


Figure 4.20: Temporal comparison between cabin noise measured on-road and quasi-steady predicted from steady wind tunnel (4000 Hz, Geometry 1)

appropriate spectral densities of the two signals determined using the complete set of on-road measured time-histories for the Geometry 1 vehicle. Figure 4.21(a) shows the cross-spectral density (CSD) of the measured and simulated traces $G_{SM}(f)$ and the autospectral density (ASD) of the simulated traces $G_{SS}(f)$. Recall that these act as precursors to the overall transfer function, which is a quotient of the CSD and ASD, with the transfer function for a selection of third-octave bands presented by Figure 4.21(b).

The third-octave bands chosen comprise two different sets of sources. The 800 Hz band, as shown previously, is dominated by road noise emanating from the contact of the tyres on the road surface. Therefore whilst this band does contain some aeroacoustic content, the fluctuations of this frequency band are primarily due to changes in the road surface, rather than fluctuations in the oncoming flow conditions. Conversely, the 4, 6.3 and 8 kHz bands are dominated by wind noise sources.

For each of these wind-noise dominated bands, the magnitude of the transfer function up to approximately 5 Hz remains close to unity, indicating quasi-steady be-



(a) Comparison of spectra (4000 Hz band) (b) Transfer functions of selected frequency bands

Figure 4.21: Transfer functions between quasi-steady predicted and on-road measured cabin noise, based on steady AWT characteristics (Geometry 1)

haviour. Above this frequency, the transfer function magnitudes rises rapidly. This is also shown specifically for the 4 kHz third-octave band spectra in Figure 4.21(a), where the higher frequency deviation indicates that there was an increase high-frequency energy contained within the measured cabin noise signal.

The road-noise dominated 800 Hz band behaves differently to the wind noise dominated bands at lower frequencies, in that the lowest frequency point is greater than unity, indicating that the steady-state SPL is greater on-road than predicted in the AWT. This has been shown previously to be the case when comparing the time-averaged SPL between on-road and in the AWT in the previous chapter, specifically in Figure 3.26, where this difference is due to the road noise not present in the AWT. At subsequently higher frequencies, the transfer function magnitude drops below unity, indicating a reduced level of 800 Hz fluctuations heard in the cabin than predicted from the oncoming flow unsteadiness. This is due to aeroacoustic fluctuations being masked by the dominant road noise as heard inside the cabin.

4. THE TIME-RESOLVED VEHICLE RESPONSE

As with the sideglass surface pressure fluctuations, the cabin noise fluctuations heard inside the vehicle are not solely due to fluctuations in the oncoming flow. Self-excited unsteadiness from the various vehicle geometry scales, ranging from the bluff body of the vehicle itself to the smaller components such as the door mirrors and wind-screen wipers lead to an ensemble of scales and fluctuation frequencies. These self-excited effects lead to fluctuations of the various cabin noise frequency bands and are ultimately the cause of having to record the cabin noise in the AWT for a period of time before averaging to determine the SPL at a given vehicle condition. These fluctuations are removed during this averaging process and thus are not captured by the AWT determined steady-state cabin noise characteristic.

A rudimentary assessment of the minimum frequency that would be affected by these self-excited effects can be determined using the Strouhl number. By assuming $St = 0.21$, the nominal flow speed as $u = 36.1 \text{ ms}^{-1}$ and a maximum characteristic length of the square-root of vehicle frontal area, where $A_f = 2.33 \text{ m}^2$, leads to a minimum self-excited fluctuation frequency of approximately 5 Hz as shown by:

$$f = \frac{St \cdot u}{\sqrt{A_f}} = 5 \text{ Hz} \quad (4.9)$$

This appears consistent with the rapid rise in transfer function magnitude as shown by Figure 4.21(b). Therefore, the transfer functions contain both self-excited content and the content relating to the response of the vehicle to unsteadiness in the onset flow. This makes it difficult to assess solely the response to the unsteady oncoming flow conditions isolated from the self-excited unsteadiness of the vehicle. Thus to be able to assess the response of the vehicle to unsteadiness in the oncoming flow alone, an alternative approach was required that allows for the self-excited effects to be captured and removed from the overall transfer function.

4.4.2.2 Broadband Modulation Approach

The previous linearised technique involves modulating the time-averaged cabin noise according to the characteristics measured in the AWT and comparing this to the time-varying cabin noise measured on-road. Thus the self-excited content is present in the on-road data, whilst it is removed during the time-averaging operation in the AWT. This is equivalent to taking a time history of a constant level, determined in the AWT at a zero yaw, nominal flow speed condition, and increasing or decreasing this level based on the steady AWT characteristic of Figure 4.19(a). This process is shown by Figure 4.22.

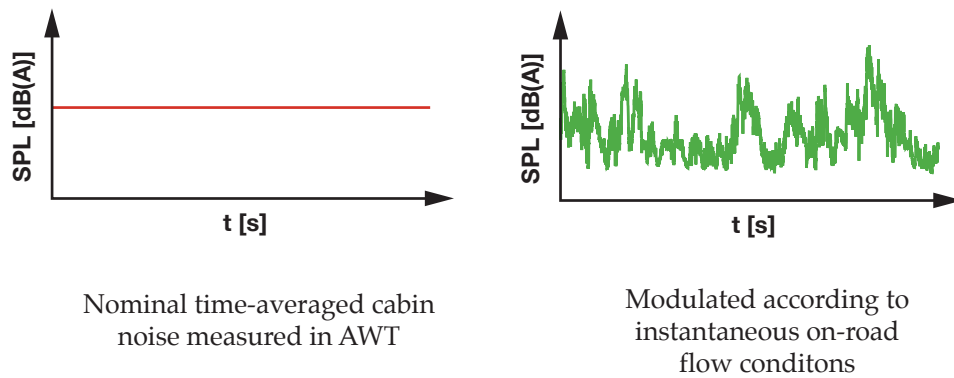


Figure 4.22: Cabin noise simulation using time-averaged characteristic alone

If instead of using the time-averaged SPL determined in the AWT, the time-varying SPL signal, as recorded in the AWT, was used and modulated according to the AWT characteristic as before, this allows the self-excited frequency content to be captured in addition to the response due to oncoming flow unsteadiness. These self-excited effects are then included in both the on-road measured and quasi-steady predicted cabin noise signals, allowing these effects to be ‘cancelled out’ in calculating the transfer function. This process is shown in Figure 4.23.

4. THE TIME-RESOLVED VEHICLE RESPONSE

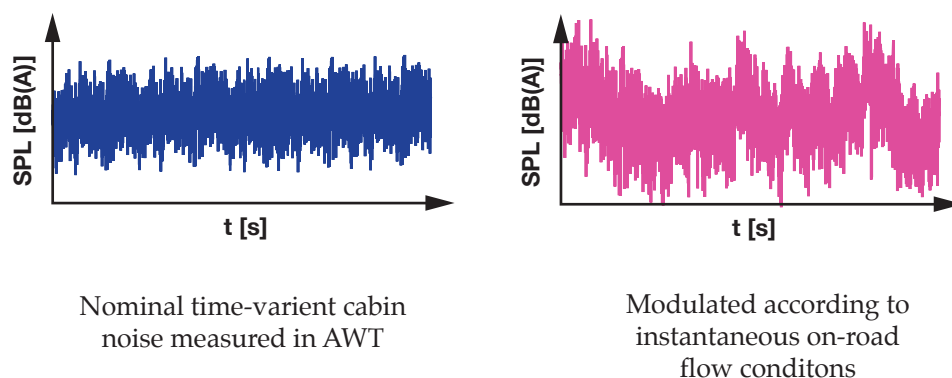
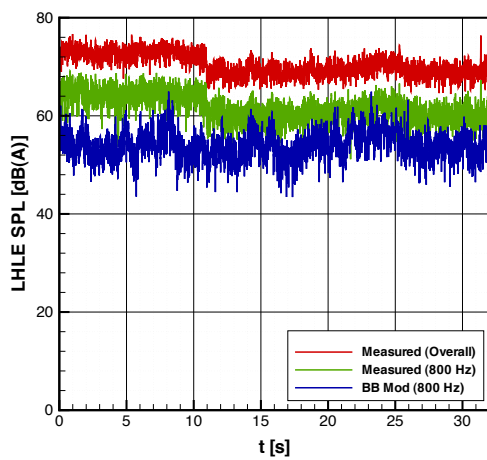


Figure 4.23: Cabin noise simulation through modulation of the time-variant cabin noise

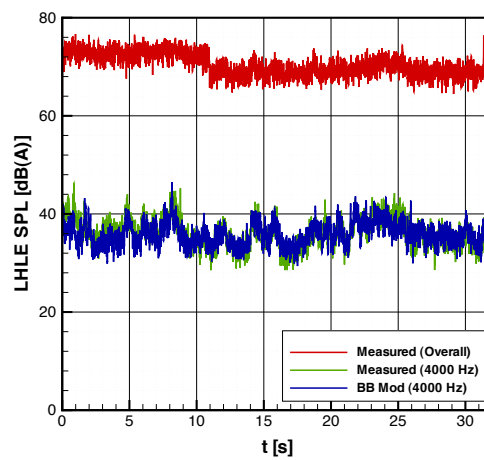
The key difference between this technique and the previous using the time-averaged characteristic alone, is that the characteristic is used to determine the increase in SPL from the SPL measured in the nominal zero yaw, 36.1 ms^{-1} vehicle speed condition. This signal is then used to modulate the overall level of the cabin noise recorded in the AWT under these nominal conditions. This technique is analogous to amplitude modulation in radio transmission.

The modulation was completed using a C-language routine which read in the nominal AWT cabin noise as a Wave (*.wav) file and modulated the signal according to the steady-state characteristic response to yaw and flow speed as measured in the AWT. Linear interpolation was used to upscale the sampling frequency of the measured flow data to match that of the audio data. A new Wave file was then produced and processed in an identical manner to the on-road measured cabin noise files, allowing the third-octave frequency bands of SPL to be extracted. A convenient by-product of this approach is that an audio file of the simulated wind noise is produced, allowing subjective listening studies to take place on various wind conditions and vehicle characteristics. This was exploited later in Section 4.5.

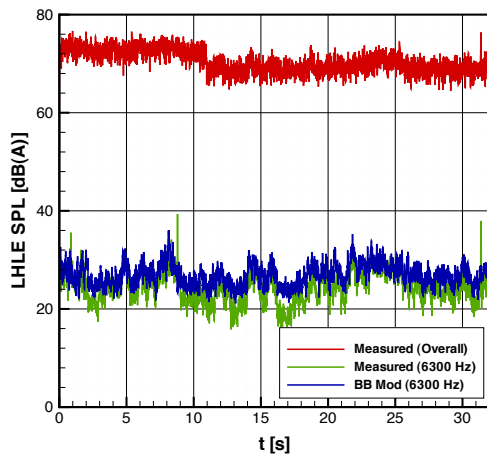
Figure 4.24 shows the results obtained using the broadband modulation approach, using an example time history to compare the signals in the time domain. The same four third-octave frequency bands are presented in Figures 4.24(a) – 4.24(d) for a Geometry 1 vehicle. For each graph, the on-road measured and quasi-steady wind tunnel predicted cabin noise time histories for each third-octave frequency band are presented and compared against the measured overall cabin noise SPL.



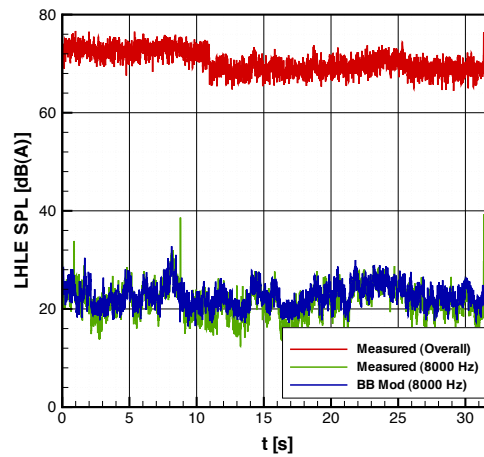
(a) 800 Hz centre frequency



(b) 4000 Hz centre frequency



(c) 6300 Hz centre frequency



(d) 8000 Hz centre frequency

Figure 4.24: Temporal comparison of broadband simulated and measured cabin noise (Geometry 1)

4. THE TIME-RESOLVED VEHICLE RESPONSE

The example history was selected particularly due to the clearly identifiable change in road surface occurring after approximately eleven seconds, where the vehicle transitions between a coarser road surface to a quieter, smoother surface. As previously shown, the 800 Hz third-octave band is dominated by road noise and this is shown by Figure 4.24(a). Comparing the overall SPL with the on-road measured 800 Hz band, the road surface transition is clearly identifiable. Since the road noise is independent of the oncoming flow conditions (and indeed unrelated to the wind noise contribution to the overall cabin noise), this transition is not captured by the simulated cabin noise.

From Figure 4.24(a), the predicted wind noise SPL is between 10–15 dB below the measured cabin noise SPL for this frequency band. From Section 1.3.5.1, Helfer and Wiedemann (2006) noted that as a rule-of-thumb, AWT background noise should be around 10 dB below the wind noise levels of interest. This ensures that the tunnel background noise is insignificant compared to the measured wind noise of the vehicle. In the same vein, since the difference between the measured and predicted 800 Hz third-octave cabin noise is of the same order of magnitude owing to the road noise contribution in the measured cabin noise, it may be argued that the wind noise fluctuations in this band will be well masked and unlikely to be perceived by the occupants of the vehicle.

For the wind noise dominated frequency bands, presented by Figures 4.24(b) – 4.24(d), the correlations between the measured and predicted signals is much stronger. From a rudimentary temporal comparison of an example time history, it appears that both the higher and lower frequency content is captured well by the AWT quasi-steady predicted method.

The previous process took the AWT characteristics for each third-octave band and predicted how each band would fluctuate based on the oncoming flow conditions. This broadband technique uses the overall SPL characteristic and modulates the nom-

inal cabin noise signal without differentiating between the various third-octave frequency bands.

An advantage of the broadband approach is that it is relatively simple to implement, with all processing taking place in the time domain. Therefore the modulation of the sound file can be completed instantaneously, with no delays in processing. Whilst this is not necessarily an advantage specifically when assessing the response of the vehicle in the context of this thesis, it would be an advantage when instantaneously generating wind noise for use in, for example, a driving simulator. This would allow the wind noise to be simulated based on the deterministic input of a driver based on a vehicle speed or location (and hence wind condition) input.

However, the fundamental disadvantage of a broadband technique is that it assumes a consistent response over the entire acoustic frequency range. To assess the validity of this technique in capturing the behaviour of the key wind noise third-octave frequency bands, the variation of these bands was compared against the overall SPL as both the flow speed and yaw angle was varied in the AWT. An equal SPL increase of both a third-octave band and the overall SPL would imply that the broadband modulation technique models that particular band well. If the increase in SPL is different, then this band will experience either an over or under amplification with the broadband technique. The results of this process are presented, with Figure 4.25 showing the relationship between a number of key third-octave bands and the overall SPL as the flow speed is increased in the Pininfarina AWT. The diagonal gridlines indicate an equal overall SPL to third-octave ratio.

The same four key third-octave bands are shown as in Figure 4.21 when presenting the transfer functions using the previous technique. For variations in flow speed as shown by Figure 4.25, the 800 Hz third-octave band shows an equal increase in SPL to the overall level increase. However, as demonstrated previously, this frequency band

4. THE TIME-RESOLVED VEHICLE RESPONSE

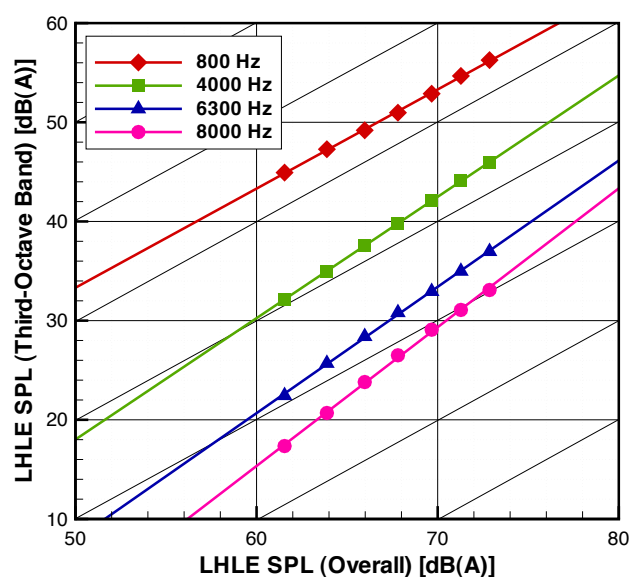


Figure 4.25: Comparison between third-octave and overall SPL under changes to resultant flow speed in AWT (Geometry 1)

tends to be less significant to an occupant's perception of wind noise on-road as this frequency band is dominated by road noise. The higher frequency third-octave bands show an increased sensitivity to flow speed, where the vehicle responds more greatly to changes in flow speed at these higher frequencies than the overall SPL. Therefore a broadband modulation technique will tend to underestimate modulations of sounds at these higher frequencies.

An alternative method to determine the behaviour of the third-octave bands against that of the overall level is the comparison on the source index of particular frequency bands, previously shown by Figure 3.14. Bands with a source index of greater than the overall index of 5.5 will tend to show an under-prediction of their modulation, with source indices of below 5.5 showing an over-prediction. However, since flow speed increases over a vehicle generally show a broadband increase in aeroacoustic noise, the behaviour of the various third-octave bands is closely related to the overall SPL increase.

Figure 4.26 assesses this behaviour with changes in oncoming flow yaw angle. Owing to the different flow regimes occurring on a particular side of the vehicle at yaw, the response to changes in yaw angle will be different under both positive and negative yaw angles.

At increasing negative yaw angle, shown by Figure 4.26(a), the response of the vehicle is similar to changes in flow speed, albeit with a smaller range of SPL. At negative yaw, the side of the vehicle adjacent to the LHLE acoustic head channel is in a leeward condition. Each of the three high-frequency third-octave bands thus will be slightly under-represented by the broadband modulation technique, with the 4 kHz band being the most significantly under-represented.

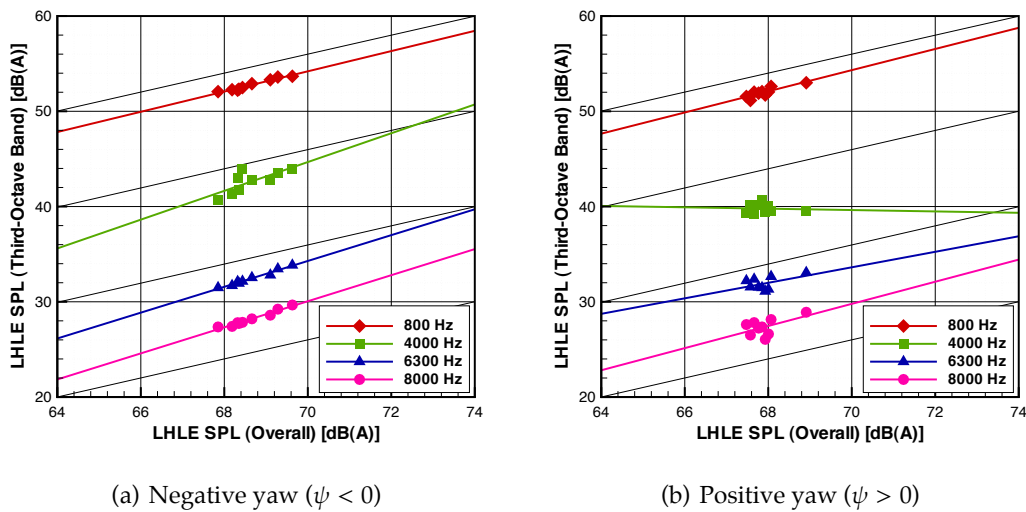


Figure 4.26: Comparison between third-octave and overall SPL under changes to yaw angle in AWT (Geometry 1)

Under positive, windward, conditions there is less of a defined relationship between the third-octave bands and the overall SPL, indicating that there is less effect in variations at positive yaw compared to under negative yaw conditions. However, there is still a generally consistent relationship between overall SPL and the various

4. THE TIME-RESOLVED VEHICLE RESPONSE

third-octave bands presented. Both the 800 Hz and 8 kHz bands behave in a similar manner under negative yaw conditions, whereas the 6.3 kHz band will be slightly over-represented by the broadband modulation technique, with SPL changes in the overall level being greater than for the third-octave band.

The most significant difference in behaviour occurring under positive yaw angle conditions is with the 4 kHz third-octave band. As the vehicle is yawed within this range, changes occurring in the overall SPL of the vehicle are not reproduced by this band, which remains relatively constant. A broadband modulation approach with therefore significantly over-estimate the level of fluctuations occurring in this frequency band for this range of flow conditions.

Whilst the focus has been on cases where it is imperfect, overall the broadband modulation approach captures the behaviour of the third-octave frequency bands well. There is a general trend towards under-estimation of the key wind noise dominated third-octave frequency bands, and this is most likely to occur when the oncoming flow is dominated by changes in flow speed or within the negative yaw angle range. For fluctuations in flow in the positive yaw angle range, these bands are more likely to over-predicted, particularly for the 4 kHz third-octave band.

However, to fully compare the cabin noise response of the vehicle to oncoming flow unsteadiness, the transfer function $H(f)$ was calculated, allowing a comparison of the magnitudes of the measured and quasi-steady predicted signal to be determined at the range of fluctuations frequencies, thereby assessing the validity of the quasi-steady environment in capturing the response to oncoming flow unsteadiness. Figure 4.27 shows the result of this process, with each of the four third-octave frequency bands presented.

The transfer function resulting from the broadband modulation technique of Figure 4.27 appears to be quite different from that based on the instantaneous AWT char-

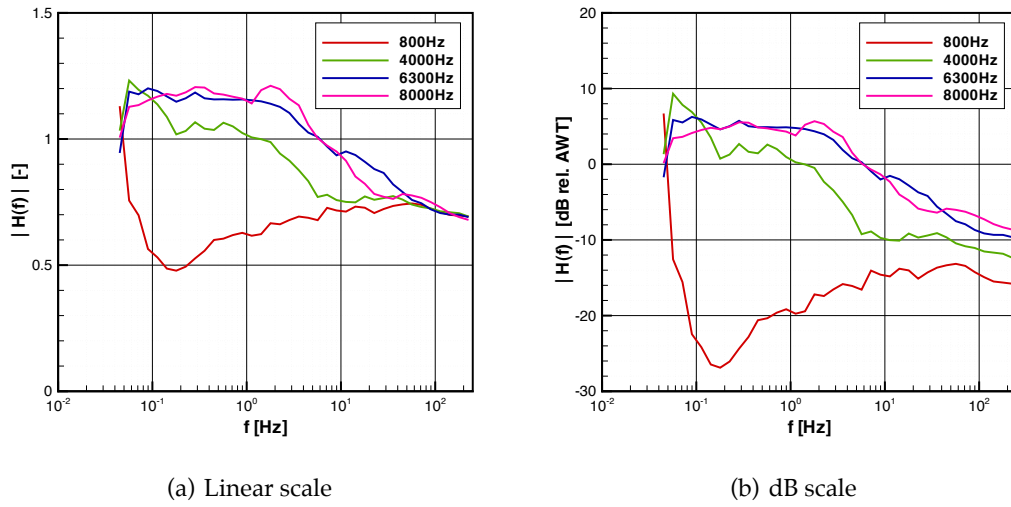


Figure 4.27: Transfer functions between quasi-steady predicted and on-road measured cabin noise, using broadband modulation simulation technique (Geometry 1)

acteristic method presented by Figure 4.21(b). To compare these transfer functions more closely, and to explain the different features, the transfer functions are divided into three key sections:

‘Steady-State’ Lowest Frequency Point: The first, lowest frequency points on the transfer functions of both the linearised and broadband techniques relates to the time-averaged cabin noise ratio between the measured on-road data and the wind tunnel data. Since the transfer function is a ratio of the on-road data divided by the wind tunnel simulated data, the 800 Hz frequency band, dominated by road noise, is significantly greater than unity. The wind noise dominated higher-frequency third-octave bands are much closer to unity, since the time-averaged cabin noise content in these frequency bands is similar between the two environments. Since the two simulation techniques do not generally affect the time-averaged cabin noise, this ‘steady-state’ point is approximately the same for both transfer functions of Figure 4.21(b) and Figure 4.27(a).

4. THE TIME-RESOLVED VEHICLE RESPONSE

Low-Frequency Content ($f < 2$ Hz): As previously shown by Figure 4.21(b), the transfer function amplitude of the non-broadband modulated technique was very close to unity up to approximately 2–5 Hz for the wind noise dominated high-frequency content. However, for the broadband modulated technique, the transfer function amplitude was up to 20% higher, indicating a greater amplitude of cabin noise fluctuations measured on-road than predicted using the broadband simulation technique.

The same transfer functions are presented in Figure 4.27(b), with a dB scale relative to the steady-state SPL as measured in the AWT. This is perhaps a more natural method of presenting ratios of SPL measured in dB. From this, it can be seen that a 20% increase in transfer function magnitude relates to an approximate increase in SPL of 5 dB. The greater-than-unity transfer function is expected from the broadband modulation technique itself. Figure 4.25 shows that the higher frequency third-octave bands show an increased sensitivity to changes in oncoming flow speed since the noise within these higher third-octave bands responds more strongly to changes in flow velocity, over that of the overall SPL. This resulted in the broadband modulation technique under-predicting the simulated cabin noise. The transfer function method used to compare both the measured and quasi-steady predicted cabin noise is the quotient of the measured over the predicted signals. Therefore, under-estimation of the predicted cabin noise leads to an increase in the transfer function amplitude.

Since the resulting transfer function amplitude is correspondingly greater, this effect is clearer with the higher frequency 6300 Hz and 8000 Hz bands, which in turn showed greater sensitivity in Figure 4.25 than the 4000 Hz band. This does not explain the low-frequency peak in the 4000 Hz transfer function, although this is likely to be due to non-linear yaw angle effects affecting each

third-octave frequency band differently when faced with a particular set of on-coming on-road flow conditions. This is shown by Figure 4.26(b), where the behaviour of the 4000 Hz band under positive yaw angles is significantly different when under negative yaw angle conditions. The 800 Hz road noise band is comparatively unchanged between simulation techniques.

Since the transfer function amplitudes are relatively constant in the low-frequency range, it is likely that this recorded deviation from quasi-steady behaviour was due to the broadband prediction technique rather than the response of the vehicle, which is likely to remain quasi-steady for the wind noise dominated cabin noise content.

High-Frequency Content ($f > 2$ Hz): As expected, the most significant difference in the transfer functions between the broadband modulation technique and the linearised AWT characteristic method occurs for the higher modulation frequencies (> 5 Hz). The previous self-excited effects were removed and the expected progressively decreasing transfer function amplitude is present at fluctuation frequencies greater than 2–5 Hz. As stated previously, at these higher frequencies the magnitude of the transfer functions gradually decreases as the smaller fluctuations of the oncoming flow unsteadiness have a progressively reduced impact on fluctuations in noise as heard inside the cabin. By 250 Hz, the decrease in transfer function amplitude had decreased by 10 dB, indicating fluctuations that would be barely perceived in the cabin.

4.4.2.3 Third-Octave Modulation Approach

A third-octave modulation approach was developed, building on both the linearised transfer function and broadband modulation methods. To recall, the linearised approach allowed linear transfer function techniques to be used when assessing the in-

4. THE TIME-RESOLVED VEHICLE RESPONSE

herently non-linear response of the cabin noise to changes in yaw angle, with the broadband modulation technique separating the response of the vehicle to external unsteadiness from that of self-excited content. Whilst the broadband modulation technique was able to capture the key features of the vehicle response, including the transfer function roll-off at frequencies greater than 2 Hz and the flat response at frequencies below this, transfer functions greater than unity were found to exist at low frequencies as an artefact of the broadband technique.

With the third-octave modulation technique, instead of using the overall cabin noise characteristic to generate the quasi-steady predicted cabin noise response, the third-octave characteristics were used. This allowed the individual sensitivity of each third-octave band to flow speed and yaw to be captured with greater accuracy, thereby removing the artificial increase in transfer function amplitude due to the broadband quasi-steady simulation technique. This therefore has the potential for allowing a clearer picture of the true vehicle response to unsteady external fluctuations, without being coloured by either self-excited effects or artefacts of the analysis process.

The third-octave modulation simulation process is outlined in Figure 4.28. Firstly, the baseline cabin noise recorded in the AWT at zero yaw and at 36.1 ms^{-1} was filtered into separate third-octave bands using sixth-order filters as specified by the standard ANSI/ASA S1.11-2004 (2004). These filtered bands were then modulated based on the on road conditions and the steady state dependence of that third octave band on yaw and flow speed as determined from the AWT, in exactly the same manner as with the previous broadband modulation approach. Finally, each of the individual bands were then recombined to produce the overall quasi-steady cabin noise simulation. This was then processed in the same way as the on-road measured data, allowing the comparative transfer functions to be generated.

Figure 4.29 shows the results obtained using the third-octave modulation approach

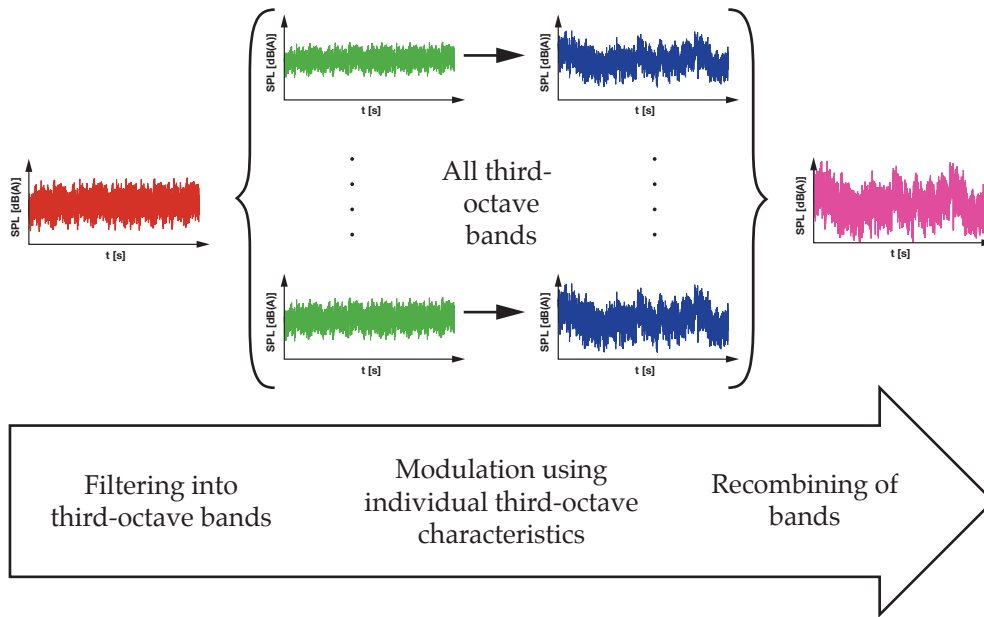


Figure 4.28: Cabin noise simulation through third-octave modulation of the time-variant cabin noise

and comparing these against the measured on-road data. The same example time history was used as when comparing the results of the broadband modulation approach in Figure 4.24. Here, the two wind-noise dominated bands centred about 6300 Hz and 8000 Hz are presented.

Overall, the third-octave modulation technique showed excellent correlation with that of the measured cabin noise. Whilst there is a slight shift in the absolute levels between the simulated and measured signals for the 6300 Hz band in Figure 4.29(a), both the higher and lower frequency content appears to be very well captured. In particular, the 8000 Hz band simulation is practically indistinguishable from the measured signal in the time domain. When comparing the results of the third-octave simulation with the previous equivalent broadband comparison of Figures 4.24(c) and 4.24(d), it can be seen that the measured amplitude fluctuations are captured more accurately than in

4. THE TIME-RESOLVED VEHICLE RESPONSE

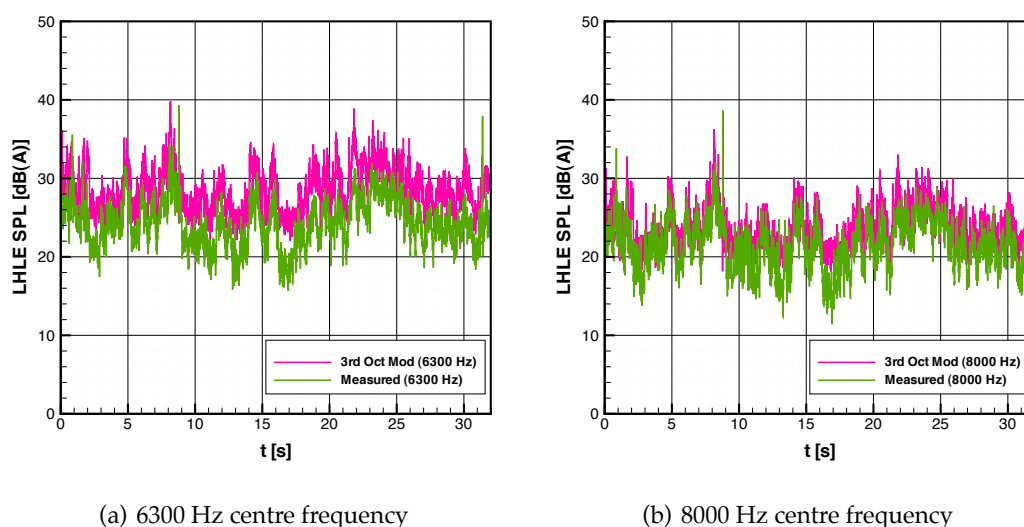


Figure 4.29: Temporal comparison of third-octave simulated and measured cabin noise (Geometry 1)

the third-octave simulation. This indicated that, in the time domain, the third-octave technique more accurately captured the quasi-steady predicted cabin noise response of the vehicle than that of the broadband approach.

For a more comprehensive analysis of the nature of the vehicle response, transfer functions were once again used to compare the measured signals with those predicted using the quasi-steady technique. As before, the transfer function was defined as a ratio comparing the measured to the quasi-steady predicted cabin noise signals. Therefore, a transfer function amplitude of less than unity indicates a reduced response measured on-road than predicted using the steady conditions of the AWT. An amplitude of greater than unity indicates an increased response on-road, with amplitudes of unity indicative of a quasi-steady response.

The resulting transfer functions generated using the third-octave modulation process are shown by Figure 4.30, focussing on three key wind noise frequency bands as previously presented. As with the broadband technique, the transfer function ampli-

tudes are shown both linearly as well as logarithmically using the SPL measured in the AWT as a reference.

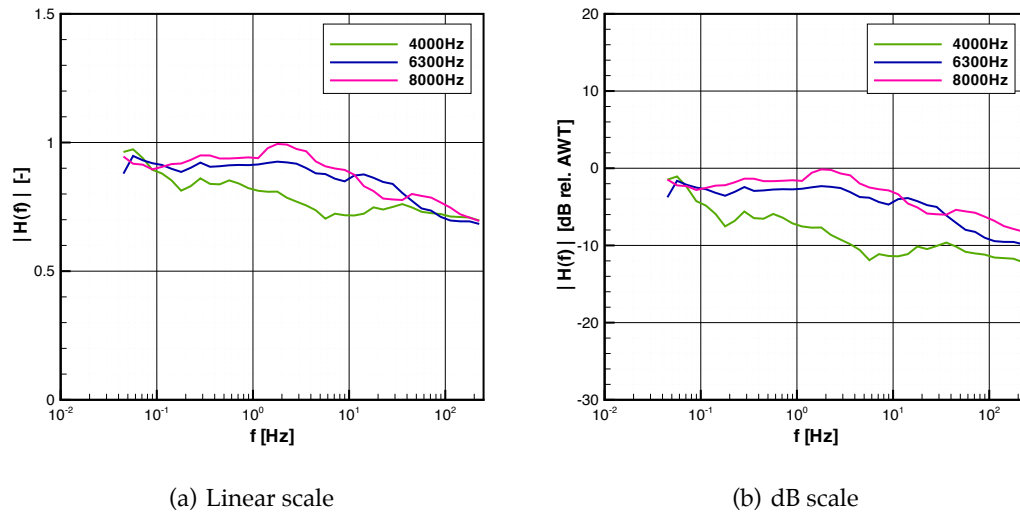


Figure 4.30: Transfer functions between quasi-steady predicted and on-road measured cabin noise, using third-octave modulation simulation technique (Geometry 1)

Since the third-octave modulation technique made no significant modifications to either the average on-road measured or the steady-state AWT overall SPL, the initial steady-state frequency point is relatively unchanged from the equivalent points on both the linearised or broadband modulations approaches. The slight decrease in transfer function amplitude at this point was due to an increase in average levels of each of the third-octave bands by the simulation technique when compared to the frequency-averaged broadband approach.

Up to 2 Hz, the transfer function amplitude for the 6300 Hz and 8000 Hz frequency bands remains at a fairly constant level, 2 dB below the SPL as measured in the AWT, providing strong evidence of the quasi-steady cabin noise response of the vehicle for frequencies up to 2 Hz. The 2 dB level reduction suggests that the third-octave modulation approach tends to over-estimate the amplitude of the cabin noise fluctuations,

4. THE TIME-RESOLVED VEHICLE RESPONSE

albeit to less of an extent than the broadband under-estimation, which resulted in transfer function amplitude increases of the order of 5 dB. A slight overestimation of the quasi-steady predicted fluctuations may be expected, owing to the additional on-road sound sources masking the full extent of the unsteadiness-driven fluctuations. With an increase in cabin noise frequency, aeroacoustic sources increasingly dominate over the powertrain and road noise contributions, as shown by Figure 3.26. This may therefore explain the increase in transfer function amplitude for the 8000 Hz frequency band over the 6300 Hz band.

As with the previous broadband technique, the 4000 Hz band deviates in behaviour to that of the 6300 Hz and 8000 Hz bands. Whilst the broadband and third-octave modulation techniques attempted to remove the self-excited content from the cabin noise response, the techniques assumes an equal level of content on-road as in the wind tunnel. The difference in noise generation between the two environments may stem from a break up of any coherent, tonal vortex shedding from the probe on-road owing to the increased levels of free-stream turbulence. This increased response under steady conditions would lead to reduced transfer function amplitudes and may be the reason why the 4000 Hz band for both vehicles is lower than expected. Therefore it appears that the anomalous 4000 Hz behaviour was due to flow measurement apparatus, rather than due to the vehicle geometry itself.

The transfer function amplitudes shown in Figure 4.30 at the highest, 250 Hz, modulation frequency are identical to those calculated for the broadband modulation technique of Figure 4.27, implying that the refined third-octave technique only affected the lower frequency content, dominated by the large-scale unsteadiness on-road. At these lower frequencies the range of yaw angle and flow speed deviations experienced on-road was greater, where there is greater differentiation between the behaviour of each of the individual third-octave steady-state characteristics. Conversely, for the much

smaller deviations from the mean flow at higher frequencies, the overall SPL characteristic captures the response well. At progressively higher frequencies the roll-off appears less severe than for the case of the broadband technique, shown in Figure 4.27. This is a function of the artificially increased transfer function amplitude of the broadband technique at the lower fluctuation frequencies, as opposed to a change in the behaviour of the higher frequency content.

To further investigate the transfer function amplitude at frequencies below 5 Hz, the standard deviations of both the on-road measured and quasi-steady predicted cabin noise samples for each time history were compared. The same two low-frequency bands as previously investigated when assessing the surface pressure response in Section 4.3.2.3 were assessed, spanning the quasi-steady response region. The two fluctuation frequency ranges are presented, with the frequency range between 0.1–0.7 Hz shown by Figure 4.31(a) and the range between 0.7–5.0 Hz shown by Figure 4.31(b).

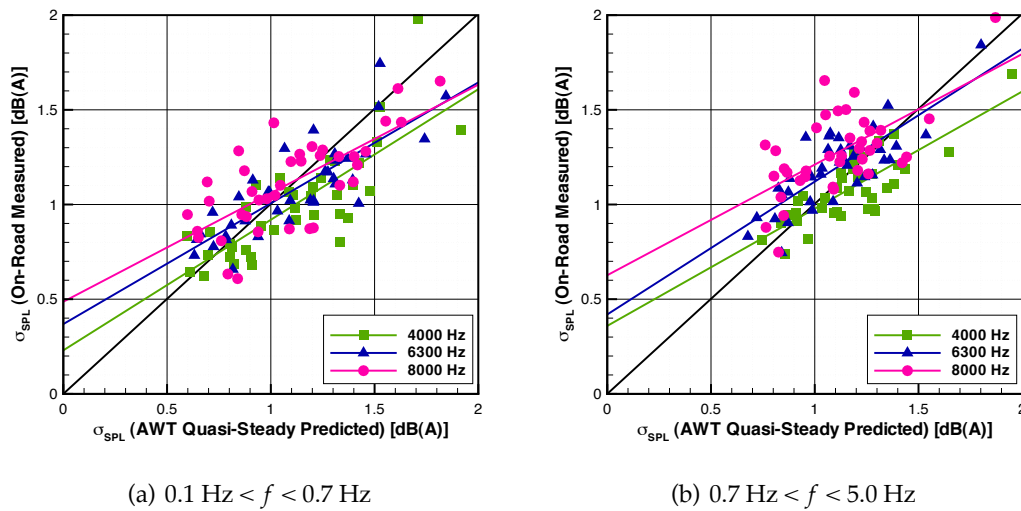


Figure 4.31: Standard deviation of quasi-steady predicted and on-road measured cabin noise fluctuations, using third-octave modulation simulation technique (Geometry 1)

As from the surface pressure investigation, the regression coefficient (slope) through

4. THE TIME-RESOLVED VEHICLE RESPONSE

the points is analogous to the amplitude of the transfer function, with the regression constant (y -axis intercept) related to a baseline level of unsteadiness present on-road but not in the averaged steady-state response. In the case of the surface pressure response, the baseline unsteadiness was linked to self-excited unsteadiness. In the case of cabin noise modulation techniques, the majority of any self-excited effects were accounted for. Therefore it is more likely that any baseline level of unsteadiness was due to cabin noise fluctuations uncorrelated to the oncoming flow and due to other acoustic fluctuations, such as variations in powertrain noise and changes in road surface.

The response for both frequency bands was similar, with each of the third-octave frequency bands showing a clear relationship between the predicted and measured unsteady cabin noise fluctuations. The regression lines plotted through the data points, each of which represents an individual record, show gradients of less than unity, corroborating with the equivalent below-unity transfer function amplitudes.

This suggests a reduced response on-road than predicted by quasi-steady theory. However, based on the consistency of response up to 2–5 Hz, combined with the range of additional uncorrelated inputs, such as other noise sources present on-road, it can be assumed that the vehicle cabin noise response remained quasi-steady up to frequencies between 2–5 Hz. At frequencies greater than this, the progressive decrease in vehicle response indicated that the smaller-scale unsteady fluctuations on-road have a correspondingly reduced impact on noise measured inside the cabin.

With the majority of unsteady energy on-road occurring below the quasi-steady boundary of 2–5 Hz, this allows the use of quasi-steady techniques to be used in the development of a vehicle in practise. Therefore, this indicates that the behaviour of a vehicle as assessed using steady-state techniques is likely to be sufficient in determining the front sideglass-dominated cabin noise performance as measured on-road.

4.5 A Subjective Assessment of Simulated Cabin Noise

A useful byproduct of the simulation techniques used to assess the cabin noise response of a vehicle to unsteady flow conditions is that it provided simulated cabin noise that can be listened to and subjectively assessed. Simulated cabin noise produced using this technique provides an accurate representation of the aeroacoustic content of a vehicle's cabin noise on-road if the response of the vehicle is quasi-steady.

This technique was used to subjectively assess various features of aeroacoustic cabin noise including changes to the sensitivity of cabin noise to yaw angle, the effect of overall shifts in sound pressure level and how changes in fluctuation frequency were perceived.

As demonstrated throughout this thesis, the sound pressure level of cabin noise fluctuates with changes in both oncoming flow speed and yaw angle. This study focussed only on the sensitivity of the cabin noise to yaw angle variations, since changes in vehicle geometry predominantly affect this response, whereas the flow speed sensitivity of a vehicle is primarily driven by the dipole-dominated aeroacoustic mechanisms that do not change significantly between vehicles with similar sealing.

The steady yaw sensitivity characteristics were chosen based on early, preliminary work in the Ford wind tunnel using a Geometry 1 vehicle, showing a relatively coarse yaw resolution. The characteristics were also based on the average dB cabin noise response to yaw.

The on-road yaw fluctuation data was an 8 second extract of data collected during a period of strong winds. The yaw angle is predominantly negative and shows characteristics of gusting, particularly between 4 and 6 seconds, and is shown in Figure 4.32.

Using the same broadband modulation technique as described in Section 4.4.2.2, the yaw time history was combined with various cabin noise characteristics to generate

4. THE TIME-RESOLVED VEHICLE RESPONSE

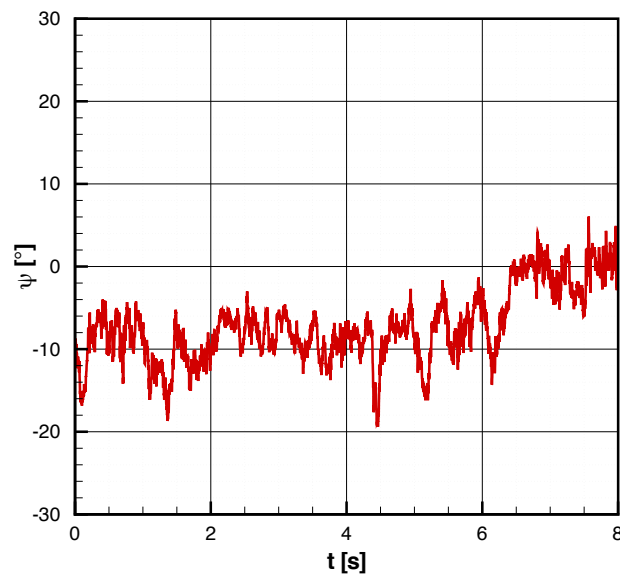


Figure 4.32: Yaw time history 20090619bHist3,8-16s used in subjective assessment

a simulated cabin noise time history. A number of different characteristics were used to subjectively assess the following effects:

1. The effect of yaw sensitivity, for instance when making a geometry change to a vehicle.
2. The effect of an increase in sound pressure level, determining the relative importance of yaw sensitivity to an overall level increase.
3. The effect of different modulation frequencies, as a result of different wind conditions, on how a vehicle with a particular yaw sensitivity may be perceived.

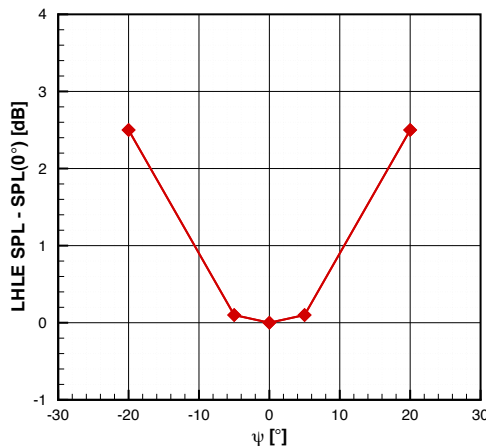
4.5.1 Generation of Cabin Noise Simulations

The characteristics and methods used to generate the various example cabin noise time histories are described in the following sections. Each sound is denoted by its shortened file name.

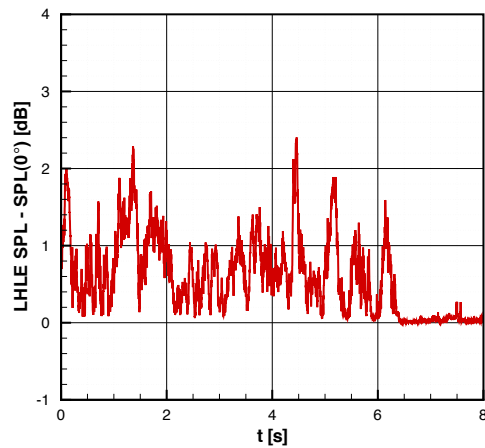
4.5.1.1 Effect of Yaw Sensitivity

YawSens0

This characteristic, shown by Figure 4.33(a), was based on the cabin noise SPL characteristic as obtained in the Ford AWT using a Geometry 1 vehicle. This was simplified to give a symmetric response to yaw, with linear interpolation used between each of the discrete measured yaw angles. The same characteristic was used for both the LHLE and LHRE channels, modulating the individual left and right binaural channels as recorded in the AWT. Characteristics unique to each channel could obviously be used and indeed were in the various simulation techniques of Section 4.4. The idealised characteristic is presented with SPL values normalised relative to those at $\psi = 0$. When combined with the example on-road yaw trace, this results in the normalised SPL time history shown by Figure 4.33(b).



(a) AWT Characteristic



(b) Normalised SPL vs. Time

Figure 4.33: YawSens0 characteristic and simulated time history

YawSens1

By modifying the YawSens0 characteristic so that there was a smaller increase in

4. THE TIME-RESOLVED VEHICLE RESPONSE

SPL over the range of yaw angles, a vehicle with a less sensitive response to yaw can be imitated, as shown by Figure 4.34(a). As shown by the time history of normalised SPL in Figure 4.34(b), this demonstrates similar modulation behaviour to YawSens0 but with a smaller amplitude range. The comparison of YawSens0 and YawSens1 allows a systematic evaluation of the importance of the level of yaw sensitivity alone to customer perception.

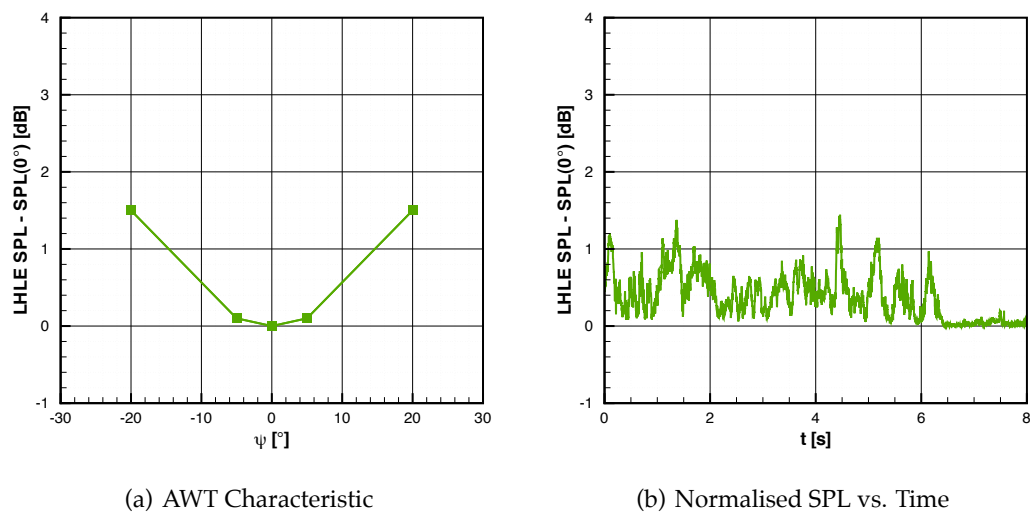


Figure 4.34: YawSens1 characteristic and simulated time history

4.5.1.2 Effect of an Increase in Level

Two characteristics were included that have the same sensitivity to yaw as YawSens0 and YawSens1 respectively, but with an increased overall SPL. This allows a comparison to be made between the effects of increased modulation amplitude versus that of an absolute SPL increase.

YawSens0Plus

YawSens0Plus has the same sensitivity as YawSens0 with an increased SPL. The average SPL of YawSens0 was added to the entire characteristic, resulting in a doubling

of the average SPL, whilst keeping the standard deviation the same. The characteristic is shown by Figure 4.35(a), with the resulting time history shown by Figure 4.35(b). This graphically shows the shift in SPL, whilst keeping the level of modulation the same as Figure 4.33(b).

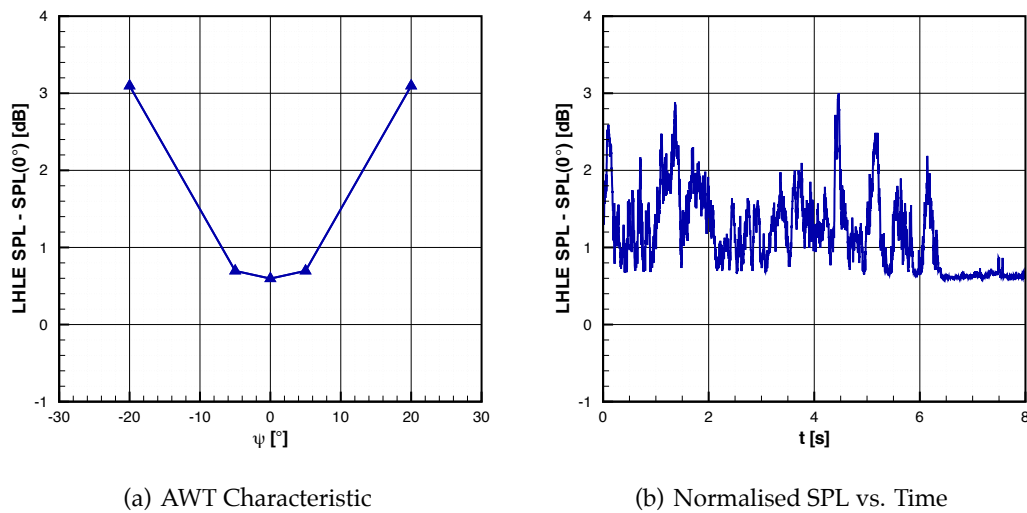


Figure 4.35: YawSens0Plus characteristic and simulated time history

YawSens1Plus

YawSens1Plus has the same overall SPL increase as YawSens0Plus, whilst keeping the yaw sensitivity the same as that in YawSens1. Since this sensitivity is less than YawSens0, this allows a comparison of customer perception between the effect of modulation and overall SPL. Both the characteristic and resulting time history are shown by Figure 4.36.

4.5.1.3 Effect of Modulation Frequency

To assess the sensitivity of a customer to different modulation frequencies, two simulated sounds were created both using the YawSens0 characteristic. A change in modulation frequency is equivalent to a vehicle experiencing different wind conditions

4. THE TIME-RESOLVED VEHICLE RESPONSE

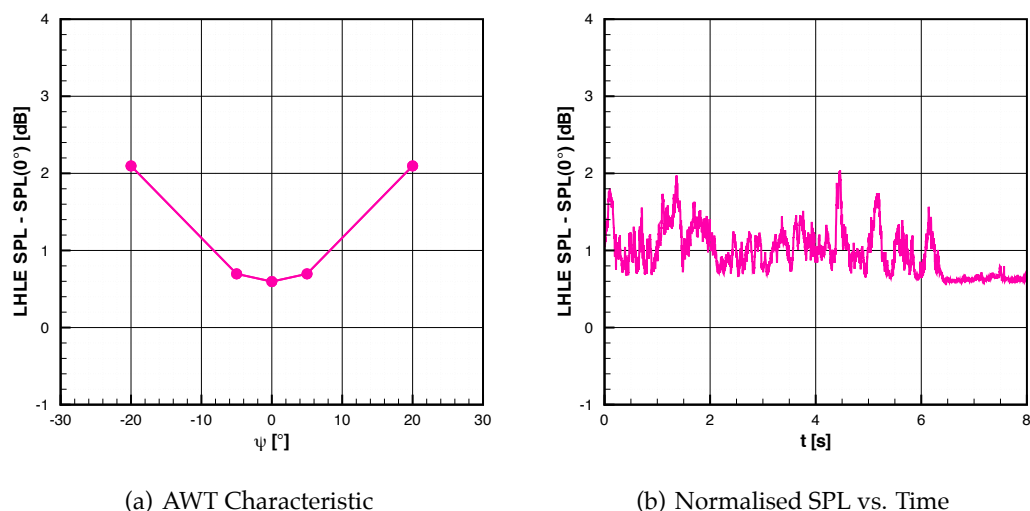


Figure 4.36: YawSens1Plus characteristic and simulated time history

whilst traversing the on-road environment. The same time history was used as with all previous characteristics, yet either stretched or compressed to vary the modulation frequency.

YawSens0Stretched

For this simulation, instead of 20090619bHist3,8–16s being used to modulate the YawSens0 characteristic, a 4 s section was used: 20090619bHist3,12–16s as shown by Figure 4.37(a). This was stretched over an 8 s time period and resampled to match the original time history. This had the effect of halving the rate of modulation of the YawSens0 simulation. To ensure only the modulation frequency differed, the output SPL, as shown in Figure 4.37(b) was adjusted to have the same absolute SPL and standard deviation as the YawSens0 simulation.

YawSens0Compressed

The YawSens0Compressed noise simulation used an extended time history to modulate the YawSens0 characteristic: 20090619bHist3,8–24s. This 16 s time history was

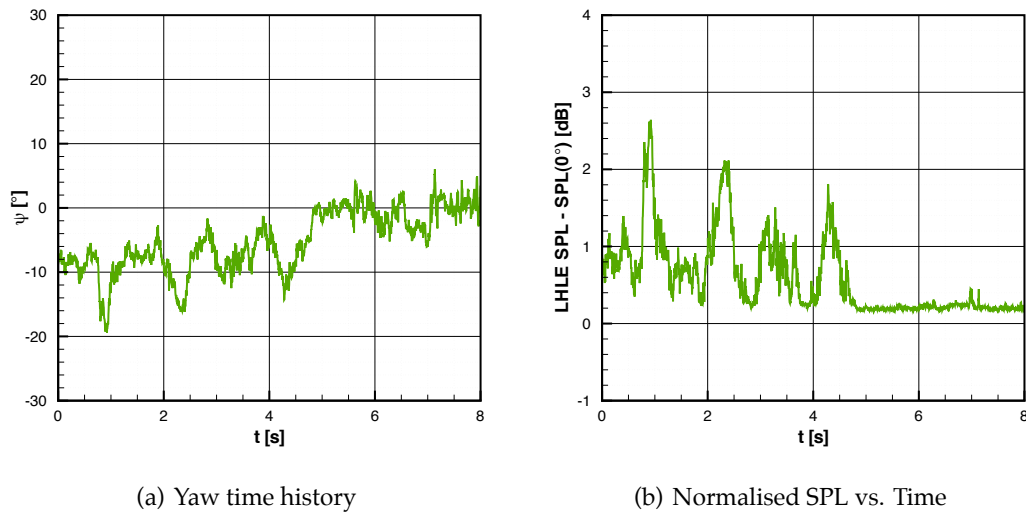


Figure 4.37: YawSens0Stretched yaw angle and simulated time history

compressed to 8 s and resampled to match the original 8 s time history and is shown by Figure 4.38(a). As with YawSens0Stretched, the resulting time history was adjusted to have the same absolute SPL and standard deviation as the YawSens0 simulation and the resulting time history is shown by Figure 4.38(b).

4.5.1.4 Control Characteristics

Control characteristics were also assessed at three different sound pressure levels, with no amplitude modulation applied. These were used to assess the relative importance of SPL modulation compared with absolute, steady-state SPL.

AWT

This is the cabin noise as measured in the wind tunnel at zero yaw and is the same sound sample as used in each of the simulations, prior to any modulation. For reference the characteristic and normalised SPL time history are shown by Figure 4.39.

AwtAve

To act as a comparison to the amplitude-modulated simulations AwtAve, like AWT,

4. THE TIME-RESOLVED VEHICLE RESPONSE

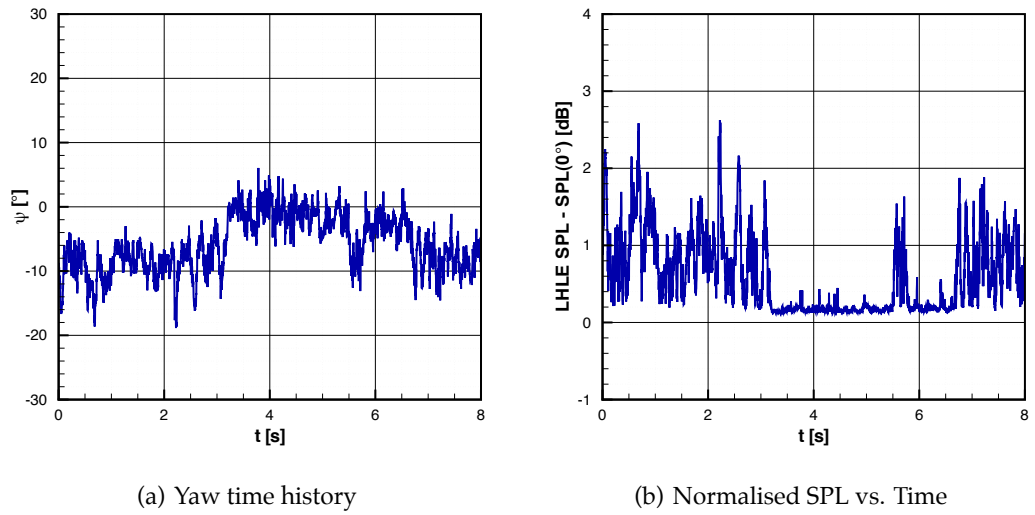


Figure 4.38: YawSens0Compressed yaw angle and simulated time history

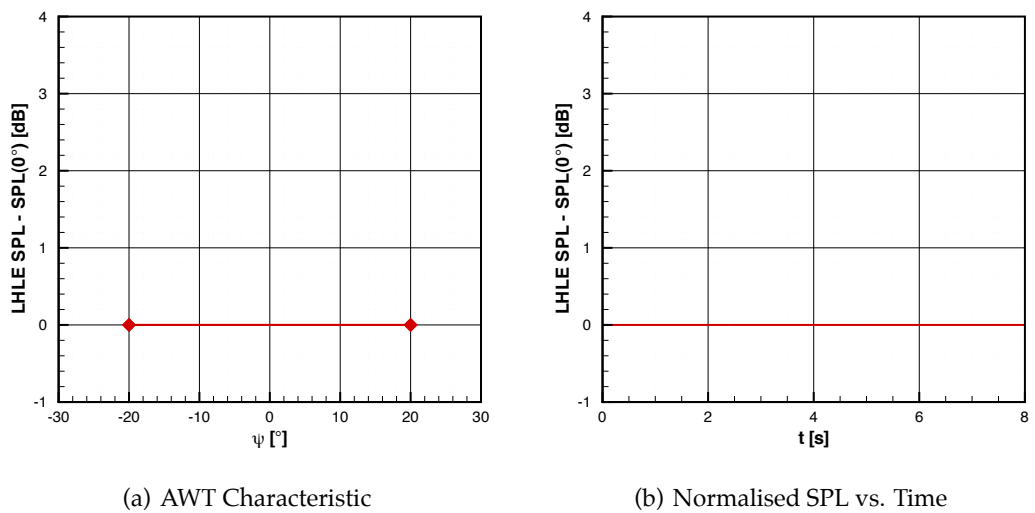


Figure 4.39: AWT characteristic and simulated time history

4.5 A Subjective Assessment of Simulated Cabin Noise

has a flat SPL response at all yaw angles. To generate this characteristic, the average normalised SPL from the YawSens0 time history was determined and used to scale the flat-response characteristic. This value is dependent on the choice of yaw angle time history, since a time history collected during a calm day would have a lower overall SPL response when modulated using the YawSens0 characteristic. This allowed a direct comparison to be made between modulated and non-modulated cabin noise, with an equal overall SPL.

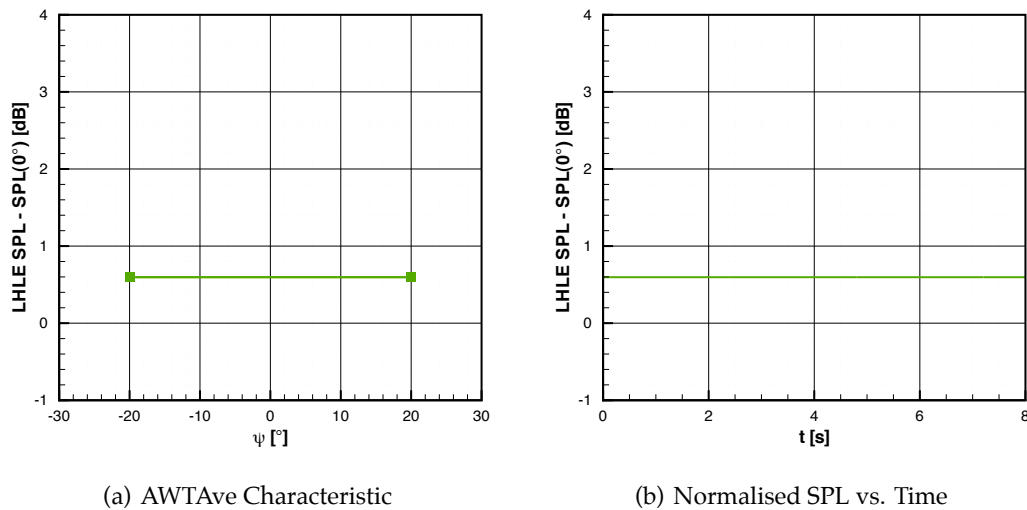


Figure 4.40: AWTave characteristic and simulated time history

AwtMax

Like AwtAve, this characteristic is flat but scaled to the maximum normalised SPL experienced in the resulting time history generated using the YawSens0 characteristic. For the particular yaw time history used, this was the maximum SPL of the YawSens0 characteristic. This allowed a comparison to be drawn between modulated and non-modulated cabin noise at the maximum level experienced.

4. THE TIME-RESOLVED VEHICLE RESPONSE

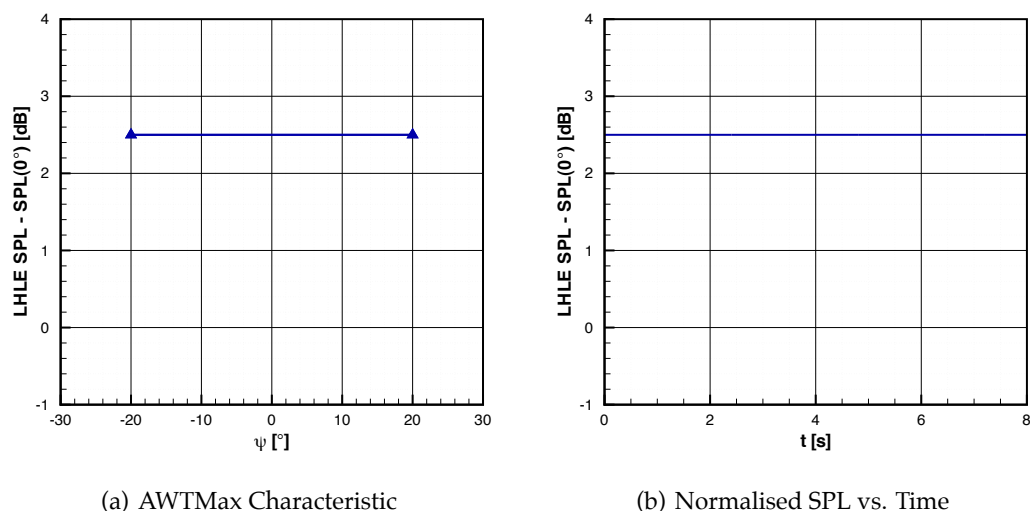


Figure 4.41: AWTMax characteristic and simulated time history

4.5.2 Responses

Subjective testing took place using the ranking technique, as described in Section 2.4.4.2, whereby each of the 9 sounds were given a score between 0 (most annoying) and 100 (least annoying). Once all of an individual's responses were completed, their score was then normalised such that the lowest ranked score was adjusted to 0, the highest score adjusted to 100, with the other scores linearly interpolated in between.

A total of 33 respondents were asked to assess the sound samples. To assess the quality of each of the participant's responses, the coefficient of determination R^2 was calculated between their responses and the average responses of the cohort. These response quality coefficients for each of the respondents are presented by Figure 4.42(a) in descending order.

A quality threshold was set such that respondents scoring $R^2 < 0.9$ were rejected from the average. This threshold can be seen graphically in Figure 4.42(a), with the 8 rejected respondents shown to have scores dropping off significantly from the scores of the retained responses.

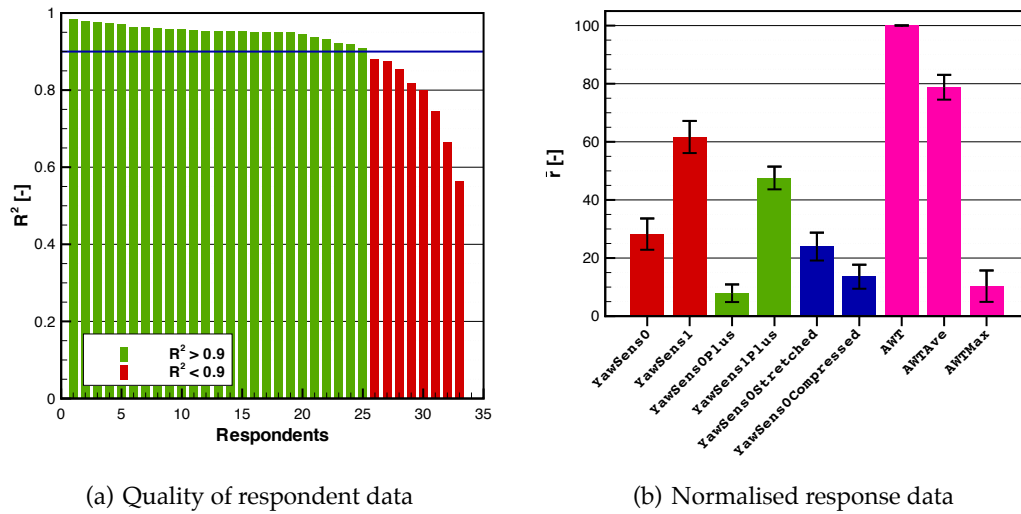


Figure 4.42: Subjective response data of cabin noise simulations

Figure 4.42(b) shows the resulting averaged normalised respondent scores for each of the sounds. The error bars are defined by the 95% confidence intervals. The following section compares and assesses each of the responses.

4.5.3 Analysis

4.5.3.1 The Impact of Level and Yaw Sensitivity on Perceived Cabin Noise

The effect of yaw sensitivity on subjective cabin noise response was assessed by comparing the results obtained from the two differing yaw sensitivity characteristics and the baseline AWT measurement, independent of yaw. The yaw sensitivity of a vehicle can generally be altered by changing parts of a vehicle that tend to result in separated flow structures at yaw. This includes door mirrors, windscreen wipers or features around the A-pillar. The results are compared in Figure 4.43(a).

The first, and perhaps most obvious, observation is that an increase in the sensitivity of cabin noise to changes in yaw angle led to a decrease in a respondent's subjective

4. THE TIME-RESOLVED VEHICLE RESPONSE

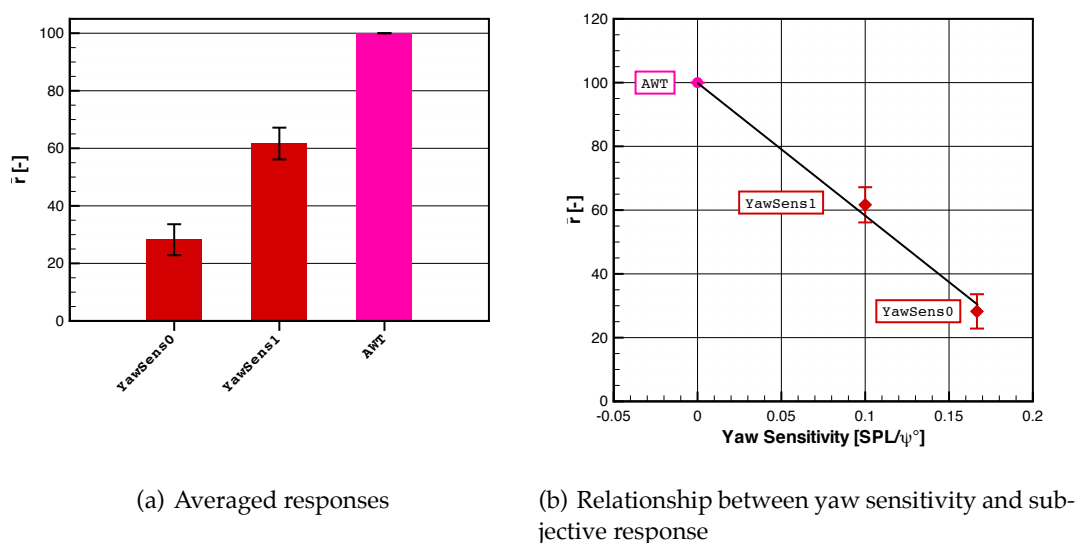


Figure 4.43: Effect of yaw sensitivity

score. Therefore, a vehicle with a greater sensitivity to yaw angle would have a likelihood of reduced wind noise performance on-road. By also comparing the gradient of the yaw characteristic between 5 and 20 degrees yaw, there appears to be a linear relationship between yaw sensitivity and subjective response. This is shown graphically by Figure 4.43(b). The results imply that if two geometry modifications were assessed on a vehicle that changed the yaw sensitivity by 10%, it is probable that the subjective response would be affected by a similar amount.

Figure 4.44 adds the yaw sensitivity characteristics of YawSens0Plus and YawSens1Plus to the comparison, in addition to the AWT measurement of AWTave.

By comparing the difference between the characteristics YawSens0 and YawSens1, and YawSens0Plus and YawSens1Plus, there is a relatively consistent shift in subjective response of the order of $\bar{r} = 40$, taking into account the uncertainty of the responses. This implies that a change in yaw sensitivity has a similar impact on subjective cabin noise response, regardless of the overall level of cabin noise, such that reducing the yaw sensitivity of a louder vehicle would have a similar impact to that of a quieter vehicle.

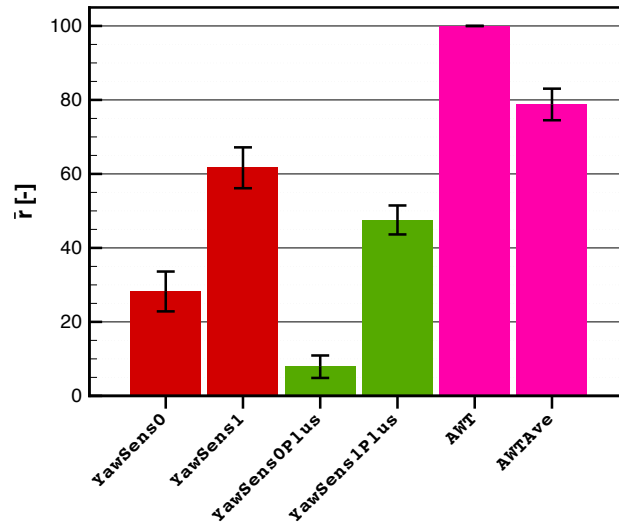


Figure 4.44: Effect of an increase in level

This consistent shift can also be interpreted as a consistent degradation in response between both YawSens0 and YawSens0Plus, and YawSens1 and YawSens1Plus of the order of $\bar{r} = 20$. This degradation was also mirrored when comparing the non-modulating sounds of AWT and AWTave, implying that the same level shift has a constant impact on subjective response, irrespective of the yaw sensitivity of the characteristic.

Figure 4.45(a) explores all three yaw-insensitive AWT control characteristics, comparing them to the shifted yaw-sensitive characteristics of YawSens0 and YawSens0Plus.

This figure reiterates the consistent reduction in subjective response for a given increase in SPL, regardless of the level of yaw sensitivity in the characteristic, with the difference between the first two pairs of results relatively constant. This also shows that whilst the large increase in cabin noise SPL in AWTMax was perceived negatively, the lower SPL characteristic of YawSens0Plus with yaw-sensitive modulations was perceived in a similar, negative fashion.

Comparing the average SPL increase from the baseline cabin noise time history,

4. THE TIME-RESOLVED VEHICLE RESPONSE

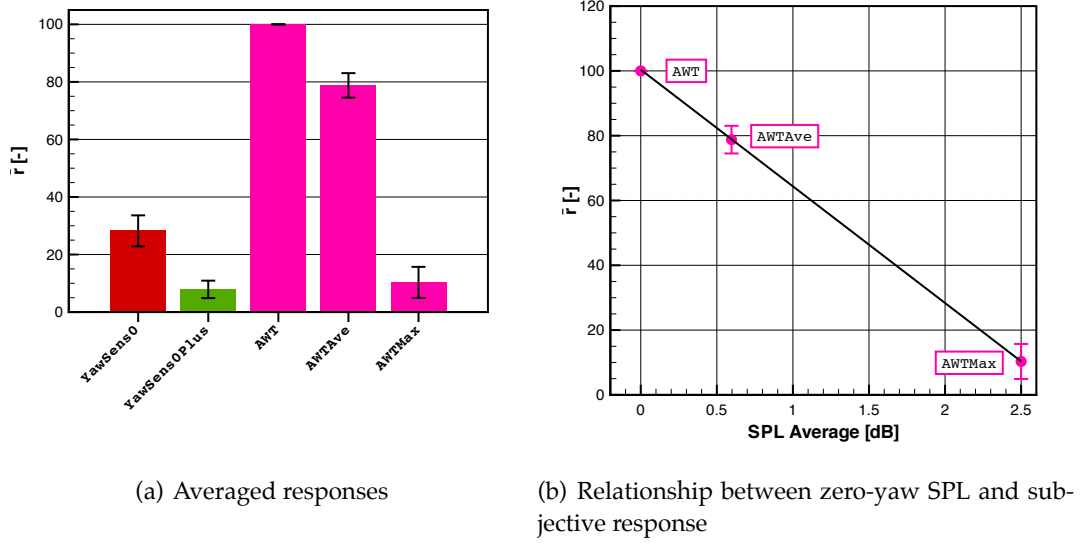


Figure 4.45: Effect of an increase in SPL

as shown by Figure 4.45(b), the very strong linear relationship between SPL (L) and subjective response can be seen. The gradient of this relationship was used to generate a sensitivity coefficient, assessing the degradation in subjective response with an increase in SPL, from:

$$\frac{d\bar{r}}{dL} = -36 \text{ dB}^{-1} \quad (4.10)$$

By also determining the gradient of the yaw sensitivity relationship of Figure 4.43(b), the comparative sensitivity coefficient assessing the change in subjective response to a change in yaw sensitivity was calculated as:

$$\frac{d\bar{r}}{d\left(\frac{dL}{d\psi}\right)} = -410 \text{ } \psi/\text{dB} \quad (4.11)$$

These two coefficients provide a comparison of the relative importance of the level of cabin noise measured in a vehicle at zero-yaw with the sensitivity that the cabin noise has towards changes in yaw angle. By determining the quotient of these quantities,

this comparison can be expressed quantitatively, defined as the ratio of level sensitivity to yaw sensitivity:

$$\frac{d\left(\frac{dL}{d\psi}\right)}{dL} = \frac{-36 \text{ dB}^{-1}}{-410 \text{ } \psi/\text{dB}} = 0.09 \text{ } \psi^{-1} \quad (4.12)$$

This ratio suggests that a change in yaw sensitivity of a vehicle by 0.09 dB/° would have the same perceived impact in the cabin as an increase of 1 dB in the overall level of cabin noise. This does depend on the range of wind conditions experienced by a particular vehicle, since under more still conditions, the impact of an increase in level will have a greater impact over yaw sensitivity, if the oncoming yaw angle remains steady. This therefore leads to the conclusion that knowledge of the range of wind conditions experienced in the intended market for a particular vehicle may be useful when assessing real-world wind noise performance.

Since both the overall level of cabin noise of a vehicle measured at zero yaw and the sensitivity of the cabin noise to changes in yaw angle can be potentially modified with changes to the vehicle geometry, this comparison provides guidance when assessing these changes during the the wind noise development of a vehicle.

4.5.3.2 The Impact of Modulation on Perceived Cabin Noise

Figure 4.46(a) compares the baseline YawSens0 characteristic with the stretched and compressed yaw angle time histories of YawSensStretched and YawSensCompressed, also generated with the same yaw sensitive characteristic.

The results suggest that there is no significant difference in subjective response between either the reference YawSens time history or YawSensStretched. The compressed cabin noise however appears to show a degradation in subjective response.

To compare the generated sounds further, modulation spectra were generated to determine the nature of the modulations generated by the differing yaw angle time

4. THE TIME-RESOLVED VEHICLE RESPONSE

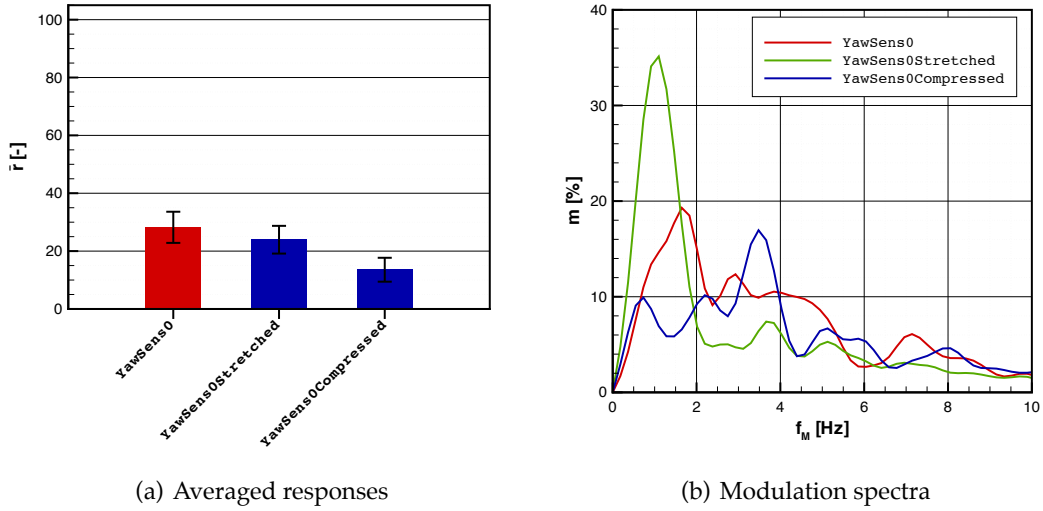


Figure 4.46: Effect of modulation

history files. Modulation of a sound signal was discussed in Section 1.3.7.4. The modulation spectrum is based on the Hilbert transform, which extracts the modulation envelope of the signal. Using an FFT, the frequency components of the envelope are then calculated to determine the depth of modulation m of the signal. This describes the ratio of the fluctuating component to the constant component of the modulation signal. Figure 4.46(b) shows the resulting modulation spectra for each of the generated time history files, presenting the depth of modulation m against modulation frequency, f_M .

The peak modulation frequency for the baseline YawSens0 case is approximately $f_M = 1.5$ Hz; the stretched case $f_M = 1$ Hz; with the compressed case peaking at approximately $f_M = 3.5$ Hz. Section 1.3.7.4 discussed the sensitivity that a human has towards modulations at 4 Hz, where at both higher and lower frequencies this sensitivity reduces. It is therefore likely that the yaw fluctuations at frequencies close to 4 Hz led to the degradation in subjective response for the YawSens0Compressed sample. This also shows that even with a large increase in modulation depth for the YawSens0Stretched sample, there appears to be little change in subjective response to

4.5 A Subjective Assessment of Simulated Cabin Noise

the baseline case, likely to be due to the reduction in frequency of the oncoming flow fluctuations.

The comparative effect of cabin noise fluctuations to an increase in level was also assessed, using the standard deviation of the cabin noise for each of the sound samples as an indication of the level of fluctuating content. This was compared to the overall average SPL of the same sound samples, allowing the comparative effects of an increase in overall SPL and the level of fluctuating content to be assessed. Figure 4.47 presents the results of this comparison, plotting these values against the resulting subjective index for a number of the samples.

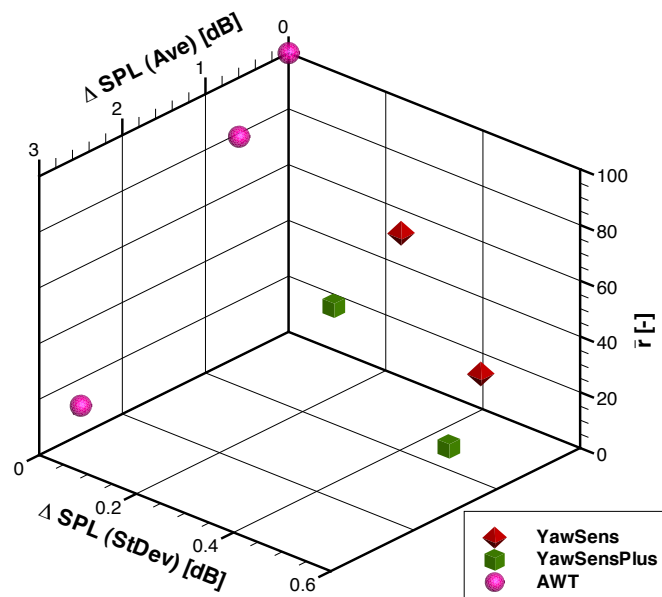


Figure 4.47: Comparative effect of overall SPL and SPL fluctuation of selected sound samples

The results of this clearly indicate a trade-off between an increase in level and fluctuating content, with higher levels of both being negatively perceived. These results also allow an approximate comparison of a listener's sensitivity to both of these changes. Figure 4.47 shows that an increase in 2.5 dB in overall SPL leads to a similar reduction in response to a pure increase in fluctuation of around 0.5 dB on the stan-

4. THE TIME-RESOLVED VEHICLE RESPONSE

dard deviation of the SPL. If a similar approach is followed as with Section 4.5.3.1, by capturing the approximate gradients of these relationships, the sensitivity ratio can be approximated as:

$$\frac{d\sigma_L}{dL} = \frac{0.5 \text{ dB}}{2.5 \text{ dB}} = 0.2 \quad (4.13)$$

This suggests that an increase in cabin noise fluctuations, increasing the standard deviation by 0.2 dB, would lead to a similar negative perception of cabin noise as that of an increase of 1 dB in the overall level.

Overall, the sensitivity of human perception towards fluctuations in cabin noise, particularly centred around modulation frequencies of 4 Hz, can lead to significantly worse performing vehicles on-road than developed under steady conditions. Therefore, knowledge of both the cabin noise sensitivity of the vehicle towards changes in oncoming flow, combined with information on the range of wind conditions that may be experienced by a vehicle on-road is important to avoid wind noise issues when developing a vehicle.

4.6 Summary

4.6.1 Surface Pressures

- Conventional admittance functions relating oncoming flow yaw angle to sideglass surface pressure response are generally not suitable due to the non-linear steady state characteristics obtained in the wind tunnel. Therefore, a quasi-steady technique combining steady state wind tunnel measurements with measurements of the fluctuating yaw angle and resultant velocity experienced by a vehicle on-road was developed. This was demonstrated to predict sideglass pressure transients with high fidelity.

- As indicated by linearised transfer functions using the quasi-steady predicted signals, at highway speeds the vehicle sideglass surface pressure response generally remained quasi-steady up to at least 2 Hz ($k > 0.5$, based on the square-root of frontal area).
- At frequencies above 10–20 Hz there is very little unsteady energy in the on-road environment and self-excited unsteadiness, for instance due to the door mirror, dominate the unsteadiness on the sideglass.
- A new method was introduced for separating the effects of externally imposed unsteadiness and self-excited unsteadiness in order to obtain a ‘true’ transfer or admittance function, unconfused by the presence of self-excited unsteadiness. This method indicates that the aerodynamic admittance in the mirror wake tends to drop below unity above a frequency of 2–10 Hz ($0.5 < k < 3$) and has dropped to less than 0.2 by 100 Hz ($k = 30$).
- In regions nearest the A-pillar and also at the downstream edge of the sideglass, this high-frequency roll-off is less pronounced. In the region closet the A-pillar, an aerodynamic admittance of 1.2 was found at frequencies nearest 10 Hz ($k = 3$), indicating a larger aerodynamic response in this region than predicted under the steady conditions of the wind tunnel.

4.6.2 Cabin Noise

- Using the same linearised transfer function technique as for the surface pressure investigation, the cabin noise response generally remained quasi-steady for the wind noise dominated higher frequency bands up to fluctuation frequencies of 2–5 Hz ($0.5 < k < 1.5$). At higher fluctuation frequencies, self-excited effects

4. THE TIME-RESOLVED VEHICLE RESPONSE

corrupted the transfer function and an alternative technique was developed to remove this.

- Using broadband modulation of the nominal cabin noise recorded in the wind tunnel, a technique was developed to better handle the modulation of wind noise by self-excited unsteadiness. Subsequent transfer functions showed an expected roll-off at higher frequencies, although transfer function amplitudes at lower frequencies were generally inaccurately greater than unity as a result of the prediction technique applying the same modulation to all third-octave bands.
- A refined third-octave modulation technique was also demonstrated to more accurately capture the transfer function amplitude at lower frequencies with greater accuracy. This predicted a quasi-steady response up to approximately 2 Hz ($k = 0.5$), with amplitudes 2 dB below that predicted using the wind tunnel. This amplitude shift was likely to be a result of the additional cabin noise content measured on-road uncorrelated to external unsteadiness. Although admittance of greater than unity was found for surface noise measurements around the A-pillar region, the admittance for cabin noise response did not exceed unity.

4.6.3 Subjective Response to Cabin Noise Modulations

- The relative impact of an increase in the level of cabin noise and the sensitivity of the cabin noise to changes in yaw angle were assessed. It was found that a change in yaw sensitivity of a vehicle by 0.09 dB/° would have the same perceived impact in the cabin as an increase of 1 dB in the overall level of cabin noise at zero yaw. The subjective comparison of these vehicle characteristics can provide guidance when assessing the on-road wind noise performance of

different vehicle modifications under steady conditions.

- The effect of cabin noise modulation was also assessed and it was found that fluctuations occurring at around modulation frequencies of 4 Hz were perceived the most negatively. A relationship between subjective response and changes in both cabin noise level and fluctuation was determined, showing that cabin noise fluctuations with a standard deviation of 0.2 dB had a similar negative impact as an increase of 1 dB in overall cabin noise level.

CHAPTER 5

Conclusions and Further Work

5.1 Conclusions

Can steady techniques predict unsteady on-road results?

- Using the frequency-dependent relationships between flow speed and cabin noise as determined in the wind tunnel, a technique was developed to determine the wind noise contribution to the overall cabin noise measured on-road. At the highway speeds used in this investigation, this demonstrated that aeroacoustic sources dominated the cabin noise spectra at frequencies above 2 kHz, whilst road noise dominated at frequencies centred around 800 Hz.
- By adopting a bin-averaging technique, whereby the cabin noise response of the vehicle was averaged based on the instantaneous on-road flow conditions, a representative comparison was made between the cabin noise on-road and that measured in the aeroacoustic wind tunnel, when comparing third-octave bands dominated by wind noise. A good comparison was also made using a similar technique when assessing surface pressures and surface noise in the sideglass region, where the aerodynamic and aeroacoustic behaviour dominate the noise inside the cabin.

5. CONCLUSIONS AND FURTHER WORK

- When assessing the aerodynamic response in the sideglass region, conventional admittance functions relating oncoming flow yaw angle to sideglass surface pressure response are generally not suitable due to the non-linear steady state characteristics obtained in the wind tunnel. Therefore, a quasi-steady technique combining steady state wind tunnel measurements with measurements of the fluctuating yaw angle and resultant velocity experienced by a vehicle on-road was developed. This was demonstrated to predict time-resolved sideglass pressure transients with high fidelity.
- As indicated by linearised transfer functions using the quasi-steady predicted signals, at highway speeds the vehicle sideglass surface pressure response generally remained quasi-steady up to at least 2 Hz ($k > 0.5$, based on the square-root of frontal area). At frequencies above 10–20 Hz there is very little unsteady energy in the on-road environment and self-excited unsteadiness, for instance due to the door mirror, dominate the unsteadiness on the sideglass.
- A new method was introduced for separating the effects of externally imposed unsteadiness and self-excited unsteadiness in order to obtain a ‘true’ transfer or admittance function, unconfused by the presence of self-excited unsteadiness. This method indicates that the aerodynamic admittance in the mirror wake tends to drop below unity above a frequency of 2–10 Hz ($0.5 < k < 3$) and has dropped to less than 0.2 by 100 Hz ($k = 30$). However, in the region closest to the A-pillar, an aerodynamic admittance of 1.2 was found at frequencies nearest 10 Hz ($k = 3$), indicating a larger aerodynamic response in this region than predicted under the steady conditions of the wind tunnel.
- Using the same linearised transfer function technique as for the surface pressure investigation, the cabin noise response generally remained quasi-steady for the

wind noise dominated higher frequency bands up to fluctuation frequencies of 2–5 Hz ($0.5 < k < 1.5$). At higher fluctuation frequencies, self-excited effects corrupted the transfer function and alternative techniques were developed to remove this.

- Two cabin noise modulation techniques to simulate the cabin noise as would be predicted under steady conditions were developed. The third-octave modulation technique was demonstrated to capture the transfer function amplitude at lower frequencies with greatest accuracy. This predicted a quasi-steady response up to approximately 2 Hz ($k = 0.5$), with amplitudes 2 dB below that predicted using the wind tunnel. This amplitude shift was likely to be a result of the additional cabin noise content measured on-road uncorrelated to external unsteadiness. The increase in admittance around the A-pillar region of the vehicle measured using surface pressure tapings was not found to result in a net cabin noise response with an admittance greater than unity.
- Overall, this work demonstrates that steady techniques are able to predict unsteady on-road results well enough to assess cabin noise. To achieve this, the varying conditions measured on-road must be taken into account. The resulting quasi-steady cabin noise simulations are a convenient by-product, allowing the predicted unsteady cabin noise to be subjectively assessed.

What is the impact of the on-road unsteadiness on perceived noise in the cabin?

- The relative impact of an increase in the level of cabin noise and the sensitivity of the cabin noise to changes in yaw angle were assessed, and it was found that a change in yaw sensitivity of a vehicle by 0.09 dB/° had the same perceived impact as an increase of 1 dB in the overall level of cabin noise at zero yaw.

5. CONCLUSIONS AND FURTHER WORK

- The effect of cabin noise modulation was also assessed, where it was found that fluctuations occurring at around modulation frequencies of 4 Hz were perceived the most negatively. A relationship between subjective response and changes in both cabin noise level and fluctuation was determined, showing that cabin noise fluctuations with a standard deviation of 0.2 dB had a similar negative impact as an increase of 1 dB in overall cabin noise level.

Can minor geometry changes have an important impact on the transient nature of the wind noise perceived on-road?

- Both on-road and in the aeroacoustic wind tunnel, a geometry modification made to the stem of a door mirror was found to improve the cabin noise performance of the vehicle. This primarily affected higher frequencies under leeward flow conditions and reduced the sensitivity of the cabin noise towards changes in yaw angle.
- The overall sound pressure level and the 4 kHz third-octave band component of the cabin noise were increased slightly with the generation of additional unsteadiness by the Pininfarina turbulence generation system. However, these increases were generally low, with the steady wind tunnel able to identify the same better-performing modification made to the door mirror as the unsteady wind tunnel.
- Since minor geometry modifications made to the vehicle can change the sensitivity of cabin noise to changes in yaw angle and because this yaw sensitivity impacts on the perception of wind noise fluctuations under transient conditions, minor geometry changes can therefore have an important impact on the unsteady wind noise perceived on-road.

5.2 Suggestions for Further Work

- The use of the simulation approaches described by this work allows the prediction of the unsteady wind noise of a vehicle to be made through the combination of steady-state cabin noise and on-road flow condition measurements. This therefore allows a prediction of how the wind noise of a vehicle may sound when driven in a particular set of wind conditions, which it has not directly experienced. This also has the further benefit of allowing non-drivable prototype vehicles or steady-state cabin noise predictions from computational methods to be assessed as they would be in the unsteady on-road environment.
- The main focus of this work has been on the sideglass of the vehicle with its corresponding impact on the noise inside the cabin. Using similar approaches, the impact of transient flow conditions on other regions of the vehicle may be explored to determine the extent of the quasi-steady vehicle aerodynamic response. Another area of interest is the impact of transient flow conditions on vehicle handling. This is relatively sensitive to transient pressures at the front and rear of the vehicle and it would therefore be appropriate to explore whether the observations of quasi-steady response apply to those different regions of the vehicle.
- Whilst the relative subjective impact of the overall level and sensitivity of cabin noise to changes in yaw angle has been explored, these findings may be applied in the development of metrics to assess and compare the subjective wind noise performance of different vehicles, providing guidance in the generation of vehicle performance targets.

References

- Ahmed, S. R. and Baumert, W. (1979). The structure of wake flow behind road vehicles. In *Aerodynamics of transportation*, pages 93–103. ASME-CSME conference, Niagara Falls. 5
- Ahmed, S. R., Ramm, G., and Faltin, G. (1984). Some salient features of the time-averaged ground vehicle wake. *SAE Technical Paper*, (840300). 6
- Alam, F., Jaitlee, R., and Watkins, S. (2007). Aerodynamic effects on an automotive rear side view mirror. In *16th Australasian fluid mechanics conference*. Crown Plaza, Gold Coast, Australia. 34
- Alam, F., Watkins, S., Song, B., Steiner, T., and Humphris, C. (1998). The flow characteristics around a car A-pillar. In *Proceedings*. 13th Australasian fluid mechanics conference, Monash University. 31
- Alam, F., Watkins, S., Zimmer, G., and Humphris, C. (2001). Effects of vehicle A-pillar shape on local mean and time-varying flow properties. *SAE Technical Paper*, SP-1600(2001-01-1086). 31
- Alam, F., Zimmer, G., and Watkins, S. (2003). A study of the A-pillar vortex of a passenger car. In *Proceedings of the international conference on mechanical engineering*. 31
- An, C.-F., Alaie, S. M., Sovani, S. D., Scislowicz, M. S., and Singh, K. (2004). Side

REFERENCES

- window buffeting characteristics of an SUV. *SAE Technical Paper*, SP-1874(2004-01-0230). 35
- An, C.-F., Puskarz, M., Singh, K., and Gleason, M. E. (2005). Attempts for reduction of rear window buffeting using CFD. *SAE Technical Paper*, SP-1931(2005-01-0603). 35
- An, C.-F. and Singh, K. (2006). Optimization study for sunroof buffeting reduction. *SAE Technical Paper*, SP-1991(2006-01-0138). 35
- An, C.-F. and Singh, K. (2007). Sunroof buffeting suppression using a dividing bar. *SAE Technical Paper*, SP-2066(2007-01-1552). 35
- ANSI/ASA S1.11-2004 (2004). *Octave-band and fractional-octave-band analog and digital filters*. ANSI, New York. 294
- ANSI/ASA S1.42-2001 (2001). *Design response of weighting networks for acoustical measurement*. ANSI, New York. 53
- ANSI/ASA S3.4-2005 (2005). *Procedure for the computation of loudness of steady sounds*. ANSI, New York. 53
- ANSI/ASA S3.5-1969 (1969). *Methods for the calculation of the articulation index*. ANSI, New York. 55
- Arnette, S., Buchanan, T., and Zabat, M. (1999). On low-frequency pressure pulsations and static pressure distribution in open jet automotive wind tunnels. *SAE Technical Paper*, (1999-01-0813). 39
- Ask, J. (2008). *Predictions of aerodynamically induced wind noise around ground vehicles*. PhD thesis, Chalmers University of Technology. 49
- Ask, J. and Davidson, L. (2010). Flow and dipole source evaluation of a generic SUV. *J. Fluid Eng.-T. ASME*, 132(051111-1). 49

- Baden Fuller, J. (2009). Measurement of side-glass fluctuating pressures in varying onset turbulence. Master's thesis, Loughborough University. 31, 95
- Baden Fuller, J. and Passmore, M. (2010). An experimental investigation into the transient aerodynamics of a small car using some unsteady test techniques. In *Proceedings*. 8th MIRA international conference on vehicle aerodynamics, Grove. 104
- Bearman, P. and Mullarkey, S. (1994). Aerodynamic forces on-road vehicles due to steady side winds and gusts. In *Road Vehicle Aerodynamics*, Loughborough, UK. Royal Aeronautical Society Conference. 77, 87, 99, 100
- Beland, O. (2007). Buffeting suppression technologies for automotive wind tunnels tested on a scale model. In Wiedemann, J., editor, *Progress in vehicle aerodynamics and thermal management V*, Renningen. Expert Verlag. 40
- Bendat, J. S. and Piersol, A. G. (1993). *Engineering applications of correlation and spectral analysis*. John Wiley & Sons inc., New York, second edition. 66, 134, 250, 267
- Bergeron, F., Astruc, C., Berry, A., and Masson, P. (2010). Sound quality assessment of internal automotive road noise using sensory science. *Acta Acust.*, 96:580–588. 60
- Bischof, G. (2008). On-road investigation of a vehicle's longitudinal response to wind gusts. *SAE Technical Paper*, SP-2151(2008-01-0472). 92, 118
- Bischof, G., Bratschitsch, E., and Mandl, M. (2005). On-road aerodynamic drag analysis by simultaneous linear inversion of the equation of motion. *SAE Technical Paper*, SP-1931(2005-01-1456). 92
- Blevins, R. D. (1990). *Flow-induced vibration*. Krieger Publishing Company, second edition. 7, 36, 264

REFERENCES

- Blumrich, R. (2006). Computational aeroacoustics in automotive engineering. In Wiedemann, J. and Hucho, W. H., editors, *Progress in vehicle aerodynamics – numerical methods*, Renningen. Expert Verlag. xvii, 29, 33, 49
- Blumrich, R. (2008). Vehicle aeroacoustics – today and future developments. In *5th international styrian noise, vibration and harshness conference*, Graz. 29, 35
- Blumrich, R. (2009). New developments in numerical vehicle aeroacoustics. In *7th FKFS conference "progress in vehicle aerodynamics and thermal management"*, Stuttgart. 50
- Bratschitsch, E., Bischof, G., Haas, A., and Kaltenhauser, A. (2004). Conservation of energy method for on-road aerodynamic drag investigation. *SAE Technical Paper*, SP-1874(2004-01-1148). 92
- Brüel & Kjær (2006). *Automotive surface microphones – types 4949 and 4949 B*. Brüel & Kjær. 142
- Carlino, G., Cardano, D., and Cogotti, A. (2007). A new technique to measure the aerodynamic response of passenger cars by a continuous flow yawing. *SAE Technical Paper*, SP-2066(2007-01-0902). 98, 118, 181
- Carlino, G. and Cogotti, A. (2006). Simulation of transient phenomena with the turbulence generation system in the Pininfarina wind tunnel. *SAE Technical Paper*, SP-1991(2006-01-1031). 98
- Chadwick, A., Garry, K., and Howell, J. (2000). Transient aerodynamic characteristics of simple vehicle shapes by the measurement of surface pressures. *SAE Technical Paper*, (2000-01-0876). 107

- Chen, K.-H., Johnson, J., Dietschi, U., and Khalighi, B. (2009). Wind noise measurements for automotive mirrors. *SAE Technical Paper*, 2009-01-0184. 34, 48
- Chometon, F., Strzelecki, A., Ferrand, V., Dechipre, H., Dufour, P. C., Gohlke, M., and Herbert, V. (2005). Experimental study of unsteady wakes behind an oscillating car model. *SAE Technical Paper*, SP-1931(2005-01-0604). 105
- Chue, S. H. (1975). Pressure probes for fluid measurement. *Prog. Aerosp. Sci.*, 16(2):147–223. 116
- Cogotti, A. (1997). Aeroacoustics development in Pininfarina. *SAE Technical Paper*, SP-1232(970402). 44, 46
- Cogotti, A. (1999). Ground effect of a simplified car model in side-wind and turbulent flow. *SAE Technical Paper*, (1999-01-0652). 96
- Cogotti, A. (2001). Flow field of a car moving in the far wake of another car. flow field of a car moving in the far wake or another car – preliminary information and interpretation. In *Presentation*. 3rd ECARA unsteady aerodynamics working group meeting, Turin. 96
- Cogotti, A. (2002). Preliminary information about unsteady aerodynamics at Pininfarina. In *Presentation*. 4th ECARA unsteady aerodynamics working group meeting, Turin. 98
- Cogotti, A. (2003a). From steady-state to unsteady aerodynamics and aeroacoustics: the evolution of the testing environment in the Pininfarina wind tunnel. In *7th international symposium on fluid control, measurement and visualization*. FLUCOME 03, Sorrento. 98, 156, 157

REFERENCES

- Cogotti, A. (2003b). Generation of a controlled level of turbulence in the Pininfarina wind tunnel for the measurement of unsteady aerodynamics and aeroacoustics. *SAE Technical Paper*, SP-1786(2003-01-0430). 96, 98
- Cogotti, A. (2003c). Unsteady aerodynamics at Pininfarina. road turbulence simulation and time-dependant techniques. In *Automotive and engine technology*, Renningen. 5th International Stuttgart Symposium, FKFS/Stuttgart University, Expert Verlag. 98
- Cogotti, A. (2004). Update on the Pininfarina turbulence generation system and its effects on the car aerodynamics and aeroacoustics. *SAE Technical Paper*, SP-1874(2004-01-0807). 41, 98
- Cogotti, A. (2006). Upgrade of the Pininfarina wind tunnel - the new 13-fan drive system. *SAE Technical Paper*, SP-1991(2006-01-0569). 39, 41, 156, 158, 165
- Cogotti, A. (2008). Evolution of performance of an automotive wind tunnel. *J. Wind Eng. Ind. Aerodyn.*, 96:667–700. 98, 222
- Cogotti, A., Cardano, D., Carlino, G., and Cogotti, F. (2005). Aerodynamics and aeroacoustics of passenger cars in a controlled high turbulence flow: some new results. *SAE Technical Paper*, SP-1931(2005-01-1455). 99
- Cogotti, A., Carlino, G., and Cogotti, F. (2003). Additional information of the Pininfarina turbulence generation system. In *Presentation*. 5th ECARA unsteady aerodynamics working group meeting, Munich. 98
- Cogotti, F. (2005). Aeroacoustics by microphone arrays: some examples regarding a rear view mirror. In *Workshop on particle image velocimetry in car industry*. PIVNET 2 thematic network. 47

- Cooper, K. R. (1976). A wind tunnel investigation into the fuel savings available from the aerodynamic drag reduction of trucks. *NRC Canada, Mech. Eng. Quarterly Bulletin*, 3. 82
- Cooper, K. R. (1991). The wind tunnel simulation of wind turbulence for surface vehicle testing. *J. Wind Eng. Ind. Aerodyn.*, 38:71–81. 15
- Cooper, K. R. (2002). Wind-tunnel simulation of gusty winds for surface vehicles. In *Presentation*. 4th ECARA unsteady aerodynamics working group meeting, Turin. 5
- Cooper, K. R. and Larose, G. (2002). Unsteady aerodynamic force measurement on automobiles. In *Presentation*. 4th ECARA unsteady aerodynamics working group meeting, Turin. 104
- Cooper, K. R. and Watkins, S. (2007). The unsteady wind environment of road vehicles, part one: a review of the on-road turbulent wind environment. *SAE Technical Paper*, SP-2066(2007-01-1236). 63, 179
- Cooper, R. K. (1981). The effect of cross-winds on trains. *J. Fluid Eng.-T. ASME*, 103(1):170–178. 86, 87, 107
- Cooper, R. K., Anandarajah, A., Clare, R., and Pope, C. W. (2002). A review of the factors affecting the overturning of trains in crosswinds. In *Proceedings*. 4th MIRA international conference on vehicle aerodynamics, Warwick. 107
- Courant, R., Friedrichs, K., and Lewy, H. (1928). Über die partiellen Differenzengleichungen der mathematischen Physik. *Math Ann*, 100(1):32–74. 49
- Crouse, B., Balasubramanian, G., Freed, D., Hazir, A., and Blumrich, R. (2009). Validation study of a flow-excited helmholtz resonance. In *Proceedings of Euromech 504*, Munich. 35

REFERENCES

- Curle, N. (1955). The influence of solid boundaries upon aerodynamic sound. *Proc. Roy. Soc.*, 231(1187):505–514. 49
- Davenport, A. G. (1961). The application of statistical concepts to the wind loading of structures. *Proc. Inst. Civil Eng.*, 19(4):449–472. 80
- Deblauwe, F., Jansen, K., and Robin, M. (2007). Extending the usability of near-field acoustic holography and beamforming by using focalization. In *Proceedings. ICSV14*, Cairns, Australia. 46, 47
- Docton, M. and Dominy, R. G. (1994). Passenger vehicles in unsteady cross winds. In *Road Vehicle Aerodynamics*, Loughborough, UK. Royal Aeronautical Society Conference. 103
- Dominy, R. G. and Hodson, H. P. (1993). An investigation of factors influencing the calibration of five-hole probes for three-dimensional flow measurements. *J. Turbomach.*, 115(3):513–519. 123, 124
- Dominy, R. G. and Ryan, A. (1999). An improved wind tunnel configuration for the investigation of aerodynamic cross wind gust response. *SAE Technical Paper*, SP-1441(1999-01-0808). 103
- Duell, E., Kharazi, A., Muller, S., Ebeling, W., and Mercker, E. (2010). The BMW AVZ wind tunnel center. *SAE Technical Paper*, SP-2269(2010-01-0118). 10
- Duncan, B. D., Sengupta, R., Mallick, S., Shock, R., and Sims-Williams, D. B. (2002). Numerical simulation and spectral analysis of pressure fluctuations in vehicle aerodynamic noise generation. *SAE Technical Paper*, SP-1667(2002-01-0597). 50
- El Hachemi, Z., Hallez, R., Mendonça, F., and Schofield, M. (2002). On the coupling

- of aeroacoustic sources from CFD and noise propagation codes. In *Proceedings. 4th MIRA international conference on vehicle aerodynamics*, Warwick. 50
- ESDU 74030 (1976). *Characteristics of atmospheric turbulence near the ground*. Engineering and sciences data unit report. 65, 69
- Fastl, H. and Zwicker, E. (2007). *Psycho-acoustics: facts and models*. Springer, Berlin, third edition. xviii, 25, 56, 57, 58, 59, 167
- Ffowcs Williams, J. E. and Hall, L. H. (1970). Aerodynamic sound generation by turbulent flow in the vicinity of a scattering half plane. *J. Fluid Mech.*, 40:657–670. 49
- Ffowcs Williams, J. E. and Hawkings, D. L. (1969). Sound generation by turbulence and surfaces in arbitrary motion. *Phil. Trans. Roy. Soc.*, 264:321–342. 49
- Fieles-Kahl, M. and Riegel, M. (2010). In-cabin tyre road noise of cars – determination and analysis. In *International conference on noise and vibration engineering*, Leuven. 37
- Flasch, M., Wickern, G., and Grogger, H. (2003). Experimental investigation into cross wind sensitivity of a passenger car. In *Presentation. 5th ECARA unsteady aerodynamics working group meeting*, Munich. 99, 104
- Fletcher, H. and Munson, W. (1933). Loudness, its definition, measurement and calculation. *J. Acoust. Soc. Am.*, 5(2):82–108. 51, 53
- Fletcher, H. and Steinberg, J. C. (1929). Articulation testing methods. *Bell Sys. Tech. Jour.*, 8:806–854. 55
- Freeman, C. and Gaylard, A. (2008). Integrating CFD and experiment: The Jaguar Land Rover aeroacoustics process. In *Proceedings. 7th MIRA international conference on vehicle aerodynamics*, Coventry. 130, 131

REFERENCES

- Gade, S. (2007). *What is sound quality?*, pages 20–23. Number 1. Brüel and Kjær Magazine. 60
- Gaylard, A. (2008). The aerodynamic development of the new Jaguar XF. In *Proceedings*. 7th MIRA international conference on vehicle aerodynamics, Coventry. 148
- Gaylard, A., Beckett, M., Gargoloff, J., and Duncan, B. (2010). Cfd-based modelling of flow conditions capable of inducing hood flutter. *SAE Technical Paper*, SP-2269(2010-01-1011). 50
- Gaylard, A. P. (2006). CFD simulation of side glass surface noise spectra for a bluff SUV. *SAE Technical Paper*, SP-1991(2006-01-0137). 32
- Gaylard, A. P., Howell, J. P., and Garry, K. P. (2007). Observation of flow asymmetry over the rear of notchback vehicles. *SAE Technical Paper*, SP-2066(2007-01-0900). 8
- Genuit, K. (1984). *A model for description of the external ear transfer function*. PhD thesis, Rheinisch-Westfälische Technische Hochschule, Aachen, Germany. 40
- George, A. R. (1990). Automobile aerodynamic noise. *SAE Technical Paper*, (900315). 27, 30, 34, 119
- Gilhome, B. R. and Saunders, J. W. (2002). The effects of turbulence on peak and average pressures on a car door. *SAE Technical Paper*, SP-1667(2002-01-0253). xviii, 85
- Gilhome, B. R., Saunders, J. W., and Sheridan, J. (2001). Time averaged and unsteady near-wake analysis of cars. *SAE Technical Paper*, SP-1600(2001-01-1040). 8
- Gillieron, P. and Noger, C. (2004). Contribution to the analysis of transient aerodynamic effects acting on vehicles. *SAE Technical Paper*, SP-1874(2004-01-1311). 108

- Gleason, M. E. (2007). Detailed analysis of the buff body blockage phenomenon in closed wall wind tunnels utilising CFD. *SAE Technical Paper*, SP-2066(2007-01-1046). 12
- Guilmineau, E. and Chometon, F. (2008). Numerical and experimental analysis of unsteady separated flow behind an oscillating car model. *SAE Technical Paper*, SP-2151(2008-01-0738). 105
- Haruna, S., Nouzawa, T., Kamimoto, I., and Sato, H. (1990). An experimental analysis and estimation of aerodynamic noise using a production vehicle. *SAE Technical Paper*. 30
- He, L. (1996). Time marching calculations of unsteady flows, blade row interaction and flutter. *Von Kármán Institute for Fluid Dynamics lecture series: Unsteady flows in turbomachines*. 78, 128
- HEAD Acoustics NVH Division (1998). *HMS III.1 datasheet*. HEAD Acoustics. 140
- HEAD Acoustics NVH Division (2006). *Artificial head equalisation*. HEAD acoustics. 141
- HEAD Acoustics NVH Division (2010). *HEAD VISOR*. HEAD Acoustics. 47
- Helfer, M. (1998a). *Wind noise*. Testing technology international. 26
- Helfer, M. (1998b). Wind noise – physics and manipulation. In *International short course: using aerodynamics to improve the properties of cars*. Euromotor / FKFS. 26
- Helfer, M. (1999). Aeroacoustics of cars. In *DGLR fachausschusssitzung T2.3 strömungsakustik*, Braunschweig. 29, 36
- Helfer, M. (2000a). Aeroacoustic testing in wind tunnels. In *Proceedings*. 3rd MIRA international conference on vehicle aerodynamics, Rugby. 28

REFERENCES

- Helfer, M. (2000b). Localization of sound sources. In Wiedemann, J. and Hucho, W. H., editors, *Progress in vehicle aerodynamics – advanced experimental techniques*, Renningen. Expert Verlag. xviii, 44, 45
- Helfer, M. (2005). General aspects of vehicle aeroacoustics. In *Lecture series: road vehicle aerodynamics*. Von Karman Institute, Rhode-Genèse, Belgium. xviii, 27, 33, 42, 43, 46
- Helfer, M. (2009). Sound source localisation with acoustic mirrors. In *NAG/DAGA congress*, Rotterdam. 42
- Helfer, M. and Busch, J. (1992). Contribution of aerodynamic noise sources to interior and exterior vehicle noise. In *DGLR workshop: aeroacoustics of cars*, Emmeloord. 1, 57, 191
- Helfer, M. and Wiedemann, J. (2006). Design of wind tunnels for aeroacoustics. In *Lecture series: experimental aeroacoustics*. Von Karman Institute, Rhode-Genèse, Belgium. 39, 40, 286
- Hellman, R. and Zwicker, E. (1987). Why can a decrease in dB(A) produce an increase in loudness? *J. Acoust. Soc. Am.*, 82(5):1700–1705. 54
- Hennig, A., Mercker, E., and Wiedemann, J. (2010). EADE correlation test 2010. Technical report, European Aerodynamic Data Exchange. 155, 156, 163
- Hooper, J. D. and Musgrove, A. R. (1997). Reynolds stress, mean velocity, and dynamic static pressure measurement by a four-hole pressure probe. *Exp. Therm. Fluid. Sci.*, 15(4):375–383. 116, 133
- Hoshino, H. and Kato, H. (2002). A new objective evaluation method of wind noise in a car based on human hearing properties. *Acoust. Sci. and Tech.*, 23(1):17–24. 59

- Howell, J. (2000). Real environment for vehicles on the road. In Wiedemann, J. and Hucho, W. H., editors, *Progress in vehicle aerospace*, Renningen. Advanced experimental techniques/Euromotor course, FKFS/Stuttgart University, Expert Verlag. 63, 64, 82
- Howell, J. (2002). Ride quality for an SUV in windy conditions. In *Proceedings*. 4th MIRA international conference on vehicle aerodynamics, Warwick. 80, 83, 106
- Howell, J. (2004). An estimation of the unsteady aerodynamic loads on a road vehicle in windy conditions. *SAE Technical Paper*, SP-1874(2004-01-1310). 80, 83
- Howell, J. (2011). The decay of bluff body wakes. *SAE Technical Paper*, SP-2305(2011-01-0178). 65
- Howell, J. and Baden Fuller, J. (2010). A relationship between lift and lateral aerodynamic characteristics for passenger cars. *SAE Technical Paper*, SP-2269(2010-01-1025). 8
- Howell, J., Baden Fuller, J., and Passmore, M. (2009). The effect of free stream turbulence on A-pillar airflow. *SAE Technical Paper*, SP-2226(2009-01-0003). 31, 95
- Howell, J., Sherwin, C., Passmore, M., and Le Good, G. (2002). Aerodynamic drag of a compact SUV as measured on-road and in the wind tunnel. *SAE Technical Paper*, SP-1667(2002-01-0529). 92, 118
- Howell, J., Windsor, S., and Le Good, G. (2006). A novel test rig for the aerodynamic development of a door mirror. *SAE Technical Paper*, SP-1991(2006-01-0340). xvii, 30, 34
- Hucho, W.-H. (1998). *Aerodynamics of road vehicles*. SAE, Warrendale, PA, fourth edition. xvii, 3, 4, 5, 10, 11, 25, 106, 163

REFERENCES

- Ih, K. D., Nam, K.-U., and Jung, S. G. (2005). Wind noise reduction of vehicle using underbody acoustic holography. *SAE Technical Paper*, SP-1931(2005-01-0605). 37
- Ingram, K. C. (1978). The wind averaged drag coefficient applied to heavy goods vehicles. Report 392, Transport and road research laboratory. 82
- Irwin, H. P. A. H., Cooper, K. R., and Girard, R. (1979). Correction of distortion effects caused by tubing systems in measurements of fluctuating pressures. *J. Ind. Aerodyn.*, 5:93–107. 133
- ISO226:1961 (1961). *Acoustics – Normal equal-loudness-level contours*. ISO, Geneva, Switzerland. 51
- ISO226:2003 (2003). *Acoustics – Normal equal-loudness-level contours*. ISO, Geneva, Switzerland. 51
- ISO532:1975 (1975). *Acoustics – Method for calculating loudness level*. ISO, Geneva, Switzerland. 53, 167
- J2071 (1994). *Aerodynamic testing of road vehicles - open throat wind tunnel adjustment*. SAE, Warrendale, PA. 9
- Jaitlee, R., Alam, F., and Watkins, S. (2007). Pressure fluctuations on automotive rear view mirrors. *SAE Technical Paper*, SP-2066(2007-01-0899). 34
- Janssen, L. J. and Hucho, W. H. (1975). *Aerodynamische entwicklung von VW Golf und Scirocco*, volume 77, pages 1–5. ATZ. 8
- Juvé, D. (2009). Aeroacoustics research in Europe: the CEAS-ASC resport on 2008 highlights. *J. Sound Vib.*, 328:213–242. 37
- Kaltenhauser, A. (2003). Wind noise in turbulent flow. In *Presentation*. 5th ECARA unsteady aerodynamics working group meeting, Munich. 116

- Karbon, K. J. and Dietschi, U. D. (2005). Computational analysis and design to minimise vehicle roof rack wind noise. *SAE Technical Paper*, SP-1931(2005-01-0602). 37
- Katoh, D., Hashizume, Y., Kohri, I., and Takagi, M. (2011). Comparison of impact due to an aerodynamic component in wind tunnel and on-road tests. *SAE Technical Paper*, SP-2305(2011-01-0157). 116
- Kendall, M. G. (1955). Further contributions to the theory of paired comparisons. *Biometrics*, 11(1):43–62. 61
- Kendall, M. G. and Babington Smith, B. (1940). On the method of paired comparisons. *Biometrika*, 31(3/4):324–345. 61
- Khalighi, B., Johnson, J. P., Chen, K.-H., and Lee, R. G. (2008). Experimental characterization of the unsteady flow field behind two outside rear view mirrors. *SAE Technical Paper*, SP-2151(2008-01-0476). 34, 48
- Kim, B. S., Kim, G. J., and Lee, T. K. (2007). The identification of tyre induced vehicle interior noise. *Applied Acoustics*, 68(1):134–156. 37
- Kim, G. J., Holland, K. R., and Lalor, N. (1997). Identification of the airborne component of tyre-induced vehicle interior noise. *Applied Acoustics*, 51(2):141–156. 37
- Kim, M.-S., Lee, J.-H., Kee, J.-D., and Chang, J.-H. (2001). Hyundai full scale aero-acoustic wind tunnel. *SAE Technical Paper*, SP-1600(2001-01-0629). 39
- Knebel, P., Kittel, A., and Peinke, J. (2010). Atmospheric wind field conditions generated by active grids. *Exp. Fluids*. 102
- Krampol, S., Riegel, M., and Wiedemann, J. (2009a). Noise synthesis – a procedure to simulate the turbulent noise interior of cars. In *7th FKFS conference "progress in vehicle aerodynamics and thermal management"*, Stuttgart. 83, 96

REFERENCES

- Krampol, S., Riegel, M., and Wiedemann, J. (2009b). A procedure to simulate the turbulent noise interior of cars. In *NAG/DAGA congress*, Rotterdam. 83
- Kryter, K. D. (1962). Methods for the calculation and use of the articulation index. *J. Acoust. Soc. Am.*, 34(11). 55
- Künstner, R., Potthof, J., and Essers, U. (1995). The aero-acoustic wind tunnel of Stuttgart University. *SAE Technical Paper*, SP-1078(950625). 39
- Lappe, U. O. and Davidson, B. (1963). On the range and validity of Taylor's hypothesis and the Kolmogoroff spectral law. *J. Atmos. Sci.*, 20(6):569–576. 71
- Lawson, A. A., Dominy, R. G., and Sheppard, A. (2003). A comparison between on-road and wind tunnel surface pressure measurements on a compact SUV. *SAE Technical Paper*, SP-1786(2003-01-0653). 85, 116
- Lawson, A. A., Dominy, R. G., and Sims-Williams, D. B. (2007). A comparison between on-road and wind tunnel surface pressure measurements on a mid-sized hatchback. *SAE Technical Paper*, SP-2066(2007-01-0898). 85, 119
- Lawson, A. A., Sims-Williams, D. B., and Dominy, R. G. (2008). Effects of on-road turbulence on vehicle surface pressures in the a-pillar region. *SAE Technical Paper*, SP-2151(2008-01-0474). 66, 85, 89
- Lawson, T. V. (1980). *Wind effects on buildings*. Applied Science Publishers, first edition. 63
- Lepley, D. J., Graf, A., Powell, R., and Senthooran, S. (2010). A computational approach to evaluate the vehicle interior noise from greenhouse wind noise sources. *SAE Technical Paper*, SP-2269(2010-01-0285). 48, 50

- Li, Y., Kamioka, T., Nouzawa, T., Nakamura, T., Okada, Y., and Ichikawa, N. (2003). Evaluation of aerodynamic noise generated in production vehicle using experiment and numerical simulation. *SAE Technical Paper*, SP-1786(2003-01-1314). 32, 48
- Li, Y., Kasaki, N., Tsunoda, H., Nakamura, T., and Nouzawa, T. (2006). Evaluation of wind noise sources using experimental and computational methods. *SAE Technical Paper*, SP-1991(2006-01-0343). 32, 41
- Lighthill, M. J. (1952). On sound generated aerodynamically, part 1, general theory. *Proc. Roy. Soc. Lond. A*, 211(1107):564–587. 20, 49
- Lighthill, M. J. (1954). On sound generated aerodynamically, part 2, turbulence as a source of sound. *Proc. Roy. Soc. Lond. A*, 222(1148):1–32. 21, 49
- Lindener, N., Miehl, H., Cogotti, A., Cogotti, F., and Maffei, M. (2007). Aeroacoustic measurements in turbulent flow on the road and in the wind tunnel. *SAE Technical Paper*, SP-2066(2007-01-1551). xviii, xix, 41, 69, 88, 89, 90, 91, 118, 119, 158, 187, 188, 191, 195
- Lock, A., Palin, R., and Knight, J. (2002). Aerodynamic stability prediction. In *Proceedings*. 4th MIRA international conference on vehicle aerodynamics, Warwick. 104
- Lock, A. S., Palin, R. B., Knight, J. J., Webb, J., and Burnett, M. (2003). Preliminary results of an investigation into unsteady aerodynamics and its influence on vehicle stability preliminary results of an investigation into unsteady aerodynamics and its influence on vehicle stability and refinement. In *Presentation*. 5th ECARA unsteady aerodynamics working group meeting, Munich. 104
- Lounsberry, T. H., Gleason, M. E., and Puskarz, M. M. (2007). Laminar flow whistle on a vehicle side mirror. *SAE Technical Paper*, SP-2066(2007-01-1549). 33

REFERENCES

- Macklin, R., Garry, K., and Howell, J. (1997). Assessing the effects of shear and turbulence during the dynamic testing of crosswind sensitivity of road vehicles. *SAE Technical Paper*, SP-1232(970135). 107
- Maffei, M., Bianco, A., and Carlino, G. (2009). Side window buffeting investigation by stereoscopic particle image velocimetry in low and high turbulence regime. *SAE Technical Paper*, SP-2226(2009-01-0182). 36
- Maffei, M. and Carlino, G. (2008). Preliminary results on effects of turbulence length scale on aerodynamic forces. In *11th ECARA unsteady aerodynamics working group meeting*. 98
- Mankowski, O., Sims-Williams, D., Dominy, R., Duncan, B., and Gargoloff, J. (2011). The bandwidth of transient yaw effects on vehicle aerodynamics. *SAE Technical Paper*, SP-2305(2011-01-0160). 50, 97, 103
- Mansor, S. and Passmore, M. A. (2008). Estimation of bluff body transient aerodynamics using an oscillating model rig. *J. Wind Eng. Ind. Aerodyn.*, 96:1218–1231. 104, 105
- Massey, B. and Ward-Smith, J. (2005). *Mechanics of fluids*. Spon Press, Abingdon, seventh edition. 116
- Matsushima, Y. and Kohri, I. (2005). Experimental study for applicable limit of acoustic analogy to predict aero-acoustic noise of commercial vehicles. *SAE Technical Paper*, SP-1931(2005-01-0606). 32
- Mayer, J., Schrefi, M., and Demuth, R. (2007). On various aspects of the unsteady aerodynamic effects on cars under crosswind conditions. *SAE Technical Paper*, SP-2066(2007-01-1548). xviii, 85, 86, 87, 101, 116, 118

- Mayer, W. and Wiedemann, J. (2003). Road load determination based on driving-torque-measurement. *SAE Technical Paper*, SP-1786(2003-01-0933). 38
- Mayer, W. and Wiedemann, J. (2007). The influence of rotating wheels on total road load. *SAE Technical Paper*, SP-2066(2007-01-1047). 38
- Mercker, E. and Pengel, K. (1994). On the induced noise of test sections in different wind tunnels and in the cabin of a passenger car. *SAE Technical Paper*, (940415). 39
- Mercker, E. and Wiedemann, J. (1996). On the correction of interference effects in open jet wind tunnels. *SAE Technical Paper*, (960671). 11
- Milbank, J. (2004). *Investigation of fluid-dynamic cavity oscillations and the effects of flow angle in an automotive context using an open-jet wind tunnel*. PhD thesis, School of Aerospace, Mechanical and Manufacturing Engineering, RMIT University, Melbourne, Australia. 33
- Miller, C. (2003). A once in 50-year speed map for Europe derived from mean sea level pressure measurements. *J. Wind Eng. Ind. Aerodyn.*, 91:1813–1826. 19
- Moore, B. C. J. and Glasberg, B. R. (1996). A revision of Zwicker's loudness model. *Acta Acust.*, 82(2):335–345. 53
- Moran, P. A. P. (1947). On the method of paired comparisons. *Biometrika*, 34(3-4):363–365. *Biometrika*. 61
- Müller, J. and Seydell, B. (2002). Numerical investigation into sunroof buffeting. In *Proceedings*. 4th MIRA international conference on vehicle aerodynamics, Warwick. 35
- Murad, N. M., Nasar, J., Alam, F., and Watkins, S. (2004). Simulation of vehicle A-pillar

REFERENCES

- aerodynamics using various turbulence models. *SAE Technical Paper*, SP-1874(2004-01-0231). 32
- National Instruments (2009). *DAQ M Series: NI USB-621x user manual*. National Instruments Corporation. 135
- National Semiconductor (2010). *LP2950/LP2951 series of adjustable micropower voltage regulators*. National Semiconductor Corporation. 132
- Newnham, P., Passmore, M., and Baxendale, A. (2008). The effect of raised freestream turbulence on the flow around leading edge radii. *SAE Technical Paper*, SP-2151(2008-01-0473). 31
- Newnham, P., Passmore, M., Howell, J., and Baxendale, A. (2006). On the optimisation of road vehicles leading edge radius in varying levels of freestream turbulence. *SAE Technical Paper*, SP-1991(2006-01-1029). 31, 235
- Nguyen, T. M., Saunders, J. W., and Watkins, S. (1997). The sideways dynamic force on passenger cars in turbulent winds. *SAE Technical Paper*, SP-1232(970405). 95
- Nor, M. J. M., Fouladi, M. H., Nahvi, H., and Ariffin, A. K. (2008). Index for vehicle acoustical comfort inside a passenger car. *Applied Acoustics*, 69(4):343–353. 41, 60
- Norton, M. P. (1989). *Fundamentals of noise and vibration analysis for engineers*. Cambridge University Press. 25
- Nouzawa, T., Hiasa, K., Nakamura, T., Kawamoto, K., and Sato, H. (1992). Unsteady-wake analysis of the aerodynamic drag on a notchback model with critical afterbody geometry. *SAE Technical Paper*, SP-908(920202). 7
- Objet (2009). *FullCure materials*. Objet Geometries Limited. 125

- Oettle, N., Mankowski, O., Sims-Williams, D., Dominy, R., Freeman, C. M., and Gaylard, A. (2012). Assessment of a vehicle's transient aerodynamic response. *SAE Technical Paper*, SP-2333(2012-01-0449).
- Oettle, N. R., Sims-Williams, D. B., Dominy, R. G., Darlington, C. J. E., and Freeman, C. M. (2011). The effects of unsteady on-road flow conditions on cabin noise: spectral and geometric dependence. *SAE Int. J. Passeng. Cars – Mech. Syst.*, 4(1):120–130.
- Oettle, N. R., Sims-Williams, D. B., Dominy, R. G., Darlington, C. J. E., Freeman, C. M., and Tindall, P. F. (2010). The effects of unsteady on-road flow conditions on cabin noise. *SAE Technical Paper*, SP-2269(2010-01-0289).
- Oettle, N. R., Sims-Williams, D. B., Dominy, R. G., and Freeman, C. M. (2013). Evaluation of the aerodynamic and aeroacoustic response of a vehicle to transient flow conditions. *SAE Int. J. Passeng. Cars – Mech. Syst.*, 6(1):389–402.
- Onusic, H., Medeiros Hage, M., and Baptist, E. (2000). Articulation index (al): Concepts and applications. *SAE Technical Paper*, (2000-01-3150). 55
- Ortega, J. M. and Salari, K. (2004). An experimental study of drag reduction devices for a trailer underbody and base. In *Proceedings. 34th AIAA fluid dynamics conference*, Portland. 82
- Otto, N. and Feng, B. J. (1995). Wind noise sound quality. *SAE Technical Paper*, (951369):1103–1107. 59
- Passmore, M. A. and Mansor, S. (2006). The measurement of transient aerodynamics using an oscillating model facility. *SAE Technical Paper*, SP-1991(2006-01-0338). 104, 105, 274

REFERENCES

- Passmore, M. A., Richardson, S., and Imam, A. (2001). An experimental study of unsteady vehicle aerodynamics. *Proc. Instn. Mech. Engrs.*, 215(D). 99, 100
- Pedley, T. J. (2001). Sir (michael) james lighthill. 23 january 1924-17 july 1998. *Biogr. Mem. Fell. R. Soc.*, 47. 20
- Peng, G. C. (2007). SEA modelling of vehicle wind noise and load case representation. *SAE Technical Paper*, (2007-01-2304). 195
- Peric, C., Watkins, S., Lindqvist, E., and Saunders, J. (1997). Effects of on-road turbulence on automotive wind noise: comparing wind-tunnel and on-road tests. *SAE Technical Paper*, SP-1232(970406). 41, 110, 116, 119
- Potthof, J., Helfer, M., and Essers, U. (1994). The new aeroacoustic wind tunnel at Stuttgart University: equipment and first results. In *Congrès SIA*, Lyon. 39
- Powell, D. C. and Elderkin, C. E. (1974). An investigation of the application of Taylor's hypothesis to atmospheric boundary layer turbulence. *J. Atmos. Sci.*, 31(4):990–1002. 71
- Rich, M. D. (2001). *A million random digits*. RAND. 170
- Riederer, S. (2003). Overtaking manoeuvres – computational and experimental data of unsteady aerodynamics. In *Presentation*. 5th ECARA unsteady aerodynamics working group meeting, Munich. 108
- Riegel, M. and Wiedemann, J. (2008). A test stand method to determine tyre-road noise in the interior of passenger vehicles. In *5th international styrian noise, vibration and harshness conference*, Graz. 37
- Riegel, M., Wiedemann, J., and Helfer, M. (2006). The effect of turbulence on in-cabin

- wind noise - a comparison of road and wind tunnel results. In *Proceedings*. 6th MIRA international conference on vehicle aerodynamics, Gaydon. 119
- Roach, P. E. (1987). The generation of nearly isotropic turbulence by means of grids. *Int. J. Heat Fluid Flow*, 8(2):82–92. 94
- Robinson, D. W. and Dadson, R. S. (1956). A re-determination of the equal-loudness relations for pure tones. *Br. J. Appl. Phys.*, 7:156–181. 51
- Ryan, A. and Dominy, R. G. (1998). The aerodynamic forces induced on a passenger vehicle in response to a transient cross-wind gust at a relative incidence of 30°. *SAE Technical Paper*, SP-1318(980392). 103
- SAE J 1594:2010 (2010). *Vehicle aerodynamics terminology*. SAE, Warrendale, PA. 13
- Saunders, J. (2003). Some turbulence scale problems and their effect on determining door seal lift-off in the wind tunnel. In *Presentation*. 5th ECARA unsteady aerodynamics working group meeting, Munich. 85
- Saunders, J. and Wordley, S. (2006). A review of measurement of ambient turbulence with respect to ground vehicles. *SAE Technical Paper*, SP-1991(2006-01-1028). 64
- Saunders, J. W. and Mansour, R. (2000). On-road and wind tunnel turbulence and its measurement using a four-hole dynamic probe ahead of several cars. *SAE Technical Paper*, (2000-01-0350). 72, 73, 75, 96, 118
- Schröck, D., Krantz, W., Widdecke, N., and Wiedemann, J. (2011). Unsteady aerodynamic properties of a vehicle model and their effect on driver and vehicle under side wind conditions. *SAE Technical Paper*, SP-2305(2011-01-0154). xix, 100, 101, 102, 105, 264, 274

REFERENCES

- Schröck, D., Widdecke, N., and Wiedemann, J. (2009a). Aerodynamic response of a vehicle to turbulent wind. In *7th FKFS conference "progress in vehicle aerodynamics and thermal management"*, Stuttgart. xix, 69, 100
- Schröck, D., Widdecke, N., and Wiedemann, J. (2009b). The effect of high turbulence intensities on surface pressure fluctuations and wake structures of a vehicle model. *SAE Technical Paper*, SP-2226(2009-01-0001). 8, 95, 96, 100
- Sedarous, J. A., Soliman, A., and Dunlop, M. (2007). Modeling and calibration of an aerodynamic cross-wind gust test facility. *SAE Technical Paper*, SP-2066(2007-01-1550). xix, 106, 107
- Seiferth, R. (1947). Pre-calculation and removal of oscillations in free-jet wind tunnels. In *AVA Monographs on German aeronautical research carried out since 1939*, volume D4.4. Ministry of aircraft production. 40
- Sensortech (2007). *HCLA series miniature amplified low pressure sensors*. Sensortech-nics GmbH. 132
- Sims-Williams, D. (2011). Cross winds and transients: reality, simulation and effects. *SAE Technical Paper*, SP-2305(2011-01-0172). 63, 80, 104
- Sims-Williams, D., Marwood, D., and Sprot, A. (2011). Links between notchback geometry, aerodynamic drag, flow asymmetry and unsteady wake structure. *SAE Technical Paper*, SP-2305(2011-01-0166). 8
- Sims-Williams, D. B. (2001). *Self-excited aerodynamic unsteadiness associated with passenger cars*. PhD thesis, University of Durham. 7
- Sims-Williams, D. B. (2008). Time resolved velocity and turbulence measurement on track and in the Pininfarina wind tunnel. Unpublished report. 64

- Sims-Williams, D. B. and Dominy, R. G. (1998). The validation and application of a 5-hole pressure probe with tubing transfer function correction for time-accurate measurements in unsteady flows. In *Proceedings*. 2nd MIRA international conference on vehicle aerodynamics, Birmingham. 133
- Sims-Williams, D. B., Dominy, R. G., and Howell, J. P. (2001). An investigation into large scale unsteady structures in the wake of real and idealized hatchback car models. *SAE Technical Paper*, SP-1600(2001-01-1041). 7
- Sims-Williams, D. B. and Duncan, B. D. (2002). The Ahmed model unsteady wake: experimental and computational analyses. *SAE Technical Paper*, SP-1667(2002-01-1315). 7
- Sims-Williams, D. B. and Hetherington, B. (2006). Support strut interference effects on passenger and racing car wind tunnel models. *SAE Technical Paper*, SP-1991. 8
- Sims-Williams, D. B., Kaye, S., and Watkins, S. (2006). Periodic structures within the formation region of trailing vortices. *SAE Technical Paper*, SP-1991(2006-01-1032). 8
- Slaboch, P. E., Morris, S. C., Ma, R., Shannon, D., Gleason, M., and Puskarz, M. (2009). Window buffeting measurements of a full scale vehicle and simplified small scale models. *SAE Technical Paper*, SP-2226(2009-01-0181). 35
- Stapleford, W. R. (1972). Aerodynamic noise in road vehicles. 2: A study of the sources and significance of aerodynamic noise in saloon cars. Technical Report 6, MIRA research report. 29
- Stapleford, W. R. and Carr, G. W. (1971). Aerodynamic noise in road vehicles. 1: The relationship between aerodynamic noise and the nature of the airflow. Technical Report 2, MIRA research report. 28, 29

REFERENCES

- Széchényi, E. (2000). Crosswind and its simulation. In Wiedemann, J. and Hucho, W. H., editors, *Progress in vehicle aerospace*, Renningen. Advanced experimental techniques/Euromotor course, FKFS/Stuttgart University, Expert Verlag. 104, 106
- Terhardt, E. (1998). *Akustische Kommunikation: Grundlagen mit Hörbeispielen*. Springer, Berlin, first edition. xviii, 58, 59
- Tews, J. (2008). Vehicle dependability study. Technical report, J.D. Power and Associates. 1
- Theissen, P., Wojciak, J., Heuler, K., Demuth, R., Indinger, T., and Adams, N. (2011). Experimental investigation of unsteady vehicle aerodynamics under time-dependent flow conditions - part 1. *SAE Technical Paper*, SP-2305(2011-01-0177). 104, 105
- Thomson, J. R. (1964). Wind noise – a practical approach. *SAE Technical Paper*, (640117). 28
- Tijdeman, H. (1975). On the propagation of sound waves in cylindrical tubes. *J. Sound. Vib*, 39(1):1–33. 133
- Tortosa, N. and Karbon, K. (2011). Aerodynamic development of the 2011 Chevrolet Volt. *SAE Technical Paper*, 2011-01-0168. 28
- Tsubokura, M., Takahashi, K., Matsuuki, T., Nakashima, T., Ikenaga, T., and Kitoh, K. (2010). HPC-LES for unsteady aerodynamics of a heavy duty truck in wind gust – 1st report: validation and unsteady flow structures. *SAE Technical Paper*, SP-2269(2010-01-1010). 50
- Ukita, T., China, H., and Kanie, K. (1997). Analysis of vehicle wind throb using CFD and flow visualization. *SAE Technical Paper*, SP-1232(970407). 35

- Ullrich, F. (2008). New possibilities for aeroacoustic optimization in the underbody region of vehicles. In Wiedemann, J., editor, *Progress in vehicle aerodynamics and thermal management V*, Renningen. Expert Verlag. 29
- Van Ligten, R. H. (1982). Interkeller S. A., Zürich. Personal communication. 55, 167
- Vino, G., Watkins, S., and Mousley, P. (2003). The passenger vehicle wake under the influence of upstream turbulence. *SAE Technical Paper*, SP-1786(2003-01-0650). 31, 235
- Volkert, R. and Kohl, W. (1987). The new Ford aerodynamic wind tunnel in Europe. *SAE Technical Paper*, (870248). 39, 158
- von Heesen, W. and Höpfer, M. (2004). Suppression of wind tunnel buffeting by flow control. *SAE Technical Paper*, SP-1874(2004-01-0805). 40
- von Heesen, W., Lindener, N., and Neise, W. (1996). Elimination of a high-frequency narrow-band noise component in a low-noise wind tunnel. *SAE Technical Paper*, (960904). 39
- von Kármán, T. (1948). Progress in the statistical theory of turbulence. *Physics Proc. N.A.S.*, 34. 69
- von Kármán, T. and Sears, W. R. (1938). Airfoil theory for non-uniform motion. *J. Aeronaut. Sci.*, 5(10):379–390. 80
- Wagner, A. (2003). *Ein Verfahren zur Vorhersage und Bewertung der Fahrerreaktion bei Seitenwind*. PhD thesis, Universität Stuttgart. 106, 118
- Wagner, A., Widdecke, N., and Wiedemann, J. (2001). Crosswind behaviour of driver and vehicle. In *Presentation*. 3rd ECARA unsteady aerodynamics working group meeting, Turin. 106

REFERENCES

- Wagner, A. and Wiedemann, J. (2002). Methods to evaluate crosswind behaviour. In *Proceedings. 4th MIRA international conference on vehicle aerodynamics*, Warwick. 106
- Wagner, A. and Wiedemann, J. (2003). An approach to predict and evaluate the driver's response to crosswind. In *Presentation. 5th ECARA unsteady aerodynamics working group meeting*, Munich. 106
- Walter, J., Duell, E., Martindale, B., Arnette, S., Geierman, R., Gleason, M., and Romberg, G. (2003). The DaimlerChrysler full-scale aeroacoustic wind tunnel. *SAE Technical Paper*, SP-1786(2003-01-0426). 39
- Walter, J., Duell, E., Martindale, B., Arnette, S., Nagle, P. A., Gulker, W., Wallis, S., and Williams, J. (2002). The driveability test facility wind tunnel no. 8. *SAE Technical Paper*, SP-1667(2002-01-0252). 10, 39
- Walter, J. A., Canacci, V., Rout, R. K., Koester, W., Williams, J., Walter, T. M., Jacob, S., and Nagle, P. A. (2005). Uncertainty analysis of aerodynamic coefficients in an automotive wind tunnel. *SAE Technical Paper*, SP-1931(2005-01-0870). 160
- Walter, J. A., Pruess, D. J., and Romberg, G. F. (2001). Coastdown/wind tunnel drag correction and uncertainty analysis. *SAE Technical Paper*, SP-1600(2001-01-0630). xix, 92
- Watkins, S. (1990). *Wind-tunnel modelling of vehicle aerodynamics: with emphasis on turbulent wind effects on commercial vehicle drag*. PhD thesis, Mech. Eng. Dept., RMIT, Melbourne, Australia. xviii, xix, 71, 72, 73, 75, 94, 95, 97, 182
- Watkins, S. (1999). *Topics in wind noise: automobile wind noise and its measurement part II*, volume SP-1457, chapter Chapter III: Gusts and transients. *SAE Technical Paper*. 30, 200

- Watkins, S. (2004). On the causes of image blurring in external rear view mirrors. *SAE Technical Paper*, SP-1874(2004-01-1309). 33
- Watkins, S. and Cooper, K. R. (2007). The unsteady wind environment of road vehicles, part two: effects on vehicle development and simulation of turbulence. *SAE Technical Paper*, SP-2066(2007-01-1237). 63, 73, 94, 104
- Watkins, S., Riegel, M., and Wiedemann, J. (2001). The effect of turbulence on wind noise: a road and wind-tunnel study. In *Automotive and engine technology*, Renningen. 4th International Stuttgart Symposium, FKFS/Stuttgart University, Expert Verlag. xviii, 41, 88, 96, 119
- Watkins, S. and Saunders, J. W. (1995). Turbulence experienced by road vehicles under normal driving conditions. *SAE Technical Paper*, (950997). 71
- Watkins, S. and Saunders, J. W. (1998). A review of the wind conditions experienced by a moving vehicle. *SAE Technical Paper*, SP-1318(981182). 66, 71
- Watkins, S., Saunders, J. W., Hoffmann, P. H., and Holmes, J. D. (1995). Turbulence experienced by moving vehicles, part 1, introduction and turbulence intensity. *J. Wind Eng. Ind. Aerodyn.*, 57:1–17. 71
- Waudby-Smith, P., Bender, T., and Vigneron, R. (2004). The GIE S2A full-scale aero-acoustic wind tunnel. *SAE Technical Paper*, SP-1874(2004-01-0808). 39
- Wickern, G. (2007). Recent literature on wind tunnel test section interference related to ground vehicle testing. *SAE Technical Paper*, SP-2066(2007-01-1050). 12, 163
- Wickern, G. and Brenberger, M. (2009a). Helmholtz resonators acting as sound sources in automotive aeroacoustics. *SAE Technical Paper*, SP-2226(2009-01-0183). 36, 195

REFERENCES

- Wickern, G. and Brenberger, M. (2009b). Scaling laws in automotive aeroacoustics. *SAE Technical Paper*, SP-2226(2009-01-0180). 27, 195
- Wickern, G. and Lindener, N. (2000). The Audi aeroacoustic wind tunnel: Final design and first operational experience. *SAE Technical Paper*, (2000-01-0868). 39
- Wiedemann, J. and Wagner, A. (2002). The driver as a sensor for cross wind effects. In *Presentation*. 4th ECARA unsteady aerodynamics working group meeting, Turin. 106
- Wojciak, J., Indinger, T., Adams, N. A., Theissen, P., and Demuth, R. (2010). Experimental study of on-road aerodynamics during crosswind gusts. In *Proceedings*. 8th MIRA international conference on vehicle aerodynamics, Grove. 76
- Wojciak, J., Theissen, P., Heuler, K., Indinger, T., Adams, N., and Demuth, R. (2011). Experimental investigation of unsteady vehicle aerodynamics under time-dependent flow conditions - part 2. *SAE Technical Paper*, SP-2305(2011-01-0164). 105
- Wordley, S. and Saunders, J. (2008). On-road turbulence. *SAE Technical Paper*, SP-2151(2008-01-0475). 73
- Wordley, S. J. (2009). *On-road turbulence*. PhD thesis, Monash University. xviii, xix, 69, 70, 73, 74, 75, 76, 78, 93, 94, 97, 116, 118, 129, 182, 184
- Wordley, S. J. and Saunders, J. W. (2009). On-road turbulence: Part 2. *SAE Technical Paper*, SP-2226(2009-01-0002). 73
- Yang, H., Sims-Williams, D. B., and He, L. (2006). Unsteady pressure measurement with correction on tubing distortion. In Hall, K. C., Kielb, R. E., and Thomas, J. P., editors, *Unsteady aerodynamics, aeroacoustics and aeroelasticity of turbomachines*, pages 521–529. Springer Netherlands. 133

- Zaccariotto, M., Burgade, L., and Chanudet, P. (1997). Aeroacoustic studies at P.S.A. In *Automotive and engine technology*, Renningen. 2nd International Stuttgart Symposium, FKFS/Stuttgart University, Expert Verlag. 35, 151
- Zimmer, G., Alam, F., and Watkins, S. (2001a). The contribution of the A-pillar vortex to passenger car in-cabin noise. In *14th Australasian fluid mechanics conference*. Adelaide University, Adelaide, Australia. 48, 87
- Zimmer, G., Alam, F., Watkins, S., and Peric, C. (2001b). Comparison of a high blockage wind tunnel, an open jet wind tunnel and on-road testing with respect to external surface pressures. *SAE Technical Paper*, SP-1600(2001-01-1087). 12

Colophon

This document was typeset in Palatino and Futura using \LaTeX . Palatino is an old-style serif typeface, designed by Hermann Zapf in 1948 and based on letter forms of the Italian Renaissance. The typeface is also an agreeable choice for a thesis submitted at Durham, with its historic status as a County Palatine.

Futura was designed by Paul Renner in 1927 and is a geometric sans-serif typeface, incorporating elements of the Bauhaus style. It features commonly in printed media and signage and is pictured here in the Stuttgart S-Bahn.

